

Chain-Growth Polymerization of 3-Hexylthiophene Towards Well-Defined Semiconductor Block Copolymers

Dissertation

zur Erlangung des akademischen Grades
eines Doktors der Naturwissenschaften (Dr. rer. nat.)
im Fach Chemie der Fakultät für
Biologie, Chemie und Geowissenschaften
der Universität Bayreuth

vorgelegt von

Ruth Lohwasser

Geboren in Bamberg/Deutschland

Bayreuth, 2011

Die vorliegende Arbeit wurde in der Zeit von September 2008 bis Dezember 2011 in der Arbeitsgruppe Angewandte Funktionspolymere am Lehrstuhl für Makromolekulare Chemie I der Universität Bayreuth unter der Betreuung von Prof. Dr. Mukundan Thelakkat angefertigt.

Vollständiger Abdruck der von der Fakultät für Biologie, Chemie und Geowissenschaften der Universität Bayreuth genehmigten Dissertation zur Erlangung des akademischen Grades Doktor der Naturwissenschaften (Dr. rer. Nat.).

Amtierender Dekan: Prof. Dr. Beate Lohnert

Tag des Einreichens der Dissertation: 07. Dez 2011

Tag des wissenschaftlichen Kolloquiums: 20. Jan 2012

Prüfungsausschuss:

Prof. Dr. Mukundan Thelakkat (Erstgutachter)

Prof. Dr. Stephan Förster (Zweitgutachter)

Prof. Dr. Peter Strohriegel (Vorsitzender)

Prof. Dr. Anna Köhler

„Wer fragt, ist ein Narr für fünf Minuten.
Wer nicht fragt, bleibt ein Narr für immer.“
(aus China)

Table of Contents

| | |
|--|--------|
| Summary/Zusammenfassung | |
| 1. Introduction | I-1 |
| 2. Overview of the Thesis | II-1 |
| 3. Toward Perfect Control of End Groups and Polydispersity in Poly-(3-hexylthiophene) via Catalyst Transfer Polymerization | III-1 |
| 4. Temperature and Molecular Weight Dependent Hierarchical Equilibrium Structures in Semiconducting Poly(3-hexylthiophene) | IV-1 |
| 5. On the Control of Aggregate Formation in Poly(3-hexylthiophene) by Solvent, Molecular Weight and Synthetic Method | V-1 |
| 6. Synthesis and Characterization of Monocarboxylated Poly(3-hexylthiophene)s via Quantitative End-Group Functionalization | VI-1 |
| 7. Synthesis of Amphiphilic Rod-Coil P3HT- <i>b</i> -P4VP Carrying a Long Conjugated Block using NMRP and Click Chemistry | VII-1 |
| 8. Donor-Acceptor, Crystalline-Crystalline P3HT- <i>b</i> -PPerAcr with Ordered Phase Separation in Bulk and Thin Film | VIII-1 |
| 9. Appendix: High Crystallinity and Nature of Crystal-Crystal Phase Transformations in Regioregular Poly(3-hexylthiophene) | IX-1 |
| 10. Appendix: Subsurface Mapping of Amorphous Surface Layers on Poly(3-hexylthiophene) | X-1 |
| 11. Appendix: Tailor-Made Synthesis of Poly(3-hexylthiophene) with Carboxylic End Groups and its Application as a Polymer Sensitizer in Solid-State Dye-Sensitized Solar Cells | XI-1 |
| 12. List of Publications | XII-1 |

Danksagung

Erklärung

Summary

This thesis deals with the synthesis, structural studies, properties and block copolymers of one of the most prominent hole conductors for organic photovoltaics, poly(3-hexylthiophene) (P3HT). Fundamental new aspects important for the control of the end groups and the capability to obtain block copolymers and low polydispersities were demonstrated. The well-defined P3HTs with different molecular weights were used to analyze crystalline structure formation in bulk and in solution. Hitherto unknown details about the microstructure and crystallinity were elucidated. Moreover, new synthetic approaches for carboxylated P3HT and block copolymers with long conjugated blocks were developed. Thus, two different types of block copolymers with a polar block (poly(4-vinylpyridine)/P4VP), capable of coordination to inorganic particles, or an electron conducting acceptor block (poly perylene bisimide acrylate/PPerAcr) were synthesized. For the first time, the required χN value for order-disorder transitions in crystalline block copolymers was realized. Their multifunctionality together with the capability to self-assemble into microphase separated structures makes them highly interesting for organic photovoltaics (OPVs). Aligned nanosize domains between donor and acceptor materials - matching the exciton diffusion length - promote charge separation and a more efficient transport of charges. Because of their well-controlled structure and their rod-coil or rod-rod nature, these block copolymers are highly relevant for fundamental studies of self-assembly in bulk and in solution.

The central point of this thesis is the detailed study of kinetics and control of the P3HT synthesis using Kumada catalyst transfer polymerization (KCTP). Kinetic studies of the active monomer formation via Grignard metathesis revealed that this reaction is rather slow, however, its completion is essential for controlled end groups. It was shown that LiCl accelerates this reaction and allows 100% H/Br end groups without long reaction times. MeOH as a quenching reagent was found to cause chain-chain coupling via disproportionation of the Ni-catalyst species. For non-functionalized P3HTs HCl was identified as the best quenching agent. The identification of these factors now allows the fast synthesis of any molecular weight with 100% homogeneous functionalizable H/Br end groups.

In the second part these well-defined P3HTs were used to investigate their equilibrium bulk structures and aggregation in solution. A temperature dependent phase diagram of the crystalline regions in P3HT was obtained in bulk. Further, the order of the P3HT side chains was elucidated for the first time as tilted and non-interdigitated. Moreover, the analysis of the semicrystalline order of P3HT showed extended chain crystals as the equilibrium structures up to a molecular weight of ~20 kDa. However, these crystals seem to be surrounded by non-crystallizable chain ends. For low molecular weight samples this effect is more pronounced, which results in a lower crystallinity. Such details have never been observed for less defined P3HTs. The study of the aggregate formation in solution revealed that the amount of aggregates and their nature (excitonic coupling, conjugation length) depends on the used solvent, the molecular weight and the synthetic method. The maximum fraction of aggregates in solution seemed to indicate the resulting charge carrier mobility measured in organic thin film field effect transistors (OFETs). For the well-defined P3HTs, even low molecular weight samples allow for high charge carrier mobility. If broad distributed P3HTs were extracted to remove the smaller molecular weight fractions, the remaining high molecular weight fraction can reach similar mobilities as the defined P3HTs.

In the third part the bromine end groups were used for the introduction of valuable carboxylic end groups in one single, selective and quantitative post-polymerization step. Thus, carboxylated polymers with a charge carrier mobility as high as $10^{-3} \text{ cm}^2/\text{Vs}$ were obtained. These functionalized polymers can be anchored onto surfaces, can coordinate nanoparticles or

can be used as end cappers for the formation of block copolymers. Additionally, a correlation of the melting enthalpies with the charge carrier mobilities indicated that the crystallinity is the determinant factor for the molecular weight dependence of the charge carrier mobility. A great challenge for the synthesis of P3HT containing block copolymers is to combine KCTP with other controlled polymerization methods. Especially conjugated blocks with high molecular weights are difficult to incorporate, because of their lower solubility and lower percentage of end groups. Here, it was demonstrated that copper catalyzed azide-alkyne cycloaddition, a so-called "click" reaction, is a simple and efficient approach to create high molecular weight P3HT macroinitiators for nitroxide mediated radical polymerization (NMRP). First, the synthesis of alkyne functionalized P3HT was optimized. HCl as a quenching reagent caused hydrohalogenation and hydration reactions and MeOH proved to be the quenching reagent of choice. In the second step, P3HT-alkyne was combined with an azide functionalized alkoxyamine to form the macroinitiator in one single post-polymerization step. Using this approach two different types of block copolymers were realized. The first type is amphiphilic P3HT-*b*-P4VP with a polar coil block, which is able to coordinate to inorganic particles. Thermal analysis showed that the crystallite size of P3HT is hardly influenced by the coil content when such long P3HT rod blocks are used. Preliminary investigations of the self-assembly in solution, demonstrated that colloidal structures with crystalline P3HT cores are obtained in P4VP selective solvents. Thus, P3HT-*b*-P4VP is an interesting system for hybrid photovoltaics and for investigating structure formation of rod-coil block copolymers in bulk and solution.

The second type of block copolymers are fully-functionalized P3HT-*b*-PPerAcrs, with PPerAcr as an electron conducting second block. With the new synthetic approach it was possible to get an exclusively P3HT-*b*-PPerAcr diblock copolymer with a high molecular weight. In this context a high content of PPerAcr of 64wt% was realized which is important for a balanced charge transport in OPVs. The pure diblock, the high molecular weight and, hence, a high χN parameter enabled for the first time the formation of a hexagonally ordered cylindrical bulk structure for a fully-functionalized crystalline-crystalline block copolymer. Additionally, in thin films, order-disorder transition and microphase separation was observed with domain sizes in the range of the exciton diffusion length. Therefore, this high molecular weight P3HT-*b*-PPerAcr is highly interesting for application in OPVs.

In conclusion, the optimization of the synthesis of P3HT allowed a better understanding of fundamental aspects about its molecular weight dependent structures and the resulting properties. Further, new end groups could be introduced to widen its applications. Additionally, long P3HT blocks were efficiently incorporated into well-defined diblock copolymers. These block copolymers are highly suitable for fundamental studies of block copolymer self-assembly in bulk and in solution.

Zusammenfassung

Diese Doktorarbeit befasst sich mit der Synthese, der Struktur, den Eigenschaften und Blockcopolymeren des wohl bekanntesten Lochleiters (Donors) für organische Photovoltaik, Poly(3-hexylthiophen) (P3HT). Es wurden neue fundamentale Aspekte für die Kontrolle der Endgruppen gezeigt, welche die Synthese von Blockcopolymeren sowie niedrige Polydispersitäten ermöglichen. Die so erhaltenen wohldefinierten P3HTs mit unterschiedlichen Molekulargewichten wurden für die Untersuchung der Kristallisation in Masse und der Aggregation in Lösung genutzt. Dadurch konnten bisher unbekannte Details über die Mikrostruktur und die Kristallinität von P3HT aufgeklärt werden. Des Weiteren wurden neue Methoden für die Synthese von monocarboxyliertem P3HT und Blockcopolymeren mit langem konjugierten Block entwickelt. Auf diese Weise konnten zwei verschiedene Typen von

Blockcopolymeren synthetisiert werden, zum einen mit einem polaren Poly(4-vinylpyridin) (P4VP)-Block, der anorganische Nanopartikel koordinieren kann, und zum anderen mit einem elektronenleitenden Akzeptor-Block (Polyperylenebisimidacrylat/ PPerAcr). Die realisierten hohen χN Parameter erlaubten zum ersten Mal Mikrophasenseparation für ein derartiges Blockcopolymer mit zwei kristallinen Blöcken. Aufgrund ihrer vielseitigen Eigenschaften und ihrer Fähigkeit zur Mikrophasenseparation haben diese Blockcopolymere ein großes Potential für die Anwendung in der organischen Photovoltaik (OPV). Nanostrukturierte Donor-Akzeptor-Systeme mit Grenzflächen im Abstand der Exzitondiffusionslänge begünstigen die Ladungstrennung und einen effizienten Transport der erhaltenen Ladungsträger zu den Elektroden. Die wohldefinierten molekularen Strukturen machen diese Blockcopolymere mit zwei kristallinen oder einem kristallinen und einem amorphen Block hoch interessant für fundamentale Studien über die Selbstorganisation derartiger Systeme in Masse und in Lösung.

Der zentrale Punkt dieser Arbeit ist die Kontrolle der Kettenwachstumspolymerisation von 3-Hexylthiophen mit Hilfe der „Kumada Catalyst Transfer Polymerisation“ (KCTP). Kinetische Studien zeigten, dass die Grignard-Metathese zur Bildung des aktiven Monomers nur sehr langsam verläuft. Eine vollständige Umsetzung ist jedoch essentiell für die Kontrolle der Endgruppen. Mit Hilfe von LiCl als Additiv konnte die Reaktion deutlich beschleunigt werden. Dadurch können ohne lange Reaktionszeiten 100% H/Br Kettenenden erreicht werden. Diese Endgruppen ermöglichen die Einführung neuer funktionaler Gruppen. Untersuchungen zu den Abbruchreagenzien haben ergeben, dass Methanol hierfür ungeeignet ist, da es zu Ketten-Ketten-Kopplung durch Disproportionierung der Nickel-Katalysatorspezies führt. Es wurde gezeigt, dass HCl das am besten geeignete Abbruchreagenz für unfunktionalisiertes P3HT ist. Diese Erkenntnisse ermöglichen somit die Synthese von P3HT mit beliebigem Molekulargewicht und 100% homogenen H/Br Kettenenden.

Im zweiten Teil wurden diese definierten Polymere genutzt um die Gleichgewichtsstrukturen in Masse und die Aggregation in Lösung zu untersuchen. In Masse wurde ein temperaturabhängiges Phasendiagramm der kristallinen Bereiche von P3HT bestimmt. Außerdem konnte erstmals die Ordnung der Seitenketten innerhalb der Kristallite identifiziert werden. Diese sind im Vergleich zur Hauptkette verkippt und die Seitenketten verschiedener Polymerketten sind nicht verzahnt. Durch die Analyse der teilkristallinen Struktur von P3HT, bestehend aus den amorphen und den kristallinen Bereichen, konnte gezeigt werden, dass die Ketten im Gleichgewichtszustand bis zu einem Molekulargewicht von etwa 20 kDa vollständig gestreckt vorliegen und keine Kettenfaltung auftritt. Dabei zeichnete sich speziell für niedermolekulares P3HT ab, dass die aus gestreckten Ketten aufgebauten Kristallite von amorphen nicht-kristallisierbaren Kettenenden umgeben sind. Dies führt zu einer geringeren Kristallinität für niedermolekulares P3HT, aufgrund des höheren Anteils an Kettenenden. Nur die genaue Kontrolle der Synthese und die somit erhaltenen wohldefinierten P3HTs ermöglichen die Beobachtung solcher struktureller Details. Untersuchungen der Aggregatbildung in Lösung zeigten, dass die Menge an gebildeten Aggregaten und ihre physikalischen Eigenschaften (exzitonische Kopplung, Konjugationslänge) vom verwendeten Lösungsmittel, dem Molekulargewicht des Polymers und dessen Synthesemethode abhängen. Dabei scheint der maximal erreichbare Anteil an Aggregaten in Lösung einen Hinweis auf die zu erwartende Ladungsträgermobilität in dünnen Filmen zu geben. Im Falle von wohldefinierten P3HTs zeigten selbst niedrige Molekulargewichte hohe Ladungsträgermobilitäten. Bei breitverteilten P3HTs konnten durch Extraktion der kurzen Ketten ähnlich hohe Ladungsträgermobilitäten in den resultierenden hochmolekularen Fraktionen erreicht werden.

Im dritten Teil wurden die Brom-Endgruppen in nur einem selektiven Funktionalisierungsschritt quantitativ in Carboxyl-Gruppen überführt. Diese funktionalisierten Polymere zeigten Ladungsträgermobilitäten von bis zu $10^{-3} \text{ cm}^2/\text{Vs}$ in organischen Feldeffekttransistoren (OFETs).

Des Weiteren ermöglicht die Carboxyl-Gruppe das Ankern auf Oberflächen, das Koordinieren von Nanopartikeln oder den Einsatz als End-Capper zur Bildung von Blockcopolymeren. Für funktionalisierte und unfunktionalisierte P3HTs unterschiedlicher Kettenlänge korrelierte die Höhe der Schmelzenthalpien in Masse mit der Höhe der Ladungsträgermobilitäten in dünnen Filmen. Dies deutet darauf hin, dass die Kristallinität der ausschlaggebende Faktor für die Molekulargewichtsabhängigkeit der Ladungsträgermobilität ist.

Die große Herausforderung für die Synthese von P3HT-haltigen Blockcopolymeren ist die Kombination der KCTP für konjugierte Polymere mit anderen kontrollierten Polymerisationsmethoden. Aufgrund der geringeren Löslichkeit und des geringeren Anteils an Endgruppen, ist vor allem der Einbau von langen konjugierten Blöcken sehr schwierig. Durch die Verwendung der Kupfer-katalysierten Azid-Alkin Cycloaddition (CuAAC), einer so genannten „click“-Reaktion, konnten hochmolekulare P3HT-Makroinitiatoren für die Nitroxid-vermittelte radikalische Polymerisation (NMRP) realisiert werden. Dazu wurde zunächst die Synthese von Alkin-funktionalisiertem P3HT optimiert, wobei sich zeigte, dass beim Abbruch der Polymerisation mit HCl Hydrohalogenierung und Addition von Wasser auftreten. In diesen Fall stellte sich Methanol als geeignetes Abbruchreagenz heraus. Im zweiten Schritt wurde das Alkin-funktionalisierte P3HT durch CuAAC mit einem Azid-funktionalisierten Alkoxyamin direkt in einen Macroinitiator überführt. Mit Hilfe dieser Methode wurden zwei verschiedene Klassen von Blockcopolymeren synthetisiert. Die erste Klasse sind amphiphile P3HT-*b*-P4VPs mit einem polaren amorphen Block, der die Koordination von anorganischen Nanopartikeln ermöglicht. Thermische Untersuchungen dieser Blockcopolymeren zeigten, dass die Kristallitgröße der P3HT-Phase kaum von der Länge des amorphen P4VP-Blocks beeinflusst wird, wenn lange konjugierte P3HT-Blöcke verwendet werden. Erste Untersuchungen der Selbstorganisation in Lösung zeigten, dass in P4VP-selektivem Lösungsmittel kolloidale Strukturen mit kristallinem Kern erhalten werden. Daher ist P3HT-*b*-P4VP ein interessantes System zur Untersuchung der Strukturbildung von Blockcopolymeren mit einem amphenen und einem kristallinen Block. Zusätzlich ermöglichen der lochleitende P3HT-Block und der Nanopartikel-koordinierende P4VP-Block die Anwendung in Hybridsolarzellen.

Die zweite Klasse an Blockcopolymeren sind vollfunktionalisierte P3HT-*b*-PPerAcrs mit Polyperylenebisimidacrylat als elektronenleitenden zweiten Block. Mit Hilfe dieser neuen Synthesemethode wurde ein reines Diblockcopolymer mit hohem Molekulargewicht realisiert. Gleichzeitig konnte ein hoher Gewichtsanteil von PPerAcr (64 wt%) erzielt werden, was essentiell für ausgeglichenen Ladungstransport in organischen Solarzellen ist. Das hohe Molekulargewicht und der daraus resultierende hohe χN Parameter ermöglichen zum ersten Mal hexagonal geordnete zylindrische Strukturen für ein vollfunktionalisiertes doppelkristallines Blockcopolymer in Masse. Auch in dünnen Filmen wurde Mikrophasenseparation mit Domänengrößen im Bereich der Exzitondiffusionslänge beobachtet, was dieses hochmolekulare P3HT-*b*-PPerAcr hochinteressant für organische Photovoltaik macht.

Zusammenfassend konnten durch die Optimierung der Synthese von P3HT fundamentale Erkenntnisse über die molekulargewichtsabhängige Strukturbildung und die daraus resultierenden Eigenschaften gewonnen werden. Darüber hinaus führt die Methode zur Monocarboxylierung zur Erweiterung der Anwendungsmöglichkeiten von P3HT. Schließlich konnten lange P3HT-Blöcke effizient in wohldefinierte Blockcopolymeren eingebaut werden. Diese eignen sich sowohl für fundamentale Studien zur Selbstorganisation von Blockcopolymeren in Masse und in Lösung.

1. Introduction

1.1 Conjugated Polymers and Organic Photovoltaics

In 2000 the Nobel Prize in chemistry was awarded to Alan J. Heeger, Alan G. MacDiarmid and Hideki Shirakawa for the development of electrically conducting polymers.^{1,2} They observed that conjugated polymers, e.g., polyacetylene, can become electrically conductive upon chemical doping with halogen.³ While the pristine materials are semiconducting, doping can lead to a conductivity of 10^5 S/m.⁴ Apart from polyacetylene a lot of different conjugated polymers have been synthesized which benefit from better solubility or improved environmental stability. Some of the most common ones are shown in Figure 1.^{5,6} Today, conjugated/conducting polymers already find commercial application in electromagnetic shieldings, antistatic coatings, electro chromic windows or sensing devices.^{1,5} Motivated by the unique properties of conjugated polymers, organic electronics has become a field of intense research. These materials are investigated as materials for organic field effect transistors (OFETs)^{7,8}, organic light emitting diodes (OLEDs)⁹ or organic photovoltaic cells (OPVs). The main advantage is the processability from solution and the capability to fabricate devices on flexible substrates by printing techniques. This allows low cost, lightweight devices on large areas.

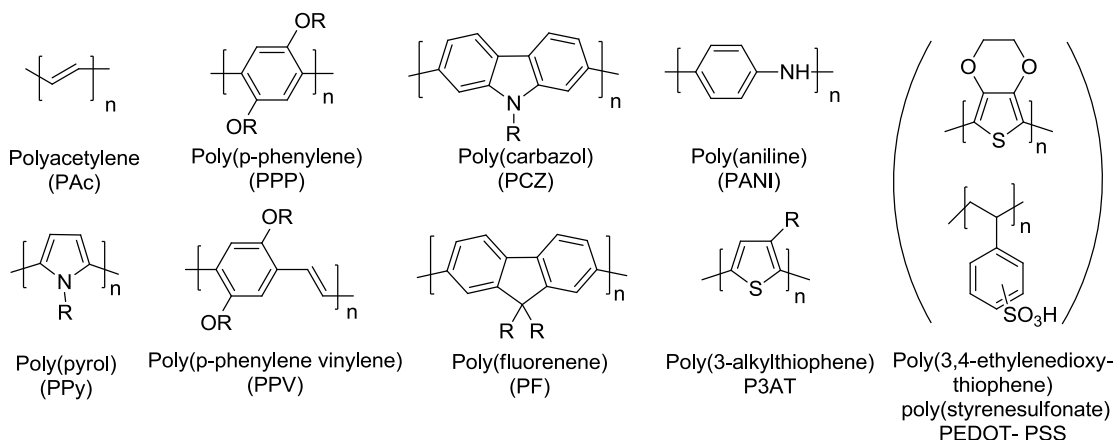


Figure 1: Chemical structures of some of the most common conjugated/conducting polymers.

The first organic photovoltaic cell made of two low molecular weight compounds with an efficiency of about 1% was shown by Tang in 1986.¹⁰ Only five years later in 1991 Grätzel et al. demonstrated a dye sensitized solar cell, TiO₂ sensitized with an organic dye in combination with an liquid electrolyte as a hole conductor.¹¹ The first conjugated polymer was incorporated into a bulk heterojunction organic cell in 1993 by Sariciftci, Heeger and Wudl.¹² Since then the field of organic photovoltaics developed strongly and covers a broad range of organic and hybrid solar cells. Today dye-sensitized solar cells with a liquid electrolyte reach efficiencies of about 11% and the efficiencies of cells with a solid hole conductor range around 5%.^{13,14} The bulk heterojunction hybrid solar cells with conjugated polymers and a fullerene derivative

reach efficiencies of 5% with Poly(3-hexylthiophene) (P3HT) and 7.4% for low bandgap polymers with broader absorption.^{15,16} Polymer-polymer blend or single active-layer devices with one material containing the donor and acceptor unit have efficiencies around 1.5-2.2%.¹⁷⁻¹⁹

In organic photovoltaics the mechanism for the conversion of sun light into electricity differs from that of conventional inorganic photovoltaics based on p- and n-doped silicon. The basic mechanistic steps of a donor-acceptor type solar cells are shown in Figure 2a. In contrast to inorganic solar cells, no free charge carriers are formed upon excitation (1), instead a bound electron-hole pair a, so called exciton, is generated (2). Only if it reaches an interface (3) between the donor and the acceptor material within its lifetime, charge transfer and separation into free charge carriers occurs (4). Furthermore, the respective donor and acceptor materials have to work as hole and electron conductors to allow transport of the free charges to the respective electrodes (5). The important parameters of a solar cell which determine its efficiency η are depicted in Figure 2b and Equation 1 and 2:

$$\eta = \frac{I_{max} U_{max}}{P_{light}} = FF \frac{I_{sc} U_{oc}}{P_{light}} \quad (1)$$

$$FF = \frac{I_{sc} U_{oc}}{I_{max} U_{max}} \quad (2)$$

FF = fill factor, U_{oc} = open circuit voltage, I_{sc} = short circuit current, P_{light} = power of incident Light, I_{max} = current at maximum power point (see Figure 2), U_{max} = voltage at maximum power point, η = power conversion efficiency, M_{pp} = maximum power point.

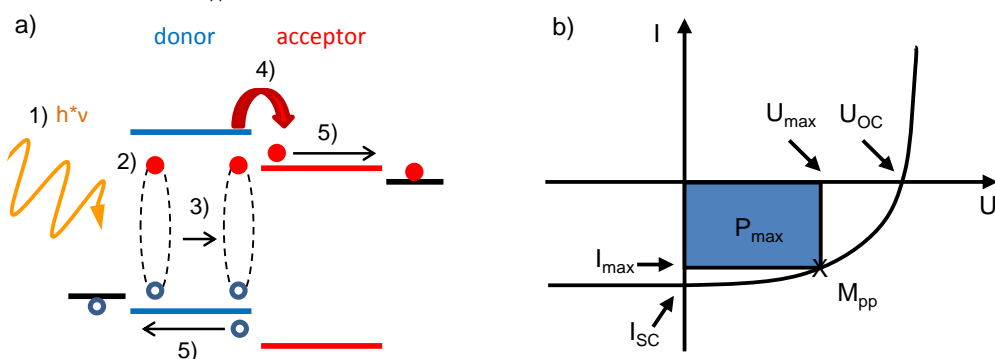


Figure 2: a) Working principle of a donor-acceptor solar cell with 1) light absorption 2) exciton formation 3) exciton diffusion 4) charge separation at the donor-acceptor interface 5) charge transport to the electrodes. b) Current-voltage characteristic of a solar cell with the respective parameters for the calculation of the efficiency η according to Equation 1 and 2. The upper red and blue lines represent the lowest unoccupied molecular orbitals (LUMOs) and lower lines indicate the highest occupied molecular orbitals (HOMOs) in a simplified way.

Many factors have been identified which influence the different parameters of an organic solar cell. For example the short circuit current I_{sc} is mainly influenced by the absorption (band gap) and charge carrier mobility of the material.²⁰ The open circuit voltage U_{oc} depends on the difference between the highest occupied molecular orbital (HOMO) of the donor and the lowest unoccupied molecular orbital (LUMO) of the acceptor.²¹ The fill factor is a measure of

the maximum realizable power of a certain device and its efficiency of charge collection. It depends on the device design, contacts and series and shunt resistances but also on the interconnectivity of phases and pathways between the electrodes.²⁰ Therefore, morphology plays an important role to provide such pathways and to create interfaces within the exciton diffusion length. In bulk heterojunction cells, blend systems are used and non-equilibrium morphologies are obtained. Therefore the device performance depends on processing conditions, e.g., the solvent used for film preparation or post-production annealing. Further long-term stability is a major problem, if the morphologies are not the equilibrium structures. This demonstrates that organic solar cells are very complex and the final efficiency is determined by many interdependent factors. The majority of these issues can be tackled by the controlled synthesis leading to electronically pure materials with fewer defects and desired equilibrium morphology (Figure 3). Only with controlled synthesis it is possible to investigate how parameters like molecular weight, polydispersity, end groups or architectures influence the physical properties and equilibrium structures. This understanding is necessary to create thermodynamically stable morphologies with desired domain sizes and orientation. Therefore fundamental questions on the synthesis and equilibrium structures of the conjugated polymer P3HT and its block copolymers are the motivation of this thesis.

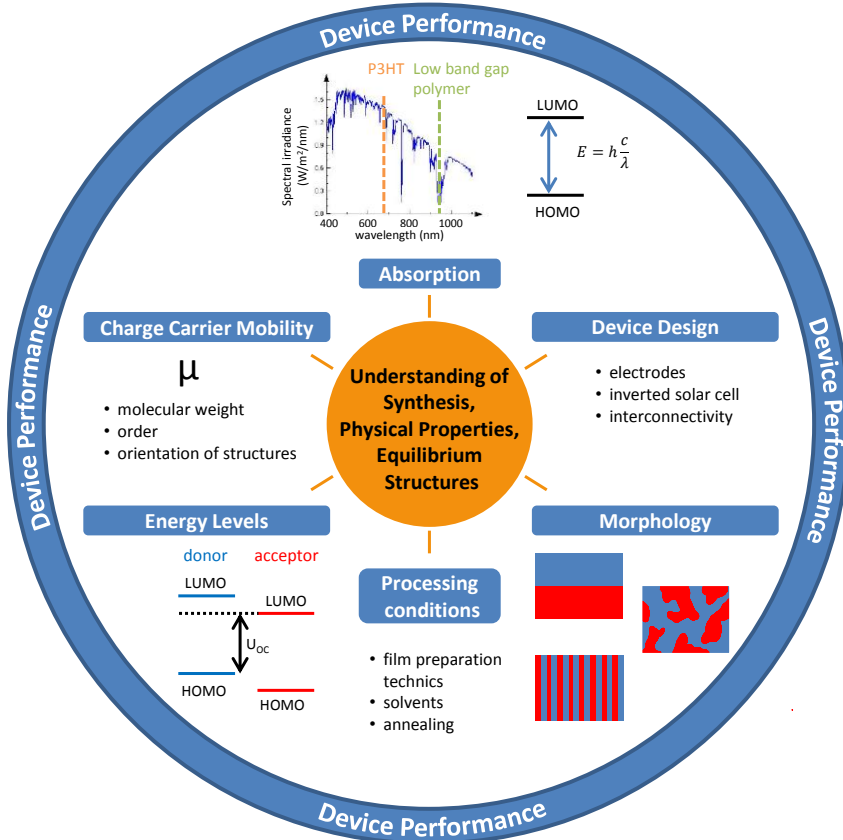


Figure 3: Controlling the synthesis, physical properties and equilibrium structures is the key for influencing all parameters which determine the efficiency of an organic solar cell. The picture of the solar spectrum is taken from reference.²²

1.2 Synthetic Development of Poly(3-hexylthiophene) and its Properties

Poly(3-alkylthiophenes) P3ATs are the most prominent class of conjugated polymers because of their high environmental and thermal stability, good solubility and high charge-carrier mobility. The semiconducting properties result from the sp₂-hybridized orbitals and the overlap of the remaining p_z-Orbitals, which form a conjugation leading to delocalization of electrons along the chain. In contrast, the alkyl chains are insulating and only act as solubilizing groups. Among all polythiophenes Poly(3-hexylthiophene) P3HT shows the best balance between good solubility and high charge-carrier mobility.²³ The properties of P3HT strongly depend on the arrangement of the attached side chains, called the regioregularity. It is defined as the amount of head-tail couplings, where head describes the position 2 in vicinity of the alkyl substituent and tail the position 5 of the thiophene ring.²⁴ While head-to-tail couplings allow for a planar orientation of the thiophene rings, head-head couplings cause steric interactions of the alkyl chains and an out of plane twist of the thiophene rings (see Figure 4). P3HT is semicrystalline and thus a two dimensional semiconductor. Irregular couplings hinder the intramolecular charge transport along the chain as well as the intermolecular transport via π-π stacking.²⁵

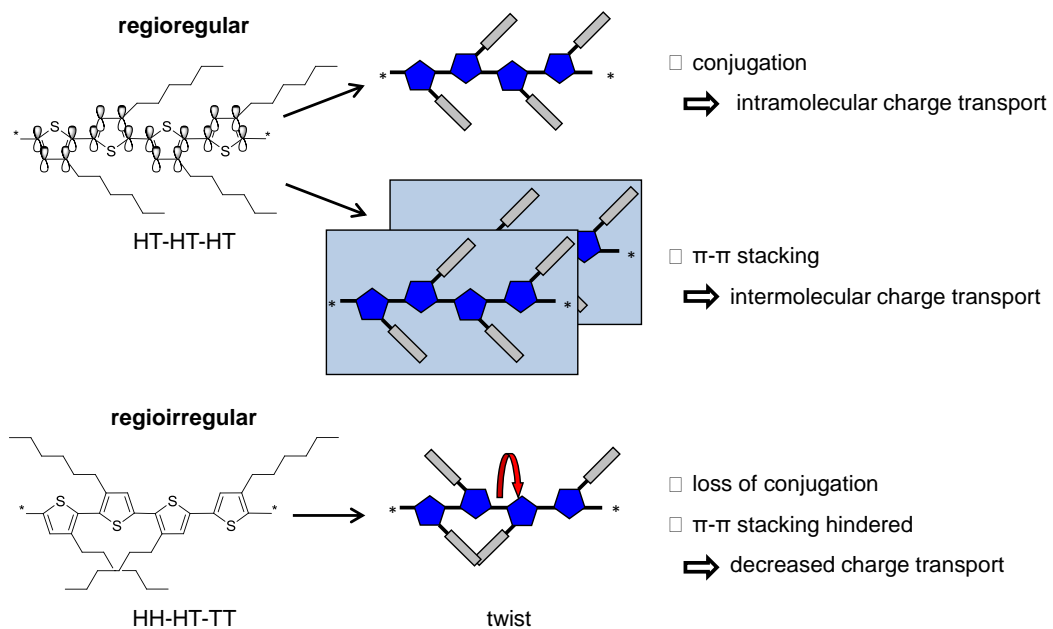


Figure 4: Influence of regioregularity on intra- and intermolecular charge transport properties of poly(3-hexylthiophene)s.

Additionally, the charge carrier mobility depends on the chain length and increases with increasing molecular weights.²⁶ A better interconnectivity between the microcrystalline domains throughout the amorphous regions and an increased crystallinity are discussed as the origin for the improved mobility of high molecular weight samples.²⁷⁻²⁹ Thus P3HT with a high molecular weight and a regioregularity of 98-99% shows charge carrier mobilities as high as

0.1-0.2 cm²/Vs.^{30,31} Further, this demonstrates that the synthetic possibilities to control the structure play an important role in determining the resulting physical properties. Therefore the major achievements in the synthesis of P3HT and the state of the art synthetic method are shortly summarized in the following section.

The synthetic development of poly(3-hexylthiophene) started in 1980 with the synthesis of unsubstituted polythiophenes and is illustrated in Figure 5.^{32,33} Unsubstituted polythiophene showed a high charge carrier mobility but suffered from being insoluble in common organic solvents. In 1986, Elsenbaumer et al. found that substitution of the thiophene core in position 3 allows for proper solubility when alkyl chains with four or more carbon atoms are used.^{34,35} However, the irregular arrangement (regioregularity of 50-80%) of the alkyl chains caused a loss of conjugation and a lower conductivity in comparison to the unsubstituted polythiophenes.³⁶ A milestone was the development of regioregular poly(3-alkyl thiophenes), which was almost parallelly achieved by McCullough and Rieke.^{37,38} The key is to use an asymmetric monomer which leads to almost exclusively head-tail couplings and a regioregularity of 98-99%. One drawback was that cryogenic temperatures were necessary for the synthesis of the asymmetric monomers which was solved in 1999 by a Grignard Metathesis reaction proposed by McCullough et al.³⁹ Here the asymmetric monomer was formed at room temperature via a Grignard exchange between 2,5-dibromo-3-alkylthiophene and an alkyl Grignard reagent. While all these methods were based on a step-growth polymerization, Yokozawa and McCullough revolutionized the synthesis when they found that nickel initiated cross coupling reactions of 3-alkylthiophenes follow a chain-growth mechanism and have a quasi "living" nature.⁴⁰⁻⁴³ This major breakthrough enabled the control of molecular weights, end groups as well as low polydispersities. The mechanism of this new polymerization method, the so called Kumada catalyst transfer polymerization (KCTP), is explained in the following paragraph.

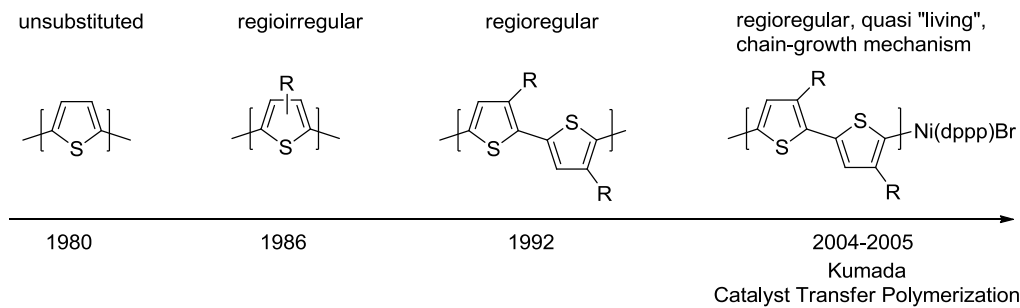
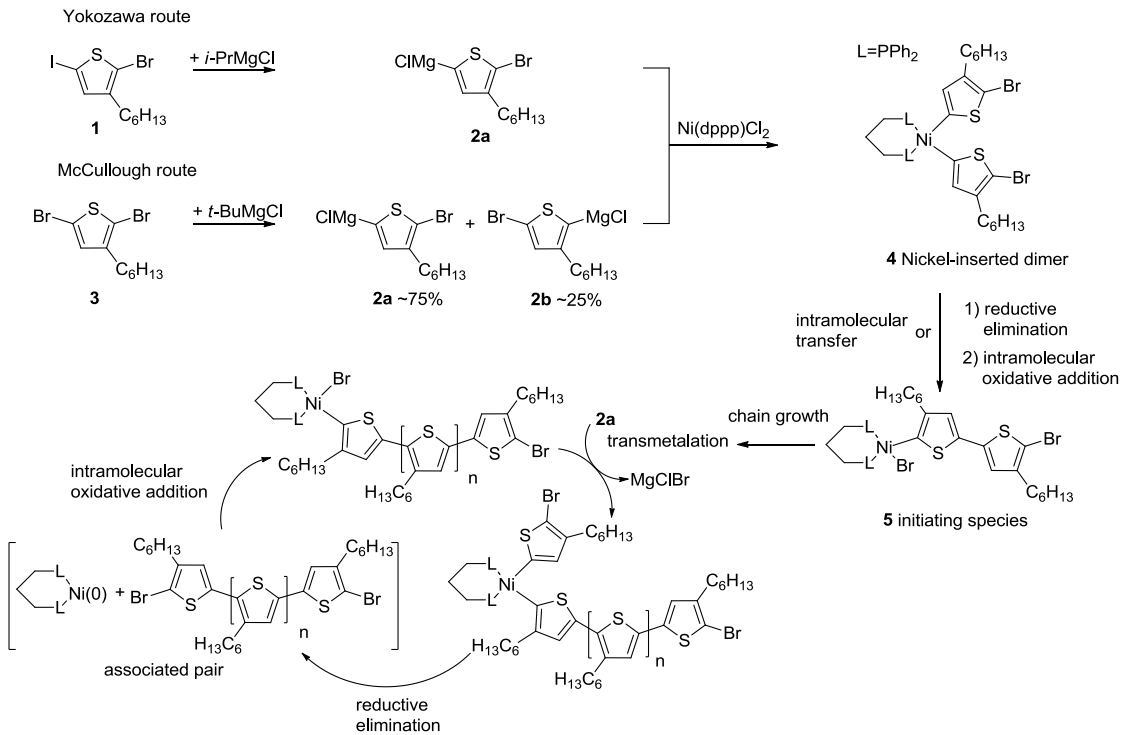


Figure 5: Synthetic developments of polythiophenes from unsubstituted polythiophenes to irregular alkyl substitution to regioregular poly(3-alkylthiophenes). The state of the art Kumada catalyst transfer polymerization proceeds via a chain-growth mechanism and has a quasi "living" nature.

1.3 Kumada Catalyst Transfer Polymerization (KCTP)

The name Kumada catalyst transfer polymerization (KCTP) arises from the used cross-coupling reaction (Kumada coupling) and the decisive step for the chain-growth mechanism, the intramolecular transfer of the catalyst. In this polymerization method the monomer is formed *in situ* via a Grignard metathesis between a dihalide and a sterically demanding Grignard reagent. Therefore, Grignard Metathesis polymerization is sometimes employed as an alternative name. In general two different approaches for the synthesis of the active monomer are known. Both are demonstrated in Scheme 1 together with the proposed mechanism for the chain-growth polymerization.^{40,41} The Yokozawa route uses an asymmetrical 2-bromo-3-hexyl-5-iodothiophene **1** as starting material and the active monomer is formed via a metathesis with *i*-PrMgCl. The reactivity of iodine is higher than that of bromine and thus only one regioisomer **2a** (2-bromo-5-chloromagnesium-3-alkylthiophene) is formed. However, the McCullough method uses a symmetrical 2,5-dibromo-3-hexylthiophene together with *t*-BuMgCl. Therefore, two different active Grignard regioisomers **2a** and **2b** are obtained. Because of the steric interactions of the *t*-BuMgCl with the alkyl chain in position 3 of the thiophene the amount of 5-bromo-2-chloromagnesium-3-alkylthiophene **2b** is only about 25%. Additionally, investigations of the reaction mixture after polymerization showed that only **2a** is consumed.^{40,44} Thus, both approaches give polymers with a high regioregularity of about 98%. After the formation of the active monomer, Ni(dppp)Cl₂ is added and a Nickel-inserted dimer **4** is formed. The side chains in **4** are oriented in a tail-tail fashion because it is the sterically least hindered conformation. Now the initiating species **5** is formed *in situ* via an intramolecular transfer or a reductive elimination followed by an intramolecular oxidative addition. The chain growth proceeds via repetitive cycles of transmetalation, reductive elimination, formation of an associated pair followed by an intramolecular oxidative addition. This intramolecular transfer is the decisive step for the chain-growth mechanism, each Nickel catalyst is *in situ* transformed into one initiating species and starts only one chain. Thus, the molecular weight is determined by the feed ratio of monomer to Nickel catalyst. The controlled and “living” nature is further confirmed by a linear increase of molecular weight with conversion. Additionally, after consumption of the monomer the Nickel catalyst is still sitting at the chain end and addition of new monomers leads to chain extension.⁴⁰ Quenching the active chain end with hydrochloric acid gives homogenous end groups. A bromine atom originating from the starting thiophene unit and a hydrogen resulting from the active chain end.⁴¹



Scheme 1: Active Grignard monomer formation via the two different monomer systems used in McCullough and Yokozawa routes and the proposed mechanism by McCullough and Yokozawa for the Kumada catalyst transfer polymerization.⁴⁵

Up to now P3HT is the best understood system polymerized with KCTP. However, apart from polythiophenes carrying various side chains³⁶ also other polymers were successfully synthesized, for example poly(2,5-dihexyloxybenzene),⁴⁶ poly(alkylfluorene),^{47,48} poly(N-dodecylpyrrole),⁴⁸ poly(N-octyl-2-carbazole),⁴⁸ poly(selenophene)⁴⁹ and poly(2,3-dihexylthieno[3,4-*b*]pyrazine).⁵⁰ Additionally non-conjugated polymers like poly(bithienylmethylenes),⁵¹ poly(arylisocyanide)⁵² or oligomers⁵³ were prepared using KCTP. Further new developments allowed the synthesis of star like polymers, brushes or surface initiated polymerization.⁵⁴⁻⁵⁶ Examples of the polymers synthesized with KCTP are summarized in Figure 6. During the extension of KCTP towards new monomers, a lot of factors have been identified which influence its success like additives,^{44,46,48} the position of the substituent on the aromatic core,⁵⁷ the metal⁵⁸ as well as the ligand of the catalyst used.^{44,45,58-61} Nevertheless, still a lot of factors even for P3HT are unknown and their identification will also be part of this thesis.

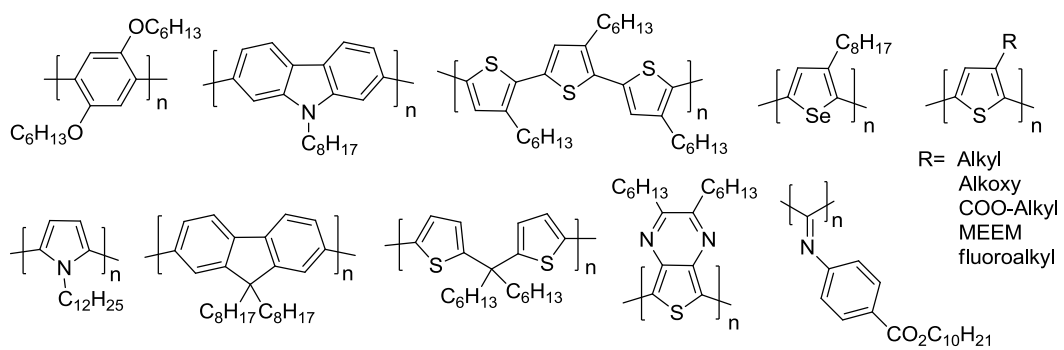


Figure 6: Polymers synthesized using Kumada catalyst transfer polymerization.^{36,46-56} MEEM = [2-(2-methoxyethoxy)ethoxy]methyl].

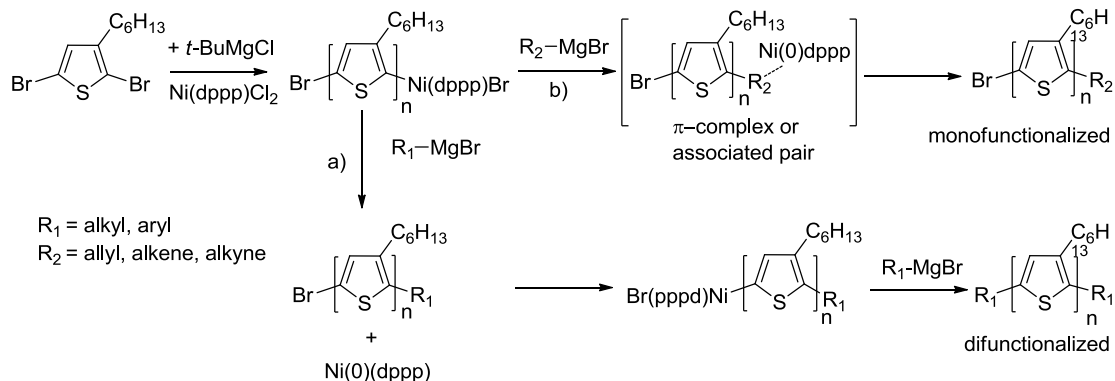
1.4 End Group Functionalization of Poly(3-hexylthiophene)s

As mentioned KCTP of P3HT proceeds via a quasi-living nature. Therefore the Ni catalyst is sitting at the active chain end after conversion of all monomers. After quenching with HCl, defined bromine and hydrogen end groups are expected. This allows for the incorporation of functional end groups and broadening the applications of P3HT. End group functionalized P3HT can be used for the synthesis of block copolymers, coupling of conjugated polymer to surfaces or as ligand for electron conducting nanoparticles.⁶²⁻⁶⁶ For example Jo et al. showed that P3HT end functionalized with fullerene can stabilize a P3HT fullerene blend cell to improve the long-term stability.⁶⁷ In principle three different ways to introduce functional end groups are known in the literature, which are explained below.

In Situ Functionalization

The *in situ* end group functionalization method exploits the living nature of KCTP and the presence of Ni catalyst at the active chain end. Jeffries et al. showed that new end groups can be introduced by quenching the active chain with monofunctionalized Grignard reagents.⁶⁸ Depending on the nature of the used end-capper, mono- or difunctionalized polymers were obtained. While unsaturated allyl-, ethynyl- or vinyl-Grignard agents lead to predominantly monofunctionalized P3HTs all other Grignard reagents result in mainly difunctionalized products. The discussed origin for this difference is explained in Scheme 2. After quenching with a monofunctionalized Grignard reagent, a Ni(0)dppp species is formed. In the case of alkyl or aryl end groups the Ni(0)dppp diffuses into the reaction mixture (Scheme 2a). Thus it can react with the bromine group at the other chain end and an oxidative addition of a second Grignard reagent occurs. After reductive elimination a difunctionalized polymer is formed. In contrast, unsaturated allyl, ethynyl or vinyl groups are known to form stable π-complex with

Ni[0] species.^{69,70} Thus a further addition to the bromine end group is hindered and predominately monofunctionalized polymers are formed.



Scheme 2: Proposed mechanism for the in situ functionalization of P3HT using different types of Grignard reagents leading to predominantly mono- or dicapped P3HTs.

Using this technique, a lot of different end groups were introduced (Figure 7). Since it is a simple one pot reaction and the catalyst is already sitting at the chain end, even high molecular weight polymer chains can easily be functionalized.⁷¹ However, the resulting type of functionalization – mono- or dicapped – is determined by the nature of the used Grignard reagent. Further this functionalization method is limited to Grignard compatible end groups and protection groups are necessary for amino, aldehyde or alcohol groups.

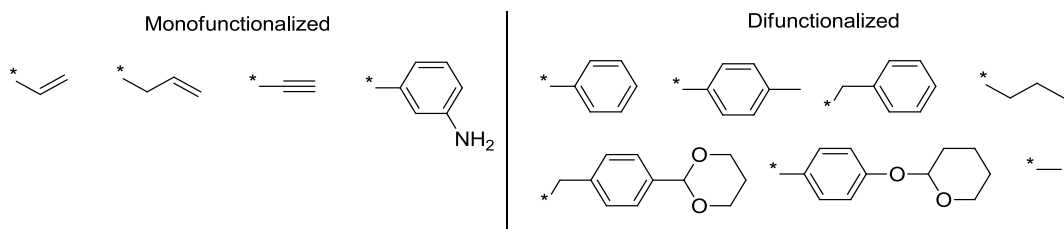
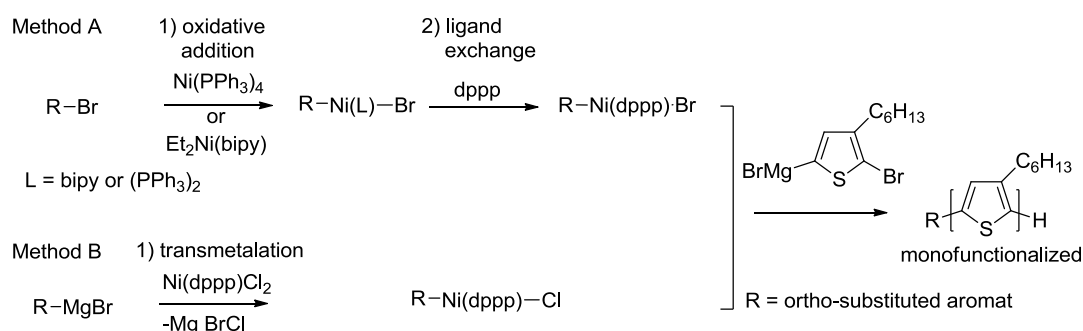


Figure 7: End groups realized with the in situ functionalization of poly(3-hexylthiophene) and the respective dominating degree of capping.^{68,72}

Ex Situ Initiation with Functionalized Nickel Catalysts

The second functionalization method is based on a Ni catalyst carrying a functional group, which remains at the polymer as the starting unit. This method is also called *ex situ* initiated KCTP, since the initiating Nickel species is formed in an independent step.⁷³ It was first introduced by the group of Kiriya for surface initiated polymerization.⁵⁵ Arylhalides were reacted with Ni(PPh₃)₄ and the resulting Ar-Ni(PPh₃)₂-Br was used as a catalyst for the polymerization of P3HT. However a major drawback was the lack of control over the polymerization because different ligands other than dppp – the best ligand for P3HT polymerization – were used. Additionally, the Ar-Ni(PPh₃)₂-Br complexes were unstable because of the addition of a second aryl halide and the formation of Ar-Ar homocoupling

products. Smeets et al. found that these complexes can be stabilized when ortho-methyl substituted arylhalides are used.⁷⁴ Further the group of Luscombe showed that in a second step, the ligand can easily be exchanged with dppp to get an initiator which allows for a well-controlled polymerization of P3HT.⁷⁵ The basics of this mechanism are shown in Scheme 3 Method A. In the first step, an ortho-substituted arylhalide is oxidatively added to a $\text{Ni}(\text{PPh}_3)_4$ or $\text{Et}_2\text{Ni}(\text{bipy})$ catalyst. In a second step these ligands are exchanged with dppp.^{75,76} By adding the Grignard monomer, the polymerization is started and the obtained polymers carry the respective aryl group as the starting unit. Just recently the method was modified and ortho-substituted arylmagnesium halides were directly reacted with the air stable and easy to handle $\text{Ni}(\text{dppp})\text{Cl}_2$ (Scheme 3 Method B).^{75,77} Again the ortho-substituent hindered a homocoupling reaction and the external initiation was simplified because a ligand exchange is no longer necessary.



Scheme 3: End group functionalization of P3HT using the ex situ initiation method with a functionalized Nickel catalyst. Method A follows a two-step procedure while method B is a one-step reaction. Ortho-substituted aromatic compounds are necessary for a good control of the end group functionalization.

Using these methods new types of end groups could be introduced as shown in Figure 8. This functionalization method allows for the introduction of end groups in one step. Here the degree of functionalization is not dependent on the nature of the initiating species. Only monofunctionalized polymers are obtained. However, the method is limited to end groups which do not influence the living nature of the polymerization, can form Grignard reagents or at least are stable against the used Grignard components.⁷⁷⁻⁸⁰ As demonstrated by Smeets et al., introduction of functional NH_2 , COOH or azide groups requires the use of protection groups and several post-polymerization steps.⁸⁰ Even then in some cases, the content of functional end groups was low.

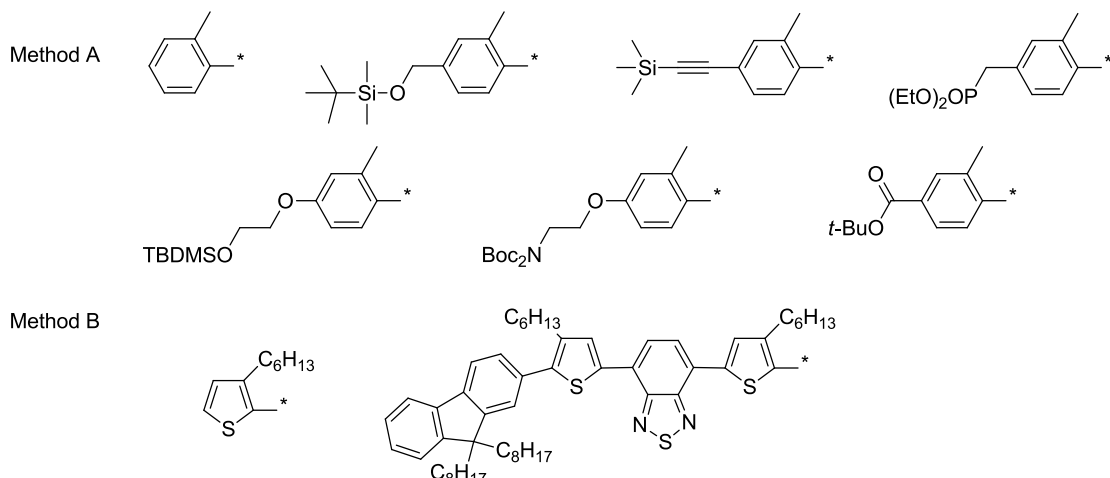
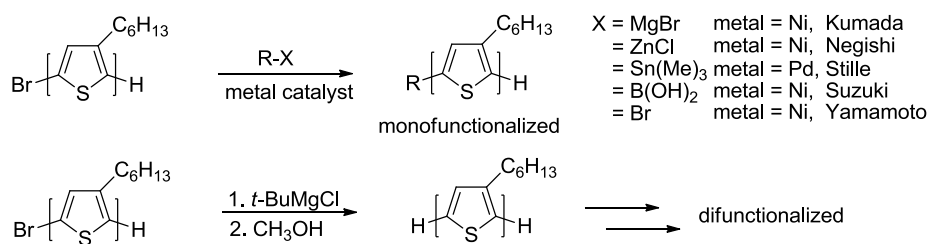


Figure 8: End groups introduced at one chain end of P3HT using the methods shown in Scheme 3.^{74,77,79-80}

Post-Polymerization Functionalization

The third functionalization method converts the end groups which are directly obtained after quenching the polymerization. As explained in the previous chapter P3HT carries a bromine end group from the starting unit and a hydrogen atom resulting from quenching the active chain end with hydrochloric acid. In the post-polymerization method, the bromine group is used for the introduction of several new end groups using Kumada, Negishi, Stille, Suzuki or Yamamoto cross coupling reactions (Scheme 4).⁸¹⁻⁸⁵ Since only one bromine chain end is available, exclusively monofunctionalized polymers can be obtained. For the synthesis of difunctionalized polymers the bromine group has to be transformed into a hydrogen and further functionalization steps lead to dicapped P3HTs using the chemical equivalence of the two hydrogen end groups.⁸³



Scheme 4: Methods for the post-polymerization functionalization of P3HT leading to mono- or difunctionalized products.

An advantage of the post-polymerization functionalization is that the end groups have no influence on the control of the polymerization and it is more versatile concerning the choice of functional groups. Additionally, the same batch of polymer can be used for the introduction of different end groups. Thus the influence of the chain end can be investigated without changing the length of the polymer. The mono- or difunctionalized end groups obtained with this

method are shown in Figure 9. However, after polymerization sometimes a mixture of the expected hydrogen/bromine and unexpected hydrogen/hydrogen end groups occurred, which hinders a 100% end group functionalization. This issue will be addressed in this thesis.

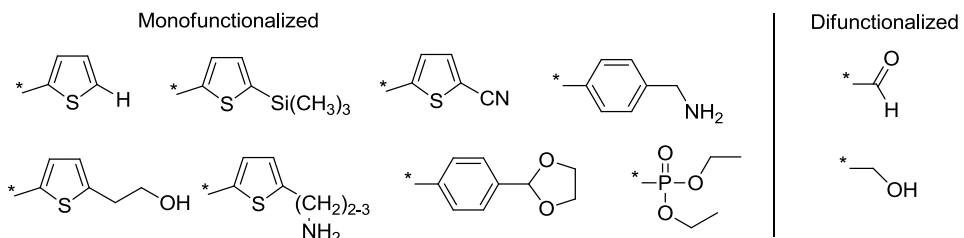


Figure 9: End groups introduced at P3HT using the methods shown in Scheme 4.^{82-84,86-88}

1.5 P3HT Containing Block Copolymers

The end group functionalization methods shown before allow the synthesis of P3HT containing block copolymers. These are of high interest for organic electronic devices, because they are known to self-assemble into various structures with nanoscale domains in bulk and solution as shown in Figure 10a.^{89,90}

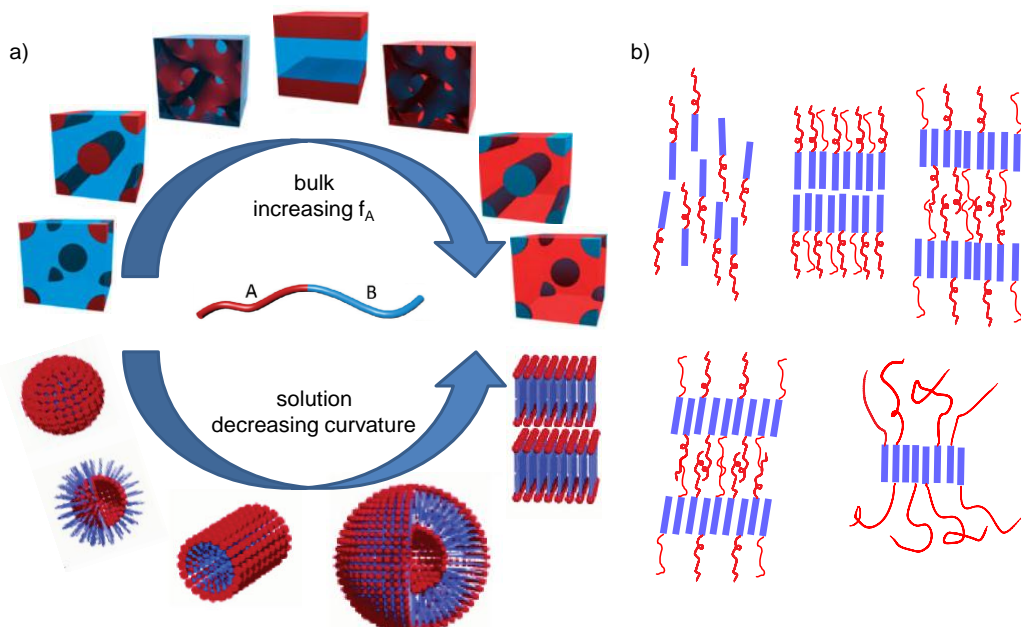


Figure 10: a) Typical self-assembled structures of coil-coil block copolymers in bulk and solution. Depending on the volume fraction f of the different blocks spherical, cylindrical, gyroid or lamellar structures are obtained in bulk. In solution micelles, inverted micelles, cylindrical micelles, vesicles or lamellas can be obtained depending on the block ratio, solvent, concentration or temperature. Here they are ordered according to the curvature radius at the interface.^{91,92} The individual pictures are taken from the literature.⁹¹⁻⁹⁴ b) Liquid crystalline morphologies of rod-coil block copolymer from up left to down right: nematic, bilayer smectic A, monolayer smectic A, monolayer smectic C and hockey pucks. Pictures are redrawn according to de Cuendias et al..⁹⁵

The domain sizes of block copolymers are in the range of the exciton diffusion length and since these are thermodynamically stable structures, they are highly interesting for long-term stable bulk heterojunction morphology in photovoltaics. Additionally, these nanoscale morphologies allow thick absorbing layers without decreasing interface areas between donor and an acceptor material. If lamellar or cylindrical phases can be aligned, direct charge transport ways to the electrodes could be obtained, which may improve charge extraction. Thus fully functionalized block copolymers containing P3HT as a hole conducting moiety and a second electron conducting moiety are of high interest. Further the aggregation of P3HT in self-assembled solution structures leads to spectral changes depending on the strength of aggregation.⁹⁶ This makes them promising candidates for sensor application.

However the self-assembly behavior of P3HT containing block copolymers differs from that of the typical coil-coil block copolymers. The conjugation of P3HT leads to a rod-like nature which additionally influences the microphase separation. For coil-coil block copolymers the microphase separation depends on the Flory-Huggins interaction parameter χ , which describes the segregation tendency of the two block segments, as well as the total chain length N and the volume fractions f of each block.⁸⁹ The self-assembly of rod-coil block copolymers containing a conjugated block is further influenced by the $\pi\text{-}\pi$ interaction of the rod, its crystalline or liquid crystalline character and the asymmetry between the length of the rod and coil block.^{97,98} Thus two additional factors are important, the Maier-Saupe parameter ω , describing the interaction of the rods, and the ratio of the coil radius of gyration in comparison to the rod length described as the asymmetry parameter v.^{97,98} The balance between ω and χ plays an important role for the resulting structures. For $\omega/\chi > 1$, the self-assembly is dominated by the alignment of the rods. Thus typical liquid crystalline morphologies as depicted in Figure 10b may be formed.²⁰ In contrast, for $\omega/\chi < 1$, the structures known from coil-coil block copolymer are more likely, because microphase separation is the main driving force. Thus for a fixed χN value, the introduction of a rod block can cause a transformation of spherical or cylindrical structures to lamella or a smectic phase, since less curved structures are preferred.⁹⁷ For the application in organic photovoltaics some additional prerequisites can be formulated. The block copolymer needs a hole conducting moiety like P3HT and a second block which can coordinate electron conducting nanoparticles or is an electron conductor itself. As explained before, the charge carrier mobility of P3HT increases with increasing molecular weight and thus P3HT blocks with a molecular weight of about 20 kDa are necessary for good charge carrier mobility.⁹⁹ Additionally, a high χN parameter is important to allow for a clear microphase separation. If χ is fixed because of the given nature of electron or hole conducting material at least high N values are necessary.

Types of P3HT Block Copolymers

Many P3HT containing block copolymers are known as summarized in Table 1. Regarding the second block they can be separated into two different groups, carrying an electronic functional or nonfunctional second block.

There are plenty of P3HT block copolymers carrying an electronic nonfunctional block, for example, polystyrene or polymethylmethacrylate.^{63,100} Most of them were synthesized to tune the mechanical properties or to prove synthetic concepts.^{63,100-102} Few of them carry a polar or a nanoparticle-coordinating block, which makes them suitable for the formation of solution structures^{71,103-105} and the application in photovoltaics as templates^{106,107} or for hybrid devices^{87,108,109} with electron conducting nanoparticles.

In the group of the electronic functional second blocks, the number of donor blocks is dominating. Most of them are all-conjugated block copolymers with substituted thiophenes or for example polyfluorene¹¹⁰ or polyparaphenylene¹¹¹. They are often used to tune the crystallinity,¹¹² the optical properties of the material¹¹³ or to introduce new functionality.^{59,114} The smallest class but the most relevant one for organic photovoltaics contains the donor-acceptor block copolymers. Most of them consist of P3HT as the hole conducting donor block and poly perylene bisimide acrylates (PPerAcr)¹¹⁵⁻¹¹⁸ or poly(fullerene)s as the electron conducting acceptor block. Together with the nanoparticle-coordinating blocks they find application in organic photovoltaics as compatibilizers,^{87,88,115,119} hybrids,^{109,120,120} or single active layer materials.^{18,99,117,118} Some important structures of block copolymers (P1-P8) with donor-acceptor units or nanoparticle-coordinating blocks are summarized in Figure 11. A comprehensive overview can be found in the reviews of Sommer et al. and Topham et al.^{20,121}

Table 1: P3HT containing block copolymers carrying electronic functional and nonfunctional second blocks. The class of the electronic functional blocks can be divided into donor and acceptor blocks.

| Electronic nonfunctional second blocks |
|---|
| polystyrene, ⁶³ polymethylmethacrylate, ⁶³ polymethylmetacrylate, ¹⁰⁰ polyurethane, ⁶³ polyethylene, ¹²² polyisoprene, ¹²³ polyacetylene, ¹²⁴ poly[4-[4-(6-methacryloyloxyhexyloxy) benzoate]-4'-hexyloxyazobenzene], ¹²⁵ poly(g-benzyl-L-glutamate), ⁸¹ poly(dimethylsiloxane), ¹²⁶ poly(2-vinlypyridine), ¹⁰⁸ poly(4-vinlypyridine), ⁸⁷ polylactide, ¹²⁷ polyacrylicacid, ¹⁰⁵ poly(3-O-methacryloyl-D-galactopyranose), ¹⁰⁴ poly(zinc methacrylate acetate), ¹⁰⁶ poly(2-(dimethylamino)ethyl methacrylate), ¹⁰³ poly(2-ethyl-2-oxazoline), ¹²⁸ poly(ethylene glycol) methyl ether acrylate, ¹²⁹ poly(tetrahydrofuran) ¹³⁰ |
| Electronic functional second blocks - Donors |
| poly(3-(4'-(3'',7''-dimethyloctyloxy)-3'-pyridinyl), ¹²⁰ poly(3-(2-ethylhexyl)thiophene), ¹³¹ poly(3-(4,4,5,5,6,6,7,7,7-nonafluoroheptyl)thiophene), ¹³² poly(3-[2-(2-methoxyethoxy)ethoxy]), ⁵⁹ poly(3-octylthiophene), ¹³³ poly(3-cyclohexylthiophene), ¹³⁴ poly(3-aminopropylmethoxymethyl thiophene), ¹¹⁴ poly(3-methanol thiophene), ¹¹⁴ poly(3-phenoxyethylthiophene), ¹³⁵ poly(3-butylthiophene), ¹³⁶ poly[3-(3,7-dimethyloctyloxy) thiophene], ¹³⁷ poly(<i>N</i> -vinylcarbazol), ¹¹³ poly(2,5-dihexyloxy-1,4-phenylene), ¹¹¹ poly(9,9-dioctylfluorene), ¹¹⁰ poly(fluorene-co-benzothiadiazole), ¹³⁸ poly(3-hexylselenophene), ¹³⁹ poly(4-vinyltriphenylamine), ¹⁴⁰ |
| Electronic functional second blocks - Acceptors |
| poly(2-phenyl-5-(4-vinylphenyl)-1,3,4-oxadiazole), ¹⁴¹ cyano-substituted poly(phenylenevinylene), ¹⁴² poly(pyridinium phenylene), ¹⁴³ poly(fullerene), ^{18,88,119,144-146} poly perylene bisimide acrylate ¹¹⁵⁻¹¹⁸ |

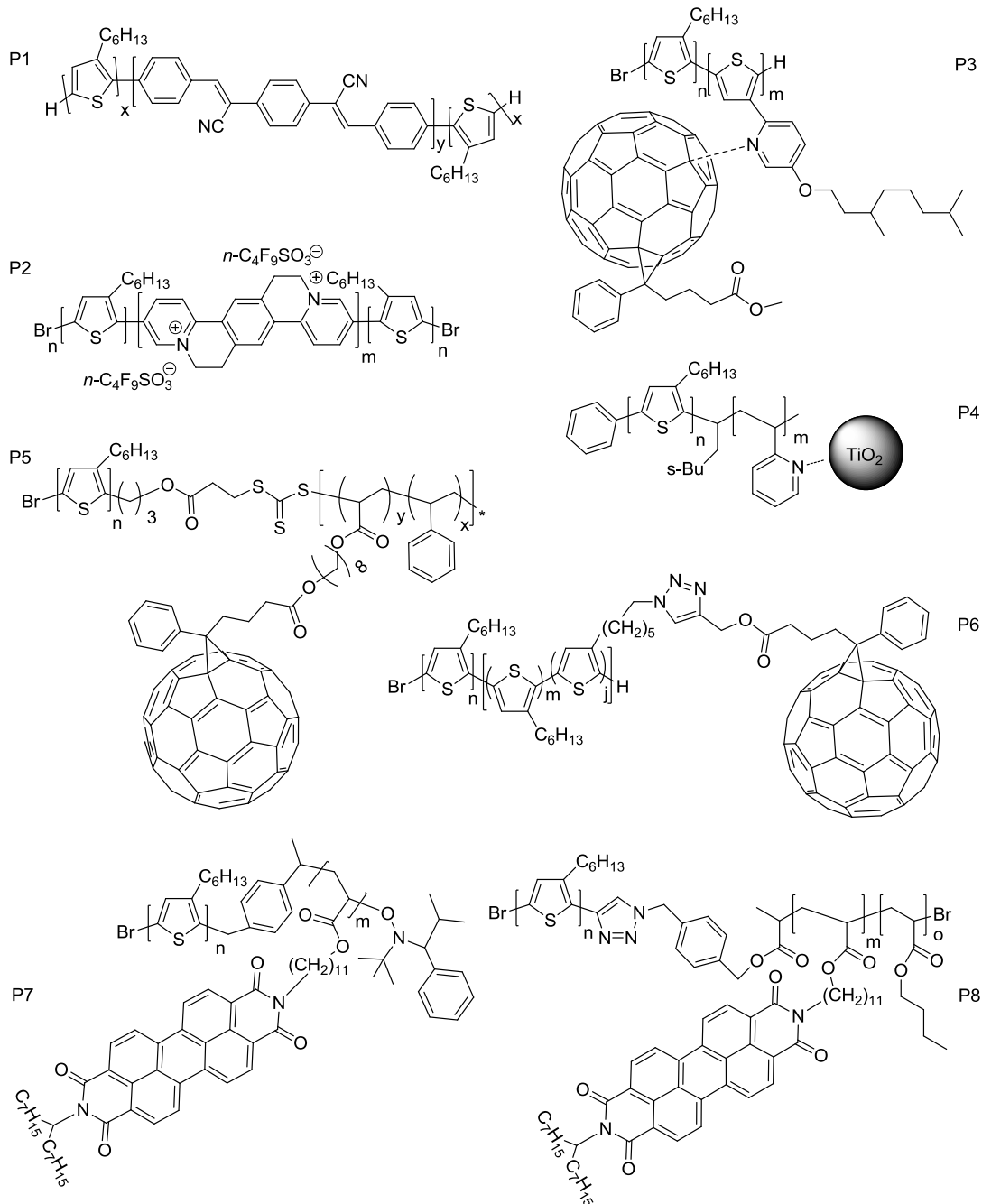


Figure 11: Examples of P3HT containing donor-acceptor polymers (P1,¹⁴² P2,¹⁴³ P5,¹⁴⁵ P6,¹⁸ P7,¹¹⁶ P8¹¹⁷) and block copolymers for hybrid systems (P3,¹²⁰ P4¹⁰⁸).

P1 and P2 are all-conjugated polymers with donor and acceptor units.^{142,143} However up to now they were not incorporated into photovoltaic cells. P3 is one example for an all-conjugated block copolymer carrying a pyridine substituted thiophene as second block with. In a blend device with PCBM it showed a power conversion efficiency of 1.89% only. But as a compatibilizer for a P3HT/PCBM blend, it increased the thermal stability.¹²⁰ P4 is one of the rare examples of rod-coil P3HT block copolymers, which shows typical phase separation known from coil-coil systems.^{108,147} Further the vinyl block allows the coordination of electron

conducting nanoparticles for example TiO_2 .¹⁰⁹ However, the efficiency of this hybrid device was very low (0.06%).

While most P3HT-*b*-Poly(fullerene) derivatives were only used as compatibilizers (e.g. P5¹⁴⁵), the polymer P6 from Hashimoto et al. showed an efficiency of 1.7% in a single active layer device.¹⁸ Even though the performance was lower than that of the blend, the block copolymer showed improved thermal stability which is crucial for the technically relevant roll-to-roll processing.

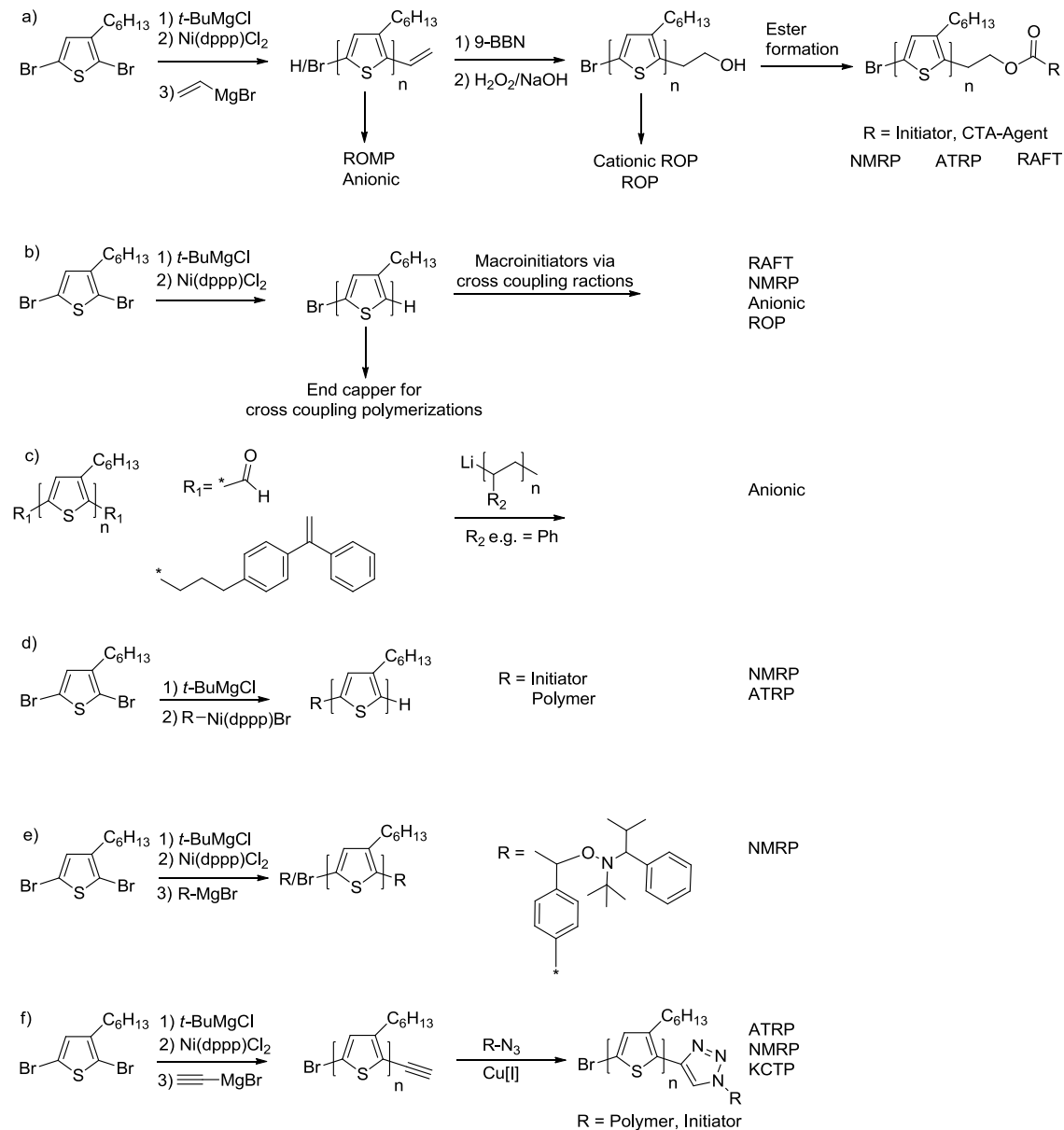
For P3HT-*b*-PPerAcr block copolymers (P7 and P8) different concepts have been applied. In P8 the poly perylene bisimide block was copolymerized with an electrically inert poly(n-butylacrylate) block to improve the chain mobility.¹¹⁷ Using a copper catalyzed azide-alkyne click reaction different poly perylene bisimide acrylate blocks were attached to P3HT carrying an alkyne function. However the device performances was very low (0.03%), which may be partly attributed to the insulating poly(n-butylacrylate) block. In P7 a pure poly perylene bisimide acrylate block was directly polymerized from an P3HT macroinitiator.¹¹⁶ It was shown that for constant block ratios the device performance strongly depends on the length of the P3HT block.⁹⁹ It drastically improved with an increase in the P3HT block length from 8.9 kDa to 17 kDa. This was mainly attributed to an increase in charge carrier mobility in P3HT. Further it was shown that blending it with a PPerAcr homopolymer led to a more balanced charge transport and a power conversion efficiency of 0.56%.¹⁴⁸

Although there are many different types of P3HT containing block copolymers, the number of systems relevant for organic photovoltaics is very low. Therefore, there is a huge demand for block copolymers carrying acceptor or nanoparticle-coordinating second blocks. Further it was shown that the device performance strongly depends on molecular parameters like crystallization, chain length, morphology and balanced charge transport between the donor and acceptor block.^{99,117,148} Thus well controlled synthetic approaches for P3HT (or any new conjugated polymer) containing block copolymers are necessary to fulfill these criteria.

Synthetic Methods for P3HT Block Copolymers

The synthesis of P3HT via KCTP was shown to proceed via a quasi “living” polymerization, with the Ni-catalyst remaining at the chain end. Thus addition of a second monomer should allow for the synthesis of all-conjugated block copolymers. However, this is difficult to achieve because the success depends on the reactivity of the monomers toward intramolecular chain transfer, the order of monomer addition and the ligand of the catalyst.^{59,110,149} Further the KCTP is up to now limited to a few monomers (see Figure 6, chapter 1.3) and the polymerization of typical vinyl or vinylacrylate polymers is not possible. Thus one of the great synthetic challenges is to combine KCTP with other controlled polymerization methods for vinyl polymers or polycondensation reactions for conjugated polymers. Up to now KCTP has been combined with controlled radical polymerizations like atom transfer radical polymerization (ATRP),⁶³ reversible addition fragmentation chain transfer (RAFT),¹²³ nitroxide

mediated radical polymerization (NMRP),¹²³ ionic polymerization,¹⁰⁸ ring opening polymerization (ROP),¹²⁷ ring opening metathesis polymerization (ROMP)¹²² as well as cross coupling reactions.¹⁴² The most common used approaches are summarized in Scheme 5.



Scheme 5: Most prominent synthetic approaches for the synthesis of P3HT block copolymers via a combination of KCTP and controlled polymerization methods or polycondensation reactions for conjugated polymers. 9-BBN = 9-Borabicyclo[3.3.1]nonan.

The first approach in Scheme 5a) is the most widely used one which uses in situ functionalization for the introduction of a vinyl group. This group is transformed into an alcohol via hydroboration and esterification leads to an initiating group for ATRP, NMRP or a chain transfer agent for RAFT.^{63,123} Further, the vinyl or alcohol group can be directly used for starting ROMP,¹²² anionic polymerization¹⁰⁸ as well as ionic¹⁰⁸ or ring opening polymerization.^{127,130} This method is very versatile and leads to exclusively diblock copolymer

formation. But it suffers from multiple post polymerization steps which are difficult for high molecular weight P3HTs. The second method in Scheme 5 b) uses the Br end group which is directly obtained after polymerization. On one hand monobrominated P3HT can be used as an end-capper for polycondensation reactions and on the other hand it can be transformed into a macroinitiator using various cross coupling reactions.^{81,87,115,143,144} This allows the synthesis of all-conjugated di- and triblock copolymers as well as rod-coil diblock copolymer. However, multiple steps towards the macroinitiator are often necessary. Therefore this method is not suitable for P3HTs with high molecular weights. Another approach in Scheme 5c) uses difunctionalized P3HTs as end-capper for living anionic chains.^{140,150} The differently functionalized P3HTs were synthesized via *in situ* end-capping or post polymerization reactions. Anionic polymerization allows a good control over the length and polydispersity of the second block but it also requires tough conditions and often low temperatures. This is sometimes difficult because of the low solubility of P3HT at low temperatures.

As shown before a new end group functionalization method is based on an *ex situ* built initiator carrying a functional group. Recently this was exploited to synthesize a bifunctional initiator for KCTP and NMRP (Scheme 5 d).¹⁰² Further this was used to transform the bromine end group obtained at the chain end of an ATRP synthesized polymer into an initiator for KCTP.¹⁵¹ This approach leads to exclusively diblock copolymers in only few steps which is helpful for high molecular weights. However bifunctionalized initiators are limited to groups which are stable against Grignard reagents and do not influence the control of KCTP, which may limit the versatility. Another simple approach (Scheme 5e) directly uses a Grignard functionalized NMRP initiator to cap the active chain end.¹¹⁶ This allows synthesizing a macroinitiator in one step. Unfortunately it suffers from a mixture of mono- and difunctionalized P3HT when high molecular weights are used. Thus always a mixture of di- and triblock copolymers is obtained after polymerization of the second monomer.⁹⁹

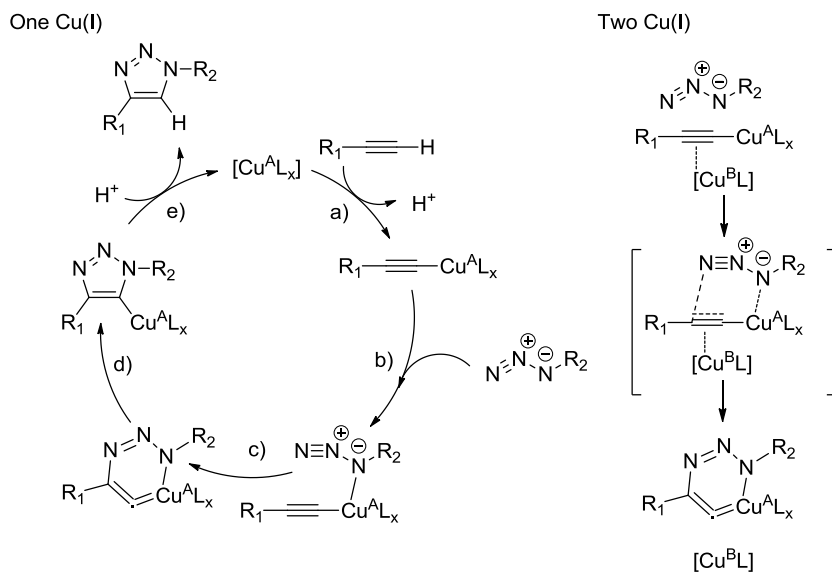
The last method shown in Scheme 5f) uses the copper catalyzed azide-alkyne cycloaddition – one of the so-called “click” reactions.¹⁵² P3HT carrying an alkyne end group can easily be synthesized via *in situ* end-capping of the active chain end with ethynylmagnesium chloride.⁶⁸ Because of the unsaturated alkyne, predominantly monofunctionalized P3HTs are obtained. The alkyne group can be reacted with any macroinitiator or polymer carrying an azide group to form diblock copolymers.^{101,153} Just recently, also azide functionalized P3HTs were realized which can react with any polymer or initiator carrying an alkyne moiety.¹⁵³ This allows for combinatorial approaches and makes this method very versatile.

Even though a lot of different routes to P3HT block copolymer have been realized, only few of them used high molecular weights of 15 kDa or more.^{63,115,142,154} However for organic photovoltaic applications this is one of the prerequisites for good charge carrier mobility and it is also necessary for high χ_N parameters and thus a strong tendency towards microphase

separation. One very promising and versatile method to incorporate high molecular weight P3HTs into block copolymer is the “click” chemistry shown in the last example.

1.6 Copper Catalyzed Azide-Alkyne Cycloaddition (CuAAC)

In 2001 Sharpless et al. published a review about well-known organic reactions which are termed as “click” reactions because they have a high thermodynamic driving force.¹⁵² Some prerequisites are simple reaction conditions, high yields, the reactions should be modular, selective, stereospecific and the products should be easy to purify. One of these reactions is the Huisgen 1,3-dipolar cycloaddition of azides and alkynes.¹⁵⁵ The use of copper(I) as a catalyst accelerates the formation of a regiospecific 1,4-substituted 1,2,3-triazole.^{156,157} High yields, its tolerance of functional groups and solvents as well as a fast reaction at low temperatures led to its application in polymer chemistry.¹⁵⁸ This copper catalyzed azide-alkyne cycloaddition (CuAAC) has been used for a polyaddition polymerization,¹⁵⁹ the attachment of new side chains¹⁶⁰ or end groups and the connection of two different polymer chains to form block copolymers.⁷¹ The mechanism of this reaction involving one or two Cu(I) species is shown in Scheme 6.



Scheme 6: Proposed mechanism of Cu(I) catalyzed azide-alkyne cycloaddition.¹⁶¹ Density functional theory calculations showed that a mechanism involving two Cu(I) species as shown on the right side is energetically favorable.

Apart from the alkyne-, azide- and Cu(I)-species, a ligand is needed. Earlier the ligand was supposed to function as a base to help deprotonating the terminal alkyne and promote the formation of a copper(I)-acetylides in the first step (Scheme 6a). However this reaction even proceeds in acidic media¹⁶² and so the role of the ligand is more to solubilize the Cu(I) species, inhibit the formation of unreactive polynuclear copper(I) acetylides and to ease the coordination of the azide in step (b).¹⁶¹ This coordination of the azide to the copper is essential for activating the formation of the C-N bond in the next step. It increases the nucleophilicity of

the β -carbon of the Cu-acetylides and the electrophilicity of the terminal nitrogen of the azide. Thus a copper metallacycle is formed in step c which is transformed into a copper-triazolide in the next step (d). Protonation (e) gives the 1,4-disubstituted 1,2,3-triazole and the Cu(I) catalyst is regenerated. Recent density functional theory (DFT) calculation showed that it is energetically favorable if a second Cu(I) atom is involved in the catalytic cycle as demonstrated in Scheme 6 right part.¹⁶¹

Since P3HT can be easily functionalized *in situ* with an alkyne group, the CuAAC can be used to introduce initiators for other controlled polymerization methods or to directly couple polymers carrying an azide.

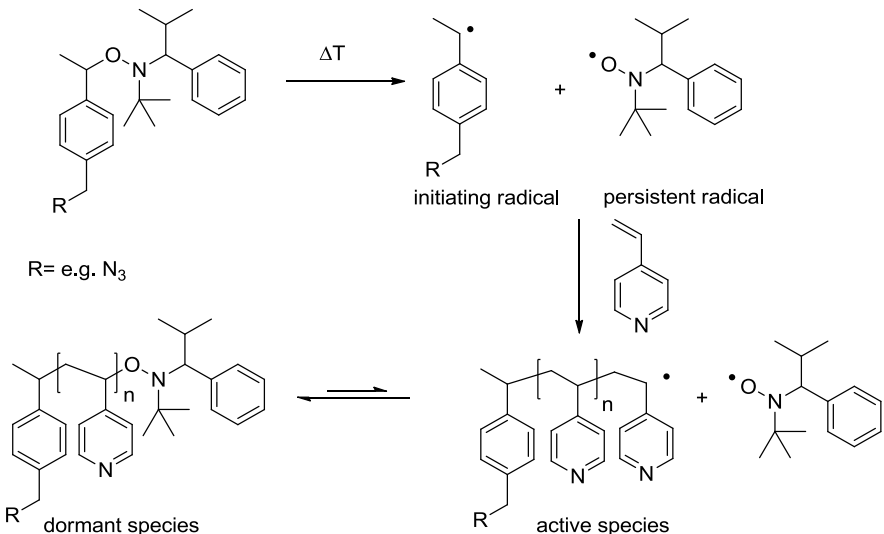
1.7 Nitroxide Mediated Radical Polymerization (NMRP)

For the synthesis of the second block controlled radical polymerizations benefit from easy processing conditions and in comparison to ionic polymerizations no cryogenic temperatures are necessary for good control. This is important as the solubility of high molecular weight P3HT is limited at these temperatures. However, ATRP is difficult for monomers like 4-vinylpyridine, because of a possible coordination of the Cu-catalyst at the free electron pair of the nitrogen.¹⁶³ Nevertheless, this coordination side was usually aimed for, to allow for example the coordination of electron conducting nanoparticles. In this thesis NMRP was used for the synthesis of the second blocks such as poly(4-vinylpyridine) (P4VP) and poly perylene bisimide acrylate (PPerAcr), since our group has already shown that both monomers can be successfully polymerized with NMRP method.^{164,165}

The main principle of nitroxide mediated radical polymerizations (NMRP) is to reduce the concentration of active chain ends and thus chain termination via recombination or disproportionation. The mechanism of NMRP is demonstrated in Scheme 7. Usually unimolecular alkoxyamine initiators are used because they have been shown to work efficiently with a lot of different monomers and low polydispersities can be obtained.^{166,167}

Upon heating they are thermally cleaved into an initiating species and a persistent radical. While the initiating species starts the polymerization the persistent radical is non-reactive towards initiation and self-termination.¹⁶⁸ However it reversibly terminates the active polymer chain end to form a dormant species. Thus the amount of active chain ends is reduced. The rate of polymerization is determined by the position of the equilibrium because chain propagation only occurs at the active species. Further the molecular weight distribution of the obtained polymer depends on the dynamics of the equilibrium between active and dormant species.

Since a functional azide group can easily be introduced at the initiating part of the alkoxyamine, NMRP can be efficiently combined with click chemistry.



Scheme 7: Mechanism of nitroxide mediated radical polymerization of 4-vinylpyridine using azide substituted alkoxyamine. The persistent radical leads to the formation of a dormant species and thus a reduction of active chain ends. Chain propagation only occurs at the side of the active species. A functional group e.g. azide can be easily introduced at the initiating species.

1.8 Characterization Methods

In the chapters before we showed the possibilities for the synthesis of P3HT and its block copolymers. Below two methods for the investigation of the resulting structures and charge carrier mobilities, e. g. XRD and OFETs, are explained.

X-Ray Diffraction on P3HT

P3HT is a semi crystalline polymer which consists of randomly orientated crystalline domains embedded in an amorphous matrix. Thus powder diffraction X-ray measurements can be used to gain information about the order within this polymer. X-rays interact with the electrons of an atom and excite them to oscillate and to emit X-rays in form of spherical waves. The simplest description of the resulting diffraction patterns is the diffraction of X-rays on lattice planes with distances in the range of the wavelength of the incident beam (Figure 12). Depending on the distance d_{hkl} (hkl denote the Miller indices of the lattice planes) between the planes, the diffracted beams interfere destructively or constructively. The condition for constructive interference is given by the Bragg Equation 3 which is also explained in Figure 12.¹⁶⁹

$$n\lambda = 2d_{hkl} \sin\theta \quad (3)$$

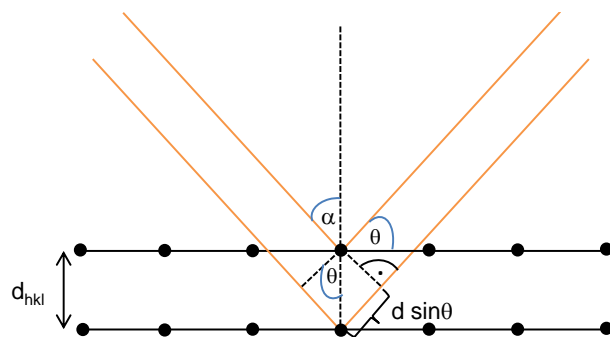


Figure 12: Scheme of the diffraction of X-rays on lattice planes together with the angles and distances necessary for the Bragg Equation (3). hkl are the Miller indices of the lattice planes.

For the microstructure of P3HT two different size ranges are known which can be analyzed with small angle (SAXS) and wide angle (WAXS) X-ray scattering, respectively (Figure 13). WAXS measurements give information about the orientation of the polymer chains within the crystalline domains. In WAXS diffractograms of P3HT, the $h00$ reflexes correspond to the lamellar stacking between the main and side chains along the a axis, $0k0$ reflexes to the $\pi-\pi$ stacking along b axis and $00l$ reflexes to the repeating units along the chain in the c axis. In contrast, SAXS measurements give information about the distance between crystalline and amorphous regions as described by the long period d_L . Further the sizes of the self-assembled structures of block copolymers are detectable with SAXS. Thus X-ray diffraction can be used to analyze the microstructure of P3HT and its respective block copolymers. Further the influence of structural changes on the charge carrier properties of the materials can be measured with organic field effect transistors.

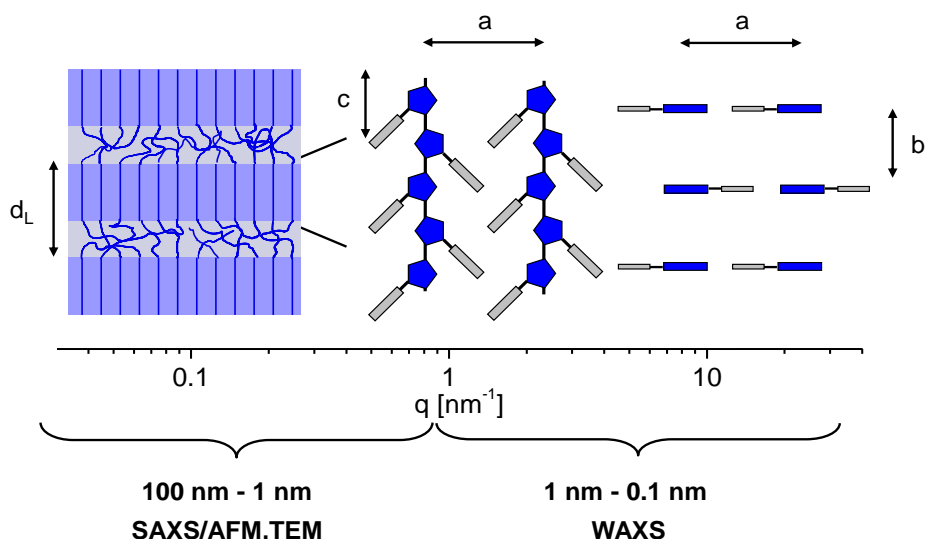


Figure 13: Scheme of the different size ranges of semicrystalline P3HT and the analysis methods which can monitor the respective structures. d_L is the long period.

Charge Carrier Mobility Measurements using Organic Field Effect Transistors

Organic field effect transistors (OFETs) are of great interest for active matrix liquid crystal displays, e-papers or radio-frequency identification (RFID) tags. The performance of these devices is mainly dominated by the charge transport in a semiconductor layer and charge injection and extraction at the different interfaces. Charge transport properties dependent on the charge carrier mobility μ of the material. Charge injection and extraction depend on the contact resistance R_c between the electrodes and the semiconductor.¹⁷⁰ Using a simple model for field-effect transistors as it is used for inorganic FETs, a value for the charge carrier mobility can be extracted. Therefore, OFETs can be used to determine charge carrier mobilities μ of an organic semiconductor. The charge transport within these devices occurs only in a very thin active layer between the semiconductor and a dielectric.¹⁷¹ Measured values may depend on the used dielectrics and the microstructure of the organic material at the dielectric interface. However, if the same setup is used, it is a simple method to monitor the influence of chemical modifications, crystallinity and microstructure on the charge transport of semiconducting polymers. In this thesis, mainly bottom contact, bottom gate devices were used as demonstrated in Figure 14a.

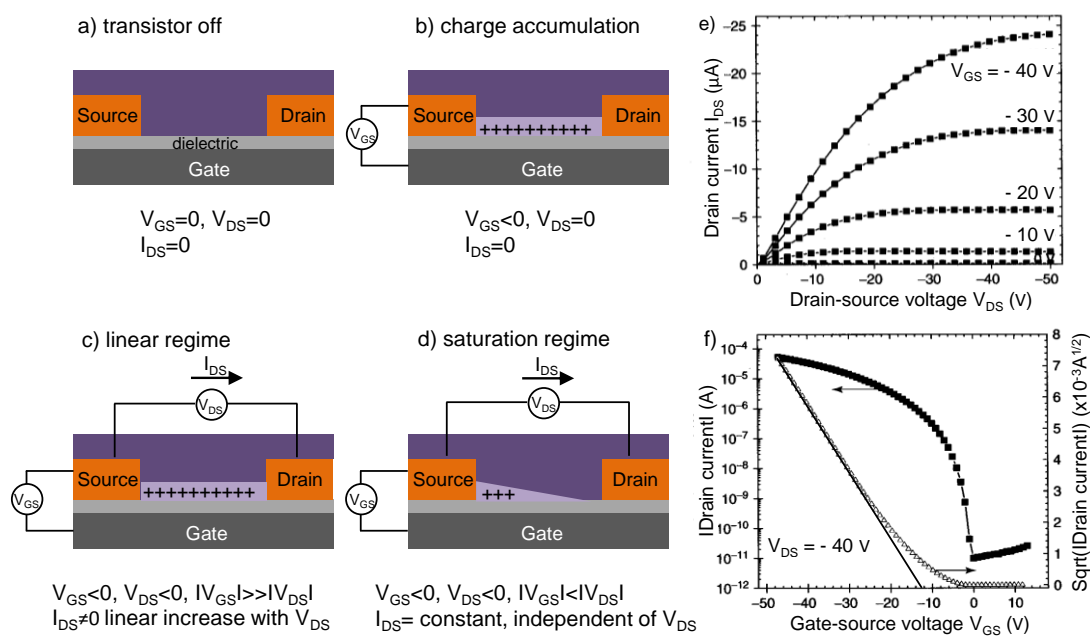


Figure 14: Working principle of an organic field effect transistor (OFET) with a) off state b) charge accumulation state and the two extreme cases c) linear regime and d) saturation regime. e) Output and f) transfer characteristics from an OFET as reproduced from Ong et al.¹⁷⁰

In principle the gate-dielectric-semiconductor OFET structure works like a capacitor (see Figure 14).¹⁷⁰ Upon applying a gate voltage V_{GS} between the gate and the source electrode charge carriers accumulate at the interface between semiconductor and dielectric which causes the formation of a conduction channel (Figure 14b). If a drain bias V_{DS} is applied between source and drain electrode, a current I_{DS} can be measured. Typical output and transfer characteristics of OFETs are shown in Figure 14e and f. In the output characteristic the drain current is measured depending on the applied drain voltage for a fixed gate bias. For small V_{DS} values the measured current follows Ohm's law and is proportional to the applied drain and gate voltages. The transistor is operating in its linear regime (Figure 14c). If the mobility μ is constant and the gradual channel approximation (electric field along channel << electric field across the channel) is valid, the current in this region can be explained with the following Equation:¹⁷⁰

$$I_{DS,lin} = \mu_{lin} C_i \frac{W}{L} \left(V_{GS} - V_T - \frac{V_{DS}}{2} \right) V_{DS} \quad (4)$$

I_{DS} = drain-source current, V_{GS} = gate source voltage, V_{DS} = drain source voltage, V_T = threshold voltage, C_i = capacitance per unit area of dielectric, W = channel width, L = channel length

With increasing V_{DS} the difference to V_{GS} becomes zero, all injected charge carriers are extracted and pinch-off of the channel occurs. If the absolute value of V_{DS} is larger than V_T the current is independent of the applied V_{DS} and saturates (Figure 14e). In the saturation regime the current can be described with Equation 5:¹⁷⁰

$$I_{DS,sat} = \frac{1}{2} \mu_{sat} C_i \frac{W}{L} (V_{GS} - V_T)^2 \quad (5)$$

The charge carrier mobility can be extracted from the transfer characteristic. Here, the square root of the drain-source current is plotted against the gate voltage and from the slope in the saturation regime, the saturation mobility μ_{sat} is obtained (Figure 14f) using Equation 6:

$$\mu_{sat} = \left(\frac{\partial \sqrt{I_{DS}}}{\partial V_{GS}} \right)^2 \frac{2L}{WC_i} \quad (6)$$

1.9 Objective

The factors influencing the performance of organic photovoltaics depend on the material properties, which in turn are decided by the capability to control and manipulate the synthesis and architecture of the active materials. This for example, can be used to study the influence of molecular weight, polydispersity and synthetic strategy on the physical properties and to understand the equilibrium structures of these materials for stable morphologies.

The KCTP is the state of the art synthetic method for poly(3-hexylthiophene) and up to now a lot of factors have been identified to affect the resulting polymer structure and the success of the chain-growth mechanism. However, to establish an universal polymerization method, applicable for any conjugated system, it is important to identify all factors influencing the kinetics of polymerization. For example is there a difference in the McCullough and Yokozawa route, which role plays the quenching agent, is there an ideal time of polymerization and many more. In this thesis factors influencing the end groups and polydispersity of P3HT should be investigated. Especially the identification of the origin of the observed loss of bromine end groups, and the appearance of unexpected hydrogen/hydrogen end group should be addressed. The aim is to allow the synthesis of any molecular weight with 100% H/Br end group and low polydispersities.

In the second part, the solution and bulk structures as well as the resulting physical properties of well-defined P3HTs should be investigated. In cooperation with the group of Prof. Thurn-Albrecht from the University of Halle, the influence of molecular weight and temperature on the hierarchical equilibrium structures in bulk should be addressed. Therefore, especially differential scanning calorimetry (DSC), SAXS and WAXS measurements are important. Further, the aggregate formation of P3HTs in solution should be investigated with optical spectroscopy together with the group of Prof. Anna Köhler from the University of Bayreuth. This is important for understanding the film formation during processing from solution. Here the influence of solvent, molecular weight and synthetic method on the aggregate formation in solution and its effect on the resulting charge carrier mobilities in OFETs should be addressed.

In a third part, the defined bromine end group of P3HT should be modified in a post-polymerization reaction to obtain functional carboxylic acid groups which are difficult to obtain by ex situ initiation or in situ functionalization methods. These carboxylic groups can be used to coordinate electron conducting nanoparticles, to anchor P3HT onto surfaces or for end-capping polymerizations to get block copolymers.

P3HT containing block copolymers are of high interest for organic photovoltaics but there is a huge need for synthetic approaches allowing the incorporation of long P3HT blocks with high charge carrier mobility. Further, block copolymers with active second blocks, which act as electron acceptors or can coordinate electron conducting nanoparticles, are necessary. Thus in this thesis the control over the P3HT synthesis should be exploited to develop a suitable

synthetic method for high molecular weight P3HT block copolymers. The second blocks should be poly(4-vinylpyridine) (P4VP) for the coordination of electron conducting nanoparticles or poly perylene bisimide acrylate (PPerAcr) as an electron conducting acceptor. For P3HT-*b*-PPerAcr block copolymers long acceptor blocks are necessary for a balanced charge transport. Further high total molecular weights increase the χN parameter and thus may help to get clear microphase separated structures with domains sizes relevant for organic photovoltaics.

References

- (1) http://nobelprize.org/nobel_prizes/chemistry/laureates/2000/chemadv.pdf, 26.10.2011.
- (2) Shirakawa, H. *Angew. Chem.* **2001**, *113*, 2642-2648.
- (3) Shirakawa, H.; Louis, E. J.; MacDiarmid, A. G.; Chiang, C. K.; Heeger, A. J. *Chem. Commun.* **1977**, 578-580.
- (4) Chiang, C. K.; Fincher, C. R., Jr.; Park, Y. W.; Heeger, A. J.; Shirakawa, H.; Louis, E. J.; Gau, S. C.; MacDiarmid, A. G. *Phys. Rev. Lett.* **1977**, *39*, 1098-1101.
- (5) Skotheim, T. A.; Reynolds, J. R.; (eds.) *Conjugated Polymers: Theory, Synthesis, Properties, and Characterization*, 3rd ed.; CRC Press: Boca Raton, 2007.
- (6) Heeger, A. J. *Chem. Soc. Rev.* **2010**, *39*, 2354-2371.
- (7) Dimitrakopoulos, C. D.; Malenfant, P. R. L. *Adv. Mater.* **2002**, *14*, 99-117.
- (8) Garnier, F.; Hajlaoui, R.; Yassar, A.; Srivastava, P. *Science* **1994**, *265*, 1684-1686.
- (9) Friend, R. H.; Gymer, R. W.; Holmes, A. B.; Burroughes, J. H.; Marks, R. N.; Taliani, C.; Bradley, D. D. C.; Santos, D. A. D.; Bredas, J. L.; Logdlund, M.; Salaneck, W. R. *Nature* **1999**, *397*, 121-128.
- (10) Tang, C. W. *Appl. Phys. Lett.* **1986**, *48*, 183-185.
- (11) O'Regan, B.; Grätzel, M. *Nature* **1991**, *353*, 737-740.
- (12) Sariciftci, N. S.; Braun, D.; Zhang, Z.; Srdanov, V. I.; Heeger, A. J.; Stucky, G.; Wudl, F. *Appl. Phys. Lett.* **1993**, *62*, 585-587.
- (13) Chen, C. Y.; Wang, M.; Li, J. Y.; Pootrakulchote, N.; Alibabaei, L.; Ngoc-le, C.; Decoppet, J. D.; Tsai, J. H.; Grätzel, C.; Wu, C. G.; Zakeeruddin, S. M.; Grätzel, M. *ACS Nano* **2009**, *3*, 3103-3109.
- (14) Snaith, H. J.; Moule, A. J.; Klein, C.; Meerholz, K.; Friend, R. H.; Grätzel, M. *Nano Lett.* **2007**, *7*, 3372-3376.
- (15) Liang, Y.; Xu, Z.; Xia, J.; Tsai, S.; Wu, Y.; Li, G.; Ray, C.; Yu, L. *Adv. Mater.* **2010**, *22*, E135-E138.
- (16) Ma, W.; Yang, C.; Gong, X.; Lee, K.; Heeger, A. J. *Adv. Funct. Mater.* **2005**, *15*, 1617-1622.
- (17) Bu, L.; Guo, X.; Yu, B.; Qu, Y.; Xie, Z.; Yan, D.; Geng, Y.; Wang, F. *J. Am. Chem. Soc.* **2009**, *131*, 13242-13243.
- (18) Miyanishi, S.; Zhang, Y.; Tajima, K.; Hashimoto, K. *Chem. Commun.* **2010**, *46*, 6723-6725.
- (19) Zhou, E.; Cong, J.; Wei, Q.; Tajima, K.; Yang, C.; Hashimoto, K. *Angew. Chem.* **2011**, *123*, 2851-2855.
- (20) Topham, P. D.; Parnell, A. J.; Hiorns, R. C. *J. Polym. Sci. B Polym. Phys.* **2011**, *49*, 1131-1156.
- (21) Scharber, M. C.; Mühlbacher, D.; Koppe, M.; Demk, P.; Waldauf, C.; Heeger, A. J.; Brabec, C. *J. Adv. Mater.* **2006**, *18*, 789-794.
- (22) http://docs.lumerical.com/en/fdtd/solar_spectrum.jpg, 23.11.2011.

- (23) Allard, S.; Forster, M.; Souharce, B.; Thiem, H.; Scherf, U. *Angew. Chem.* **2008**, *120*, 2-32.
- (24) Loewe, R. S.; Ewbank, P. C.; Liu, J.; Zhai, L.; McCullough, R. D. *Macromolecules* **2001**, *34*, 4324-4333.
- (25) Sirringhaus, H.; Brown, P. J.; Friend, R. H.; Nielson, M. M.; Bechgaard, K.; Langeveld-Voss, B. M. W.; Spiering, A. J. H.; Janssen, R. A. J.; Meijer, E. W.; Herwig, P.; De Leeuw, D. M. *Nature* **1999**, *401*, 685-688.
- (26) Kline, R. J.; McGehee, M. D.; Kadnikova, E. N.; Liu, J.; Fréchet, J. M. J. *Adv. Mater.* **2003**, *15*, 1519-1522.
- (27) Lan, Y.; Huang, C. *J. Phys. Chem. B* **2009**, *113*, 14555-14564.
- (28) Kline, R. J.; McGehee, M. D.; Kadnikova, E. N.; Liu, J.; Frechet, J. M. J.; Toney, M. F. *Macromolecules* **2005**, *38*, 3312-3319.
- (29) Zen, A.; Saphiannikova, M.; Neher, D.; Grenzer, J.; Grigorian, S.; Pietsch, U.; Asawapirom, U.; Janietz, S.; Scherf, U.; Lieberwirth, I.; Wegner, G. *Macromolecules* **2006**, *39*, 2162-2171.
- (30) Sirringhaus, H.; Tessler, N.; Friend, R. H. *Science* **1998**, *280*, 1741-1744.
- (31) Wang, G.; Swensen, J.; Moses, D.; Heeger, A. J. *J. Appl. Phys.* **2003**, *93*, 6137-6141.
- (32) Lin, J. W. P.; Dudek, L. P. *Polym. Sci., Polym. Chem. Ed.* **1980**, *18*, 2869-2873.
- (33) Yamamoto, T.; Sanechika, K.; Yamamoto, A. J. *Polym. Sci., Polym. Lett. Ed.* **1980**, *18*, 9-12.
- (34) Elsenbaumer, R. L.; Jen, K. Y.; Oboodi, R. *Synth. Met.* **1986**, *15*, 169-174.
- (35) Sugimoto, R. I.; Takeda, S.; Gu, H. B.; Yoshino, K. *Chem. Express* **1986**, *11*, 635-638.
- (36) Osaka, I.; McCullough, R. D. *Acc. Chem. Res.* **2008**, *41*, 1202-1214.
- (37) Chen, T.; Rieke, R. D. *J. Am. Chem. Soc.* **1992**, *114*, 10087-10088.
- (38) McCullough, R. D.; Lowe, R. D. *Chem. Commun.* **1992**, *70*-72.
- (39) Loewe, R. S.; Khersonsky, M. S.; McCullough, R. D. *Adv. Mater.* **1999**, *11*, 250-253.
- (40) Iovu, M. C.; Sheina, E. E.; Gil, R. R.; McCullough, R. D. *Macromolecules* **2005**, *38*, 8649-8656.
- (41) Miyakoshi, R.; Yokoyama, A.; Yokozawa, T. *J. Am. Chem. Soc.* **2005**, *127*, 17542-17547.
- (42) Sheina, E. E.; Liu, J.; Iovu, M. C.; Laird, D. W.; McCullough, R. D. *Macromolecules* **2004**, *37*, 3526-3528.
- (43) Yokoyama, A.; Miyakoshi, R.; Yokozawa, T. *Macromolecules* **2004**, *37*, 1169-1171.
- (44) Lanni, E. L.; McNeil, A. J. *Macromolecules* **2010**, *43*, 8039-8044.
- (45) Lohwasser, R. H.; Thelakkat, M. *Macromolecules* **2011**, *44*, 3388-3397.
- (46) Miyakoshi, R.; Shimono, K.; Yokoyama, A.; Yokozawa, T. *J. Am. Chem. Soc.* **2006**, *128*, 16012-16013.
- (47) Huang, L.; Wu, S.; Qu, Y.; Geng, Y.; Wang, F. *Macromolecules* **2008**, *41*, 8944-8947.
- (48) Stefan, M. C.; Javier, A. E.; Osaka, I.; McCullough, R. D. *Macromolecules* **2009**, *42*, 30-32.

- (49) Heeney, M.; Zhang, W.; Crouch, D. J.; Chabiny, M. L.; Gordeyev, S.; Hamilton, R.; Higgins, S. J.; McCulloch, I.; Skabara, P. J.; Sparrowe, D.; Tierney, S. *Chem. Commun.* **2007**, 5061-5063.
- (50) Wen, L.; Duck, B. C.; Dastoor, P. C.; Rasmussen, S. C. *Macromolecules* **2010**, *41*, 4576-4578.
- (51) Wu, S.; Sun, Y.; Huang, L.; Wang, J.; Zhou, Y.; Geng, Y.; Wang, F. *Macromolecules* **2010**, *43*, 4438-4440.
- (52) Wu, Z.; Ono, R. J.; Chen, Z.; Bielawski, C. W. *J. Am. Chem. Soc.* **2010**, *132*, 14000-14001.
- (53) Beryozkina, T.; Senkovskyy, V.; Kaul, E.; Kiriy, A. *Macromolecules* **2008**, *41*, 7817-7823.
- (54) Khanduyeva, N.; Senkovskyy, V.; Beryozkina, T.; Horecha, M.; Stamm, M.; Uhrich, C.; Riede, M.; Leo, K.; Kiriy, A. *J. Am. Chem. Soc.* **2008**, *131*, 153-161.
- (55) Senkovskyy, V.; Khanduyeva, N.; Komber, H.; Oertel, U.; Stamm, M.; Kuckling, D.; Kiriy, A. *J. Am. Chem. Soc.* **2007**, *129*, 6626-6632.
- (56) Senkovskyy, V.; Beryozkina, T.; Bocharova, V.; Tkachov, R.; Komber, H.; Lederer, A.; Stamm, M.; Severin, N.; Rabe, J. P.; Kiriy, A. *Macromol. Symp.* **2010**, *291*-292, 17-25.
- (57) Boyd, S. D.; Jen, K.-Y.; Luscombe, C. K. *Macromolecules* **2009**, *42*, 9387-9389.
- (58) Chen, T.; Wu, X.; Rieke, R. D. *J. Am. Chem. Soc.* **1995**, *117*, 233-244.
- (59) Adachi, I.; Miyakoshi, R.; Yokoyama, A.; Yokozawa, T. *Macromolecules* **2006**, *39*, 7793-7795.
- (60) Lanni, E. L.; McNeil, A. J. *J. Am. Chem. Soc.* **2009**, *131*, 16573-16579.
- (61) Smeets, A.; Van den Bergh, K.; De Winter, J.; Gerbaux, P.; Verbiest, T.; Koeckelsberghs, G. *Macromolecules* **2009**, *42*, 7638-7641.
- (62) Briseno, A. L.; Holcombe, T. W.; Boukai, A. I.; Garnett, E. C.; Shelton, S. W.; Fréchet, J. M. J.; Yang, P. *Nano Lett.* **2010**, *10*, 334-340.
- (63) Liu, J.; Sheina, E. E.; Kowalewski, T.; McCullough, R. D. *Angew. Chem., Int. Ed.* **2002**, *41*, 329-332.
- (64) Lohwasser, R.; Bandara, J.; Thelakkat, M. *J. Mater. Chem.* **2009**, *19*, 4126-4130.
- (65) Xu, J.; Wang, J.; Mitchell, M.; Mukherjee, P.; Jeffries-El, M.; Petrich, J. W.; Lin, Z. J. *Am. Chem. Soc.* **2007**, *129*, 12828-12833.
- (66) Zhang, Q.; Russell, T. P.; Emrick, T. *Chemi. Mater.* **2007**, *19*, 3712-3716.
- (67) Lee, J. U.; Jung, J. W.; Emrick, T.; Russell, T. P.; Jo, W. H. *J. Mater. Chem.* **2010**, *20*, 3287-3294.
- (68) Jeffries-El, M.; Sauve, G.; McCullough, R. D. *Adv. Mater.* **2004**, *16*, 1017-1019.
- (69) Crabtree, R. H. *The Organometallic Chemistry of the Transition Metals*, 3rd ed.; John Wiley & Sons: New York, 2011.
- (70) Tolman, C. A.; Seidel, W. C.; Gosser, L. W. *Organometallics* **1983**, *2*, 1391-1396.
- (71) Li, Z.; Ono, R. J.; Wu, Z.; Bielawski, C. W. *Chem. Commun.* **2011**, *47*, 197-199.
- (72) Jeffries-El, M.; Sauve, G.; McCullough, R. D. *Macromolecules* **2005**, *38*, 10346-10352.

- (73) Kiriy, A.; Senkovskyy, V.; Sommer, M. *Macromol. Rapid Commun.* **2011**, *32*, 1503-1517.
- (74) Smeets, A.; Van den Bergh, K.; De Winter, J.; Gerbaux, P.; Verbiest, T.; Koeckelsberghs, G. *Macromolecules* **2009**, *42*, 7638-7641.
- (75) Bronstein, H. A.; Luscombe, C. K. *J. Am. Chem. Soc.* **2009**, *131*, 12894-12895.
- (76) Senkovskyy, V.; Tkachov, R.; Beryozkina, T.; Komber, H.; Oertel, U.; Horecha, M.; Bocharova, V.; Stamm, M.; Gevorgyan, S. A.; Krebs, F. C.; Kiriy, A. *J. Am. Chem. Soc.* **2009**, *131*, 16445-16453.
- (77) Senkovskyy, V.; Sommer, M.; Tkachov, R.; Komber, H.; Huck, W. T. S.; Kiriy, A. *Macromolecules* **2010**, *43*, 10157-10161.
- (78) Doubina, N.; Ho, A.; Jen, A. K. Y.; Luscombe, C. K. *Macromolecules* **2009**, *42*, 7670-7677.
- (79) Doubina, N.; Paniagua, S. A.; Soldatova, A. V.; Jen, A. K. Y.; Marder, S. R.; Luscombe, C. K. *Macromolecules* **2011**, *44*, 512-520.
- (80) Smeets, A.; Willot, P.; De Winter, J.; Gerbaux, P.; Verbiest, T.; Koeckelsberghs, G. *Macromolecules* **2011**, *44*, 6017-6025.
- (81) Hundt, N.; Hoang, Q.; Nguyen, H.; Sista, P.; Hao, J.; Servello, J.; Palaniappan, K.; Alemsegued, M. G.; Biewer, M. C.; Stefan, M. C. *Macromol. Rapid Commun.* **2011**, *32*, 302-308.
- (82) Langeveld-Voss, B. M. W.; Janssen, R. A. J.; Spiering, A. J. H.; Van Dongen, J. L. J.; Vonk, E. C.; Claessens, H. A. *Chem. Commun.* **2000**, 81-82.
- (83) Liu, J.; McCullough, R. D. *Macromolecules* **2002**, *35*, 9882-9889.
- (84) Liu, J.; Tanaka, T.; Sivula, K.; Alivisatos, A. P.; Fréchet, J. M. J. *J. Am. Chem. Soc.* **2004**, *126*, 6550-6551.
- (85) Watanabe, N.; Mauldin, C.; Fréchet, J. M. J. *Macromolecules* **2007**, *40*, 6793-6795.
- (86) Briseno, A. L.; Holcombe, T. W.; Boukai, A. I.; Garnett, E. C.; Shelton, S. W.; Fréchet, J. M. J.; Yang, P. *Nano Lett.* **2009**, *10*, 334-340.
- (87) Sary, N.; Richard, F.; Brochon, C.; Leclerc, M.; Leveque, P.; Audinot, J.; Berson, S.; Heiser, T.; Hadzioannou, G.; Mezzenga, R. *Adv. Mater.* **2009**, *21*, 1-6.
- (88) Sivula, K.; Ball, Z. T.; Watanabe, N.; Fréchet, J. M. J. *Adv. Mater.* **2006**, *18*, 206-210.
- (89) Matsen, M. W.; Bates, F. S. *Macromolecules* **1996**, *29*, 1091-1098.
- (90) Leibler, L. *Macromolecules* **1980**, *13*, 1602-1617.
- (91) Scherf, U.; Adamczyk, S.; Gutacker, A.; Koenen, N. *Macromol. Rapid Commun.* **2009**, *30*, 1059-1065.
- (92) Vriezema, D. M.; Comellas Aragon, M.; Elemans, J. A. A. W.; Cornelissen, J. J. L. M.; Rowan, A. E.; Nolte, R. J. M. *Chem. Rev.* **2005**, *105*, 1445-1490.
- (93) Botiz, I.; Darling, S. B. *Mater. Today* **2010**, *13*, 42-51.
- (94) Darling, S. B. *Prog. Polym. Sci.* **2007**, *32*, 1152-1204.
- (95) de Cuendias, A.; Hiorns, R. C.; Cloutet, E.; Vignau, L.; Cramail, H. *Polym. Int.* **2010**, *59*, 1452-1476.

- (96) Park, S.; Kang, S.; Fryd, M.; Saven, J. G.; Park, S. *J. Am. Chem. Soc.* **2010**, *132*, 9931-9933.
- (97) Liu, C.; Lin, C.; Kuo, C.; Lin, S.; Chen, W. *Prog. Polym. Sci.* **2011**, *36*, 603-637.
- (98) Olsen, B. D.; Segalman, R. A. *Mater. Sci. Eng., R* **2008**, *62*, 37-66.
- (99) Sommer, M.; Hüttner, S.; Steiner, U.; Thelakkat, M. *Appl. Phys. Lett.* **2009**, *95*, 183308.
- (100) Iovu, M. C.; Zhang, R.; Cooper, J. R.; Smilgies, D. M.; Javier, A. E.; Sheina, E. E.; Kowalewski, T.; McCullough, R. D. *Macromol. Rapid Commun.* **2007**, *28*, 1816-1824.
- (101) Urien, M.; Erothu, H.; Cloutet, E.; Hiorns, R. C.; Vignau, L.; Cramail, H. *Macromolecules* **2008**, *41*, 7033-7040.
- (102) Kaul, E.; Senkovskyy, V.; Tkachov, R.; Bocharova, V.; Komber, H.; Stamm, M.; Kiriy, A. *Macromolecules* **2010**, *43*, 77-81.
- (103) Huang, K.; Fang, Y.; Hsu, J.; Kuo, C.; Chang, W.; Chen, W. *J. Polym. Sci., Part A: Polym. Chem.* **2011**, *49*, 147-155.
- (104) Aissou, K.; Pfaff, A.; Giacomelli, C.; Travelet, C.; Müller, A. H. E.; Borsali, R. *Macromol. Rapid Commun.* **2011**, *32*, 912-916.
- (105) Craley, C. R.; Zhang, R.; Kowalewski, T.; McCullough, R. D.; Stefan, M. C. *Macromol. Rapid Commun.* **2009**, *30*, 11-16.
- (106) Yuan, K.; Li, F.; Chen, Y.; Wang, X.; Chen, L. *J. Mater. Chem.* **2011**, *21*, 11886-11894.
- (107) Botiz, I.; Darling, S. B. *Macromolecules* **2009**, *42*, 8211-8217.
- (108) Dai, C.; Yen, W.; Lee, Y.; Ho, C.; Su, W. *J. Am. Chem. Soc.* **2007**, *129*, 11036-11038.
- (109) Yen, W. C.; Lee, Y. H.; Lin, J. F.; Dai, C. A.; Jeng, U. S.; Su, W. F. *Langmuir* **2010**, *27*, 109-115.
- (110) Javier, A. E.; Varshney, S. R.; McCullough, R. D. *Macromolecules* **2010**, *43*, 3233-3237.
- (111) Wu, S.; Bu, L.; Huang, L.; Yu, X.; Han, Y.; Geng, Y.; Wang, F. *Polymer* **2009**, *50*, 6245-6251.
- (112) He, M.; Han, W.; Yang, Y.; Qiu, F.; Lin, Z. *Energy Environ. Sci.* **2011**, *4*, 2894-2902.
- (113) Heo, M.; Kim, J.; Kim, J. Y.; Yang, C. *Macromol. Rapid Commun.* **2011**, *31*, 2047-2052.
- (114) Hammer, B. A. G.; Bokel, F. A.; Hayward, R. C.; Emrick, T. *Chem. Mater.* **2011**, *23*, 4250-3256.
- (115) Rajaram, S.; Armstrong, P. B.; Kim, B. J.; Fréchet, J. M. J. *Chem. Mater.* **2009**, *21*, 1775-1777.
- (116) Sommer, M.; Lang, A. S.; Thelakkat, M. *Angew. Chem., Int. Ed.* **2008**, *47*, 7901-7904.
- (117) Tao, Y.; McCulloch, B.; Kim, S.; Segalman, R. A. *Soft Matter* **2009**, *5*, 4219-4230.
- (118) Zhang, Q.; Cirpan, A.; Russel, T. P.; Emrick, T. *Macromolecules* **2009**, *42*, 1079-1082.
- (119) Lee, J. K.; Cirpan, A.; Emrick, T.; Russel, T. P.; Jo, W. H. *J. Mater. Chem.* **2009**, *19*, 1483-1489.
- (120) Lai, Y.; Ohshimizu, K.; Takahashi, A.; Hsu, J.; Higashihara, T.; Ueda, M.; Chen, W. *J. Polym. Sci., Part A: Polym. Chem.* **2011**, *49*, 2577-2587.

- (121) Sommer, M.; Hüttner, S.; Thelakkat, M.; *Semiconductor Block Copolymers for Photovoltaic Applications In Ideas in Chemistry and Molecular Sciences: Advances in Nanotechnology, Materials and Device* (Ed: B.Pignataro), WILEY-VCH Verlag GmbH & Co. KGaA, Weinheim, **2010**, Ch. 12.
- (122) Radano, C. P.; Schermen, O. A.; Stingelin-Stutzmann, N.; Müller, C.; Breiby, D. W.; Smith, P.; Janssen, R. A. J.; Mejier, E. W. *J. Am. Chem. Soc.* **2005**, *127*, 12502-12503.
- (123) Iovu, M. C.; Craley, C. R.; Jeffries-El, M.; Krancowski, A. B.; Zhang, R.; Kowalewski, T.; McCullough, R. D. *Macromolecules* **2007**, *40*, 4733-4735.
- (124) Higashihara, T.; Liu, C.; Chen, W.; Ueda, M. *Polymers* **2011**, *3*, 236-251.
- (125) Han, D.; Tong, X.; Zhao, Y.; Zhao, Y. *Angew. Chem., Int. Ed.* **2010**, *49*, 9162-9165.
- (126) Patra, S. K.; Ahmed, R.; Whittell, G. R.; Lunn, D. J.; Dunphy, E. L.; Manners, I. *J. Am. Chem. Soc.* **2011**, *133*, 8842-8845.
- (127) Boudouris, B. W.; Frisbie, C. D.; Hillmyer, M. A. *Macromolecules* **2008**, *41*, 67-75.
- (128) Alemsegbed, M. G.; Servello, J.; Hundt, N.; Sista, P.; Biewer, M. C.; Stefan, M. C. *Macromol. Chem. Phys.* **2010**, *211*, 1291-1297.
- (129) Sarkar, S.; Zou, J.; Liu, J.; Xu, C.; An, L.; Zhai, L. *ACS Appl. Mater.* **2010**, *2*, 1150-1156.
- (130) Alemsegbed, M. G.; Gowrisanker, S.; Servello, J.; Stefan, M. C. *Macromol. Chem. Phys.* **2009**, *210*, 2007-2014.
- (131) Zhang, Y.; Tajima, K.; Hirota, K.; Hashimoto, K. *J. Am. Chem. Soc.* **2008**, *130*, 7812-7813.
- (132) Yamada, I.; Takagi, K.; Hayashi, Y.; Soga, T.; Shibata, N.; Toru, T. *Int. J. Mol. Sci.* **2010**, *11*, 5027-5039.
- (133) Wu, P.; Ren, G.; Li, C.; Mezzenga, R.; Jenekhe, S. A. *Macromolecules* **2009**, *42*, 2317-2320.
- (134) Wu, P.; Ren, G.; Kim, F. S.; Li, C.; Mezzenga, R.; Jenekhe, S. A. *J. Polym. Sci., Part A: Polym. Chem.* **2009**, *48*, 614-626.
- (135) Oshimizu, K.; Ueda, M. *Macromolecules* **2008**, *41*, 5289-5294.
- (136) He, M.; Zhao, L.; Wang, J.; Han, W.; Yang, Y.; Qiu, F.; Lin, Z. *ACS Nano* **2010**, *4*, 3241-3247.
- (137) Van den Bergh, K.; Huybrechts, J.; Verbiest, T.; Koeckelberghs, G. *Chem. Eur. J.* **2008**, *14*, 9122-9125.
- (138) Verduzco, R.; Botiz, I.; Pickel, D. L.; Kilbey, S. M.; Hong, K.; Dimasi, E.; Darling, S. B. *Macromolecules* **2011**, *44*, 530-539.
- (139) Hollinger, J.; Jahnke, A. A.; Coombs, N.; Seferos, D. W. *J. Am. Chem. Soc.* **2010**, *132*, 8546-8547.
- (140) Higashihara, T.; Ohshimizu, K.; Hirao, A.; Ueda, M. *Macromolecules* **2008**, *41*, 9505-9507.
- (141) Fang, Y.; Liu, C.; Li, C.; Lin, C.; Mezzenga, R.; Chen, W. *Adv. Funct. Mater.* **2010**, *20*, 3012-3024.
- (142) Tu, G.; Li, H.; Forster, M.; Heiderhoff, R.; Balk, L. J.; Scherf, U. *Macromolecules* **2006**, *39*, 4327-4331.

- (143) Izuhara, D.; Swager, T. M. *Macromolecules* **2011**, *44*, 2678-2684.
- (144) Richard, F.; Brochon, C.; Leclerc, N.; Eckhardt, D.; Heiser, T.; Hadzioannou, G. *Macromol. Rapid Commun.* **2008**, *29*, 885-891.
- (145) Yang, C.; Lee, J. K.; Heeger, A. J.; Wudl, F. *J. Mater. Chem.* **2009**, *19*, 5416-5423.
- (146) Dante, M.; Yang, C.; Walker, B.; Wudl, F.; Nguyen, H. *Adv. Mater.* **2010**, *22*, 1835-1839.
- (147) Lee, Y. H.; Yen, W. C.; Su, W. F.; Dai, C. A. *Soft Matter* **2011**, *7*, 10429-10442.
- (148) Singh, C. R.; Sommer, M.; Himmerlich, M.; Wicklein, A.; Krischock, S.; Thelakkat, M.; Hoppe, H. *Phys. Status Solidi RRL* **2011**, *5*, 247-249.
- (149) Miyakoshi, R.; Yokoyama, A.; Yokozawa, T. *J. Polym. Sci., Part A: Polym. Chem.* **2008**, *46*, 753-765.
- (150) Moon, H. C.; Anthonysamy, A.; Lee, Y.; Kim, J. K. *Macromolecules* **2010**, *43*, 1747-1752.
- (151) Yu, X.; Xiao, K.; Chen, J.; Lavrik, N.; Hong, K.; Sumpter, B. G.; Geohegan, D. B. *ACS Nano* **2011**, *5*, 3559-3567.
- (152) Kolb, H. C.; Finn, M. G.; Sharpless K.B. *Angew. Chem., Int. Ed.* **2001**, *40*, 2004-2021.
- (153) Britze, A.; Möllmann, V.; Grundmeier, G.; Luftmann, H.; Kuckling, D. *Macromol. Chem. Phys.* **2011**, *212*, 679-690.
- (154) Iovu, M. C.; Jeffries-El, M.; Zhang, R.; Kowalewski, T.; McCullough, R. D. *J. Macromol. Sci., Part A: Pure Appl. Chem.* **2006**, *43*, 1991-2000.
- (155) Huisgen, R. *Angew. Chem., Int. Ed.* **1963**, *2*, 565-598.
- (156) Rostovtsev, V. V.; Green, L. G.; Fokin, V. V.; Sharpless, K. B. *Angew. Chem., Int. Ed.* **2002**, *41*, 2596-2599.
- (157) Tornøe, C. W.; Christensen, C.; Meldal, M. *J. Org. Chem.* **2002**, *67*, 3057-3064.
- (158) Binder, W. H.; Sachsenhofer, R. *Macromol. Rapid Commun.* **2007**, *28*, 15-54.
- (159) Van Steenis, D. J. V. C.; David, O. R. P.; Maarseveen, J. H.; Reek, J. N. H. *Chem. Commun.* **2005**, 4333-4335.
- (160) Sumerlin, B. S.; Tsarevsky, N. V.; Louche, G.; Lee, R. Y.; Matyjaszewski, K. *Macromolecules* **2005**, *38*, 7540-7545.
- (161) Hein, J. E.; Fokin, V. V. *Chem. Soc. Rev.* **2010**, *39*, 1302-1315.
- (162) Mykhalichko, B. M.; Temkin, O. N.; Mys'kiv, M. G. *Russ. Chem. Rev.* **2000**, *69*, 957-984.
- (163) Xia, J.; Zhang, X.; Matyjaszewski, K. *Macromolecules* **1999**, *32*, 3531-3533.
- (164) Maria, S.; Susha, S.; Sommer, M.; Talapin, D. V.; Thelakkat, M. *Macromolecules* **2008**, *41*, 6081-6088.
- (165) Lindner, S. M.; Thelakkat, M. *Macromolecules* **2004**, *37*, 8832-8835.
- (166) Benoit, D.; Chaplinski, V.; Braslau, R.; Hawker, C. J. *J. Am. Chem. Soc.* **1999**, *121*, 3904-3920.
- (167) Hawker, C. J.; Bosman, A. W.; Harth, E. *Chem. Rev.* **2001**, *101*, 3661-3688.
- (168) Fischer, H. *Chem. Rev.* **2001**, *101*, 3581-3610.

- (169) Abou-Ras, D.; Kirchartz, T.; and Rau, U.; (eds.) *Advanced Characterization Techniques for Thin Film Solar Cells*; Wiley-VCH Verlag GmbH & Co. KGaA: Weinheim, **2011**.
- (170) Li, F. M.; Nathan, A.; Wu, Y.; Ong, B. S.; (eds.) *Organic Thin Film Transistor Integration*; Wiley-VCH Verlag GmbH & Co. KGaA: Weinheim, **2011**.
- (171) Dinelli, F.; Murgia, M.; Levy, P.; Cavallini, M.; Biscarini, F.; de Leeuw, D. M. *Phys. Rev. Lett.* **2004**, 92, 116802.

2. Overview of the Thesis

This thesis contains nine papers. Six of them (Chapter 3 - 8) appear in the main part and three (Chapter 9 - 11) in the appendix. In the main part three are published, one is accepted, one is submitted and one is intended for submission. The three in the appendix are already published.

The main aim of this thesis was to study the factors controlling the synthesis of P3HT. This knowledge was used for understanding the physical properties and structure formation of the homopolymer. Furthermore, the defined end groups were used to introduce a carboxylic acid chain end. Additionally, block copolymers containing a high molecular weight P3HT block as well as second blocks relevant for organic photovoltaics were synthesized. Thus the central topic of the thesis connecting all chapters is the *control of synthesis* of P3HT including molecular weight, end groups and polydispersity as presented in chapter 3. The remaining chapters can be divided into three additional categories based on the basic question involved (Figure 1).

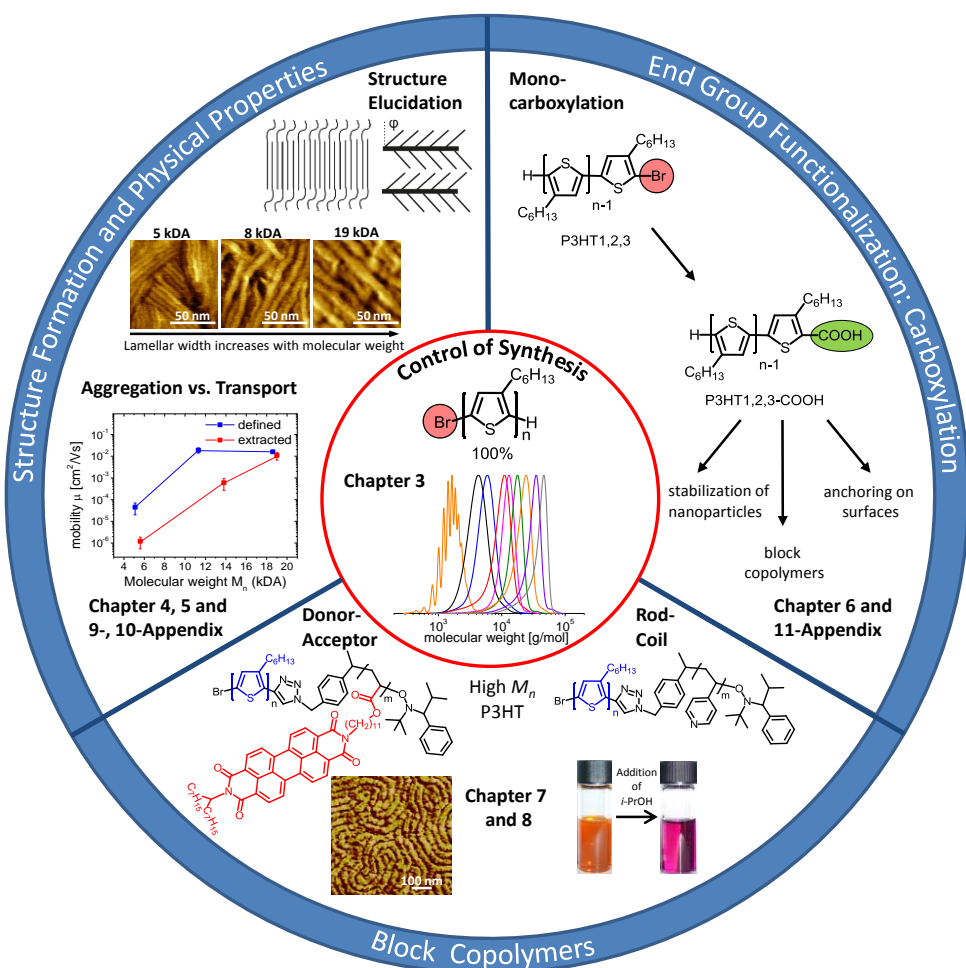


Figure 1: Overview of the thesis with the “control of synthesis” of P3HT including end groups, molecular weight and polydispersity as the core topic (chapter 3), “structure formation and physical properties” (chapter 4, 5, 9, and 10), “end group functionalization: carboxylation” (Chapter 6 and 11) and “block copolymers” (chapter 7 and 8) as the additional three categories resulting from the controlled synthesis.

The first category, *structure formation and physical properties* containing chapter 4, 5, 9 and 10 deals with understanding the physical properties and structure formation in bulk, solution and thin films. In Chapter 4 and 9, the equilibrium bulk structures of P3HT were investigated using small and wide angle X-ray scattering (SAXS, WAXS), differential scanning calorimetry (DSC) and solid state ^{13}C -NMR. Especially the influence of temperature and molecular weight on the equilibrium structures of P3HT is addressed. Chapter 9 appears in the appendix because I synthesized the low molecular weight P3HT, but the main analysis and interpretation was done by the group of Prof. Saalwächter from the University of Halle. Chapter 5 deals with the aggregate formation of P3HT in solution depending on the used solvent mixture, molecular weight and synthetic approach. UV-vis spectroscopy together with theoretical models was used to elucidate the percentage of aggregates as well as their nature concerning excitonic coupling and conjugation length. Further a correlation between the propensity of aggregate formation in solution and the charge carrier mobility in thin film OFETs was obtained. In chapter 10, a special AFM technic developed by the group of Prof. Magerle from the University of Chemnitz was used to map the subsurface of a thin film of well-defined P3HT. It was found that even the crystalline regions are covered with an amorphous layer which becomes thinner after thermal annealing. This layer can influence the charge extraction between P3HT at interfaces with acceptor materials or electrodes.

The second category, *end group functionalization: carboxylation* (chapter 6 and 11) exploits the well-defined H/Br end groups of P3HT for the introduction of carboxylic acid groups. Some work of chapter 11 appearing in the appendix was partly done during my diploma thesis. At this stage, a control of end groups directly after polymerization was not possible. The used functionalization method led to mainly dicarboxylated P3HT, but a loss of semicrystalline nature. However the carboxylation allowed the use of P3HT as a polymer sensitizer in solid-state dye-sensitized solar cells. The control over end groups directly after polymerization as shown in chapter 3 allowed a more defined carboxylation at only one chain end as presented in chapter 6. The influence of the end groups on the crystallinity, optical properties and charge carrier mobility was investigated for monocarboxylated P3HTs with different chain lengths.

The third category, *block copolymers* (chapter 7 and 8) includes P3HT containing block copolymers with a long P3HT block. Some prerequisites to exploit the thermodynamically stable self-assembly structures of block copolymers for organic photovoltaics is the combination of a hole conducting block like e.g. P3HT and an electron conducting or nanoparticle-coordinating second block. High χN parameters are necessary for order-disorder transitions leading to defined structures based on microphase separation. Further, it is well known that high molecular weight P3HT blocks are important for good charge carrier mobility within the block copolymer domains. Thus in chapter 7, a method for the incorporation of high molecular weight P3HTs into block copolymers is introduced using a combination of click chemistry and NMRP. Block copolymers containing P3HT and P4VP as polar, nanoparticle-

coordinating block were synthesized. It was demonstrated that these amphiphiles are not only interesting for organic photovoltaics but also for investigating the structure formation of rod-coil systems in solution. In chapter 8 this synthetic approach was used for the synthesis of fully-functionalized P3HT-*b*-PPerAcr. Its high molecular weight allowed phase separation in the melt and highly ordered cylindrical morphologies in bulk and thin film after annealing above the melting point. The observed structures had sizes in the range of the exciton diffusion length.

The main results of the individual manuscripts are shortly summarized in the following section. Further, differences and analogies between them are discussed. More details about the synthesis, characterization and the resulting properties can be found in the respective chapters.

Control of End Groups and Polydispersity in P3HT (chapter 3)

To develop an universal chain growth polymerization method for conjugated polymers, it is important to identify all factors influencing the resulting molecular weight, end groups, polydispersity and the success of the polymerization. The KCTP proceeds via an active Grignard monomer which is built *in situ* from a dihalide and a sterically demanding Grignard reagent like *t*-BuMgCl or *i*-PrMgCl. Thus the rate of the active Grignard monomer formation was investigated in detail using ^1H -NMR spectroscopy. We found out that the reaction is rather slow requiring 20-30 h for completion. However this step proved to be essential for the control of the end groups. If the polymerization was started after the active Grignard reaction was complete and no unreacted *t*-BuMgCl remained, 100% H/Br end groups were obtained independent of the polymerization time (Figure 2a). However if a complete consumption of *t*-BuMgCl was not guaranteed, the amount of Br end groups decreased linear with polymerization time leading to unintended H/H end groups (Figure 2b). Even if an excess of *t*-BuMgCl was present during polymerization no chain termination and broadening of the polydispersity occurred. This is one of the major differences between the Yokozawa and McCullough route presented in the introduction. While *i*-PrMgCl used in the Yokozawa method can terminate the active chain ends and thus broaden the PDI, *t*-BuMgCl used by McCullough is sterically hindered and does not react with the active Nickel catalyst sitting at the chain end. Additionally we found that LiCl can efficiently accelerate the active Grignard formation from 20 h to about 5 h. Further it accelerated the polymerization and small amounts of the second regioisomer were incorporated, leading to higher degrees of polymerization and a small decrease in regioregularity. Yet the charge carrier mobility remained unaffected by the small decrease in regioregularity.

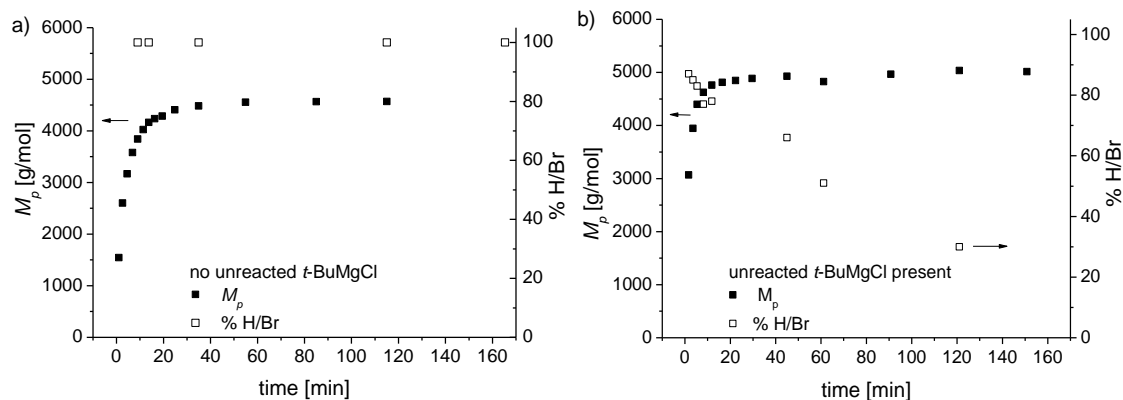


Figure 2: Peak molecular weight M_p (solid squares) and percentage of H/Br chain ends (open squares) versus polymerization time for a polymerization a) without unreacted $t\text{-BuMgCl}$ and b) with unreacted $t\text{-BuMgCl}$ present during chain growth. With increasing polymerization time, the H/Br content remains constant if no unreacted Grignard reagent is present, whereas the number of H/Br end groups decreases for unreacted $t\text{-BuMgCl}$.

Further we investigated which influence the different quenching reagents have on the end groups and PDI of the resulting polymer. We found that methanol causes chain-chain coupling mainly via disproportionation. Thereby the amount of coupling decreased with increasing chain length (Figure 3a). If hydrochloric acid was used for quenching disproportionation was absent and monomodal distributed P3HTs are obtained.

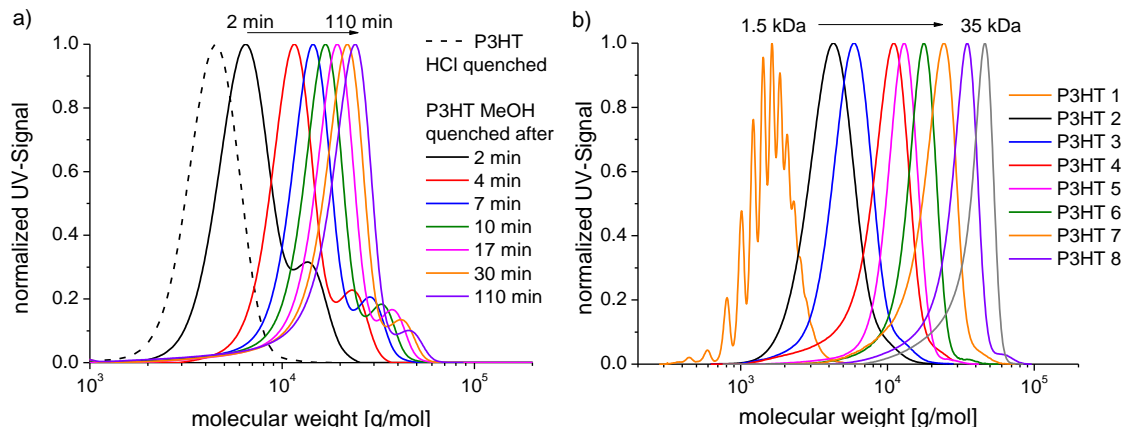


Figure 3: a) SEC curves of P3HT quenched with HCl or methanol for different polymerization times. For MeOH quenched samples chain-chain coupling occurs which decreases with increasing chain length. b) SEC curves of the synthesized molecular weights using the optimized polymerization conditions and quenched with HCl.

With the explanation of the role of unreacted $t\text{-BuMgCl}$ and the choice of the right quenching reagents the decisive factors for low PDIs and homogenous end group were identified. Now we are able to synthesize any molecular weight with 100% H/Br end groups in very fast KCTP using LiCl (see Figure 3b). The identification of these factors will lead to a better understanding of KCTP and help to broaden its application to new monomer systems.

Structure Formation and Physical Properties

Hierarchical Equilibrium Structures in Bulk (chapter 4 and 9)

In cooperation with the group of Prof. Thurn-Albrecht from the University of Halle, these well-defined P3HTs were used to study the influence of the molecular weight on bulk structures (chapter 4). Three different molecular weights (5.2 kDa, 7.9 kDa, 18.5 kDa) were investigated using DSC, SAXS, WAXS and AFM. DSC together with temperature dependent WAXS allowed to elucidate a temperature dependent phase diagram for the lowest molecular weight sample of 5.2 kDa (see Figure 4). Below 60 °C the crystalline regions consist of a 3D crystal with ordered main and side chains. Above 60 °C the main chains remain two-dimensionally ordered, but the side chains are disordered. This loss of side chain order was indicated by a loss of the reflexes with mixed hkl indices. Before melting, a smetic layered structure of main and side chains is observed with liquid like packing within the respective layers. These transitions were general for all molecular weights but the side-chain recrystallization was kinetically hindered for the higher molecular weight samples. Further the order of the side chains was investigated in detail by comparing the packing density inside the monoclinic unit cell with that of polyethylene. The side chains seem to be tilted with an angle of 51° towards the plane of the main chains and no interdigitation occurs between different layers as depicted in the inset in Figure 4.

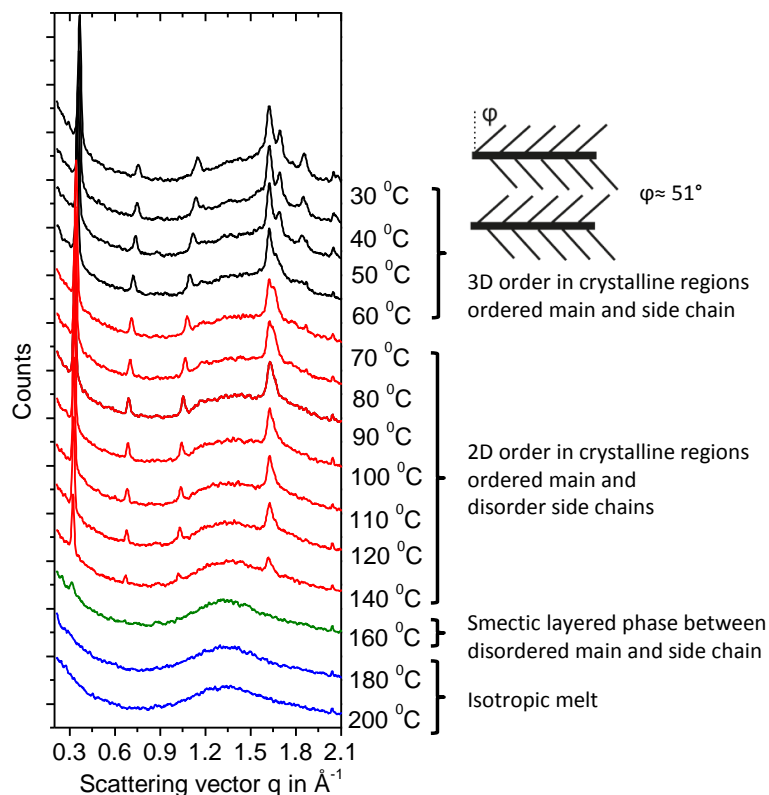


Figure 4: Temperature dependent WAXS diffractograms of P3HT with an SEC molecular weight of 5.2 kDa. The phases occurring at different temperatures are indicated. The inset shows the order of the side chains as tilted and non-interdigitated.

Apart from the structure within the crystalline domains the semicrystalline packing into crystalline and amorphous regions was investigated using DSC, SAXS and AFM. DSC measurements showed an increasing melting temperature T_m with an increase of molecular weight. According to the Gibbs-Thompson equation, this indicates an increase in the size of the crystallites. This was in agreement with structures observed in AFM phase images of thin film samples annealed above their melting temperature and slow cooling to room temperature (see Figure 5a). With increasing molecular weight, the width of the crystalline lamella increases. SAXS measurements gave a quantitative measure about the long period of the lamellae. There was a close agreement between the long period derived from SAXS measurements and the contour length of the polymer calculated from the repeating units obtained by MALDI-TOF MS. This indicates the presence of extended chain crystals up to a molecular weight of 19 kDa. For the smallest molecular weight sample the long period was slightly larger than the contour length which suggests that the tail-tail coupling usually sitting at the beginning of each chain is not incorporated into the crystal and form a noncrystallizable amorphous layer (Figure 5b). The effect of the end groups is more pronounced for lower molecular weight samples which may account for the lower crystallinity observed by comparing ΔH_m values from DSC. Recent synthetic investigations show that this tail-tail unit can also wander inside the chain, which may account for the amorphous regions between the crystalline domains.¹

The observed side chain melting and the crystal-crystal phase transition were further confirmed by solid state ^{13}C -NMR spectroscopy in cooperation with the group of Prof. Saalwächter from the University of Halle (chapter 9). While quantitative determination of the total crystallinity was not possible with XRD measurement, the ^{13}C -NMR studies showed that the literature value² for the melting enthalpy of a totally crystalline sample ΔH_m^∞ with 99 J/g is too high and leads to an underestimation of the real crystallinity of P3HT. The real value was shown to be rather closer to ≈ 37 J/g.

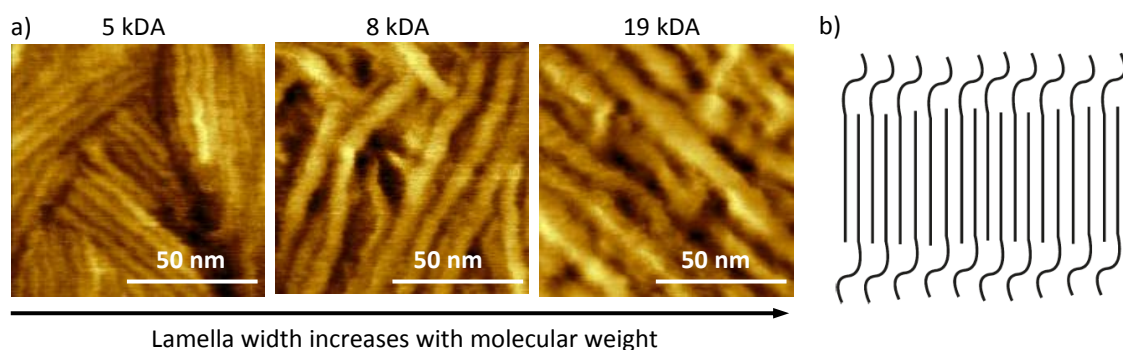


Figure 5: a) AFM images of the crystalline lamella of thin films of P3HT after annealing above T_m and slow cooling to room temperature. The lamella width increases with increasing molecular weight. b) Scheme of the extended chain crystals of P3HT with an amorphous layer of noncrystallizable chain ends.

This knowledge about the temperature dependent phase diagram and semicrystalline equilibrium structures of P3HT in bulk will help to choose the right annealing conditions which allow for proper chain mobility and better packing on cooling. Only the well-defined nature of these P3HT allowed the observation of the side chain melting for the first time. Such detailed structural features have never been observed for less defined polymers.

Molecular weight, Solvent and Synthetic Method Dependent Aggregate Formation (chapter 5)

While in chapter 4 only one series of defined P3HTs was analyzed in solid state, in chapter 5 two different series were investigated in solution. The first series were well-defined P3HTs synthesized with KCTP. The second series was obtained by extracting a broad distributed P3HT synthesized with the original McCullough method. The broad distributed sample was extracted with hexane, dichlormethane and chloroform to get fractions with molecular weights similar to the series synthesized with KCTP (ca. 5 kDa, 11 kDa and 19 kDa). The aim was to investigate the effect of the synthetic method, molecular weight and quality of solvent on the aggregate formation of the respective materials. Therefore solutions from a varying ratio of chloroform (as good solvent) and ethyl acetate (as poor solvent) with constant concentrations of polymer were analyzed using UV-vis spectroscopy. In general two distinct features could be observed in the UV-vis spectra of partially aggregated samples. A high energy band belonging to the fraction of amorphous coiled chains and a structured low energy band belonging to planar weakly interacting H-aggregates are seen (Figure 6). Taking into account the oscillator strength of the different species, the percentage of aggregates can be elucidated. The amount of aggregates depended on all three factors: molecular weight, solvent quality and synthetic approach. For the lower molecular weight samples (5 kDa and 11 kDa), a huge difference between the directly synthesized well-defined and the extracted samples was observed. Extracted P3HTs needed a higher amount of poor solvent to form aggregates and the maximum percentage of resulting aggregates was lower. For high molecular weights (19 kDa) no distinct difference was observed for the extracted and the well-defined sample. A maximum percentage of about 55% aggregates was obtained for the well-defined 11 kDa sample as well as for both samples with 19 kDa. This again indicates that the ΔH_m^∞ of 99 J/g from the literature² is too high, because the maximum bulk crystallinities determined using this value were much lower than the 55% determined from solution, assuming that the aggregation in P3HT is solely caused by crystallization.

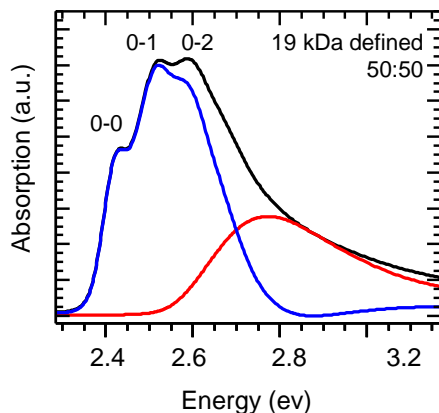


Figure 6: UV-vis absorption spectrum of the defined 19 kDa sample in a 50:50 volume mixture of chloroform and ethyl acetate (black). Extracted absorptions from the amorphous coiled chains (red) and the aggregated species (blue).

In a second part, a theoretical model from Spano was used to investigate the nature of chain packing inside the aggregates. Therefore the intensity ratio of the 0-0 and 0-1 vibronic bands was used to calculate the excitonic coupling with the help of the Franck-Condon analysis. Additionally, a model of Gierschner allowed to extract the conjugation lengths (from the excitonic coupling), which were compared with the repeating units of the defined P3HTs obtained by MALDI-ToF MS. For the well-defined low molecular weight sample, the conjugation length was in the same range as the theoretical length based on repeating units, which indicates fully stretched chains within the aggregates. For the higher molecular weight samples, the conjugation length was lower than their respective contour lengths. This shows that in contrast to the bulk structures discussed in chapter 4, where extended chain crystals were observed for all investigated molecular weights, non-equilibrium structures with different packing are obtained in solution.

Further, the charge carrier mobility in thin films prepared from pure chloroform solution was analyzed. Interestingly the charge carrier mobility did not depend on the excitonic coupling, but correlated with the maximum fraction of aggregates possible in mixed solutions. Similar to the higher percentage of aggregates, the charge carrier mobility of the well-defined 5 kDa sample was up to two orders of magnitude higher than that of the extracted sample. For the well-defined 11 kDa sample and both 19 kDa samples, the maximum percentage of aggregates in solution was nearly the same and all showed a charge carrier mobility of $10^{-2} \text{ cm}^2/\text{Vs}$ (see Figure 7). These results indicate that the maximum percentage of aggregates formed in solution may be an indication of the propensity to aggregate in thin films. Therefore the crystallinity seems to play an important role for the molecular weight dependence of the charge carrier mobility. Further it demonstrates that for defined P3HTs high charge carrier mobilities may be obtained with even medium molecular weights of about 11 kDa. When small molecular weights are extracted out from the broad distributed sample, high charge carrier mobilities can be reached for the final extracted sample. The value of the mobility matches

with that of the directly synthesized well-defined sample with a molecular weight of about 19 kDa.

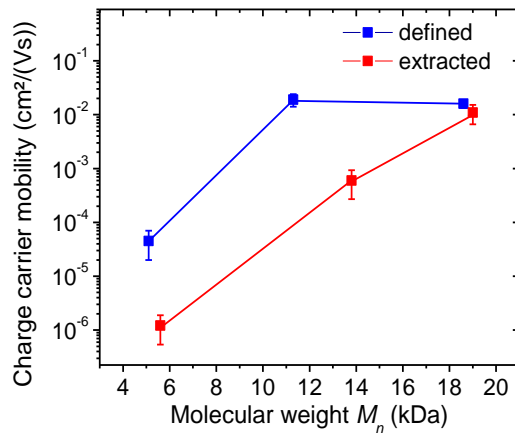


Figure 7: Charge carrier mobilities for different molecular weights of directly synthesized well-defined and extracted P3HT samples.

Even if extraction of broad distributed P3HTs helps to improve the charge carrier mobility of the final sample, no controlled end groups are obtained. For the introduction of new functionalities, as shown in chapter 6 as well as the incorporation into block copolymers as shown in chapter 7 and 8, control of end groups in the synthesis is essential.

End Group Functionalization: Carboxylation (chapter 6 and 11)

The control of the end groups demonstrated in chapter 3 allowed developing a simple method for the introduction of highly valuable carboxylic acid groups in one single, selective and quantitative post-polymerization step (chapter 6). These groups can be used for anchoring onto surfaces as demonstrated in chapter 11 in the appendix, to coordinate nanoparticles or for end capping polymerizations to obtain block copolymers.

In chapter 11, we used P3HTs with an undefined mixture of H/H and H/Br end groups because these samples were synthesized before the optimized procedure was known. Therefore, we used *s*-BuLi to generate active sites for carboxylation. This led to predominately dicarboxylation, because it reacted with both hydrogen and bromine end groups. Unfortunately, this method of carboxylation caused a loss of crystallinity of P3HT, which negatively affects the charge transport properties. However, we could demonstrate that the anchoring groups allow the application of carboxylated P3HT as a sensitizer in solid-state dye-sensitized solar cells reaching efficiencies of 0.9% in non-optimized devices.

As we developed the new carboxylation method (chapter 6) we used P3HT samples with a high content of 80% H/Br end groups. Here, also the role of unreacted *t*-BuMgCl in KCTP was not yet known, but we knew that the end groups depended on polymerization time. The high content of bromine end groups was obtained by quenching the polymerization after short polymerization times, directly after reaching the molecular weight plateau (Figure 2b of the

overview). The bromine groups were selectively transferred into a Grignard species via Grignard metathesis using *i*-PrMgCl. Introduction of gaseous CO₂ and quenching with HCl gave quantitatively monocarboxylated P3HTs. This functionalization was confirmed using MALDI-ToF MS as seen in Figure 8a. The signal for the H/Br terminated P3HT vanishes and new signals for H/COOH functionalized P3HT appear. Three different molecular weights of 1.5 kDa (P3HT1), 5 kDa (P3HT2) and 10 kDa (P3HT3) were monocarboxylated (Figure 8b).

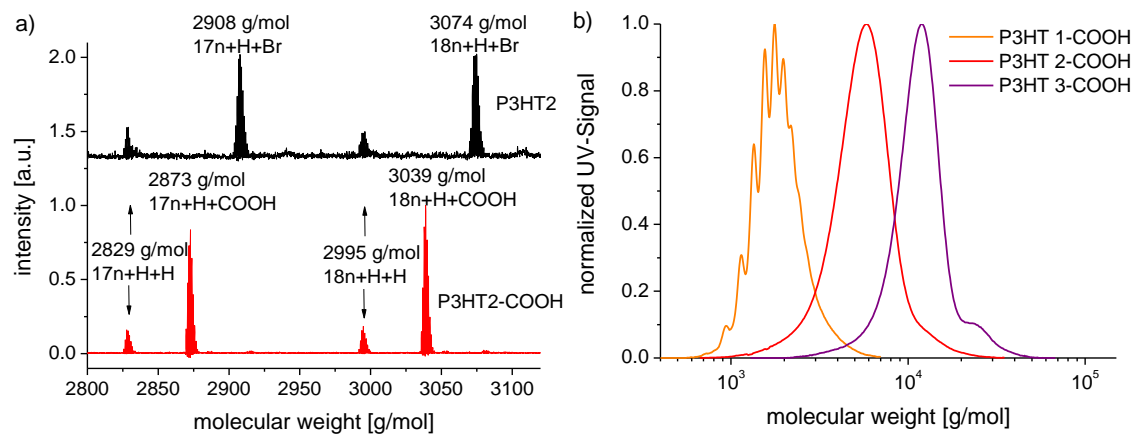


Figure 8: a) Magnified part of the MALDI-ToF MS spectra for 17 and 18 repeating units of P3HT2 (black) and P3HT2-COOH (red). The indicated end groups show that the bromine groups are quantitatively transformed into COOH groups. b) SEC curves of the monocarboxylated P3HTs.

Further the influence of the carboxylic acid group on the thermal, optical and electronic properties was studied in bulk and thin film. Analysis of the thermal properties in bulk with DSC revealed that for the smallest molecular weight samples, the influence of the carboxylic end group is most distinct. The COOH end group shifted the melting temperature to higher values and kinetically hindered the recrystallization. Only after a few days storing at room temperature a melting point was recovered in the next heating cycle. For the 5 kDa sample the influence of the carboxylic acid group was low and only the side chain melting was kinetically hindered. Both samples P3HT2 and P3HT2-COOH showed equal melting and recrystallization temperatures as well as similar melting enthalpies. For the highest molecular weight samples the behavior was likewise but a difference in the melting enthalpy was observed. While the melting enthalpy and thus the crystallinity increased with molecular weight from P3HT2 to P3HT3 it remained almost the same for P3HT2-COOH and P3HT3-COOH. IR measurements indicated hydrogen bonds between the carboxylic acid groups, which may hinder the comparatively weaker π-π interaction and thus may lower the maximum melting enthalpy. Further the influence of the COOH group on the charge carrier mobility in thin films using OFETs was investigated for the higher molecular weight carboxylated samples (P3HT2-COOH and P3HT3-COOH) and non-functionalized (P3HT2 and P3HT3) samples. Interestingly the charge carrier mobility in thin films correlated with the crystallinity measured in bulk. P3HT2, P3HT2-COOH and P3HT3-COOH had similar melting enthalpies in bulk and all showed charge

carrier mobilities in the range of 10^{-3} cm 2 /Vs. P3HT3 with a higher melting enthalpy showed one order of magnitude higher charge carrier mobility in the range of 10^{-2} cm 2 /Vs. A commercial sample with a higher molecular weight of 19 kDa but similar crystallinity as P3HT2, P3HT2-COOH and P3HT3-COOH also showed a charge carrier mobility of 10^{-3} cm 2 /Vs.

These results again indicate that the crystallinity may be the main factor influencing the charge carrier mobility. Further this demonstrates that with the new carboxylation method, P3HTs with anchoring groups and a high charge carrier mobility in the range of 10^{-3} cm 2 /Vs can be obtained.

Block Copolymers with Long P3HT Blocks (chapter 7 and 8)

The challenge was to find a synthetic method for block copolymers, which allows incorporating long P3HT blocks with molecular weights above 15 kDa. Long chains are less soluble and end group functionalization is more difficult because of the low percentage of end groups in comparison to the repeating units. Even though the OFET measurements in chapter 5 showed that the charge carrier mobility of the 10 kDa sample was similar to that of 19 kDa, the situation is different for block copolymers. Here P3HT crystallizes in the confinement of the block copolymer and earlier work showed improved performance for P3HT blocks above 15 kDa. Further, high molecular weights are required for high χN parameters to obtain order-disorder transitions based on microphase separation, which will be demonstrated below.

Controlling the Alkyne-Functionalization and Synthesis of P3HT-*b*-P4VP (chapter 7)

In this chapter we show that a combination of click chemistry and NMRP can be used for the synthesis of P3HT-*b*-P4VP with a P3HT block length of 19 kDa.

The key step was to control the *in situ* functionalization of P3HT with an alkyne. We could show that HCl, the best quenching agent for non-functionalized P3HTs, causes hydrohalogenation and hydration reactions leading to a loss of alkyne functionality. The respective addition products were confirmed using MALDI-ToF MS and 1 H-NMR spectroscopy. Thus for P3HT carrying an alkyne group, methanol was identified as the proper quenching reagent. Further, the alkyne function proved to be thermally unstable and the resulting P3HT-alkynes need to be stored below 0°C to avoid chain-chain coupling reactions. In the second step, P3HT-alkyne was coupled with an alkoxyamine carrying an azide using copper catalyzed azide-alkyne cycloaddition (CuAAC), a so called “click” reaction (Figure 9a). A quantitative functionalization was confirmed by 1 H-NMR spectroscopy. The formed P3HT-alkoxyamine was used as a macroinitiator for NMRP of 4-vinylpyridine to synthesize two block copolymers with 55 and 77wt% of P4VP. Their thermal and optical properties as well as structures in bulk and solution were investigated. In the literature, an influence of coil block length on the melting point of the rod block in rod-coil block copolymers is reported.³ Interestingly when such long P3HT blocks are incorporated into rod-coil block copolymers, there is only little influence of the P4VP coil block on the size of the P3HT crystallites. Even at a coil content of 77wt%, only a

small (4°C) decrease of the melting temperature was observed in comparison to the pure P3HT macroinitiator (Figure 9b). In bulk a mixture of lamellar and cylindrical structures were observed for P3HT-*b*-P4VP with 55wt% P4VP and a mixture of spheres and cylinders for 77wt%. The P4VP block is a polar block and thus not only interesting for the coordination of nanoparticles and application in solar cells. The amphiphilic nature of the P3HT-*b*-P4VP makes it interesting for the investigation of structure formation in solution. Upon addition of *i*-propanol (a P4VP selective solvent) to a chloroform solution of the block copolymer, stable colloidal aggregates are formed (Figure 9c). Within these aggregates crystalline cores of P3HT have been confirmed with UV-vis spectroscopy. Thus P3HT-*b*-P4VP is a good system for studying self-assembly of rod-coil block copolymers in solution.

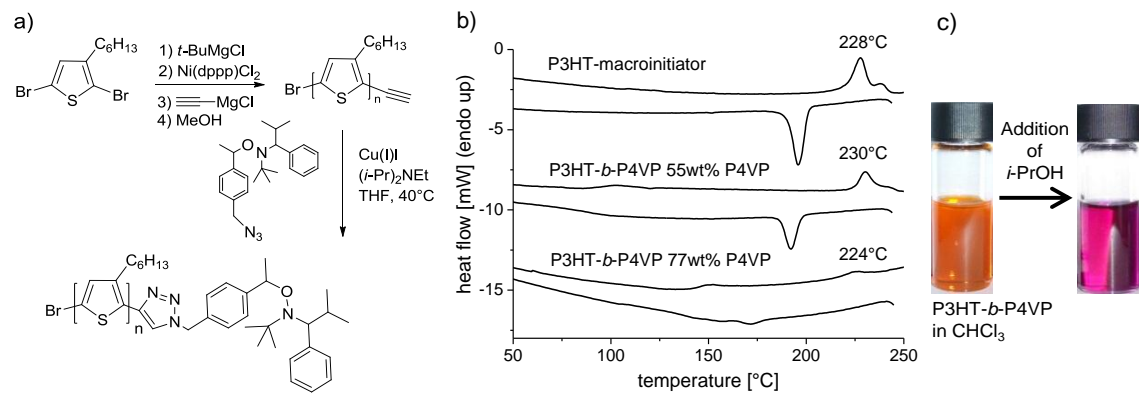
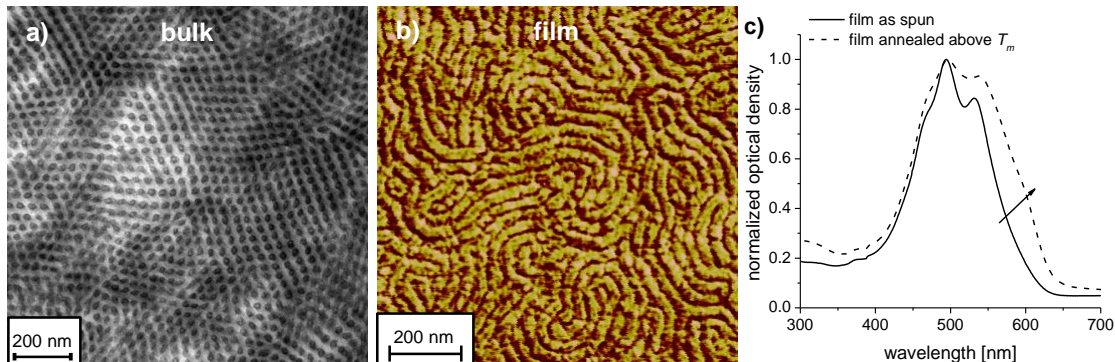


Figure 9: a) Scheme with the optimized conditions for the synthesis of a high molecular weight P3HT macroinitiator. b) Second heating and cooling curves from DSC with a scan rate of 10 K/min. Almost no shift in the P3HT melting temperature is observed even at 77wt% P4VP. c) Pictures of a P3HT-*b*-P4VP solution in chloroform (left) and after addition of *i*-Propanol and formation of colloidal aggregates with crystalline cores (right).

Donor-Acceptor Crystalline-Crystalline Block Copolymers, P3HT-*b*-PPerAcr with Hexagonally Ordered Cylinders (chapter 8)

We used the synthetic method from chapter 7 to synthesize fully-functionalized crystalline-crystalline P3HT-*b*-PPerAcr block copolymers with a long P3HT block. For the first time, we obtained exclusively diblock copolymers with very high molecular weights of 35.5 kDa. Further we were able to get a high content of PPerAcr (64wt%) which was shown to be important for a balanced charge transport between P3HT and PPerAcr. After thermal annealing of the bulk sample above the melting temperature of the P3HT and the PPerAcr block, we observed for the first time hexagonally ordered cylinders for a fully-functionalized crystalline-crystalline block copolymer (Figure 10a). Such curved structures are rather unexpected for a crystalline-crystalline system but fit to the respective volume ratios of 37% P3HT as the cylindrical phase and 63% PPerAcr as the matrix. We also tried to transfer these structures to thin films. The raw films directly after spin coating did not show any phase separation. However upon annealing above the melting point clear phase separation was observed as depicted in Figure 10b. These structures could be obtained independent of the underlying substrate. UV-vis measurements

in thin films (Figure 10c) showed that the crystallinity of P3HT was suppressed after spin coating, but annealing above T_m allows P3HT to recrystallize and to form well-defined phase separated structures. The structure sizes were in the range of the exciton diffusion length.



*Figure 10: a) Transmission electron microscopy image of a bulk sample of P3HT-*b*-PPerAcr (64wt% PPerAcr) annealed above T_m for 2 h showing hexagonally ordered cylinders. b) Atomic force microscopy phase image of a thin film of P3HT-*b*-PPerAcr spin coated from CHCl₃ after annealing for 20 min above T_m . c) UV-vis spectra of thin films of P3HT-*b*-PPerAcr directly after spin-coating from chloroform and after annealing 20 min above T_m . The intensity of the absorption band at 600 nm increases after annealing, which indicates crystallization of P3HT.*

Thus this block copolymer, P3HT-*b*-PPerAcr (64wt% PPerAcr) is very promising for the application in organic photovoltaics. The clean diblock, the high molecular weight along with a high χN parameter and phase separation in the melt allowed highly ordered structures for a solar cell relevant block copolymer.

References

- (1) Tkachov, R.; Senkovskyy, V.; Komber, H.; Sommer, J. U.; Kiriy, A. *J. Am. Chem. Soc.* **2010**, *132*, 7803-7810.
- (2) Malik, S.; Nandi, A. K. *J. Polym. Sci. B Polym. Phys.* **2002**, *40*, 2073-2085.
- (3) Lee, Y. H.; Yen, W. C.; Su, W. F.; Dai, C. A. *Soft Matter* **2011**, *7*, 10429-10442.

Individual Contributions to Joint Publications

In the following section, the individual contributions of the authors to each manuscript are specified.

Chapter 3

This manuscript is published in *Macromolecules* (2011, 44, 3388-3397) with the title:

“Toward Perfect Control of End Groups and Polydispersity in Poly-(3-hexylthiophene) via Catalyst Transfer Polymerization”

by **Ruth H. Lohwasser** and Mukundan Thelakkat

I synthesized and characterized the polymers, did the analysis and wrote the paper.

Mukundan Thelakkat supervised the project, was involved in the scientific discussion and corrected the manuscript.

Chapter 4

This manuscript is published in *Macromolecules* (2010, 43, 4646-4653) with the title:

“Temperature and Molecular Weight Dependent Hierarchical Equilibrium Structures in Semiconducting Poly(3-hexylthiophene)”

by Zhiyong Wu, Albrecht Petzold, Thomas Henze, Thomas Thurn-Albrecht,

Ruth H. Lohwasser, Michael Sommer, and Mukundan Thelakkat

I synthesized the 5.2 kDa sample and characterized all used samples with MALDI-ToF MS, SEC and ¹H-NMR spectroscopy. Further I wrote the “Synthesis and Chemical Characterization” part, was involved in the scientific discussions and corrected the manuscript.

Zhiyong Wu performed the structural characterization with SAXS and WAXS and did the main analysis.

Albrecht Petzold was involved in the SAXS measurements and their evaluation.

Thomas Henze measured the AFM phase images.

Thomas Thurn-Albrecht supervised the project regarding the X-ray measurements, was involved in the scientific discussions and corrected the main part of the manuscript.

Michael Sommer synthesized the 7.9 kDa and 18.5 kDa sample.

Mukundan Thelakkat supervised the project regarding the synthesis and chemical characterization, was involved in the scientific discussion and corrected the manuscript.

Chapter 5

This manuscript is accepted in The Journal of Polymer Science Part B: Polymer Physics with the title:

“On the Control of Aggregate Formation in Poly(3-hexylthiophene) by Solvent, Molecular Weight and Synthetic Method”

by Christina Scharsich, **Ruth Lohwasser**, Michael Sommer, Udom Asawapirom, Ullrich Scherf, Mukundan Thelakkat, Dieter Neher, and Anna Köhler

I synthesized the 5 kDa and the 11 kDa sample of the defined P3HT series and characterized all defined P3HTs with MALDI-ToF MS, SEC and ¹H-NMR spectroscopy. Further I was involved in the scientific discussion and corrected the manuscript.

Christina Scharsich performed the UV-vis measurements, did the corresponding theoretical analysis, measured the OFETS and wrote the manuscript.

Michael Sommer synthesized the 19 kDa sample of the defined P3HTs.

Udom Asawapirom and Ullrich Scherf provided the extracted P3HT samples and were involved in the scientific discussion.

Dieter Neher was involved in the discussion of the OFET results.

Mukundan Thelakkat and Anna Köhler supervised the project, were involved in the scientific discussion and corrected the manuscript.

Chapter 6

This manuscript is published in *Macromolecules* (**2010**, *43*, 7611-7616) with the title:

“Synthesis and Characterization of Monocarboxylated Poly(3-hexylthiophene)s via Quantitative End-Group Functionalization”

by **Ruth H. Lohwasser** and Mukundan Thelakkat

I synthesized all the non-functionalized and monocarboxylated P3HTs except for the smallest non-functionalized sample. Further, I characterized all polymers, did the analysis and wrote the manuscript.

Mukundan Thelakkat supervised the project was involved in the scientific discussion and corrected the manuscript.

Chapter 7

This manuscript is submitted to *Macromolecules* with the title:

“Synthesis of Amphiphilic Rod-Coil P3HT-*b*-P4VP Carrying a Long Conjugated Block using NMRP and Click Chemistry”

by **Ruth H. Lohwasser** and Mukundan Thelakkat

I synthesized the macroinitiator and all the block copolymers, characterized them and wrote the manuscript.

Mukundan Thelakkat supervised the project, was involved in the scientific discussion and corrected the manuscript.

Chapter 8

This manuscript is intended for submission with the title:

“Donor-Acceptor, Crystalline-Crystalline P3HT-*b*-PPerAcr with Ordered Phase Separation in Bulk and Thin Film”

by **Ruth H. Lohwasser**, Andreas S. Lang, and Mukundan Thelakkat

I synthesized and characterized the macroinitiator and the block copolymer, prepared the TEM and AFM samples and wrote the manuscript.

Andreas Lang synthesized the PerAcr monomer.

Mukundan Thelakkat supervised the project, was involved in the scientific discussion and corrected the manuscript.

Appendix: Chapter 9

This publication appears in the appendix because the main discussion and analysis was done by Ovidiu F. Pascui and Kay Saalwächter.

This manuscript is published in *Macromolecules* (**2010**, *43*, 9401-9410) with the title:

“High Crystallinity and Nature of Crystal-Crystal Phase Transformations in Regioregular Poly(3-hexylthiophene)”

by Ovidiu F. Pascui, **Ruth Lohwasser**, Michael Sommer, Mukundan Thelakkat, Thomas Thurn-Albrecht, and Kay Saalwächter

I synthesized the small molecular weight sample, characterized both samples with MALDI-ToF MS, SEC and ¹H-NMR spectroscopy and corrected the manuscript.

Ovidiu F. Pascui measured the solid state ¹³C-NMR spectra and did the analysis, was involved in the main scientific discussion and the preparation of the manuscript.

Michael Sommer synthesized the 7.9 kDa sample.

Mukundan Thelakkat supervised the synthetic part of the project and corrected the manuscript.

Thomas Thurn-Albrecht was involved in the scientific discussion.

Kay Saalwächter supervised the project concerning ¹³C NMR spectroscopy was involved in the scientific discussion, analysis and preparation of the manuscript.

Appendix: Chapter 10

This publication appears in the appendix because the main AFM work and discussion was done by Mario Zerson, Eike-Christian Spitzner and Robert Magerle.

This manuscript is published in *Macromolecules* (**2011**, *44*, 5874-5877) with the title:

“Subsurface Mapping of Amorphous Surface Layers on Poly(3-hexylthiophene)”

by Mario Zerson, Eike-Christian Spitzner, Christian Riesch, **Ruth Lohwasser**, Mukundan Thelakkat, and Robert Magerle

I synthesized and characterized the well-defined P3HT with SEC and DSC and corrected the manuscript.

Mario Zerson performed the subsurface mapping using AFM and wrote the manuscript.

Eike-Christian Spitzner developed the general subsurface imaging technic and was involved in the scientific discussion.

Christian Riesch developed the analysis software for the used AFM method.

Mukundan Thelakkat supervised the synthetic part of the project and corrected the manuscript.

R. Magerle supervised the project, was involved in the scientific discussion and corrected the manuscript.

Appendix: Chapter 11

This publication appears in the appendix because the synthesis and part of the analysis was done during my diploma thesis. The XRD measurements and the preparation of the manuscript were performed during my PhD thesis.

This manuscript is published in *Journal of Materials Chemistry* (**2009**, *19*, 4126-4130) with the title:

“Tailor-made Synthesis of Poly(3-hexylthiophene) with Carboxylic End Groups and its Application as a Polymer Sensitizer in Solid-State Dye-Sensitized Solar Cells”

by **Ruth H. Lohwasser**, Jayasundera Bandara, and Mukundan Thelakkat

I synthesized and characterized all polymer materials and wrote the paper.

Jayasundera Bandara prepared the solar cell.

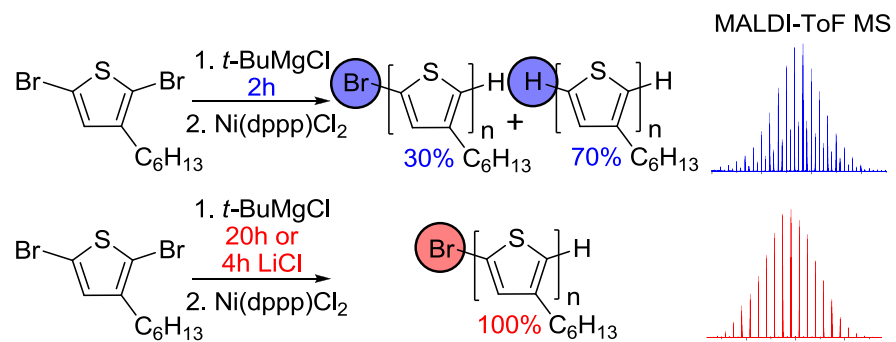
Mukundan Thelakkat supervised the project, was involved in the scientific discussion and corrected the manuscript.

3. Toward Perfect Control of End Groups and Polydispersity in Poly(3-hexylthiophene) via Catalyst Transfer Polymerization

Ruth H. Lohwasser and Mukundan Thelakkat*

Applied Functional Polymers, Department of Macromolecular Chemistry I,
University of Bayreuth, Universitätsstraße 30, 95444 Bayreuth, Germany

*E-mail corresponding author: mukundan.thelakkat@uni-bayreuth.de



Published in *Macromolecules* **2011**, *44*, 3388-3397

Abstract

We report the influence of the active Grignard monomer formation on the end groups and polydispersity of poly(3-hexylthiophene) (P3HT) for the catalyst transfer polymerization. The rate of the active Grignard monomer formation of 2,5-dibromo-3-hexylthiophene using *t*-BuMgCl was studied using ^1H NMR. Only in the absence of unreacted/excess *t*-BuMgCl, polymers with 100% H/Br end groups were formed. If the active Grignard monomer formation was incomplete and thus unreacted *t*-BuMgCl remained, the end groups depended on the polymerization time; the ratio of H/Br to H/H end groups decreased with increasing time. LiCl was shown to accelerate the active Grignard monomer formation but negatively affects the regioregularity to a small extent. It also increases the molecular weight of P3HT when used in combination with Ni(dppp)Cl₂ as a catalyst. Further, MeOH as a quenching reagent was identified to cause chain-chain coupling and hence an increase in the polydispersity. Thus, important parameters influencing the kinetics of the catalyst transfer polymerization were studied, and a series of P3HTs with 100% H/Br end groups and low polydispersities were synthesized by an optimized procedure. These findings are very relevant for extending this polymerization method to new monomers and for the realization of well-defined block copolymers.

Introduction

Organic semiconductors and especially conjugated polymers are a prominent class of materials finding application in organic field effect transistors (OFETs)¹ or organic photovoltaics.² Poly(3-hexylthiophene) (P3HT) is one of the most common and prototype conjugated polymers used as a hole conductor in these devices. Its development, starting from unsubstituted insoluble poly(thiophenes) to irregular alkyl substitution to regioregular P3HT, reached a new level of control of polymerization with the discovery of a chain growth mechanism by Yokozawa and McCullough.³⁻⁷ This allows for the synthesis of P3HTs with low polydispersities (PDIs) and adjustable molecular weights. The polymerization is called Grignard metathesis polymerization or catalyst transfer polycondensation/polymerization; the former name describes the formation of the monomer via metathesis reaction and the latter one the decisive step for the chain growth mechanism, namely the intramolecular transfer of the catalyst. In general, good control of well-defined end groups and molecular weights as well as low polydispersities is necessary to analyze the effect of molecular weight on the charge carrier mobility, to obtain block copolymers, or to tune the performance of such materials in organic solar cells.⁸⁻¹³ Recently, this method of polymerization was extended to obtain a few other polymers such as poly(2,5-dihexyloxybenzene)¹⁴, poly(alkylfluorene)^{15,16}, poly(*N*-dodecylpyrrole),¹⁶ poly(*N*-octyl-2-carbazole)¹⁶ and poly(2,3-dihexylthieno[3,4-*b*]pyrazine).¹⁷ Also nonconjugated polymers like poly(bithienylmethylenes)¹⁸ or oligomers¹⁹ were successfully polymerized. Additionally, new approaches allowed for surface initiated polymerization and the synthesis of brushes.^{20,21}

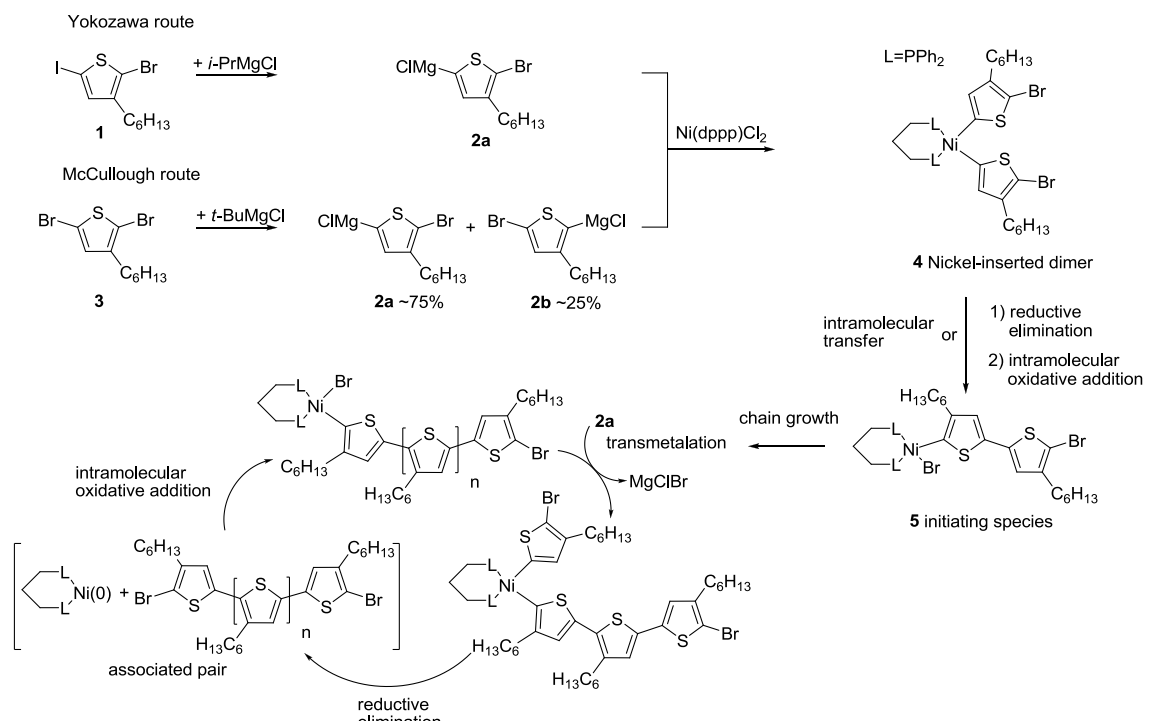
In all cases, the polymerization proceeds via the active Grignard monomer formed from its dihalide. Therefore, the conditions of active monomer formation and its polymerization decide the final polymer structure, molecular weight, and PDI. Thus, detailed understanding of kinetics is necessary to extend this valuable method toward relevant new monomers. A lot of factors have been identified which influence the structure and PDI of the polymers or the success of the chain growth polymerization: for example, the additives,^{14,16,22} the position of the substituent on the aromatic core,²³ the metal,²⁴ and the ligand of the catalyst used.^{22,24-27} To establish a universal chain growth polymerization for conjugated polymers, it is essential to identify all parameters that affect the kinetics and nature of the resulting polymers. Thus, the following relevant questions have yet to be answered. What is the effect of the different monomer systems, for example, *i*-PrMgCl and 2-bromo-3-hexyl-5-iodothiophene, as used by the Yokozawa group, in contrast to *t*-BuMgCl and 2,5-dibromo-3-hexylthiophene, as used by McCullough and co-workers? How are the kinetics of the formation of the active Grignard monomer and what is its influence on polymerization? Is there an ideal time of polymerization toward good control? Does the quenching reagent methanol affect the end groups and polydispersity of the resulting polymer? How does LiCl influence the polymerization of P3HT?²⁸

Here we address these questions and reveal factors that influence the kinetics, leading to clarity regarding end groups and polydispersity. While McCullough and Yokozawa showed that P3HT can be obtained with homogeneous H/Br end groups, we and several other groups often observed a mixture of H/H and H/Br end groups.^{18,23,29} Here, we study in detail the parameters causing H/H end groups. We show that one crucial step is the active Grignard monomer formation from the dihalides. Its control is important to obtain homogeneous H/Br end groups, which can be transformed into many functional groups.²⁹⁻³¹ In general, the end group analysis is also seen as a measure of polymerization control and thus often used for mechanistic studies.²⁷ Therefore, it is essential to know which factors can influence the end groups. Additionally, we present how LiCl - recently used for other polymers - efficiently accelerates the active Grignard monomer formation of P3HT. It also negatively affects the regioregularity and increases the molecular weight of the resultant P3HT polymer. Further, we show that the choice of the right quenching reagent - HCl or methanol - has a major influence on the molecular weight distribution of P3HT. With the help of MALDI-TOF MS, we prove for the first time the formation of coupled polymer chains upon quenching the polymerization with methanol. Thus, general parameters influencing the kinetics of active Grignard monomer formation and catalyst transfer polymerization relevant for any monomer are discussed.

Results and Discussion

Active Grignard Monomer Formation

In the catalyst transfer polymerization the active Grignard monomer is built *in situ* from the dihalide via a Grignard metathesis reaction. The two main approaches toward this monomer and the mechanism of the polymerization are shown in Scheme 1.^{32,33} Generally, the Yokozawa method uses 2-bromo-3-hexyl-5-iodothiophene as a starting material together with *i*-PrMgCl as the Grignard reagent for the metathesis reaction. Because of the higher reactivity of the iodine in comparison to bromine, only one active Grignard monomer **2a** is formed. In contrast, the McCullough method uses 2,5-dibromo-3-hexylthiophene with *t*-BuMgCl as the Grignard reagent. The missing chemical selectivity caused by the two bromine substituents leads to two regioisomers of the active Grignard monomer, **2a** and **2b**. Still the steric hindrance of *t*-BuMgCl along with the 3-alkyl side chain leads to a high amount of the desired isomer **2a** (ca. 75%). The addition of the nickel catalyst Ni(dppp)Cl₂ results in a nickel-inserted dimer **4** with the sterically least hindered tail-tail conformation. Further, according to the proposed mechanisms, the initiating species **5** is built via an intermolecular transfer or an associated pair followed by intramolecular oxidative addition. Now the chain growth proceeds via multiple cycles of transmetalation, reductive elimination, and intramolecular oxidative addition. During chain growth, the insertion of the unintended regioisomer **2b** is sterically hindered, and thus it is not consumed during polymerization.^{22,32} Therefore, both methods lead to a polymer with a high regioregularity of about 98%, resulting from the insertion of **2a** only.



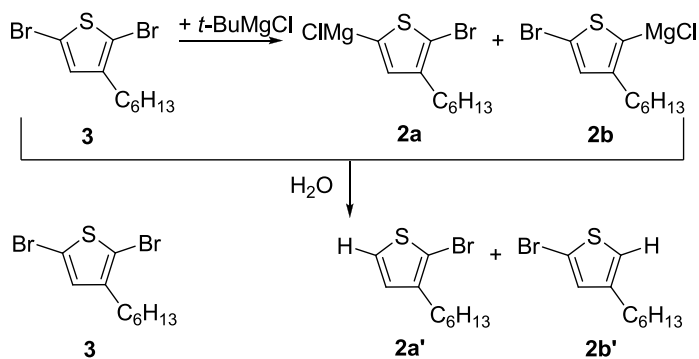
Scheme 1: Active Grignard monomer formation via the two different monomer systems used in McCullough and Yokozawa routes and the proposed mechanism by McCullough and Yokozawa for the catalyst transfer polymerization.

In one of the first publications about chain growth mechanism, Yokozawa et al. described the ratio of 2-bromo-3-hexyl-5-iodothiophene to *i*-PrMgCl as a critical factor to get low molecular weight distributions and homogeneous H/Br end groups.³³ They recommended 0.95-1 mol equiv of *i*-PrMgCl to 2-bromo-3-hexyl-5-iodothiophene in order to obtain low PDIs and homogeneous H/Br end groups. When we used a similar molar ratio of 1:1 or 1:0.95 for 2,5-dibromo-3-hexylthiophene and *t*-BuMgCl, we still were not able to gain 100% H/Br end groups. Instead, mixtures of H/H and H/Br end groups were obtained for different batches of polymerizations.^{23,29} In the literature various procedures were used for the formation of the active Grignard monomer which varied from 1 h at 0 °C^{23,33} for the reaction of 2-bromo-3-hexyl-5-iodothiophene with *i*-PrMgCl and 2 h reflux³² or 2 h at room temperature³⁴ for the reaction of 2,5-dibromo-3-hexylthiophene with *t*-BuMgCl. Concerning the difference in chemical reactivity of the starting compounds **1** and **3**, fast reactions are expected for 2-bromo-3-hexyl-5-iodothiophene (**1**). However, the time required for the complete formation of the active Grignard monomer, especially for the less reactive 2,5-dibromo-3-hexylthiophene, was uncertain. In the following, the detailed kinetics of active Grignard monomer formation followed by polymerization using Ni(dppp)Cl₂ as catalyst were studied. An overview of the parameters and molecular weights of all polymer samples prepared can be found in Table 1. Several samples were withdrawn during polymerization, and only the molecular weight of the final sample is given here. In the text the first number indicates the polymer batch number and the second number the number of the sample. For example, P3HT 1.15 corresponds to the 15th sample of P3HT 1.

*Table 1: Overview of polymers synthesized using different reaction conditions. For all P3HTs a monomer **3** to Ni(dppp)Cl₂ catalyst ratio of 26:1 was used except for the P3HT 6 series where the ratio was 89:1. The ratio of monomer to *t*-BuMgCl was maintained at 1:0.96 except for P3HT 2 and P3HT 6 for which the ratio was 1:1. Thus in all cases, an excess of *t*-BuMgCl was avoided.*

| polymer | additive | time for active Grignard monomer [h] | polymerization time [min] | quenching reagent | M _n (SEC) [g/mol] | PDI | H/Br: H/H |
|---------|----------|--------------------------------------|---------------------------|-------------------|------------------------------|------|-----------|
| P3HT 1 | - | 20 | 165 | HCl | 4000 | 1.10 | 100:0 |
| P3HT 2 | - | 2 | 151 | HCl | 4000 | 1.15 | 30:70 |
| P3HT 3 | LiCl | 6 | 22 | HCl | 6800 | 1.10 | 100:0 |
| P3HT 4 | - | 2.20 | 25 | HCl | 5300 | 1.14 | 80:20 |
| P3HT 5 | LiCl | 6 | 8 | MeOH | 6300 | 1.16 | 100:0 |
| | LiCl | 6 | 8 | HCl | 5900 | 1.10 | 100:0 |
| P3HT 6 | - | 2 | 110 | MeOH | 17600 | 1.28 | - |
| P3HT 7 | - | 15 | 2 | MeOH | 1800 | 1.30 | - |

We first investigated the time-dependent formation of the active Grignard species **2a** and **2b** at room temperature from 2,5-dibromo-3-hexylthiophene (**3**) (0.5 M solution in THF) and *t*-BuMgCl (1.23 M solution in THF). The amount of *t*-BuMgCl for all reactions was kept purposefully the same as or a little below (0.96 equiv) that of the dihalide **3** to ensure the complete consumption of *t*-BuMgCl. Room temperature was chosen because earlier reports showed that at higher temperatures the ratio of the two different regioisomers is shifted toward the undesired isomer ((5-bromo-3-hexylthiophen-2-yl)magnesium chloride) **2b**.³² During the reaction, samples were withdrawn and quenched with H₂O, and the resulting product mixture was analyzed with ¹H NMR spectroscopy. All possible quenching products are shown in Scheme 2. After quenching the molecules carry a proton at the position of the respective MgCl group.



*Scheme 2: Structures of possible products after quenching the reaction between 2,5-dibromo-3-hexylthiophene and *t*-BuMgCl with H₂O.*

A typical ¹H NMR spectrum after 2 h of reaction - a time often used in the literature - is compared to that of the starting compound **3** in Figure 1a. Unreacted 2,5-dibromo-3-hexylthiophene (**3**) has a singlet at 6.78 ppm. In the spectrum of the quenched sample in addition to this signal, two doublets with a coupling constant of 5.6 Hz are observed at 7.18 and 6.79 ppm, which belong to the quenching product of the desired active regioisomer **2a'**. Another doublet for the isomer **2b'** with a smaller coupling constant of 1.6 Hz is observed at 6.88 ppm. The second doublet of **2b'** is visible as a small shoulder, and it overlaps with the high field signal of **2a'**. Thus, after 2 h of reaction, the unreacted dibromo compound **3** is still present in the reaction mixture along with the expected active Grignard monomers **2a'** and **2b'**. The magnified section of the ¹H NMR spectra at different reaction times in Figure 1b shows a slow decrease of the singlet corresponding to **3**. Integration of all signals and subtraction of the respective overlapping signals allows for the quantitative determination of all compounds within the accuracy limit of 5% in NMR techniques.

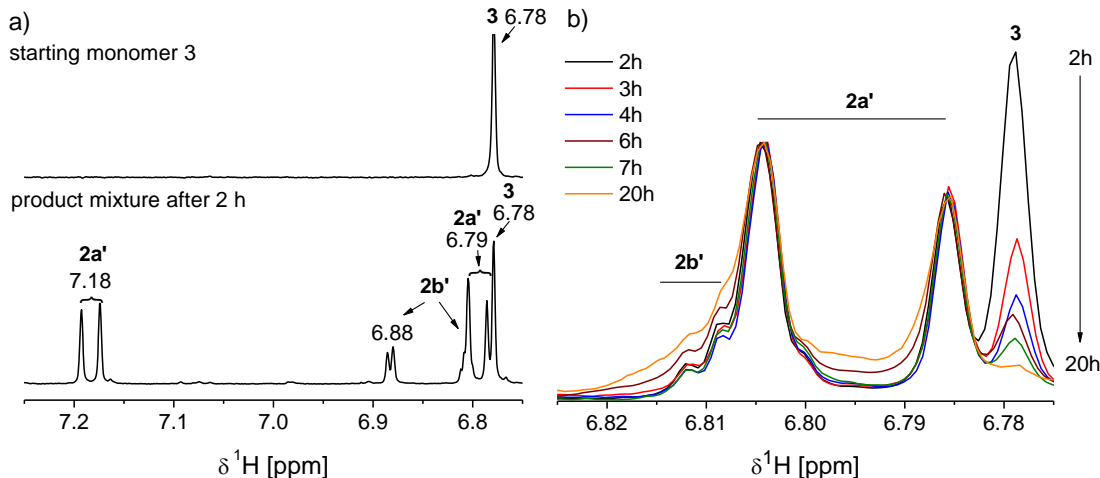


Figure 1: (a) Aromatic region of the ¹H NMR spectra of 2,5-dibromo-3-hexylthiophene (**3**) and of a sample quenched with H₂O after 2 h reaction between 2,5-dibromo-3-hexylthiophene and t-BuMgCl. The signals are assigned according to Scheme 2. (b) Magnified section of the aromatic region (6.78–6.82 ppm) normalized to the high field doublet of **2a'** at different reaction times. The content of 2,5-dibromo-3-hexylthiophene **3** decreases with reaction time continuously up to 20 h.

Table 2: Percentage of components present at different reaction times of 2,5-dibromo-3-hexylthiophene with t-BuMgCl at room temperature. The samples were quenched with H₂O and the components are assigned according to Scheme 2.

| time [h] | 3 [%] | 2a' [%] | 2b' [%] | 2a':2b' |
|----------|--------------|----------------|----------------|----------------|
| 2 | 34 | 46 | 20 | 70:30 |
| 3 | 20 | 59 | 21 | 74:26 |
| 4 | 16 | 63 | 22 | 74:26 |
| 6 | 12 | 65 | 23 | 74:26 |
| 7 | 11 | 66 | 23 | 75:25 |
| 20 | 7 | 68 | 25 | 73:27 |

The percentage of each component present at different reaction times is summarized in Table 2. After 2 h, about 34% of the educt **3** is still unreacted. After 20 h, no detectable decrease of the educt peak could be observed. The ratio of the two isomers **2a:2b** remained nearly constant at about 75:25 for all samples (ranging from 3 to 20 h), and the reaction was very slow. Thus, for the used reaction conditions, almost 20 h is required for the maximum conversion of the dihalide **3** to the active Grignard monomers, **2a** and **2b**.

Since detection of changes in the ¹H NMR signal of **3** after 20 h became very difficult and maximum conversion has been achieved, we initiated the polymerization after 20 h. The monomer **3** to Ni(dppp)Cl₂ catalyst ratio was kept at 26:1 to get moderate molecular weights, which allows for proper end group analysis using matrix-assisted laser desorption ionization spectroscopy with time-of-flight detection mass spectroscopy (MALDI-TOF MS). Fifteen samples (P3HT 1.(1-15)) were withdrawn at different stages of the polymerization, quenched with HCl, and analyzed with size exclusion chromatography (SEC) and MALDI-TOF MS. All polymer samples, independent of the polymerization time, had 100% H/Br end groups as

observed in the single peak series in MALDI-TOF MS. A representative MALDI-TOF MS spectrum of the final sample P3HT 1.15 (polymerization time: 165 min) with a number-average molecular weight M_n (SEC) of 4000 g/mol and a PDI of 1.10 is presented in Figure 2a. P3HT 1.15 shows the highest peak for the 17-mer with H/Br end groups (Figure 2a). The difference between adjacent peaks corresponds to a 3-hexylthiophene main unit with 166.3 g/mol. To enable a comparison of MALDI-TOF MS spectra at short times of polymerization as well, we selected the 12-mer peak range as a suitable example. These spectra for 14 min (P3HT 1.7), 35 min (P3HT 1.14), and 165 min (P3HT 1.15) of polymerization time are shown in Figure 2b. In all cases, only one signal at 2076 g/mol corresponding to 12-mer with H/Br end groups is seen. A signal for the H/H terminated 12-mer, which would occur at 1997 g/mol, is not visible. Hence, 100% H/Br end groups are formed when a 1:0.96 ratio of 2,5-dibromo-3-hexylthiophene to *t*-BuMgCl is used and a long enough reaction time of 20 h for *in situ* monomer formation, and thus the complete consumption of *t*-BuMgCl is guaranteed. However, the time at which the polymerization was started (here 20 h) is not of general validity for complete conversion of **3**. It can vary depending on the concentration of *t*-BuMgCl. For each experiment, the completion of conversion of **3** must be verified before initiating the polymerization.

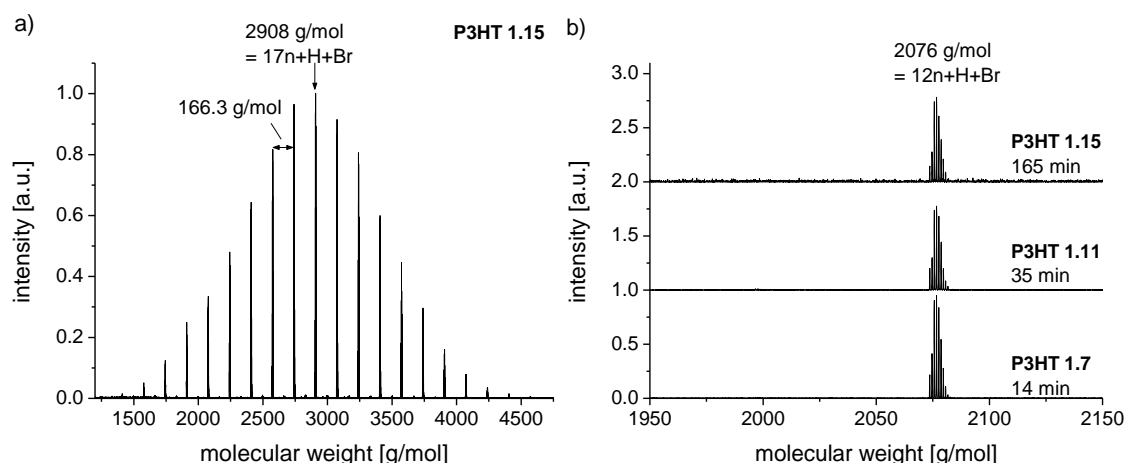


*Figure 2: MALDI-TOF MS spectra of (a) P3HT 1.15 obtained after a polymerization time of 165 min, without any unreacted *t*-BuMgCl present during polymerization, and (b) magnified part in the range of 12 repeating units at different polymerization times of 14, 35, and 165 min. Only one series of signals for polymers with H/Br end groups is observed at all polymerization times, and no signal for the 12-mer with H/H end groups is visible at 1997 g/mol.*

Influence of Incomplete Active Grignard Monomer Formation

To study the influence of incomplete *in situ* monomer formation and hence unreacted *t*-BuMgCl, we also initiated a polymerization after 2 h of active Grignard monomer formation. As shown in Table 2, about 34% of the unreacted **3** or an equivalent amount of unreacted *t*-BuMgCl is present in the reaction mixture. The ratio of monomer to Ni catalyst was again kept constant at 26:1. Thirteen samples were withdrawn at different polymerization times, quenched with HCl, and analyzed with SEC and MALDI-TOF MS to get a second series of

polymers P3HT 2.(1-13). SEC analysis delivered a final molecular weight of $M_n = 4000$ g/mol for P3HT 2 similar to that of P3HT 1. One would have expected a lower molecular weight for P3HT 2 compared to P3HT 1, since the available amount of active Grignard reagent **2a** is less for the formation of P3HT 2. But it is possible that other complex reactions may be taking place during the polymerization due to the presence of unreacted dibromide, unreacted Grignard reagent, and MgClBr in the case of P3HT 2, which requires additional studies. While similar molecular weights were reached as in the P3HT 1 series, the end groups were no longer homogeneous and both H/H and H/Br ends groups were obtained. Also, the amount of H/Br end groups in comparison to H/H end groups decreased with the progress of the polymerization. This behavior is visualized in Figure 3 with the MALDI-TOF MS spectra of the final polymer P3HT 1.13 and the ratio of the two peak series for 12 repeating units at different polymerization times of 22, 61, and 151 min. The difference between the two series is 79 g/mol, which is consistent with the difference between a bromine and a hydrogen atom.

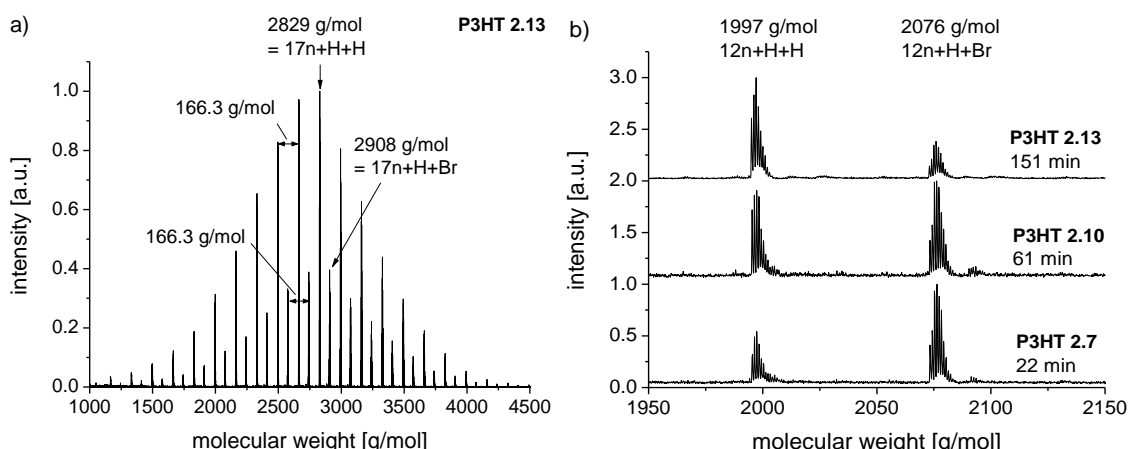


Figure 3: MALDI-TOF MS spectra of a) P3HT 2.13 obtained after a polymerization time of 151 min with unreacted t-BuMgCl present during polymerization and b) magnified part for 12 repeating units at different polymerization times. Two peak series H/Br and H/H are observed and the intensity of the H/Br end group signal decreases with polymerization time, while the intensity of the undesired H/H signal increases.

To show more clearly the time dependence of the amount of H/Br terminated chains, the evolution of the peak molecular weights and the resulting ratios of H/Br to H/H end groups are plotted against polymerization time for both the P3HT 1 and P3HT 2 series in Figure 4. The peak molecular weights were chosen and not the number-average molecular weights to exclude any possible differences caused by different PDIs.

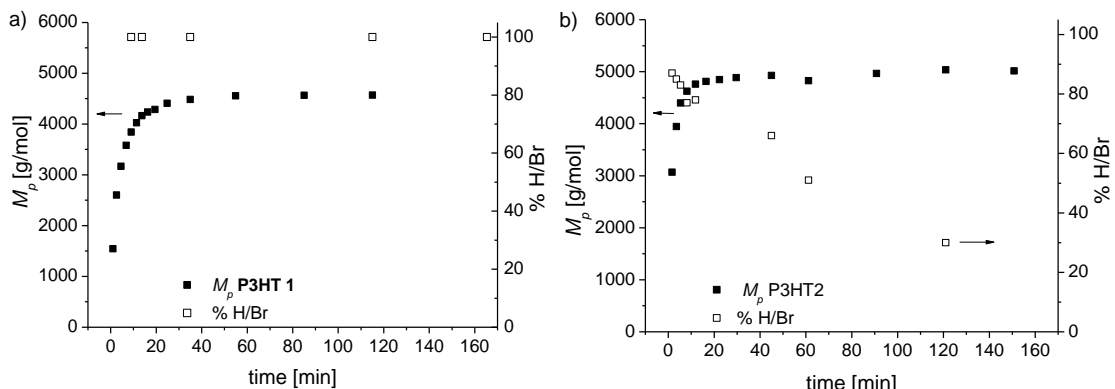
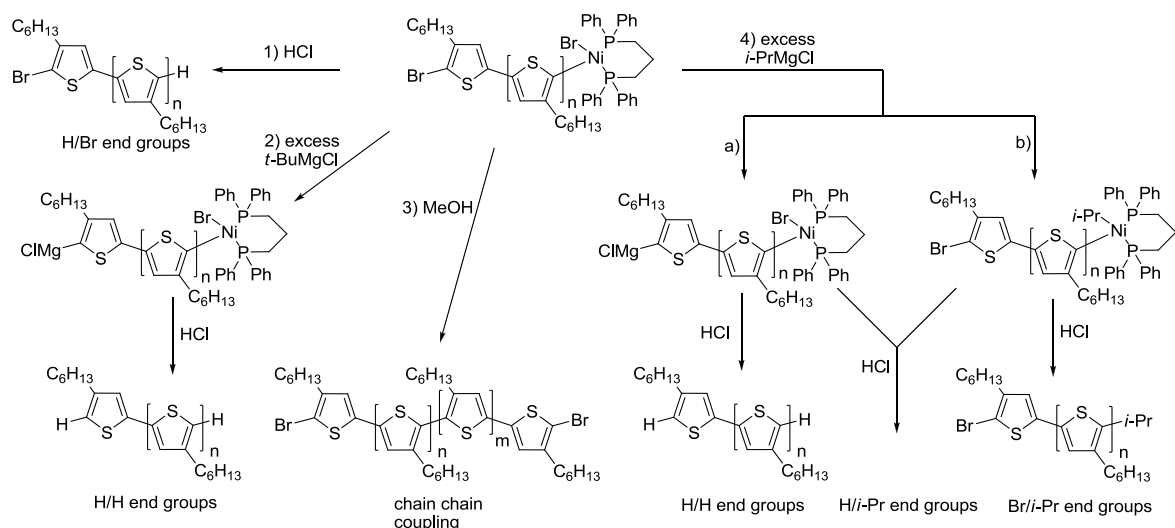


Figure 4: Plot of peak molecular weights M_p and percentage of H/Br chain ends versus polymerization time for (a) P3HT 1.(1-15) without any unreacted *t*-BuMgCl and (b) P3HT 2.(1-13) with incomplete active Grignard monomer formation and thus with an excess of *t*-BuMgCl. With increasing polymerization time, the H/Br content remains constant for P3HT 1, whereas for P3HT 2 the number of H/Br end groups decreases.

In both cases, the polymerization proceeded quite fast, and after a quick rise of the molecular weight, an almost constant molecular weight was reached after about 20 min. Highly interesting was the development of the end groups during the polymerization. For the P3HT 1 series, where the active Grignard monomer formation was complete and no unreacted *t*-BuMgCl was present, all polymer samples had 100% H/Br end groups independent of the polymerization time. The bromine end originates from the starting unit and the hydrogen end group from quenching the active chain end with hydrochloric acid as shown in Scheme 3 (route 1). On the other hand, in the P3HT 2 series (obtained in the presence of unreacted *t*-BuMgCl) at the early stage of polymerization, the amount of H/Br end groups was high, around 80%. With prolonged polymerization time the amount of H/Br end groups decreased linearly with time, and the undesired H/H end groups became dominating. This can be understood as follows. Incomplete active Grignard monomer formation in the case of the P3HT 2 series causes unreacted *t*-BuMgCl in the polymerization mixture, which can react with the bromine chain end of the polymer to form an active Grignard species (Scheme 3, route 2).^{19,35} After quenching with hydrochloric acid, this results in polymer chains with H/H end groups. Since this reaction is rather slow compared to the polymerization, the content of H/Br chain ends is high for short reaction times, during which the chain grows very fast. Thus, short polymerization times are necessary to get a polymer with a high content of H/Br end groups if complete consumption of *t*-BuMgCl during Grignard monomer formation does not take place. For example, we analyzed the end groups of P3HT 2.5, which was quenched after a reaction time of 12 min. The polymer had ~80% H/Br end groups as can be seen in the MALDI-TOF MS spectrum in the Supporting Information. In conclusion, 100% H/Br end groups are only possible when there is no excess of *t*-BuMgCl, which can be realized by the right ratio of 2,5-dibromo-3-hexylthiophene to *t*-BuMgCl and guaranteeing a complete consumption during active Grignard monomer formation. If these prerequisites are not fulfilled, the amount of H/Br end groups will decrease with polymerization time. In the presence of unreacted

t-BuMgCl, only a maximum of 80% H/Br chain ends can be achieved for short polymerization times. However, since the time for reaching the molecular weight plateau is different for different monomer to catalyst ratios, the quenching time has to be adjusted for each ratio if there is an excess of *t*-BuMgCl in the reaction mixture. Thus, the quintessence of this study is that 100% H/Br end groups for any desired molecular weight can be obtained by guaranteeing no unreacted *t*-BuMgCl in the polymerization mixture.



*Scheme 3: Possible reactions of the active chain end with an excess of different Grignard species and quenching reagents. An excess of *t*-BuMgCl affects only the end groups, whereas *i*-PrMgCl can cause both, broader PDI (via end capping) and undesired H/H or H/i-Pr end group formation if present in excess.*

The next question was the influence of excess or unreacted *t*-BuMgCl on the PDI of the resulting P3HT. Therefore, the PDI of both series of P3HT 1.(1-15) and P3HT 2.(1-13) are plotted against polymerization time in Figure 5.

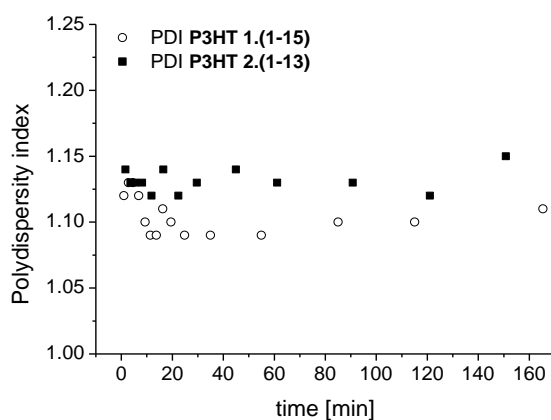


*Figure 5: Polydispersity index PDI of P3HT 1.(1-15) and P3HT 2.(1-13) versus polymerization time. The PDIs of both polymer series are low, and that of P3HT 2.(1-13) was also not significantly affected by unreacted *t*-BuMgCl.*

The polydispersity of both polymers was low between 1.09 and 1.15. The final samples, P3HT 1.15 and P3HT 2.13, had a polydispersity of 1.1 and 1.15, respectively. Thus, there is no noticeable effect of unreacted *t*-BuMgCl on the PDI. Usually end-capping reactions can cause an increase in PDI. However, because the steric demand of *t*-BuMgCl is high, end-capping reactions do not occur, and so a low PDI is maintained. McCullough et al. showed that when *t*-BuMgCl was used as a potential end-capping reagent, no chains with a *t*-Bu end group were formed.³⁶ Thus, the steric hindrance of the tertiary Grignard reagent is too high for this reaction with the active chain end and does not abort the chain growth or cause a broader PDI.

The difference in the steric demand of the Grignard reagents *i*-PrMgCl and *t*-BuMgCl is also one important factor when the monomer routes of McCullough and Yokozawa are compared. Yokozawa et al. showed that already a 1.2 M excess of *i*-PrMgCl does not only affect the end groups, but also the molecular weight distribution of P3HT.³³ Recently, it was shown that by using *i*-PrMgCl as Grignard reagent for the polymerization of P3HT and poly(9,9-dioctylfluorene), the resulting polymers had small amounts of *i*-Pr end groups.^{16,33} This indicates that *i*-PrMgCl can at least partly react with the active chain end and thus cause dead ends and a broad polydispersity (Scheme 3, route 4). On the other hand, an excess of *t*-BuMgCl does not influence the PDI but causes a loss of Br end groups, depending on the time of polymerization. Thus, the observed major differences for the two different monomer systems depend on the steric demand of the Grignard reagents.

Influence of LiCl as an Additive

As shown above, a complete consumption of *t*-BuMgCl is essential to get homogeneous H/Br end groups. However, this is difficult to realize at room temperature. Continuous monitoring of the reaction is necessary, and the reaction times are very long, varying between 20 and 30 h. Increasing the temperature would be an alternative, but McCullough et al. showed that it also influences the ratio of the two active Grignard isomers. More and more of the undesired active monomer **2b** (whose incorporation decreases the regioregularity of the polymers) is formed at higher temperatures.³² Recently, LiCl was used as an additive for the polymerization of different polymers such as poly(*p*-(2,5-bis(hexyloxy)phenylene), poly(9,9-dioctylfluorene), poly(*N*-dodecylpyrrole), and P3HT with *i*-PrMgCl as the Grignard reagent.^{14,16,22,28} Knochel et al. showed that LiCl can significantly accelerate the Br/Mg exchange between a Grignard reagent and aryl halides. It also increases the total yield of the metathesis reaction.^{37,38} LiCl breaks up Grignard aggregates through the formation of a Grignard-LiCl complex with a strong magnesiate character ($\text{RMgCl}_2\text{-Li}^+$). This is discussed as the origin of the high reactivity of these complexes.

Therefore, we studied (i) if LiCl can also be used as an additive in conjunction with *t*-BuMgCl and 2,5-dibromo-3-hexylthiophene to accelerate the active Grignard monomer formation and (ii) the influence of LiCl on the end groups and the PDI. We reacted 2,5-dibromo-3-hexylthiophene, LiCl, and *t*-BuMgCl at a molar ratio of 1:1:0.96. The influence of the LiCl on the

rate of formation of the active Grignard monomer was very strong. Already after 4 h the dibromide **3** was consumed completely, as shown in Figure 6. In contrast to activation by temperature, the acceleration using LiCl did not negatively affect the ratio of the two regioisomers **2a':2b'**. The ratio obtained was 78:22. Without adding LiCl at room temperature it was about 74:26.

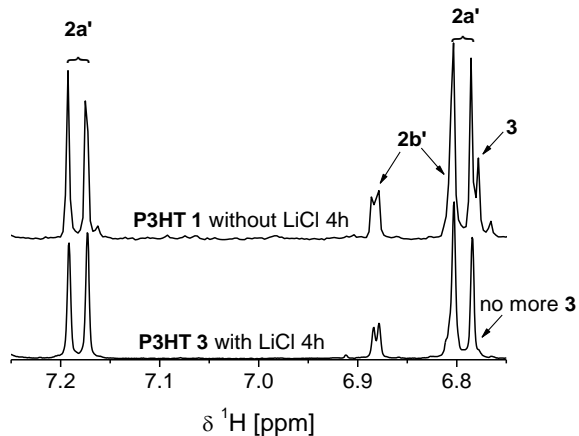


*Figure 6: Aromatic region of the ^1H NMR spectra of samples quenched with H_2O after 4 h reaction for the expected active Grignard monomers between 2,5-dibromo-3-hexylthiophene (**3**) and *t*-BuMgCl with and without LiCl. For P3HT 3 with LiCl as an additive no signal for **3** is observed, which shows the completion of the reaction in 4 h.*

For the polymerization the ratio of monomer to Ni catalyst was kept at 26:1 as in the former experiments. Ten samples were withdrawn at different times, quenched with HCl, and analyzed with SEC and MALDI-TOF MS to get a third series of polymers P3HT 3.(1-10). The resulting polymer P3HT 3.10 (after 22 min of polymerization) had 100% H/Br end groups (for MALDI-TOF MS see Supporting Information) as expected because of the complete consumption of *t*-BuMgCl. Unexpected was the influence of LiCl on the molecular weight and the regioregularity of the polymer. In Figure 7 the peak molecular weights M_p of P3HT 1 series and P3HT 3 series are plotted against the polymerization time. In both series no unreacted *t*-BuMgCl was present during the polymerization. Only the data for the first 30 min are shown here, since a plateau was already reached in both cases.

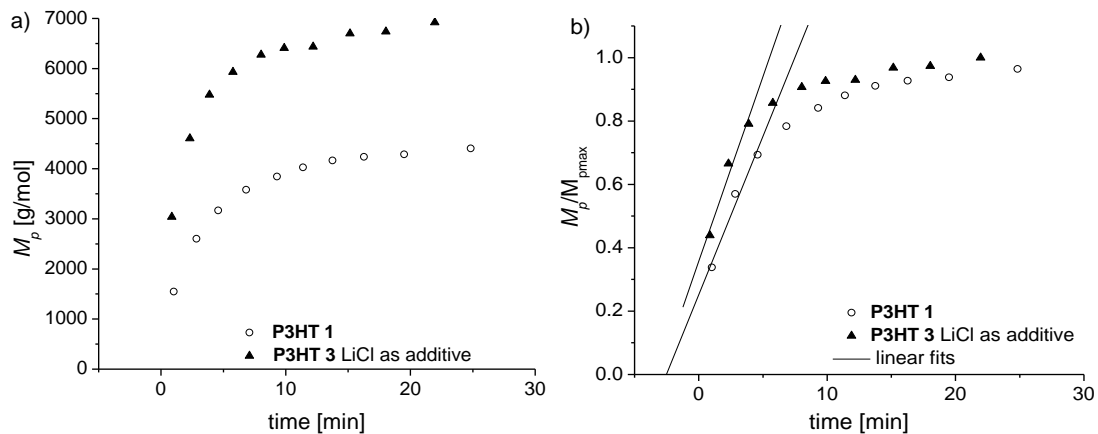


Figure 7: Plot of (a) peak molecular weights M_p and (b) $M_p/M_{p\max}$ versus polymerization time for the P3HT 1 series without and the P3HT 3 series with LiCl as an additive. For both polymers no unreacted *t*-BuMgCl was present in the polymerization mixture, and a monomer-to-catalyst ratio of 26:1 was used. In (b) the straight lines indicate fits for the linear regions.

For the P3HT 3 series with LiCl as an additive, the final molecular weight plateau is reached after the same polymerization time (~ 15 -20 min) as for the P3HT 1 series. However, the resulting molecular weight is higher for the P3HT 3 series. The final sample P3HT 3.10 (22 min of polymerization time) has a number-average molecular weight of 6800 g/mol, whereas the molecular weight for P3HT 1.15 (2 h of polymerization time) was 4000 g/mol. SEC molecular weights of P3HT are usually overestimated because of the chain stiffness of P3HT in comparison to the polystyrene calibration standards. Thus, the more reliable repeating units are calculated from MALDI-TOF MS. For P3HT 1.15 the M_n (MALDI) was 3000 g/mol, corresponding to 18 repeating units and for P3HT 3.10 3700 g/mol, corresponding to 22 repeating units. This was unexpected since the same monomer-to-catalyst ratio was used for both P3HTs. The effect of LiCl on the molecular weight was much higher than any expected experimental error possible during the polymerization procedure. This difference in molecular weight was reproducible for different batches and for different monomer-to-catalyst ratios.

The increase in molecular weight caused by LiCl can be either due to an increase in polymerization rate or due to incorporation of the second isomer **2b** or both. To distinguish between these effects, the normalized peak molecular weights (obtained by dividing by the maximum molecular weight) are plotted in Figure 7b. To quantify the difference in rate of polymerization, we measured the slope in the linear range of both curves. We observed a 17% increase in rate by using LiCl. Thus, this is the main cause for the increase in molecular weight. Further we studied if **2b** is incorporated, which should negatively affect the regioregularity of P3HT and irregular couplings should be visible in ^1H NMR. Indeed, the polymers obtained with LiCl as an additive showed a small amount of irregular couplings at 7.02 (HT-HH; H = head; T = tail) and 7.05 ppm (TT-HH) (see Supporting Information). In contrast, for P3HTs polymerized without LiCl no irregular couplings could be observed. An estimation of the quantitative change in regioregularity is not possible because it lies within the 5% accuracy

limit of ^1H NMR. For qualitative information, the aromatic regions of relevance for the regioregularity in ^1H NMR are shown in the Supporting Information for two different molecular weights. Thus, LiCl increases the rate of polymerization considerably and facilitates the incorporation of the undesired monomer **2b** to a small extent.

The effect of even small changes of the regioregularity on the charge carrier mobility and the performance of organic solar cells has often been discussed in the literature.³⁹⁻⁴² Thus, we measured OFETs to see whether the charge carrier mobility is affected by this small change in regioregularity. To eliminate differences in mobility caused by differences in molecular weight, two polymers with similar number-average molecular weights - one without LiCl (P3HT 4 $M_n = 5300$ g/mol) and one with LiCl as an additive (P3HT 5 $M_n = 5900$ g/mol) - were synthesized and compared as representative examples. Both polymers show the same charge carrier mobility (μ_{sat}) of 2×10^{-3} cm 2 /(Vs). Thus, the effect of the small decrease in regioregularity caused by the use of LiCl on the charge carrier mobility is negligible. Therefore, LiCl is a very helpful additive for efficient acceleration of the active Grignard formation and rate of polymerization. It increases the molecular weight without changing the monomer to catalyst ratio and allows for the easy access of 100% H/Br end groups.

Influence of Quenching Reagent on Polydispersity

Apart from the active Grignard monomer formation, there are other factors such as quenching agents which strongly influence the polymerization of P3HT. Rawlins et al. reported that there is no effect on the polydispersity when methanol is used as a quenching agent instead of hydrochloric acid.⁴³ In contrast to their findings, we see a clear increase in the polydispersity via coupling when using methanol as a quenching reagent. Therefore, we studied in detail the influence of quenching agents on chain-chain coupling. We compared P3HT 5 (obtained by adding LiCl) and P3HT 6 (without LiCl) and analyzed the effect of the quenching reagents, methanol or HCl, on the resulting polymers (Figure 8). During the polymerization of P3HT 5, two samples were taken after 8 min and quenched with either HCl or methanol. The SEC curves of the respective samples of P3HT 5 are presented in Figure 8a. The sample with methanol as a quenching reagent shows an undesired shoulder exactly at double the molecular weight, while the sample quenched with hydrochloric acid has a monomodal distribution. Thus, the origin for the chain-chain coupling could only be the quenching reagent, which increases the polydispersity from 1.10 to 1.16. This is supported by the fact that all polymers synthesized without adding LiCl and quenched with HCl also showed a monomodal distribution. The SEC curve of P3HT 1.15 is shown as a representative example in Figure 8b. Further, during polymerization of P3HT 6 (without LiCl as additive) seven samples were withdrawn and quenched with MeOH and analyzed with SEC. It can be clearly seen that the amount of chain-chain coupling depends on the molecular weight as depicted in Figure 8b. This can be understood as follows. With increasing molecular weight it is less likely for two active chain ends to meet and react. This causes a decreasing amount of coupling. The fact

that P3HT 5 was polymerized with LiCl as an additive and P3HT 6 without it shows that MeOH and not LiCl is the reason for chain-chain coupling.

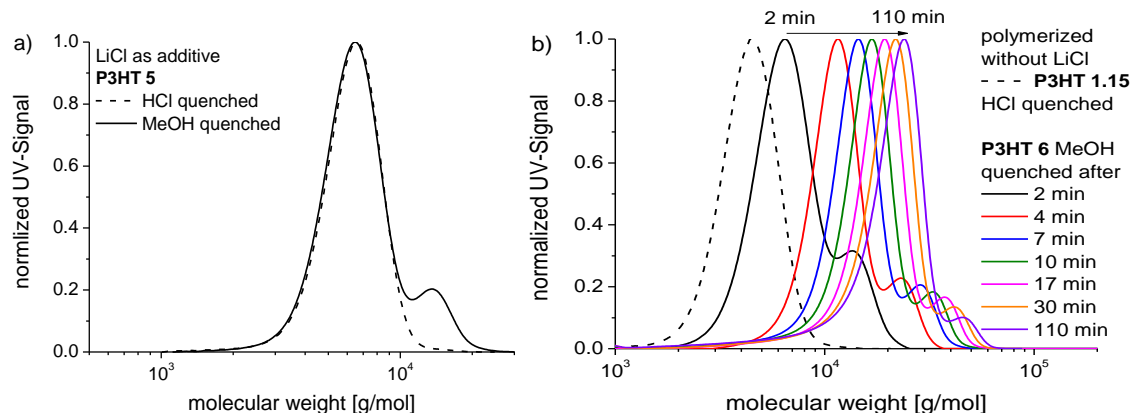


Figure 8: (a) SEC curves of samples of P3HT 5 (polymerized with LiCl as an additive) taken after 8 min and quenched with either methanol or with hydrochloric acid. (b) SEC curves of samples of P3HT 6. (1-7) taken at different polymerization times and quenched with methanol together with P3HT 1.15 quenched with HCl. With increasing molecular weight of P3HT 6. (1-7), the amount of coupled chains decreases.

These findings are in agreement with the observation of Yokozawa et al. when they used water as quenching reagent instead of hydrochloric acid.⁴⁴ They proposed that the slow quenching with water can result in disproportionation of the NiL₂ group at the active chain end, leading to coupled chains. This results in a bimodal molecular weight distribution and a higher polydispersity. To verify this, the end groups of P3HT 5 were analyzed with MALDI-TOF MS. Accordingly, a low molecular weight peak series with H/Br end groups and a high molecular weight peak series with Br/Br end groups are expected. This is because disproportionation of active Ni chain ends would lead to polymers with two bromine end groups at double the molecular weight. Unfortunately, only the low molecular weight series could be detected in MALDI-TOF MS (see Supporting Information). The reason is that it is difficult to observe the minor component of coupled chains at higher molecular weights because of the broad distribution and due to the better tendency of the low molecular weight series to ionize into the gas phase. Therefore, we used preparative SEC to separate the two fractions and additionally used a sample with very low molecular weight (P3HT 7) to observe the coupled chains (see supporting information for SEC). A MALDI-TOF MS spectrum of the high molecular weight fraction containing the coupled chains is shown in Figure 9. One major peak series is observed which corresponds to P3HT with two bromine end groups and one methanol unit ($3019 \text{ g/mol} = 17 \times 166.3 \text{ g/mol} + 2 \times 79.9 \text{ g/mol} + 32 \text{ g/mol}$). The fact that two bromine groups are present in one polymer chain proves the disproportionation. Thus, the origin of the high molecular weight fraction during quenching with methanol is elucidated as chain-chain coupling for the first time. However, the mechanism of incorporation of the MeOH molecule remains unclear. Negligible peaks seen in Figure 9 belong to P3HT with H/Br, H/Br + MeOH and Br/Br chain ends.

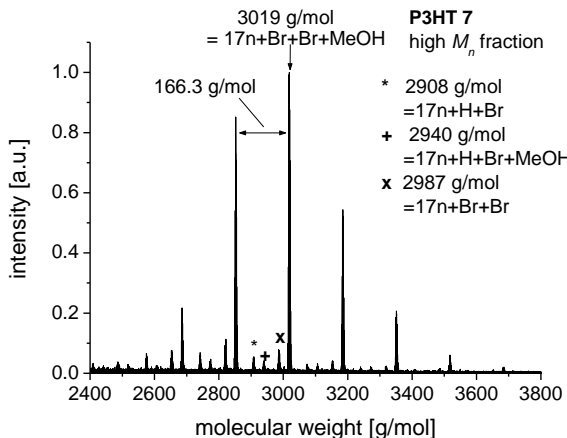


Figure 9: MALDI-TOF MS spectrum of the coupled chain fraction of P3HT 7, which was obtained by preparative SEC. One main peak series for P3HT with two bromine end groups and one MeOH unit is observed. Minor peaks are explained in the legend.

Conclusion

We have shown that a complete active Grignard monomer formation and thus an entire consumption of *t*-BuMgCl are crucial to get polymer chains with 100% H/Br end groups. If this is not guaranteed, the amount of H/Br end groups will decrease with polymerization time. The full monomer conversion requires long reaction times when *t*-BuMgCl and 2,5-dibromo-3-hexylthiophene are used at room temperature. This leads to tedious control via ^1H NMR to ensure the completion of the reaction. To overcome these problems, we used LiCl as an additive to effectively accelerate the active monomer formation. Furthermore, adding LiCl leads to an increase in molecular weight without changing the monomer-to-catalyst ratio. The origin of this effect is due to both an increase in rate of polymerization and the incorporation of small amounts of the undesired isomer 2b, which causes a slight decrease of the regioregularity. This did not negatively affect the charge carrier mobility of P3HT. Additionally, we demonstrated that methanol as a quenching reagent causes chain-chain coupling via disproportionation. The amount of coupling decreased with increasing molecular weight. With the importance of the right quenching reagent and the role of unreacted *t*-BuMgCl, we identified all the factors relevant for catalyst transfer polymerization toward perfect end group control and low PDIs. This will lead to a better understanding of the chain growth polymerization and its use for complex polymer architectures in combination with other polymerization techniques.

Acknowledgments

R. H. Lohwasser thanks the Universität Bayern e.V. for a research stipend according to the Bayerisches Eliteförderungsgesetz. We also acknowledge DFG (SPP 1355 and SFB 840) for financial support.

Supporting Information Available: Experimental details, MALDI-TOF MS spectra, ¹H NMR spectra, SEC curves and output characteristics of OFETs. This material is available free of charge via the Internet at <http://pubs.acs.org>.

References

- (1) Sirringhaus, H.; Tessler, N.; Friend, R. H. *Science* **1998**, *280*, 1741-1744.
- (2) Ma, W.; Yang, C.; Gong, X.; Lee, K.; Heeger, A. J. *Adv. Funct. Mater.* **2005**, *15*, 1617-1622.
- (3) Chen, T.; Rieke, R. D. *J. Am. Chem. Soc.* **1992**, *114*, 10087-10088.
- (4) Jen, K.-Y.; Miller, G. G.; Elsenbaumer, R. L. *Chem. Commun.* **1986**, 1346-1347.
- (5) McCullough, R. D.; Lowe, R. D. *Chem. Commun.* **1992**, 70-72.
- (6) Sheina, E. E.; Liu, J.; Iovu, M. C.; Laird, D. W.; McCullough, R. D. *Macromolecules* **2004**, *37*, 3526-3528.
- (7) Yokoyama, A.; Miyakoshi, R.; Yokozawa, T. *Macromolecules* **2004**, *37*, 1169-1171.
- (8) Zhang, Y.; Tajima, K.; Hirota, K.; Hashimoto, K. *J. Am. Chem. Soc.* **2008**, *130*, 7812-7813.
- (9) Kline, R. J.; McGehee, M. D.; Kadnikova, E. N.; Liu, J.; Fréchet, J. M. J. *Adv. Mater.* **2003**, *15*, 1519-1522.
- (10) Ma, W.; Kim, J. Y.; Lee, K.; Heeger, A. J. *Macromol. Rapid Commun.* **2007**, *28*, 1776-1780.
- (11) Iovu, M. C.; Craley, C. R.; Jeffries-El, M.; Krankowski, A. B.; Zhang, R.; Kowalewski, T.; McCullough, R. D. *Macromolecules* **2007**, *40*, 4733-4735.
- (12) Radano, C. P.; Schermen, O. A.; Stingelin-Stutzmann, N.; Müller, C.; Breiby, D. W.; Smith, P.; Janssen, R. A. J.; Mejier, E. W. *J. Am. Chem. Soc.* **2005**, *127*, 12502-12503.
- (13) Schilinsky, P.; Asawapirom, U.; Scherf, U.; Biele, M.; Brabec, C. J. *Chem. Mater.* **2005**, *17*, 2175-2180.
- (14) Miyakoshi, R.; Shimono, K.; Yokoyama, A.; Yokozawa, T. *J. Am. Chem. Soc.* **2006**, *128*, 16012-16013.
- (15) Huang, L.; Wu, S.; Qu, Y.; Geng, Y.; Wang, F. *Macromolecules* **2008**, *41*, 8944-8947.
- (16) Stefan, M. C.; Javier, A. E.; Osaka, I.; McCullough, R. D. *Macromolecules* **2009**, *42*, 30-32.
- (17) Wen, L.; Duck, B. C.; Dastoor, P. C.; Rasmussen, S. C. *Macromolecules* **2010**, *41*, 4576-4578.
- (18) Wu, S.; Sun, Y.; Huang, L.; Wang, J.; Zhou, Y.; Geng, Y.; Wang, F. *Macromolecules* **2010**, *43*, 4438-4440.
- (19) Beryozkina, T.; Senkovskyy, V.; Kaul, E.; Kiriy, A. *Macromolecules* **2008**, *41*, 7817-7823.
- (20) Khanduyeva, N.; Senkovskyy, V.; Beryozkina, T.; Horecha, M.; Stamm, M.; Uhrich, C.; Riede, M.; Leo, K.; Kiriy, A. *J. Am. Chem. Soc.* **2008**, *131*, 153-161.
- (21) Senkovskyy, V.; Khanduyeva, N.; Komber, H.; Oertel, U.; Stamm, M.; Kuckling, D.; Kiriy, A. *J. Am. Chem. Soc.* **2007**, *129*, 6626-6632.
- (22) Lanni, E. L.; McNeil, A. J. *Macromolecules* **2010**, *43*, 8039-8044.
- (23) Boyd, S. D.; Jen, K.-Y.; Luscombe, C. K. *Macromolecules* **2009**, *42*, 9387-9389.

- (24) Chen, T.; Wu, X.; Rieke, R. D. *J. Am. Chem. Soc.* **1995**, *117*, 233-244.
- (25) Adachi, I.; Miyakoshi, R.; Yokoyama, A.; Yokozawa, T. *Macromolecules* **2006**, *39*, 7793-7795.
- (26) Lanni, E. L.; McNeil, A. J. *J. Am. Chem. Soc.* **2009**, *131*, 16573-16579.
- (27) Smeets, A.; Van den Bergh, K.; De Winter, J.; Gerbaux, P.; Verbiest, T.; Koeckelsberghs, G. *Macromolecules* **2010**, *42*, 7638-7641.
- (28) Takahashi, A.; Rho, Y.; Higashihara, T.; Ahn, B.; Ree, M.; Ueda, M. *Macromolecules* **2010**, *43*, 4843-4852.
- (29) Lohwasser, R.; Thelakkat, M. *Macromolecules* **2010**, *43*, 7611-7616.
- (30) Briseno, A. L.; Holcombe, T. W.; Boukai, A. I.; Garnett, E. C.; Shelton, S. W.; Fréchet, J. M. J.; Yang, P. *Nano Lett.* **2010**, *10*, 334-340.
- (31) Watanabe, N.; Mauldin, C.; Frechet, J. M. J. *Macromolecules* **2007**, *40*, 6793-6795.
- (32) Iovu, M. C.; Sheina, E. E.; Gil, R. R.; McCullough, R. D. *Macromolecules* **2005**, *38*, 8649-8656.
- (33) Miyakoshi, R.; Yokoyama, A.; Yokozawa, T. *J. Am. Chem. Soc.* **2005**, *127*, 17542-17547.
- (34) Jeffries-El, M.; Sauve, G.; McCullough, R. D. *Macromolecules* **2005**, *38*, 10346-10352.
- (35) Liu, J.; Loewe, R. S.; McCullough, R. D. *Macromolecules* **1999**, *32*, 5777-5785.
- (36) Jeffries-El, M.; Sauve, G.; McCullough, R. D. *Adv. Mater.* **2004**, *16*, 1017-1019.
- (37) Krasovskiy, A.; Knochel, P. *Angew. Chem.* **2004**, *116*, 3396-3399.
- (38) Krasovskiy, A.; Straub, B. F.; Knochel, P. *Angew. Chem., Int. Ed.* **2006**, *45*, 159-162.
- (39) Kim, Y.; Cook, S.; Tuladhar, S. M.; Choulis, S. A.; Nelson, J.; Durrant, J. R.; Bradley, D. D. C.; McCulloch, I.; Ha, C.; Ree M., *Nature Mater.* **2006**, *5*, 193-203.
- (40) Sirringhaus, H.; Brown, P. J.; Friend, R. H.; Nielson, M. M.; Bechgaard, K.; Langeveld-Voss, B. M. W.; Spiering, A. J. H.; Janssen, R. A. J.; Meijer, E. W.; Herwig, P.; De Leeuw, D. M. *Lett. Nature* **1999**, *401*, 685-688.
- (41) Sirringhaus, H.; Brown, P. J.; Friend, R. H.; Nielson, M. M.; Bechgaard, K.; Langeveld-Voss, B. M. W.; Spiering, A. J. H.; Janssen, R. A. J.; Meijer, E. W. *Synth. Met.* **2000**, *111-112*, 129-132.
- (42) Woo, C. H.; Thompson, B. C.; Kim, B. J.; Toney, M. F.; Fréchet, J. M. J. *J. Am. Chem. Soc.* **2008**, *130*, 16324-16329.
- (43) Achord, B. C.; Rawlins, J. W. *Macromolecules* **2009**, *42*, 8634-8639.
- (44) Miyakoshi, R.; Yokoyama, A.; Yokozawa, T. *Macromol. Rapid Commun.* **2004**, *25*, 1663-1666.

Supporting Info**Experimental Section****Materials and Characterization**

¹H-NMR spectra were recorded in chloroform on a Bruker Avance 250 spectrometer at 300 MHz. Coupling constants are given in Hz. The spectra were calibrated according to the solvent signal at 7.26 ppm. Size exclusion chromatography (Poly-SEC) measurements were performed utilizing a Waters 515-HPLC pump with stabilized THF as the eluent at a flow rate of 0.5 mL/min. A 20 μ L volume of a solution with a concentration of approximately 1 mg/mL was injected into a column setup, which consists of a guard column (Varian, 50 \times 0.75 cm, ResiPore, particle size 3 μ m) and two separation columns (Varian, 300 \times 0.75 cm, ResiPore, particle size 3 μ m). The compounds were monitored with a Waters UV detector at 254 nm. Polystyrene was used as external standard and 1,2-dichlorobenzene as an internal standard for calibration. Matrix assisted laser desorption ionizations spectroscopy with time of flight detection mass spectroscopy (MALDI-TOF MS) measurements were performed on a Bruker Reflex III using Dithranol as matrix and a mixture of 1000:1 (Matrix:Polymer). The Laser intensity was set to around 70%. The reflection mode was calibrated with a fullerite mixture from Sigma–Aldrich (CAS 131159-39-2).

The monomer 2,5-dibromo-3-hexylthiophene and the catalyst 1,3-bis(diphenylphosphino)propanenickel(II) chloride [Ni(dppp)Cl₂] were synthesized according to the literature.¹ All glass apparatus for polymerization were heated and cooled down under argon. Dry THF was distilled over calcium hydride and potassium. t-BuMgCl (1.7 M in THF) was purchased from Acros and titrated according to Krasovskiy and Knochel.² Hexamethyldisilazane (HMDS) (99% Aldrich) for the OFETs was used as received. LiCl puriss p.a. water free was purchased from Fluka and dried prior to use.

General Procedure for the Synthesis of P3HT

In a dry schlenk flask 1.5 g (4.6 mmol) 2,5-dibromo-3-hexylthiophene was dissolved in 9 ml THF and 3.6 ml (4.41 mmol) of t-BuMgCl were added with a syringe. After complete active Grignard monomer formation the solution was diluted with 33 mL of dry THF and the reaction was initiated with Ni(dppp)Cl₂ (96 mg, 0.18 mmol) suspended in 1 ml THF. For kinetic studies samples of ca. 0.5 mL were withdrawn quenched in HCl and washed with MeOH. The polymerization was stopped by adding 5 ml of 5N HCl. After precipitation in Methanol the polymer was filtered into a Soxhlet thimble and extracted with methanol over night to wash away the monomer and low molecular impurities. The pure polymer was gained by dissolving the polymer in chloroform and precipitation in methanol.

P3HT 1: GPC M_p =4400 g mol⁻¹, M_n =4000 g mol⁻¹, M_w =4300 g mol⁻¹, M_w/M_n =1.10;

δ_H (300 MHz; CDCl₃) 6.98 (1 H, s, H_{ar}), 2.80 (2 H, t, J_{ab} 7.6, α -CH₂), 1.85–1.50 (2 H, m, β -CH₂), 1.50–1.10 (6 H, m), 1.0–0.75 (3 H, m, CH₃); FTIR ν_{max} (film)/cm⁻¹ 3056w, 2955s, 2927s, 2857s, 1512w, 1456m, 1378m, 821m, 726w.

General Procedure for the Synthesis of P3HT using LiCl

In a schlenk flask LiCl was dried under vacuum at 140°C for 4h. After cooling to room temperature dry THF was added and stirred over night to form a 0.5 M LiCl solution. In a dry schlenk flask 1.5 g (4.6 mmol) 2,5-dibromo-3-hexylthiophene was dissolved in 9.2 ml of 0.5 M LiCl solution and 3.6 ml (4.41 mmol) of *t*-BuMgCl were added with a syringe. After complete active Grignard monomer formation the solution was diluted with 33 ml THF. The polymerization was initiated with a suspension of 98 mg (0.18 mmol) Ni(dppp)Cl₂ in 1 mL THF. The polymerization was stopped by adding 5 ml of 5N HCl. After precipitation in Methanol the polymer was filtered into a Soxhlet thimble and extracted with methanol over night to wash away the monomer and low molecular impurities. The pure polymer was gained by dissolving the polymer in chloroform and precipitation in methanol.

OFET Preparation and Measurements

OFET substrates were purchased from Fraunhofer IMPS, Dresden. The geometry of the device was a bottom gate top electrode type, with n-doped (doping at wafer surface: $n \approx 3^{17} \text{ cm}^{-3}$) silicon as gate electrode and a 230 nm SiO₂ layer as gate dielectric. The source and drain electrodes were ITO (indium tin oxide) (10 nm) as adhesion layer with a high work function and gold (30 nm). The analysed channel length was 20 μm and the width was 10 mm. The substrates were cleaned with acetone, H₂O₂/H₂SO₄ (15 min), VE-water, acetone (ultrasonic bath, 15 min), *i*-propanol (ultrasonic bath, 15 min) and rinsed with hexane. The H₂O₂/H₂SO₄ solution should be handled with care because it is highly corrosive. After plasma etching for 15 min the substrates were hydrophobized with hexamethyldisilazane (HMDS) vapour for 3 hours. Excess HMDS was washed off with hexane. All following steps were done under inert gas atmosphere in a glovebox. The active polymer layers were spin coated at 2000 rpm from a 1 wt% solution in CHCl₃. Output and transfer characteristics were measured with a Hewlett Packard 41555A semiconductor parameter analyser. The hole transport mobilities were determined from the transfer characteristics according to equation 1.³ Since the mobility did not reach a saturation regime for all devices, all the given mobilities are for a fixed gate voltage of -40 V.

$$\mu_{sat} = \left(\frac{\partial \sqrt{I_{SD}}}{\partial V_G} \right)^2 \frac{2L}{WC_i} \quad (1)$$

Additional MALDI-TOF MS Spectra

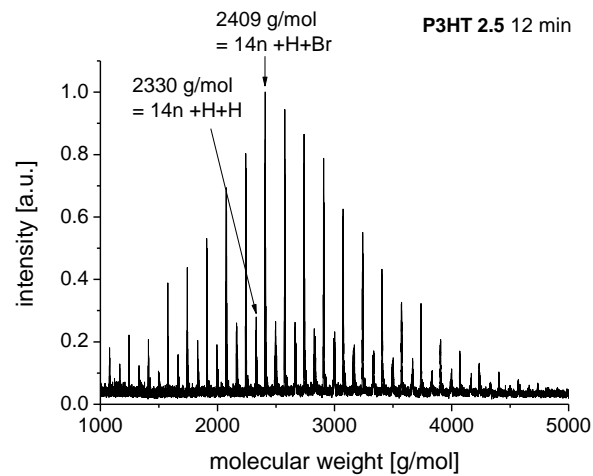


Figure SI-1: MALDI-TOF MS spectrum of P3HT 2.5 with incomplete active Grignard monomer formation after 12 min of polymerization. Two peak series H/Br and H/H are observed. The amount of chain with H/Br end groups is ca 80%.

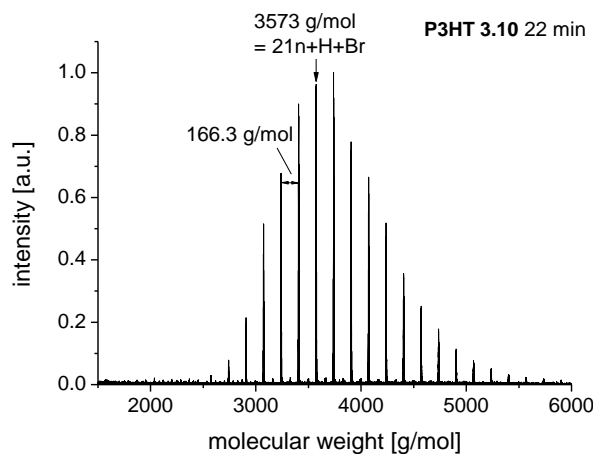


Figure SI-2: MALDI-TOF MS spectrum of P3HT 3.10 polymerized with LiCl as an additive and after complete active Grignard monomer formation after 22 min of polymerization. Only one peak series for polymer with H/Br chain ends is observed.

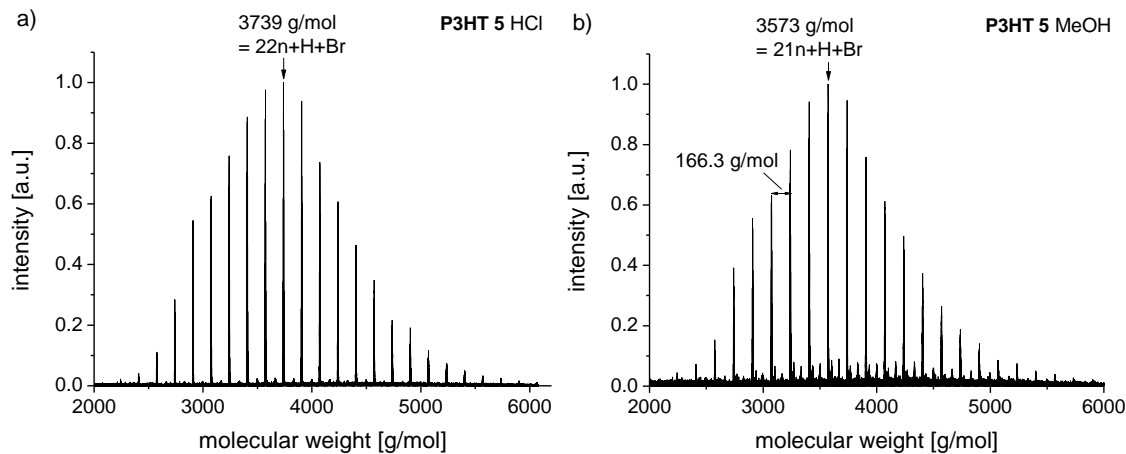


Figure SI-3: MALDI-TOF MS spectra of P3HT 5 polymerized with LiCl as an additive and a) quenched with HCl and b) MeOH. Only one main peak series for chains with H/Br end groups are observed. A monomodal distribution for the P3HT 5 sample quenched with MeOH shows that coupled chains observed in SEC are not visible in MALDI-TOF MS.

Output Characteristics of P3HT 4 and P3HT 5

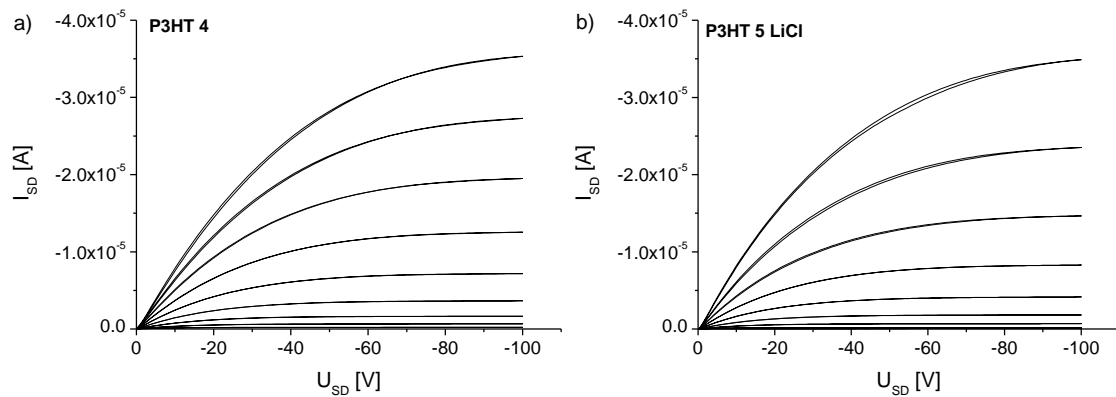


Figure SI-4: Output characteristics (I_{D_s} - U_{D_s}) of organic thin film transistors of a) P3HT 4 synthesized without LiCl and b) P3HT 5 synthesized with LiCl. The geometry was a bottom gate device with SiO₂ as gate dielectric coated with a hexamethyldisilazane (HMDS) layer. The gate Voltage U_G was varied in -10 V steps from 0 V to -80 V.

¹H NMR Spectra of Two Different Molecular Weights of P3HTs Synthesized with and without LiCl

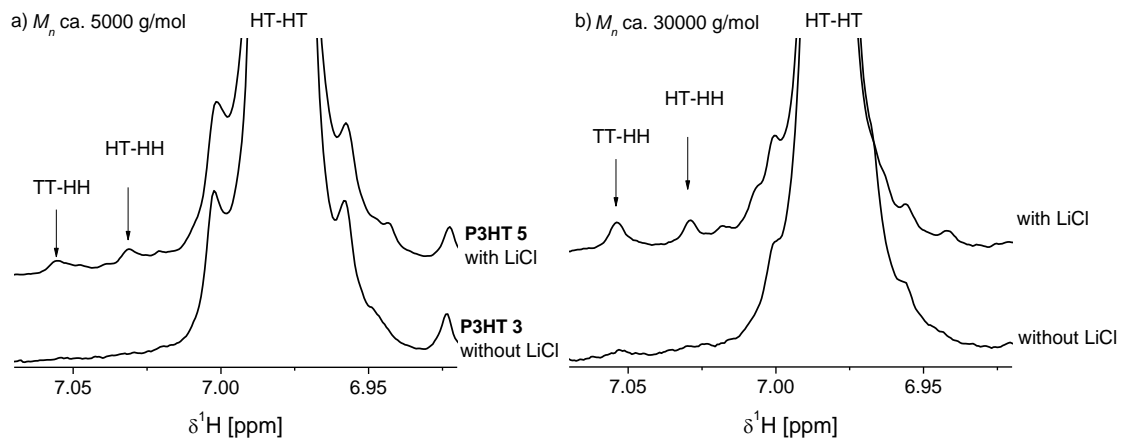


Figure SI-5: Enlarged aromatic region of relevance for regioregularity in the ¹H NMR spectra of P3HTs synthesized with and without LiCl as an additive for samples with a M_n of a) ca. 5000 g/mol and b) ca. 30000 g/mol. While no irregular couplings are observed for P3HTs which were polymerized without adding LiCl, TT-HH and HT-HH couplings are visible for P3HTs polymerized with LiCl as an additive. The irregular couplings are more pronounced for the higher molecular weight samples.

SEC Curves of P3HT 7 before and after Separation with Preparative SEC

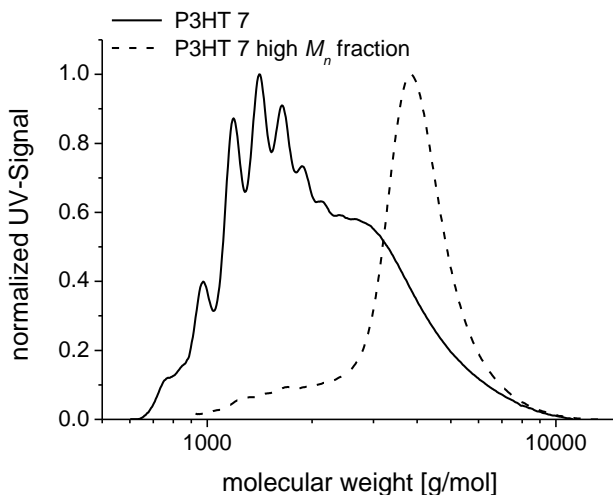


Figure SI-6: SEC curves of P3HT 7 and the high molecular weight fraction of P3HT 7, containing the coupled chains. The high molecular weight fraction was separated using preparative SEC.

References

- (1) Van Hecke, G. R.; Horrocks, W. *Inorg. Chem.* **1966**, 5, 1968-1974.
- (2) Krasovskiy, A.; Knochel, P. *Synthesis* **2006**, 5, 890-891.
- (3) Sze, S. M.; Ng, K. K. *Physics of semiconductor devices*, Wiley-Interscience: Hoboken, NJ, 2007.

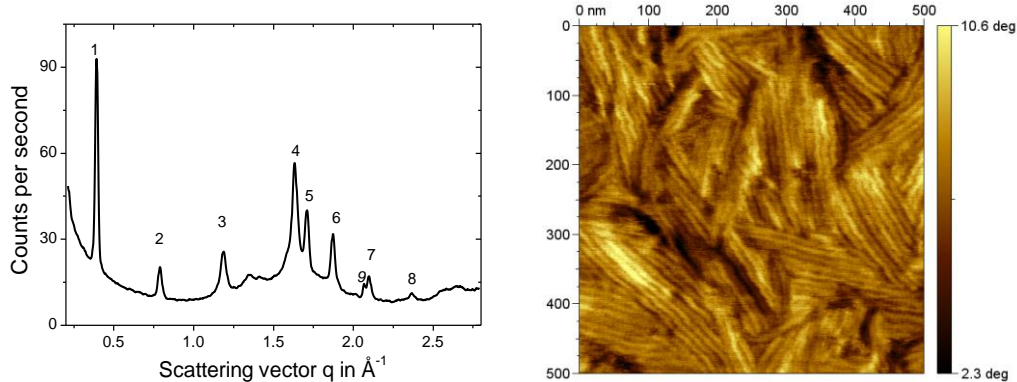
4. Temperature and Molecular Weight Dependent Hierarchical Equilibrium Structures in Semiconducting Poly(3-hexylthiophene)

Zhiyong Wu,^a Albrecht Petzold,^a Thomas Henze,^a Thomas Thurn-Albrecht,^{*a}
Ruth Lohwasser,^b Michael Sommer,^b and Mukundan Thelakkat^{*b}

^aInstitut für Physik, Martin-Luther-Universität Halle-Wittenberg, 06099 Halle, Germany,

^bAngewandte Funktionspolymere, Makromolekulare Chemie I, Universität Bayreuth,
95440 Bayreuth, Germany

*E-mail corresponding authors: thomas.thurn-albrecht@physik.uni-halle.de;
mukundan.thelakkat@uni-bayreuth.de



Abstract

We report on structural investigations of a series of regioregular poly(3-hexylthiophene) with well-defined molecular weight (5-19 kg/mol) using DSC, small angle and wide-angle X-ray scattering, and AFM. With increasing temperature, we identify three ordered phases, namely 3D crystalline, 2D crystalline with disordered side chains, and a layered phase of smectic symmetry, followed by complete melting. Although all samples crystallize in extended chain conformation, the lower molecular weight material exhibits a lower crystallinity, most likely caused by noncrystallizable end groups. The crystallinity increases strongly with increasing molecular weight, which could be a possible explanation for the known dependence of charge transport properties on molecular weight.

Introduction

Semiconductor conjugated polymers have attracted widespread scientific interest triggered by their potential applications in electronic devices like solar cells, light emitting diodes or field effect transistors.¹⁻⁴ The steady increase in material performance parameters as, e.g., charge carrier mobility over the last 2 decades has brought these applications closer to reality. Devices based on organic materials and especially solvent processable polymers have potential advantages such as low cost, light weight, and flexibility compared to those made from inorganic semiconductors. Compared to low molecular weight materials, polymers in general tend to be more disordered and to exhibit a complex, hierarchical microstructure. Even chemically very regular, crystallizable polymers form usually only semicrystalline materials and display a crystalline-amorphous superstructure on a scale comparable to the size of the chain,⁵ a fact which should be of relevance especially for charge transport.

Because of their high mobility poly(3-hexylthiophene) (P3HT) and other polythiophenes belong to the most promising polymers for optoelectronic applications.⁶⁻⁸ With their relatively stiff main chain⁹ to which flexible alkyl side chains are attached in order to increase solubility, they generally develop layered crystalline structures with separated main and side chains. π - π stacking of planar backbones leads to delocalization of electronic states across different chains.¹⁰ The crystalline structure of P3HT has been studied at several instances, in the initial reports an orthorhombic unit cell as schematically depicted in Figure 1 was reported.¹¹⁻¹⁴ More recent investigations find slight deviations and monoclinic unit cells are suggested.^{15,16} As mentioned, a full description of the structure of P3HT requires further elements. First there is the question about the order and the dynamic state of the side chains. While originally a well ordered arrangement of side chains tilted with respect to the main chain without interdigitation was proposed,¹³ there is no complete agreement about this point in the literature and recently Kline et al. concluded from spectroscopic experiments that the side chains are disordered at room temperature.^{13,17-19} There is some evidence, mostly from DSC data, that at elevated temperatures a separate side chain melting can occur,^{14,20-23} but the results are less clear for P3HT than for poly(3-alkylthiophenes) with longer side chains. Also

there is no conclusive set of complementary calorimetric and structure analysis experiments. Upon crystallization, polymers generally form lamellar crystals separated by amorphous layers, the same is true for P3HT.²⁴ As additional parameters the thicknesses of the crystalline and amorphous layers d_c and d_a are therefore needed to describe the full structure (cf. Figure 1). The amorphous part can contain folds or other topological defects but also chemical defects like noncrystallizable comonomers or in case of P3HT regiodefects. Generally, for polymers the melting temperature depends on the crystal thickness. As a special characteristic, P3HT adapts a layered phase of smectic symmetry at elevated temperatures in between the crystalline and the isotropic phase. In this phase the separation between main and side chains remains intact.²⁵ Given the complex phase diagram of P3HT, the thermal history as well as the exact chemical structure can be decisive for the formation of a special morphology. The design of annealing procedures has to be based on the temperature dependent phase diagram, as the molecular mobility in the different phases is largely different.²⁵

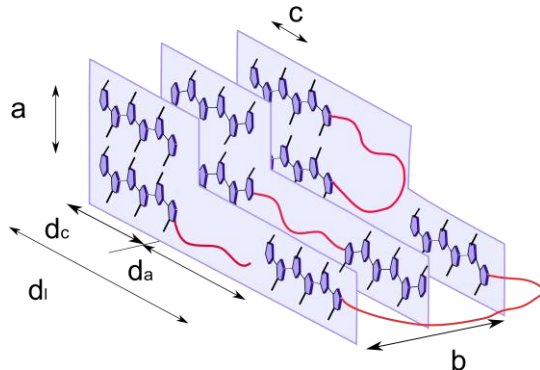


Figure 1: Scheme of the typical microstructure of regioregular P3HT. Key: a, b, c, crystal lattice parameters; d_c , thickness of lamellar crystals; d_a , thickness of amorphous layers, d_l , long period, $d_l = d_a + d_c$ (scheme not to scale: the long period d_l is about on order of magnitude larger than the lattice parameters a, b, c).

Given the fact that electronic transport properties are typically much more favorable in highly ordered, crystalline materials than in amorphous disordered materials, it is clear that the properties of polymer electronic devices will heavily depend on the extent to which structure and morphology of the corresponding materials can be controlled.²⁶ An exemplary yet ambiguous current debate in this context concerns the molecular weight dependence of the charge carrier mobility of regioregular P3HT in thin films, as measured in an OFET device. With increasing molecular weight the charge carrier mobility increases and the absorption spectrum shows a red shift.²⁷⁻³¹ On the structural side the observations are less clear. While the long period and presumably the crystal thickness as observed by AFM and GISAXS increases with molecular weight, experiments also seem to indicate that the amount of order decreases with increasing molecular weight. AFM images show a small scale nodular structure as opposed to a lamellar structure and Bragg intensities in X-ray diffraction experiments become weaker for higher molecular weight. Several possible explanations are proposed to solve the obvious

discrepancies. While Kline et al. attributed the higher mobility in high molecular weight materials to a higher interconnectivity of the crystalline network,²⁸ Neher et al. on the other hand suggested that the correlation between mobility and molecular weight is related to a larger distortion of the backbone in the low molecular weight materials.³¹ On the basis of the recent observation that the crystallinity and the melting temperature of P3HT increase with increasing molecular weight,³² the same authors recently suggested that the transport properties are largely determined by the crystallinity of the samples. Somewhat in contradiction Brinkmann et al. found by electron microscopy that the thickness of crystalline lamellae is independent of the molecular weight.³³

We here report on a study of a series of chemically well-defined P3HT samples with high regioregularity and narrow molecular weight distribution, using a combination of different experimental techniques (DSC,SAXS,WAXS,AFM) in order to determine the temperature and molecular weight dependent equilibrium crystal structure and morphology in bulk. While technologically often thin film samples are relevant, we here on purpose start with a study of bulk samples as a basis from which additional interfacial effects can be understood. We contribute to a clarification of some of the open questions mentioned above, concerning state and structure of the side chains, the occurrence of a separate side chain melting transition, and the molecular weight dependence of the morphology for low and intermediate molecular weight, i.e. the range which is most probably of practical relevance. While we do not address the mobility problem directly, we believe that our results should hold at least qualitatively in general and should be of relevance for a basic understanding and optimization of the electronic properties of P3HT.

Experiments

DSC. A Diamond differential scanning calorimeter from Perkin-Elmer was used to investigate the thermal properties of the samples. Background contributions to the signal were subtracted resulting in measurements of the apparent heat capacity $c_p(T)$.

SAXS. Small angle X-ray scattering experiments were carried out on a Kratky compact camera connected to a conventional X-ray tube, equipped with a focusing X-ray multilayer optics, a scanning scintillation detector and a temperature-controlled sample holder in which the sample was held in between aluminum foil. As the camera uses a slit focus, data were deconvoluted applying the desmearing algorithm by Strobl.³⁴ During the measurements, the sample chamber was evacuated.

WAXS. Wide angle X-ray scattering measurements were performed on a Siemens D5000 powder diffractometer in reflection geometry (θ - 2θ , Rowland circle) equipped with a heatable sample support plate (HTK1200, Anton Paar, Austria). The sample holder consisting of a silicon base plate and a copper frame was mounted on the heatable plate and kept in N₂-atmosphere during the measurement. For both SAXS and WAXS CuK_α radiation was used ($\lambda = 1.54 \text{ \AA}$). For a

precise analysis the angular scale of the diffractometer was calibrated by comparison with the SAXS scale using the (100) Bragg reflection of P3HT, which was visible in both setups.

AFM. Atomic force microscopy was performed with a Nanowizard from JPK Instruments (Berlin, Germany) using silicon cantilevers from Nanoworld with a nominal resonance frequency of 320 kHz and a stiffness of about 42 N/m. The instrument was operated in intermittent contact mode under ambient conditions.

Chemical Characterization. ^1H NMR spectra were recorded on a Bruker DRX 500 spectrometer at 500 MHz in chloroform solution. Size exclusion chromatography SEC measurements were carried out in THF using a UV detector from Waters and a mixed-C PL-Gel (PL) column. Polystyrene was used for calibration and 1,2-dichlorobenzene as an internal standard. MALDI-TOF MS measurements were performed on a Bruker Daltonic Reflex TOF using dithranol as matrix and a mixture of 1000:1 (matrix:polymer). The laser intensity was set to around 70%.

Samples. Synthesis and Chemical Characterization. Regioregular Poly(3-hexylthiophene) (P3HT) samples were synthesized using the Grignard metathesis polymerization (GRIM) developed by McCullough and co-workers.³⁵ The basic characteristics such as molecular weight, polydispersity and chain length are given in Table 1. The molecular weights and the polydispersities were determined by size exclusion chromatography (SEC) using polystyrene as external standard for calibration. The results are shown in Figure 2. Since the hydrodynamic radii of rather stiff conjugated polymers like poly(3-hexylthiophenes) are larger than for polystyrene the molecular weight values are overestimated.³⁶ The peak maximum of the molecular weight distribution measured by SEC is about twice the number-average molecular weight determined on an absolute scale by MALDI-TOF MS, matrix assisted laser desorption/ionization mass spectroscopy with time-of-flight detection (for $M \approx 5000\text{-}20000\text{ g/mol}$). These latter values were used to determine the degree of polymerization, i.e. the number of repeating units, and the contour length. For the synthetic method used, the first two units are coupled tail-tail,³⁷ while otherwise the number of irregular defects within the chain is very low and even hard to detect quantitatively by NMR. In general the regioregularity can be calculated from the NMR peaks for the four different triads TT-HH (7.05 ppm), TT-HT (7.00 ppm), HT-HH (7.02 ppm), and HT-HT (6.98 ppm).^{38,39} Therefore, the range between 7.06 and 7.01 ppm for irregular couplings was integrated and compared to the range for the regioregular HT-HT couplings. The TT-HT (7.00 ppm) coupling could not be separated from the regioregular peak at 6.98 ppm even with a 500 MHz NMR. Thus, the given regioregularity takes into account only the defects within the chains, the tail-tail coupling from the starting unit is not included. For comparison, data from a commercial sample, obtained from Aldrich, have been included. Measurements on this sample were already published.²⁵ MALDI-TOF MS could not be carried out for this sample due to its large molecular weight and large polydispersity. The polymers are named according to their MALDI-TOF MS molecular weight and C.S. indicates commercial sample.

Table 1: Molecular Characteristics of Samples Used in This Study^a

| sample | P3HT 3 | P3HT 6 | P3HT 12 | C.S. |
|--|--------|--------|---------|------|
| M_n (SEC) in kDa | 5.2 | 7.9 | 18.5 | 20.0 |
| M_w (SEC) in kDa | 6.0 | 10.1 | 21.6 | 48.3 |
| M_n by MALDI in kDa | 3.2 | 6.6 | 12.4 | |
| no. of repeating units (thiophene rings) | 20 | 39 | 74 | |
| calculated contour length in nm | 7.7 | 14.9 | 28.3 | |
| PDI (SEC) | 1.15 | 1.28 | 1.16 | 2.41 |
| %regioregularity (NMR) | 97 | 97 | 97 | 94 |

^a The contour length was calculated as the product of the number of repeating units times half of the lattice parameter c determined below. Note that M_w of the sample C.S. is considerably higher than that of sample P3HT 12.

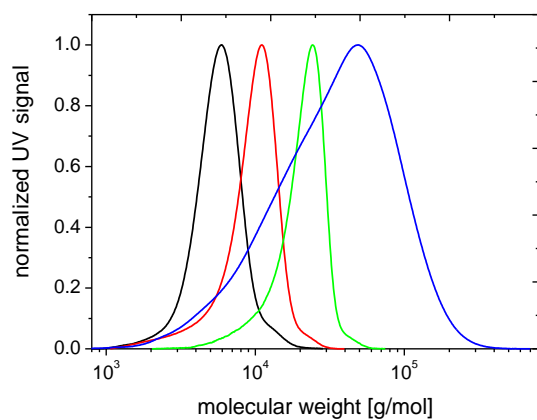


Figure 2: Molecular weight distribution of the P3HT samples under study as measured by size exclusion chromatography (black, P3HT 3; red, P3HT 6; green, P3HT 12; blue, C.S.).

Sample Preparation. For the DSC measurements, P3HT flakes obtained from synthesis were used without any further treatment. Aluminum pans were filled with a mass of about 10 mg. To prepare homogeneous isotropic bulk samples for WAXS and SAXS, the materials were put into the respective holder (transmission geometry for SAXS, reflection geometry for WAXS), placed in an oven with nitrogen atmosphere, heated to the melt state and then cooled down slowly to room temperature. Films for AFM were spin coated with 2000 rpm from 0.3 to 0.5wt% chloroform solution onto silicon wafers covered with a natural oxide layer. Subsequently, the films were heated in nitrogen atmosphere above their respective melting temperatures and cooled down slowly to room temperature.

Results and Discussion

Crystal Structure-Temperature Dependence. *Sequence of Phases with Temperature.* As described in the introduction P3HT exhibits a hierarchical structure which covers several length scales and comprises π - π stacking, separation between main and side chains, and a semicrystalline morphology consisting of lamellar crystals and amorphous interlayers. To investigate the temperature dependence of this complex structure in detail we selected the sample with the lowest molecular weight (P3HT 3). It shows most clearly the phenomena which we think are general. A first overview can be gained from the DSC measurement shown in Figure 3.

There are four transitions from low to high temperatures. A small step in specific heat capacity, c_p around -10 °C indicates the glass transition of the amorphous part of the sample. The value of T_g is comparable to the glass transition temperature observed in regiorandom P3HT.²⁵ Consistently we find a reversible phase transition around 50-60 °C. As we will show below using X-ray scattering experiments, this transition can be attributed to side chain melting. While this attribution was presumed before,²³ it has to our knowledge not been proven by direct structural evidence as, e.g., by X-ray scattering. The reason might be that generally thermal properties of P3AT's depend strongly on the length of the side chains, on the molecular weight, and on the details of the chemical structure. For these reasons, experimental results reported in the literature vary corresponding to advances in the synthesis of well-defined polymers. Correspondingly some temperature dependent structural changes have been observed in this intermediate temperature range,¹⁴ but no clear reversible phase transition. As we will show also in our samples the transition is difficult to observe for higher molecular weights. The next peak around 170 °C is related to crystal melting. In the cooling run, a shoulder on the high temperature side can be recognized (cf. inset), suggesting that melting and crystallization occurs in two steps, namely over an intermediate layered mesophase of smectic symmetry,²⁵ as it is consistent with the scattering experiments shown below. For the slight bump in the DSC signal around 125 °C, we did not find any corresponding structural changes.

To find out what kind of structural changes take place at the transitions observed in DSC, we performed temperature dependent SAXS and WAXS measurements as shown in Figure 4. The Bragg peaks visible in WAXS for intermediate temperatures (above 60 °C) correspond to the typical pattern usually reported for room temperature measurements of commercial P3HT (cf., e.g., ref 25). For the sample P3HT 3 in the low temperature phase, additional reflections showed up, indicating that the transition at 60 °C is related to structural changes in the crystalline part of the sample. Details will be discussed below. Measurements taken during a cooling run (not shown) confirmed that the changes in the scattering pattern were reversible. A comparison of the data obtained at 140, 160, and 180 °C shows that melting occurs in two steps. At 160 °C, all Bragg reflections but the first (peak 1), which reflects the layered structure

resulting from a separation between main and side chains, have disappeared. Only the next measurement taken at 180 °C corresponds to a completely amorphous sample giving rise to diffuse scattering only, without Bragg reflections. The SAXS data are consistent with the occurrence of a two-step melting process. They show two peaks, namely again peak 1 discussed above and peak 0 at $q \approx 0.065 \text{ \AA}^{-1}$ which is caused by stacks of alternating lamellar crystals and amorphous layers with a periodicity $d_1 = 2\pi/q \approx 9.7 \text{ nm}$. In an intermediate temperature range ($T = 170\text{-}180 \text{ }^\circ\text{C}$) peak 1 is still observable, while peak 0 has already disappeared; i.e., there is an intermediate layered structure of separated main and side chains but without lamellar crystals. As it can be noticed from the fact that the smectic phase is still observable at 180 °C in SAXS and not in WAXS, there are slight deviations in the temperature calibration between the two instruments. This does not affect the overall result.

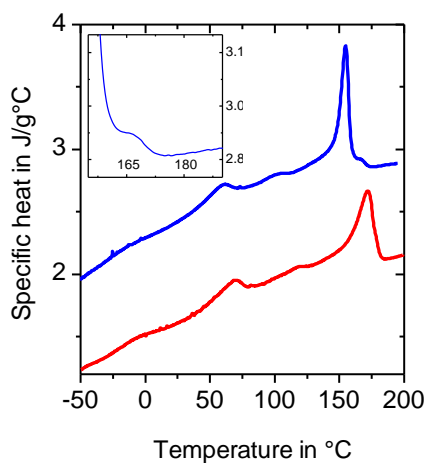


Figure 3: DSC heating (red) and cooling (blue, vertically shifted) curves of P3HT 3 measured with a rate of 20 K/min. The inset shows an enlarged part of the crystallization peak measured during cooling.

Crystal Structure at Room Temperature. A close inspection of the WAXS profiles in Figure 4 reveals that above the transition at about 60 °C peaks 5, 6, and 7 disappear. In order to understand the corresponding structural changes, it is necessary to index the additional Bragg reflections of the low temperature phase. Figure 5 shows a WAXS scattering profile measured at room temperature with better statistics and a broader q -range than in Figure 4. While powder diffraction profiles of P3HT have been reported many times in the literature, such detailed diffraction patterns as in Figure 5 are rare and were more often measured on thin films.^{15,16} In general scattering patterns of P3HT could be explained based on the orthorhombic unit cell originally proposed by Prosa et al.^{13,14} A second structure with reduced main-chain side-chain layer distance was also reported in the literature,⁴⁰ but the additional features appearing in our samples relate to the lateral packing of the chains. In our case we could not explain the positions of the higher order reflections with an orthorhombic unit cell, but satisfactory agreement between calculated and measured positions of the reflections could be obtained using the monoclinic structure proposed by Brinkmann and Rannou.¹⁵ The corresponding analysis is shown in Table 2.

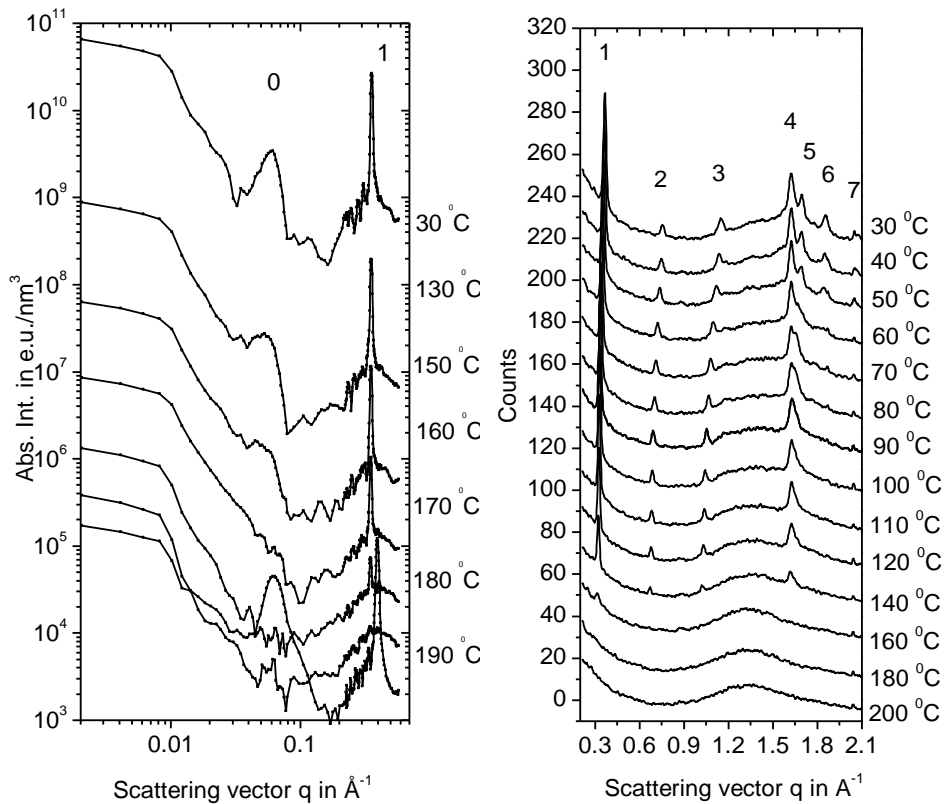


Figure 4: Temperature dependent small angle (left) and wide angle (right) X-ray powder scattering profiles of P3HT 3 reflecting the semicrystalline morphology and the crystal structure (cf. Figure 1). All data were taken during heating. Bragg reflections are numbered from low to high scattering vector. Peak 7 contains a contribution which comes from the substrate and remains therefore visible up to the highest temperatures. The temperatures at which the transitions occur differ slightly between the two series of measurements due to temperature calibration errors, mainly in the WAXS chamber.

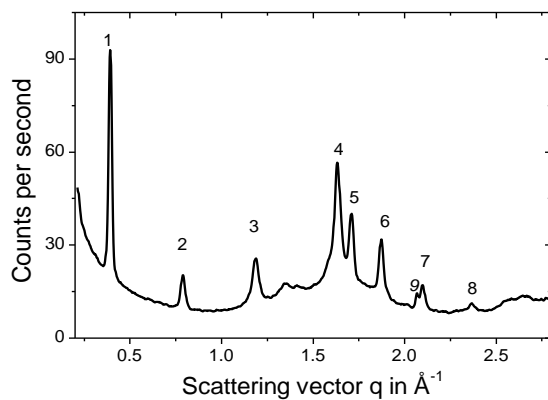


Figure 5: Powder diffraction profile of P3HT 3 measured at room temperature. Bragg reflections are numbered from low to high scattering vector. Peak 9 originates from the sample holder.

Table 2: Proposed Indices of the Bragg Reflections Visible in Figure 5^a.

| peak | (hkl) | $2\theta_B$ [deg] | q [\AA^{-1}] | q_{calc} [\AA^{-1}] | d [\AA] |
|------|---------|-------------------|---------------------------|---|----------------------|
| 1 | 100 | 5.61 | 0.399 | | 15.73 |
| 2 | 200 | 11.20 | 0.796 | 0.80 | |
| 3 | 300 | 16.84 | 1.19 | 1.20 | |
| 4 | 020/002 | 23.20 | 1.64 | | 7.66 |
| 5 | 120 | 24.28 | 1.72 | 1.71 | |
| 6 | 220 | 26.63 | 1.88 | 1.86 | |
| 7 | 320 | 29.90 | 2.11 | 2.08 | |
| 8 | 420 | 33.83 | 2.37 | 2.35 | |

^a Bragg angles $2\theta_B$ were calibrated by comparison with the corresponding position of the (100) peak in the SAXS measurement. q_{calc} is the value of the scattering vector q_{hkl} calculated from a monoclinic unit cell with lattice cell parameters a , b , c determined from reflections 1 and 4, and $\gamma = 93^\circ$ as proposed by Brinkmann.

The first three peaks 1-3 shown in the X-ray diffraction profile in Figure 5 can be identified as series of (h00) reflections. We used the (100) reflection to calibrate the angular scale of the diffractometer, the fact that q_{200} and q_{300} were close to the expected values confirms the validity of this procedure. As shown by Tashiro,¹⁴ peak 4 is a superposition of the (020) and a weak (002) reflection. Having identified these first four reflections the lattice parameters could be determined as $a = 15.73 \text{ \AA}$, $b = 7.66 \text{ \AA}$, $c = 7.66 \text{ \AA}$ for P3HT 3. Compared to the values in the literature, our lattice parameters are slightly smaller.^{14,15,25} Starting from these values we could consistently attribute the indices (120), (220), (320), and (420) to the remaining reflections 5, 6, 7, and 8, as the corresponding data in Table 2 show.

Obviously, the peaks disappearing at the phase transition around 60 °C have all mixed indices, i.e. $h \neq 0 \wedge k \neq 0$. The corresponding lattice planes connect different layers of main chains (or side chains) and therefore require registry in the a - and b - direction of the chain positions in different layers. This is only possible if the side chains are in an ordered state, we therefore attribute the disappearance of the additional peaks to a loss of order in the side chains, i.e., side chain melting. Above this transition the material exhibits a peculiar state of order. In one direction there is a regular periodic stack of alternating side chains and main chains, and the main chains within the layers are arranged on a regular 2D lattice. But this arrangement is uncorrelated between different layers, as the side chains separating different layers are disordered and probably at least in the outer part very mobile. Figure 6 illustrates this point schematically.

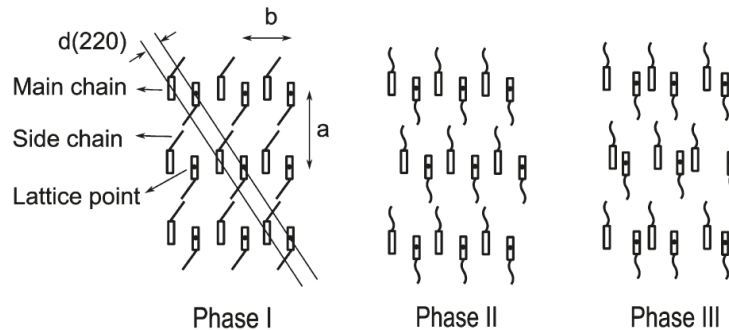


Figure 6: Schematic illustration of structure and order in the different phases of P3HT. (220) planes are indicated. (viewing direction along c). Phase I: regular 3D-crystal with ordered main and side chains. Phase II: regular packing of the main chains only. The side chains are molten and disordered; correspondingly different main chain layers lose correlation with each other (schematically shown for the central layer). Phase III: liquid-like packing of main and side chains, but the separation between main and side chains still exists.

Side Chain Packing in Room Temperature Phase. The exact conformation and packing of the side chains in P3HT has been under discussion for a long time. Recently it was concluded from a detailed study on a P3HT with higher molecular weight that the side chains are disordered.¹⁹ Given that we have strong evidence for an ordered arrangement of the side chains in the low temperature phase, namely the registry between different layers, we tried to explore the consequences for the packing of side chains similarly as in ref 19. Basically there are three possibilities discussed in the literature, all schematically depicted in Figure 7.

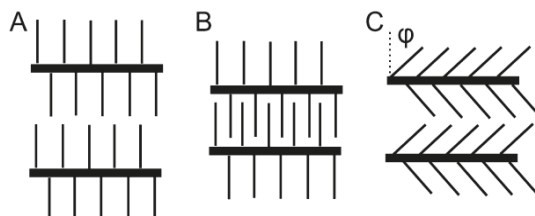


Figure 7. Schemes of possible types of side chains packing. Key: (A) noninterdigitated, nontilted; (B) interdigitated, nontilted; (C) noninterdigitated, tilted.

It is the question if the chains interdigitate and if they are tilted with respect to the normal of the $b-c$ plane. We assume as a basic presupposition that the lateral packing density of the hexyl side chains p_{ch} in the side chain layers must be similar as in polyethylene (PE) or alkane crystals. The corresponding value reflects the intermolecular interaction potential between neighboring $(\text{CH}_2)_n$ chains in all-trans conformation. For PE $p_{ch,PE} \approx 5.44 \text{ nm}^{-2}$, corresponding to two chains per orthorhombic unit cell with lattice parameters $a = 7.42 \text{ \AA}$ and $b = 4.95 \text{ \AA}$. Starting with the assumption of noninterdigitating, nontilted side chains, the corresponding value for P3HT amounts to only about 2/3 of this value, $p_{ch,P3HT} \approx 3.41 \text{ nm}^{-2}$ (2 side chains per unit cell with lattice parameters $b = 7.66 \text{ \AA}$, $c = 7.66 \text{ \AA}$). For interdigitating chains this value would increase by a factor of 2, $p_{ch,P3HT} \approx 6.82 \text{ nm}^{-2}$, i.e. about 25% higher than in PE. Tilting the

side chains leads to increasing values of $p_{ch,P3HT}$ by a factor $\cos \varphi^{-1}$, with φ being the angle between side chain axis and the normal of the b - c plane, i.e.

$$\varphi \approx \arccos \frac{3.41 \text{ nm}^{-2}}{5.42 \text{ nm}^{-2}} \approx 51.0^\circ$$

Taking molecular dimensions into account, this value is compatible with the measured value of the lattice parameter a .

Comparison with Higher Molecular Weights. The observation of the phase transition around 60 °C and the highly ordered crystal structure at room temperature are essential for the structural scheme summarized in Figure 6. As this transition was not clearly observed before in other P3HT materials the question arises how general our results are. On the basis of some additional evidence presented below we think that the phase scheme above is indeed general, but that the phase transition is kinetically hindered for higher molecular weights.

Figure 8 shows a comparison of three DSC heating measurements on P3HT 12, one taken directly after cooling, one after two months of storage at room temperature, and the third corresponding to the first heating of the pristine sample as obtained. While during heating directly after cooling the transition at 60 °C could not be detected, the latter two samples clearly showed a peak indicative of the phase transition. Establishing the correlation between the main chain layers is obviously a slow process for high molecular weight materials; i.e., the phase transition is kinetically hindered. However, the equilibrium state for the high molecular weight sample seems to be the same as for the low molecular weight sample.

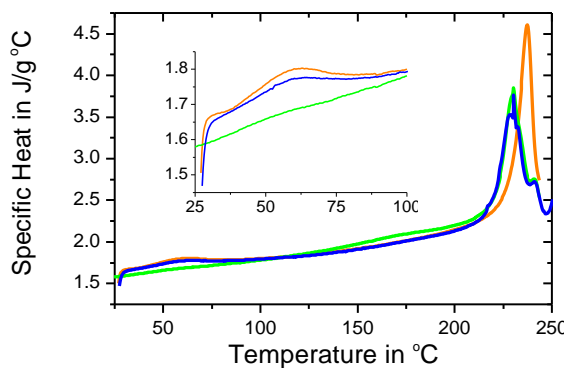


Figure 8: DSC measurements of sample P3HT 12: directly after cooling from the melt (green), after annealing for 2 months at room temperature (blue), and first heating of pristine sample as obtained (orange). The inset shows the range around the phase transition around 60 °C in more detail. For the high molecular weight samples, the phase transition appears only after prolonged storage time at room temperature.

Semicrystalline Morphology. We now turn our attention to the larger scale structure, the semicrystalline morphology. In the crystalline state, oligomers and polymers generally adopt a stretched, often helical conformation and form thin lamellar crystals. For higher molecular weight chain folding sets in. The crystals are separated by amorphous layers consisting of noncrystallizable end groups, folds, or other topological defects. It has been shown that

basically the same phenomena happen for the somewhat stiffer P3HT chains.^{15,24} The materials under study here with their high chemical regularity are of course no exception, as it can be easily visualized by scanning force microscopy (AFM).

Exemplary AFM phase images of P3HT thin films on silicon are shown in Figure 9. For such samples, after heating above the respective melting temperature and subsequent slow cooling the *a*-direction is typically oriented perpendicular to the substrate;²⁵ i.e., in the images the *b-c* plane is visible, showing the typical pattern of lamellar or fibrillar crystals. AFM phase contrast is related to the Fourier transform of the interaction force between tip and sample during approach and penetration of the sample.⁴¹ As the corresponding height images do not show the same pattern and as the surface of the film is chemically uniform, it is obvious that the phase signal reflects mainly the different mechanical properties of crystalline and amorphous parts of the sample. For a sample with hard-soft contrast generally higher values of the phase correspond to the stiffer material.⁴¹ Clearly with increasing molecular weight the thickness of the crystals increased and the arrangement of the crystals became somewhat less well ordered. A direct quantitative determination of the thicknesses of the crystals and the amorphous layers is difficult due to resolution problems.

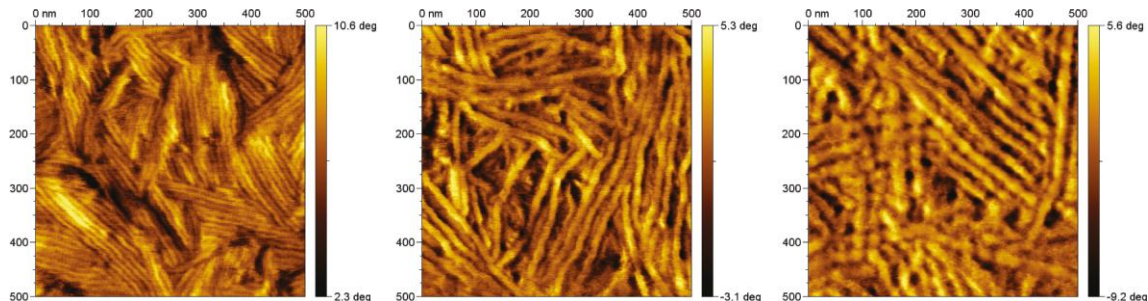


Figure 9: Intermittent contact mode AFM phase images of thin P3HT films of different molecular weight (from left to right: P3HT 3, P3HT 6, P3HT 12).

We tried to correlate these observations to a more quantitative analysis based on DSC and SAXS measurements. Figure 10 shows DSC measurements of all three P3HT samples under study. Additionally a measurement of the commercial sample is shown, data on this sample were already published by Hugger et al.²⁵

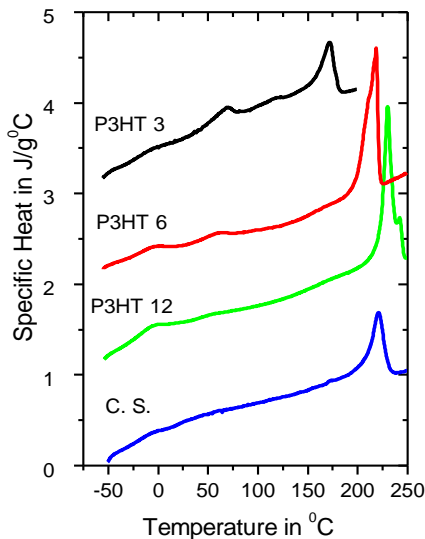


Figure 10: DSC heating curves for all samples (heating rate = 20 K/min, C.S., P3HT 6, P3HT 3 vertically shifted by -1, 1, 2 J/g °C, respectively, with P3HT 12 not shifted).

As already mentioned the phase transition related to side chain melting disappears for the higher molecular weight, but also the transition from the crystalline state to the melt changes. The melting temperature as well as the latent heat of melting increases with increasing molecular weight. The increase of the melting temperature can be explained by the increase of lamellar thickness with increasing molecular weight. This effect is normally well described by the Gibbs-Thomson equation

$$T_m(d) = T_m^\infty \left(1 - \frac{2\sigma}{\Delta h} \frac{1}{d} \right)$$

giving the melting temperature of a lamellar crystal of thickness d . Here T_m^∞ is the equilibrium melting temperature, σ the surface energy, Δh the heat of melting per volume for a 100% crystalline material, and d the thickness of the lamellar crystal.⁵ The observed melting point depression is therefore consistent with the AFM observations. The fact that also ΔH is higher for the samples P3HT 6 and P3HT 12 indicates that not only the crystal thickness but also the crystallinity increases for higher molecular weight; i.e., the thickness of the amorphous layers does not increase in the same way as the crystalline layers. The results of a quantitative analysis of the DSC measurements are given in Table 3.

Table 3: Quantitative Analysis of DSC and SAXS Measurements on P3HT Samples of Different Molecular Weights.

| sample | P3HT 3 | P3HT 6 | P3HT 12 | C.S. |
|--|---------|---------|---------|---------|
| no. of repeating units (thiophene rings) | 20 | 39 | 74 | |
| calculated contour length in nm | 7.7 | 14.9 | 28.3 | |
| DSC | | | | |
| ΔH_m in J/g | 11.3 | 21.1 | 22.4 | 14.7 |
| T-range of integration in °C | 110-186 | 150-228 | 170-248 | 160-237 |
| T_m (peak) in °C | 172 | 216 | 230 | 221 |
| T_m (onset) in °C | 154 | 200 | 223 | 208 |
| SAXS | | | | |
| long period d_l in nm | 9.2 | 14.8 | 27.0 | |

Here the integration for the determination of ΔH comprises the full transition from the crystalline state over the layered phase to the isotropic melt (not for sample C.S.). It is interesting to note that obviously these two transitions (crystalline to layered and layered to isotropic) are both affected by the molecular weight. For the second transition from the layered to the isotropic state this effect is obviously not caused by crystal thickness. If we understand the ordered, layered state as a result of the separation between main and side chains, it is clear that the degree of polymerization of the main chain enters the free energy balance, because $n = Nm$ CH₂ units participate in the demixing (N -degree of polymerization, m -number of alkyl units in side chains per monomer). In this context, it is worthwhile to compare the results obtained for the commercial sample. While the molecular weight is substantially higher, the values for melting temperature and the heat of melting are comparable or lower than for the sample P3HT 12. Obviously neither the crystal thickness nor the crystallinity increases further with molecular weight. Most likely this effect is dominantly caused by the lower regioregularity of C.S.. Additional contributions from the higher polydispersity of C.S. might also contribute. It is wellknown that chemical defects or counits which cannot be built into the crystal structure strongly limit the crystallinity as well as the crystal thickness in semicrystalline polymers. The phase transition from the layered structure to the melt on the other hand is shifted toward higher temperatures outside the range of the measurement,²⁵ as this transition is obviously not as strongly affected by regioregularity. To get more direct quantitative information about the semicrystalline morphology we performed SAXS measurements of the samples P3HT 3, 6, and 12. The data are shown in Figure 11.

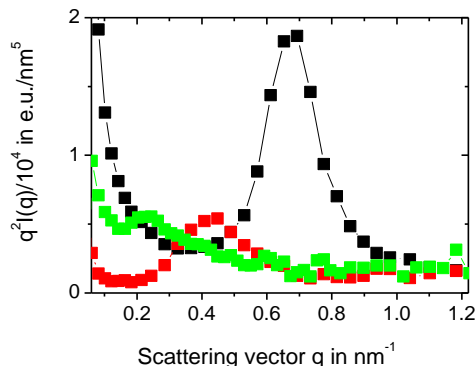


Figure 11: Lorentz corrected SAXS scattering intensity $I(q)q^2$ vs q . The peak position corresponds to the inverse long period $2\pi/d$, (black, P3HT 3; red, P3HT 6; green, P3HT 12).

All three data sets show a peak indicating a periodic arrangement of lamellar crystals. The peak position allows to determine the average long period d of the lamellar stack. As the intensity at higher q is masked by the peak from the (100) reflection, a more quantitative analysis giving d_a and d_c separately⁴² was not successful. Nevertheless already a comparison of the long period and the contour length is instructive. For P3HT 3 d_1 is larger than the contour length, while for the higher molecular weight samples the two values are comparable. This result gives a hint to what causes the small crystallinity of P3HT 3 which is somewhat unexpected, taking into account that normally oligomers form extended chain crystals with very high crystallinity. Although the direct comparison of contour length and long period does not take into account the additional space needed for the side chains, it certainly shows that P3HT 3 forms extended chain crystals. But obviously there is a layer of noncrystallizable material on both sides of the crystals as it is schematically illustrated in Figure 12. In this morphology one end of every chain is not built into the crystal, taking into account the tail-to-tail coupling of the first two units as well as polydispersity effects. Clearly this effect will be present also for higher molecular weights but show up most strongly for P3HT 3. In conclusion P3HT 3, 6, and 12 dominantly form extended chain crystals covered by an amorphous layer of decreasing relative weight for the higher molecular weight materials. Additionally partial chain folding might set in for higher molecular weight, but this is certainly not yet a strong effect in the molecular weight range of our samples.

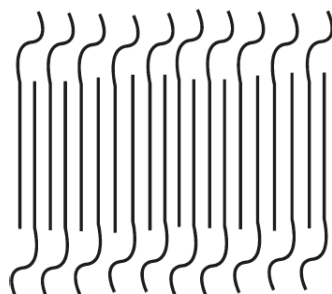


Figure 12: Scheme of lamellar crystal with amorphous layer containing noncrystallizable end groups. The rounded shape of the chains outside the crystals stands for a nonstretched, amorphous conformation, which is of course in reality not the same for all chains.

Conclusions and Outlook

Our measurements demonstrate that by studying a chemically very well-defined P3HT series structural features of the material can be observed which are otherwise hidden and difficult to detect. Using DSC, SAXS, and WAXS for a P3HT with low molecular weight, we were able to determine the temperature dependent phase diagram. There are strong indications that with increasing temperature the following order of structures is general for P3HT: 3D-crystal with ordered main and side chains; regular packing of the main chains in 2D with disordered side-chains; layered structure of separated main and side chains with liquid like packing within the layers; isotropic liquid. For higher molecular weights the first transition at 60 °C, which happens at a temperature relevant for photovoltaic applications, seems to be kinetically hindered. This points to the importance of long time annealing effects. All materials studied are semicrystalline, and the crystallinity increases with molecular weight. While it is unusual that polymers of modest molecular weight, forming extended chain crystals, contain an appreciable fraction of amorphous material, it here has to be taken into account that for synthetic reasons chain ends show a different coupling of the 3-hexylthiophene units and cannot be included into the crystals. This effect becomes less important for higher molecular weights. For the crystallization conditions and samples studied we do not observe strong indications for chain folding. What remains open at this point is a quantitative value for the crystallinity of our samples. It would require a detailed analysis of the scattering pattern in order to separate amorphous and crystalline contributions to the WAXS pattern. Qualitatively the results suggest a crystallinity somewhat below 50% for P3HT3. This estimate questions the often used value for ΔH of 99 J/g deduced in literature from a DSC analysis of crystallization of P3HT in solution.²³ On the basis of this value, we would estimate a crystallinity of only about 10% for P3HT 3, which is hard to reconcile with the qualitative features of the powder WAXS pattern.

Concerning the relation between molecular weight, structure and morphology on one hand and charge transport properties on the other hand, we can draw general conclusions from this work. Certainly P3HT is a complex material, for which the molecular weight, the exact chemical microstructure as well as the thermal history determine structure and morphology. Therefore, one should probably distinguish between fractionated material and polymers resulting from a controlled polymerization as the molecular weight distribution can be still largely different. Furthermore, it is difficult to conclude on the crystallinity from measurements based on thin film samples alone. A well ordered surface pattern does not necessarily mean high crystallinity and X-ray intensities might be strongly affected by orientation effects. Another comment concerns the way how thin films are prepared. In order to determine inherent material properties it is in our view advantageous to look in a first instance at equilibrium structures. The morphology resulting from a process like spin coating or drop casting will in most cases not correspond to equilibrium and will therefore depend on kinetic factors, too. An annealing

step is only expected to lead to equilibrium if the annealing temperature is high enough to ensure sufficient molecular mobility, which will often be related to the phase transition temperature of the corresponding ordering process. Additionally in thin films there might be orientation induced by interfacial interactions or confinement which is important as the electronic properties of P3HT are anisotropic.^{43,44}

Acknowledgment.

We thank M. Beiner for helpful discussions about side chain packing, I. Gunkel for complementary SAXS measurements, C. Eisenschmidt for help with the WAXS measurements and K. Herfurt for technical help with DSC measurements. Furthermore, T.T.-A. is grateful to W. de Jeu for previous discussions about scattering analysis of side chain melting. This work was supported by the DFG-German Science Foundation (SPP 1355) and the state Sachsen-Anhalt. R. L. acknowledges BayEFG for a stipend and the “ENB-Macromolecular Science” study program.

References

- (1) Kim, Y.; Cook, S.; Tuladhar, S.; Choulis, S.; Nelson, J.; Durrant, J.; Bradley, D.; Giles, M.; McCulloch, I.; Ha, C.; Ree, M. *Nat. Mater.* **2006**, 5, 197-203.
- (2) Li, G.; Shrotriya, V.; Huang, J.; Yao, Y.; Moriarty, T.; Emery, K.; Yang, Y. *Nat. Mater.* **2005**, 4, 864-868.
- (3) Kroon, R.; Lenes, M.; Hummelen, J. C.; Blom, P.W. M.; De Boer, B. *Polym. Rev.* **2008**, 48, 531-582.
- (4) Forrest, S. *Nature* **2004**, 428, 911-918.
- (5) Strobl, G. *The physics of polymers: Concepts for understanding their structures and behavior*, 3rd ed.; Springer: Berlin and Heidelberg, Germany, **2007**.
- (6) Bao, Z.; Dodabalapur, A.; Lovinger, A. *J. Appl. Phys. Lett.* **1996**, 69, 4108-4110.
- (7) Ong, B. S.; Wu, Y.; Li, Y.; Liu, P.; Pan, H. *Chem.; Eur. J.* **2008**, 14, 4766-4778.
- (8) DeLongchamp, D. M.; Kline, R. J.; Jung, Y.; Germack, D. S.; Lin, E. K.; Moad, A. J.; Richter, L. J.; Toney, M. F.; Heeney, M.; McCulloch, I. *ACS Nano* **2009**, 3, 780-787.
- (9) Heffner, G. W.; Pearson, D. S. *Macromolecules* **1991**, 24, 6295-6299.
- (10) Jiang, X. M.; Österbacka, R.; Korovyanko, O.; An, C. P.; Horovitz, B.; Janssen, R. A. J.; Vardeny, Z. V. *Adv. Funct. Mater.* **2002**, 12, 587-597.
- (11) Winokur, M. J.; Spiegel, D.; Kim, Y. H.; Hotta, S.; Heeger, A. J. *Synth. Met.* **1989**, 28, 419-426.
- (12) McCullough, R. D.; Tristramnagle, S.; Williams, W. P.; Lowe, R. D.; Jayaraman, M. *J. Am. Chem. Soc.* **1993**, 115, 4910-4911.
- (13) Prosa, T. J.; Winokur, M. J.; Moulton, J.; Smith, P.; Heegert, A. J. *Macromolecules* **1992**, 25, 4364-4372.
- (14) Tashiro, K.; Ono, K.; Minagawa, Y.; Kobayashi, M.; Kawai, T.; Yoshino, K. *J. Pol. Sci. Part B: Polym. Phys.* **1991**, 29, 1223-1233.
- (15) Brinkmann, M.; Rannou, P. *Adv. Funct. Mater.* **2007**, 17, 101-108.
- (16) Joshi, S.; Grigorian, S.; Pietsch, U. *Adv. Funct. Mater.* **2002**, 12, 587-597.
- (17) Yamamoto, T.; Komarudin, D.; Arai, M.; Lee, B.-L.; Suganuma, H.; Asakawa, N.; Inoue, Y.; Kubota, K.; Sasaki, S.; Fukuda, T.; Matsuda, H. *J. Am. Chem. Soc.* **1998**, 120, 2047-2058.
- (18) Mena-Osteritz, E.; Meyer, A.; Langeveld-Voss, B. M. W.; Jassen, R. A. J.; Meijer, E. W.; Baeuerle, P. *Angew. Chem., Int. Ed.* **2000**, 39, 2679-2684.
- (19) Kline, R. J.; DeLongchamp, D. M.; Fischer, D. A.; Lin, E. K.; Richter, L. J.; Chabinyc, M. L.; Toney, M. F.; Heeney, M.; McCulloch, I. *Macromolecules* **2007**, 40, 7960-7965.
- (20) Park, K. C.; Levon, K. *Macromolecules* **1997**, 30, 3175-3183.
- (21) Liu, S. L.; Chung, T. S. *Polymer* **2000**, 41, 2781-2793.
- (22) Causin, V.; Marega, C.; Marigo, A.; Valentini, L.; Kenny, J. M. *Macromolecules* **2005**, 38, 409-415.
- (23) Malik, S.; Nandi, A. J. *Polym. Sci., Part B: Polym. Phys.* **2002**, 40, 2073-2085.

- (24) Brinkmann, M.; Wittmann, J.-C. *Adv. Mater.* **2006**, 18, 860-863.
- (25) Hugger, S.; Thomann, R.; Heinzel, T.; Thurn-Albrecht, T. *Colloid Polym. Sci.* **2004**, 282, 932-938.
- (26) Street, R. *Nat. Mater.* **2006**, 5, 171-172.
- (27) Kline, R.; McGehee, M.; Kadnikova, E.; Liu, J.; Fréchet, J. *Adv. Mater.* **2003**, 15, 1519-1522.
- (28) Kline, R. J.; McGehee, M. D. *Macromolecules* **2005**, 38, 3312-3319.
- (29) Verilhac, J.-M.; LeBlevennec, G.; Djurado, D.; Rieutord, F.; Chouiki, M.; Travers, J.-P.; Pron, A. *Synth. Met.* **2006**, 156, 815-823.
- (30) Zhang, R.; McCullough, R. D. *J. Am. Chem. Soc.* **2006**, 128, 3480-3481.
- (31) Zen, A.; Pflaum, J.; Hirschmann, S.; Zhuang, W.; Jaiser, F.; Asawapirom, U.; Rabe, J.; Scherf, U.; Neher, D. *Adv. Funct. Mater.* **2004**, 14, 757-764.
- (32) Zen, A.; Saphiannikova, M.; Neher, D.; Grenzer, J.; Grigorian, S.; Pietsch, U.; Asawapirom, U.; Janietz, S.; Scherf, U.; Lieberwirth, I.; Wegner, G. *Macromolecules* **2006**, 39, 2162-2171.
- (33) Brinkmann, M.; Rannou, P. *Macromolecules* **2009**, 42, 1125-1130.
- (34) Strobl, G. R. *Acta Crystallogr.* **1970**, A26, 367-375.
- (35) Sheina, E. E.; Liu, J.; adn D. W. Laird, M. C. I.; McCullough, R. D. *Macromolecules* **2004**, 37, 3526-3528.
- (36) Holdcroft, S. *J. Polym. Sci., Part B: Polym. Phys.* **1991**, 29, 1585-1588.
- (37) Miyakoshi, R.; Yokoyama, A.; Yokozawa, T. *J. Am. Chem. Soc.* **2005**, 127, 17542-17547.
- (38) Chen, T.; Rieke, R. D. *J. Am. Chem. Soc.* **1992**, 114, 10087-10088.
- (39) Barbarella, G.; Bongini, A.; Zambianchi, M. *Macromolecules* **1994**, 27, 3039-3045.
- (40) Prosa, T. J.; Winokur, M. J.; McCullough, R. D. *Macromolecules* **1996**, 29, 3654-3657.
- (41) Schröter, K.; Petzold, A.; Henze, T.; Thurn-Albrecht, T. *Macromolecules* **2009**, 42, 1114-1124.
- (42) Albrecht, T.; Strobl, G. *Macromolecules* **1995**, 28, 5827-5833.
- (43) Yang, H.; LeFevre, S. W.; Ryu, C. Y.; Bao, Z. *Appl. Phys. Lett.* **2007**, 90, 172116.
- (44) Kline, J.; McGehee, M.; Toney, M. F. *Nat. Mater.* **2006**, 5, 222-228.

5. On the Control of Aggregate Formation in Poly(3-hexylthiophene) by Solvent, Molecular Weight and Synthetic Method

Christina Scharsich¹, Ruth Lohwasser², Michael Sommer², Udom Asawapirom^{3§}, Ullrich Scherf³, Mukundan Thelakkat², Dieter Neher⁴ and Anna Köhler^{1*}

¹ Organic Semiconductors, Experimental Physics II, Department of Physics,
University of Bayreuth, Bayreuth 95440, Germany.

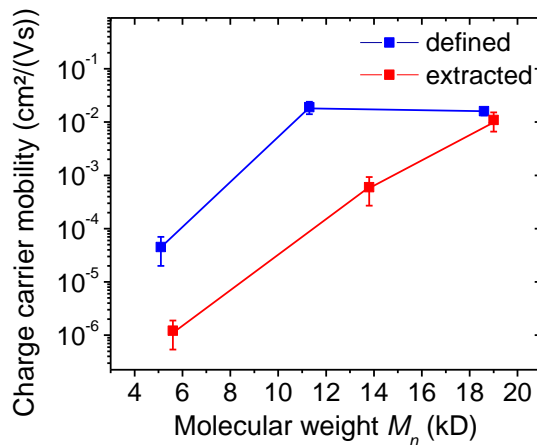
² Applied Functional Polymers, Macromolecular Chemistry I, Department of Chemistry,
University of Bayreuth, Bayreuth 95440, Germany

³ Macromolecular Chemistry, Bergische Universität Wuppertal, Wuppertal 42097, Germany

⁴ Soft Matter Physics, Institute of Physics and Astronomy, University of Potsdam,
Potsdam 14476, Germany

[§] National Nanotechnology Center (NSTDA), 130 Thailand Science Park, Phahonyothin Rd.,
Klong 1 Klong Luang, Pathumthani 12120, Thailand

*E-mail corresponding author: anna.koehler@uni-bayreuth.de



Abstract

Aggregate formation in poly(3-hexylthiophene) depends on molecular weight, solvent and synthetic method. The interplay of these parameters thus largely controls device performance. In order to obtain a quantitative understanding on how these factors control the resulting electronic properties of P3HT, we measured absorption in solution and in thin films as well as the resulting field effect mobility in transistors. By a detailed analysis of the absorption spectra we deduce the fraction of aggregates formed, the excitonic coupling within the aggregates and the conjugation length within the aggregates, all as a function of solvent quality for molecular weights from 5 kD to 19 kD. From this we infer in which structure the aggregated chains pack. While the 5 kD samples form straight chains, the 11 kD and 19 kD chains are kinked or folded, with conjugation lengths that increase as the solvent quality reduces. There is a maximum fraction of aggregated chains (about 55±5 %) that can be obtained, even for poor solvent quality. We show that inducing aggregation in solution leads to control of aggregate properties in thin films. As expected, the field-effect mobility correlates with the propensity to aggregation. Correspondingly, we find that a well-defined synthetic approach, tailored to give a narrow molecular weight distribution, is needed to obtain high field effect mobilities of up to $0.01 \text{ cm}^2/\text{Vs}$ for low molecular weight samples ($\leq 11 \text{ kD}$), while the influence of synthetic method is negligible for samples of higher molecular weight, if low molecular weight fractions are removed by extraction.

Introduction

The optical and electronic properties of regioregular poly(3-hexylthiophene) (rrP3HT) are relevant for many applications in the field of organic semiconductors such as solar cells and field-effect transistors. Regioregular P3HT is known to show high mobilities that provide promising application on the industrial level.¹⁻⁴ For this reason, the focus is often placed in the charge carrier mobility in P3HT thin films. It is well-known that several parameters affect the charge carrier mobility, such as the degree of crystallization, the molecular weight of P3HT chains and the intermolecular coupling between these chains.⁴⁻⁷ Especially, the aggregation of polymer chains plays an important role in the performance of organic field effect transistors (OFETs) and organic solar cells.⁸ Indeed, the number and the nature of the aggregates is of central importance for these applications. Properties such as conjugation length, intermolecular coupling within the aggregates as well as the packing behavior of the polymer chains and disorder affect the applicable optic and electronic properties of P3HT.⁹⁻¹¹ Another important parameter is the polydispersity of the polymer chains which depends strongly on the synthetic approach. It was shown that low molecular weight polythiophene with low polydispersity forms highly ordered structures in thin films.¹² Despite investigations on phase control in polymer films, the relation between molecular weight, polydispersity and aggregation behavior of chains is still not fully understood.¹³

Here, we investigate the effect of molecular weight as well as the effect of synthetic approach to P3HT on the aggregate formation. We obtain information on the fraction of aggregates and on the packing behavior of P3HT chains within aggregates by combining spectroscopic methods with the theoretical works by Spano and Gierschner et al.^{9,11} Furthermore, we observe variations in excitonic coupling within P3HT aggregates and use this information to clarify to which extent the results obtained in solution can be transferred to P3HT thin films. We find that the synthetic approach affects the packing behavior of P3HT chains with low molecular weight. A synthesis defined to a specific molecular weight results in more accurate aggregates in both solution and thin films and thus in better FET performance. When going to higher molecular weights, these differences disappear which implies that specific synthetic approaches to obtain defined high molecular weights, such as catalyst transfer polymerization, are not necessary. The early McCullough route with subsequent extraction of low molecular weight fractions is sufficient to obtain comparable performances.

Experimental Methods

The poly(3-hexylthiophene) samples differ in molecular weight and belong to two groups of different synthetic approach. The first group of poly(3-hexylthiophene)s was synthesized according to the catalyst transfer polymerization reaction method.^{14,15} These compounds, listed in Table 1, were tailor-made to their specific molecular weight. They have a very sharp molecular mass distribution and thus a very low polydispersity index (PDI). The number-average molecular weights (M_n) and the weight-average molecular weights (M_w) were measured by two methods. We used gel permeations chromatography (GPC) in tetrahydrofuran (THF) with polystyrene as calibration standard as well as matrix-assisted laser desorption ionization-time of flight mass spectroscopy (MALDI-TOF MS). Both methods are known to be associated with some experimental error. The molecular weight determined by MALDI-TOF MS is significantly lower than the one obtained from GPC measurements, since calibration against the polystyrene standard overestimates the molecular weight of rigid polymers.¹⁶ The degree of polymerization, DP, refers to the number of repeat units and it is derived from the molecular weight as determined by MALDI-TOF, though we note that an uncertainty of about 2 repeat units remains. Throughout this paper, the compounds in this group are referred to as “defined P3HT”.

The second group of poly(3-hexylthiophene)s was synthesized according to the original McCullough route¹⁷ that does not allow for molecular weight control and that leads to broad molecular weight distributions.¹⁸ In order to obtain different molecular weight samples, the initial molecular mass distribution was fractionated with different solvents as listed in Table 2. Molecular mass distributions of the different samples were again obtained via GPC measurements with polystyrene standard. The compounds from this group are below referred to as “extracted P3HT”. We consider the average degree of polymerization of each extracted

compound to be similar to the DP of the corresponding defined compounds since the M_n values of the defined and extracted samples are comparable in pairs.

Table 1: Molecular weights (MW) of defined P3HTs directly synthesized to get well-controlled molecular weights (M_n , number-average molecular weight; M_w , weight-average molecular weight; PDI= M_w/M_n , polydispersity index; DP, degree of polymerization, i.e. the number of repeating units).

| Poly(3-hexylthiophene) | M_n [g/mol] | M_w [g/mol] | PDI | M_n [g/mol] | DP |
|------------------------|------------------|------------------|------|------------------|--------------|
| Based on | GPC | GPC | GPC | MALDI-TOF MS | MALDI-TOF MS |
| 5 kD | 5100 | 6300 | 1.22 | 3200 | 19 |
| 11 kD | 11300 | 15200 | 1.11 | 7100 | 43 |
| 19 kD | 18600 | 21600 | 1.16 | 12400 | 74 |

Table 2: Poly(3-hexylthiophene) fractionated from a broad molecular mass distribution sample with different solvents. Molecular weights measured with GPC (M_n , number-average molecular weight; M_w , weight-average molecular weight; PDI= M_w/M_n , polydispersity index).

| Poly(3-hexylthiophene) fractionated with | M_n [g/mol] | M_w [g/mol] | PDI |
|---|------------------|------------------|------|
| Hexane | 5600 | 6600 | 1.18 |
| Dichloromethane | 13800 | 20400 | 1.48 |
| Chloroform | 19000 | 25600 | 1.35 |

Solutions were prepared from a ratio of good to moderately poor solvents, denoted subsequently as A:B, where A gives the volume fraction of good solvent and B the corresponding volume fraction of poor solvent, each as percent. Both solvents had a similar boiling point (bp) to eliminate different behaviors of volatilization. The good solvent for all compounds was chloroform (CHCl_3) ($\text{bp} = 61^\circ\text{C}$), whereas the moderately poor solvent was ethyl acetate (EtAc) ($\text{bp} = 77^\circ\text{C}$). Since both boiling points are close enough, only the influence of solubility was studied. The worse solubility of P3HT in ethyl acetate results from its slightly higher polarity as compared to chloroform. The difference in hildebrandt solubility parameter is not large ($9.10 \text{ cal}^{0.5} \text{ cm}^{-1.5}$ for EtAc vs $9.21 \text{ cal}^{0.5} \text{ cm}^{-1.5}$ for CHCl_3), yet it is sufficient to induce planarization (as evidenced further below by the absorption spectra). Importantly, the solubility of P3HT in the solvent mixtures at room temperature remains sufficiently high to ensure that the solution remains visibly clear, without any noticeable changes in the absorption spectra over a period of 24 hours. This is necessary to ensure the absorption spectra are not altered due to the effects of light scattering or changes of concentration due to a fall-out of larger aggregates. While the solutions do not change on the time scale of our experiments, they are not in thermal equilibrium, as detailed in the supporting information (SI). This is in agreement with findings by Xu et al. on solvent-induced crystallization of related poly(thiophene)s using a mixture of chlorobenzene (solvent) and anisole (poor solvent).¹⁹

All solutions within one series had the same concentration. The defined compounds were studied at a concentration of 0.25 mg/mol, whereas the solutions of the extracted P3HT

samples had a concentration of 0.10 mg/mol. For each molecular weight of the defined compounds, additional absorption measurements have also been carried out on a few samples at a concentration of 0.10 mg/mol. This control experiment confirmed that the slight difference in concentration between the two series does not have any significant effect. In order to keep the concentrations within each series constant, every single solution within each solution series was prepared separately in new and isopropanol-rinsed dark sample glasses. Thereby, the P3HT was first completely dissolved in CHCl₃ before the fraction of EtAc, the poor solvent, was added. The absorption of the solutions was measured in 1 mm-quartz cuvettes with a Varian Carry UV/Vis spectrometer in a standard double-beam transmission alignment. The absorption of thin films was measured with the same Varian Carry UV/Vis spectrometer by means of the diffuse reflectance accessory (integrating sphere). P3HT films were spin coated from solution with a concentration of 15 mg/ml at a constant speed of 1500 rpm on Spectrosil B, a silica glass substrate. Prior to spin coating the substrate was cleaned with common solvents such as acetone and isopropanol.

Organic field effect transistors were prepared in a bottom-gate, top-source/drain geometry under nitrogen atmosphere from solutions with a concentration of 10 mg/ml. The substrates were n-doped silicon plates with a grown layer of insulating silicon dioxide of approximately 300 nm thickness. Substrates were silanized using hexamethyldisilazane (HDMS) vapor for 1 h at 90 °C and 3 h at 60 °C. Prior to silanization, the substrate surface was cleaned thoroughly with several common solvents and treated with oxygen plasma for 5 min at a power of 200 W. Thereafter, the substrates were annealed under nitrogen atmosphere at 130 °C for 1 h and cooled down slowly to room temperature. After spin coating, 100 nm thick gold electrodes were evaporated on top of the P3HT layer. The resulting field effect transistors had a channel width $W = 14.85$ cm, a channel length $L = 100$ μm and a capacitance of the insulating layer per unit area $C_i = 11.9$ nF/cm². The charge carrier mobilities were determined from a plot of the square root of the drain current in the saturation regime using

$$I_{DS,sat} = \frac{WC_i}{2L} \mu_{sat} (V_G - V_T)^2$$

with V_T being the threshold voltage.

Results

Figure 1 shows the absorption of rrP3HT in solutions of constant concentration. The solvent was a mixture of chloroform and ethyl acetate with increasing ratios of ethyl acetate. The latter is a moderately poor solvent for P3HT and is thus used to induce planarization/aggregation. Measurements were done for samples of three different molecular weights and made by two different synthetic approaches: rrP3HTs directly synthesized to get a specific molecular weight (5 kD, 11 kD and 19 kD) and rrP3HT extracted from a large molecular mass distribution to get different molecular weight fractions (6 kD, 14 kD and 19 kD).

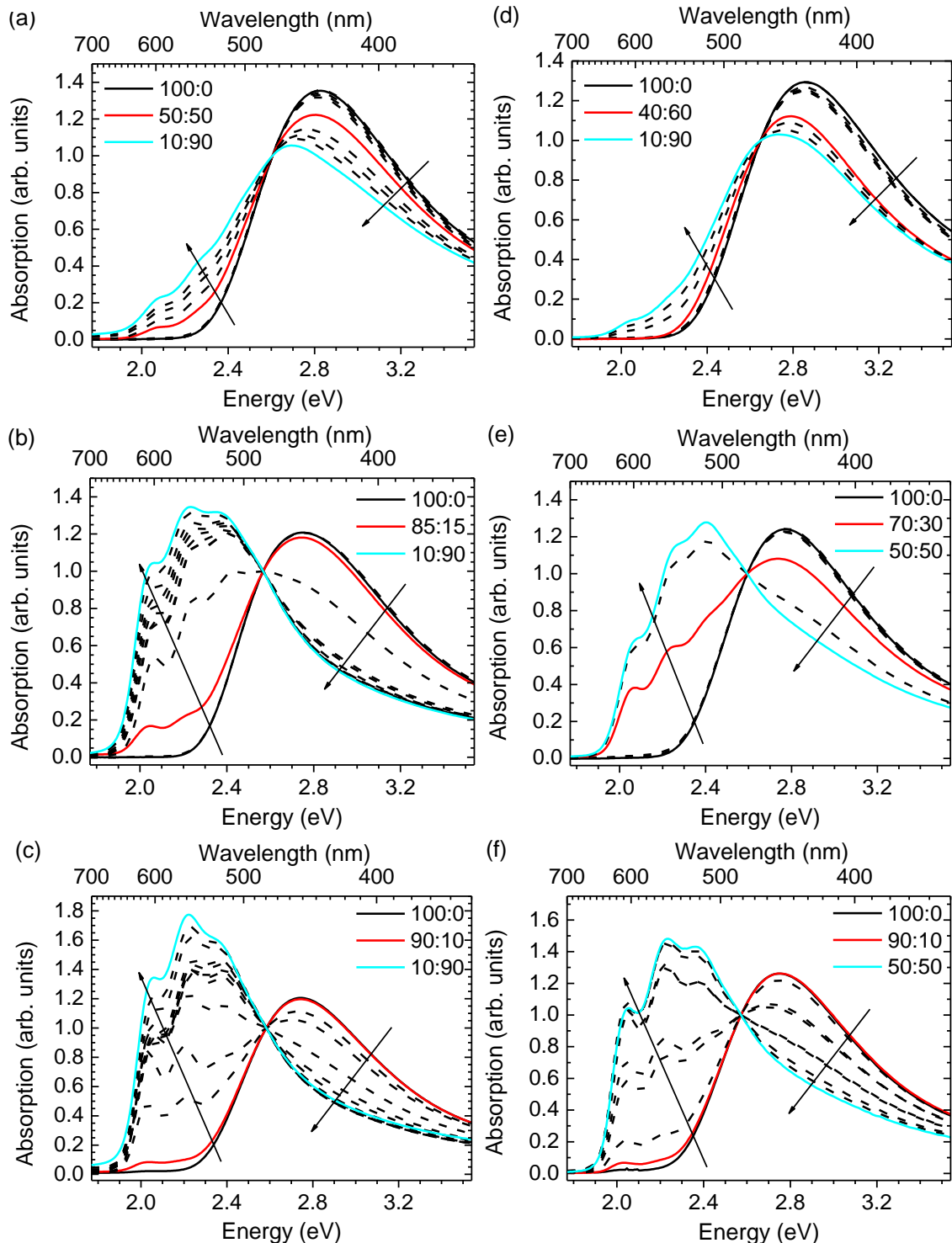


Figure 1: Absorption spectra of solutions with ratios of good:poor solvent ($\text{CHCl}_3:\text{EtAc}$). Dashed lines show increments of about 10% of poor solvent. Solutions with maximum and minimum fraction of good solvent used are indicated as black and blue solid line, respectively. The red solid line highlights the solvent fraction at which the onset of aggregation takes place. Adjacent graphs show samples of comparable molecular weight. Left column: Defined P3HTs with molecular weight (a) 5 kD, (b) 11 kD, (c) 19 kD. Right column: Extracted P3HTs with molecular weight (d) 6 kD, (e) 14 kD, (f) 19 kD.

For both, defined and extracted P3HT samples, we observe two absorption features, an unstructured peak centered around 2.80 eV and a band with structure at lower energy (three peaks at about 2.05 eV, 2.20 eV and 2.40 eV). The low-energy band increases in intensity with increasing fraction of poor solvent. Simultaneously, the ratio of the 0-0 vibrational peak at 2.05 eV to the 0-1 vibrational peak at 2.20 eV changes. With increasing molecular weight, the contribution of the low energy band to the overall spectrum increases. Furthermore, the high-energy band shifts slightly from 2.85 eV to 2.75 eV when going from 5 kD/6 kD to higher molecular weights. In contrast to the defined P3HT, the absorption of the high-energy band of the extracted P3HT with 6 kD shifts to lower energies (2.80 eV) with increasing fraction of poor solvent before the low-energy band appears. The high-energy band has been identified as arising from coiled chains that form amorphous regions. The structured low-energy band is associated with absorption from planar chains that form weakly interacting H-aggregates.^{6,9} While these spectra contain absorption due to both, aggregated and coiled chains, it is possible to extract the absorption spectra of the aggregated chains. As detailed in the supporting information (SI), this is obtained by taking the spectra obtained in 100% chloroform solution where the chains are fully dissolved and coiled, scaling it to the high-energy shoulder of the solution spectra containing the absorption of aggregated and coiled chains, and subtracting it. We have also deduced the relative oscillator strength that describes the change in oscillator strength when going from a non-planar chain as present in solution to a planar polymer chain in the aggregate, using the approach by Clark et al.²⁰ This procedure is described further in the SI.

When the change in oscillator strength is known, the fraction of aggregated chains in the solution (as a total of the overall number of chains) can be derived from the fraction of absorption due to aggregated chains. This is shown in Figure 2. We observe that, for the defined P3HT sample with 5 kD, aggregation starts at 50% of poor solvent and increases linearly with decreasing solvent quality up to a fraction of 35% of aggregates. The difference to the extracted sample with comparable molecular weight is considerable. The latter does not aggregate below 70% of poor solvent and reaches only a fraction of 10% of aggregates at 90% of ethyl acetate. For the samples with 11 kD and 14 kD, respectively, the aggregation starts much earlier. The defined sample shows aggregation at 15% of poor solvent and higher. Its fraction of aggregates increases steeply and reaches a saturation value of about 55%. Whereas the extracted sample with 14 kD starts to aggregate at 20% of poor solvent and shows fraction of aggregates below the defined sample. For the 19 kD samples from the defined and extracted synthetic approaches, aggregation starts at 10% of poor solvent and reaches as well a maximum value of about 50%. No difference in aggregate fraction between the defined and extracted P3HT with 19 kD can be seen. The interesting feature to note is that for none of the samples the fraction of aggregated chains exceeds 55%, even when 90% ethyl acetate is used. In other words, a substantial part of the chains remains dissolved. A 100% ethyl acetate

solution becomes turbid, indicating the formation of larger aggregated structures. The earlier onset of aggregation for P3HT with higher molecular weight, i.e. longer chains, is consistent with Flory-Huggins theory that predicts less solubility for longer polymer chains.²¹

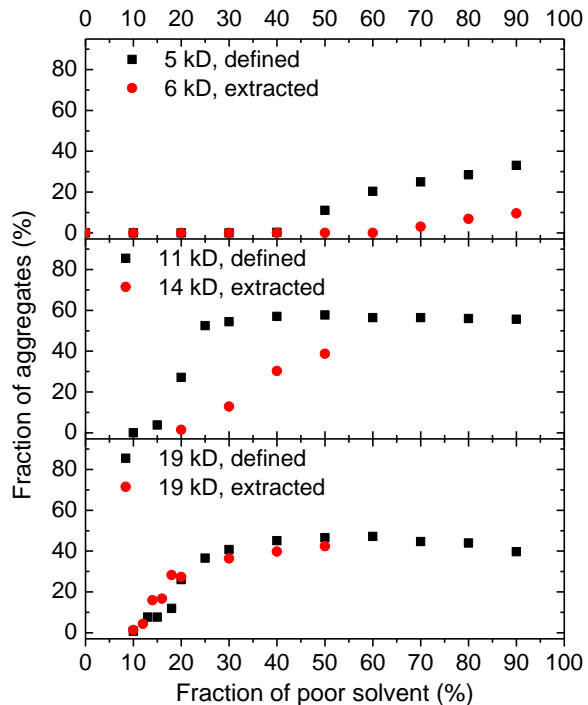


Figure 2: The fraction of aggregates present in solution as a function of poor solvent fraction for defined and extracted P3HT. The molecular weight increases from top to bottom.

From Figure 2 it is evident that a substantial fraction of the chains forms aggregates in solution. It is known that such aggregates that are present in solution can later serve as nucleation points for aggregate formation in the film when prepared by spin-coating.¹³ To get a more thorough understanding on the nature of these aggregates, we now consider the spectral shape of the aggregate absorption. The aggregate absorption (derived as outlined in the SI), normalized to 0-1 peak, is shown in Figure 3 for the defined P3HT samples. Very similar spectra can be obtained for the extracted samples. From Figure 3 we see ,first, that the relative height of the 0-0 absorption peak increases with molecular weight. Second, the ratio of the 0-0 to 0-1 absorption peak changes significantly with solvent quality. For the 5 kD sample the 0-0 intensity increases with increasing fraction of poor solvent. For the 11 kD and 19 kD sample the 0-0 intensity first increases and then decreases with increasing fraction of ethyl acetate. The absorption spectra of the weakly interacting H-aggregates can be analyzed in a framework for excitonic coupling in weakly interacting H-aggregates that has been developed by Spano.^{9,22} According to this model, the relative height of the 0-0 peak is a measure for the degree of excitonic coupling present in the aggregate. The very high 0-0 peak (0-0/0-1 ratios larger than unity) observed for the 19 kD sample at 90:10 EtAc:CHCl₃ mixtures (red line in Figure 3) thus implies excitonic coupling is largely absent, even though the chain

must adopt conformations that are already partially planarized as evidenced by the low energy of the 0-0 peak. In contrast, excitonic coupling is particularly strong for the 50:50 mixture (black line) and then reduces somewhat when adding more ethyl acetate. Quantitatively, the 0-0/0-1 absorption peak ratio relates to the excitonic coupling J as follows

$$\frac{A_{0-0}}{A_{0-1}} = \frac{n_{0-0}}{n_{0-1}} \frac{\left(1 - \frac{J}{\omega_0} e^{-s} \sum_{v>0} \frac{S^v}{v!v}\right)^2}{S \left(1 - \frac{J}{\omega_0} e^{-s} \sum_{v\neq1} \frac{S^v}{v!(v-1)}\right)^2}$$

where S is the Huang Rhys parameter of the single emitter and ω_0 is its effective vibrational energy, n_{0-0} and n_{0-1} refer to the refractive index at the position of A_{0-0} and A_{0-1} . To allow for an exact analysis, we have taken photoluminescence spectra and applied a Franck-Condon analysis in order to derive S and ω_0 . Through this analysis we found S to be 0.90 (5 kD sample) and 0.84 (11 and 19 kD samples) and ω_0 to be 1390 cm^{-1} . Full details of the Franck-Condon analysis are given as supporting information.

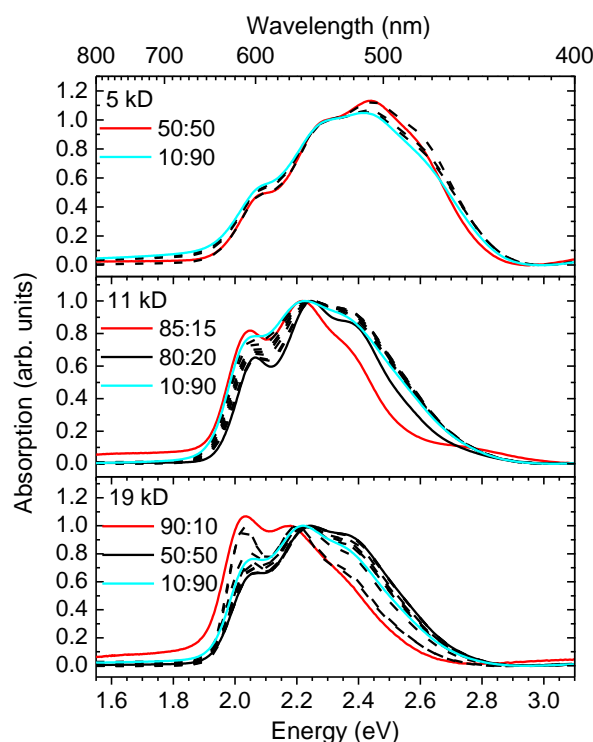


Figure 3: The absorption spectra of aggregates in solutions of defined P3HT. The spectra are normalized to the second absorption peak and presented for different fractions of poor solvent. The given ratios denote the volume fractions of good:poor solvent ($\text{CHCl}_3:\text{EtAc}$). The dashed lines show increments of about 10% of poor solvent. Red and blue lines indicate samples with the minimum and maximum amount of poor solvent used. With increasing fraction of poor solvent, the relative intensity of the second absorption peak decreases up to the fraction indicated by the black line. From then onwards, it increases again. The molecular weight increases from top to bottom.

Using this approach, we obtained the excitonic couplings shown in Figure 4. We first consider the defined P3HT samples. For all compounds, we observe an initial rise of the excitonic coupling up to a peak followed by a decrease. For the 5 kD sample, the rise is not visible, only the decrease. For the extracted P3HT samples with 6 kD and 14 kD, the excitonic coupling is slightly higher than for the comparable defined samples, whereas the defined and extracted samples with 19 kD show no significant difference in excitonic coupling. The excitonic coupling within the P3HT aggregates depends clearly on the fraction of the poor solvent and thus on solvent quality. We attribute this to a conjugation length dependence of the excitonic coupling. It is well-known that the strength of intermolecular coupling is related to the extent of the conjugated system. The breakdown of the point-dipole model for polymers is due to extended conjugations. While for a point-dipole, the coupling between chains increases with conjugation length, this is not the case for very extended π -systems. Thus, a longer conjugation length implies a lower excitonic coupling and vice versa.¹⁰

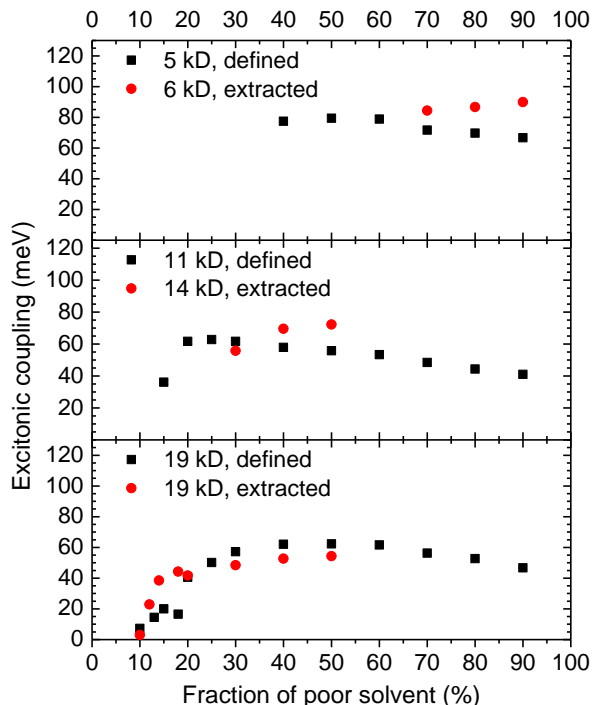


Figure 4: The excitonic coupling as function of poor solvent fraction for aggregates of defined and extracted P3HTs. The molecular weight increases from top to bottom. The excitonic coupling is calculated from the ratio of the first two absorption peaks according to Spano's model⁹ for weakly interacting H-aggregates.

By means of the theoretical work of Gierschner et al. who calculated the excitonic coupling in thiophene-based conjugated polymers as a function of repeating units, we derive the conjugation lengths within the aggregates of the defined and extracted P3HT as a function of poor solvent fraction.¹¹ The excitonic coupling in regioregular P3HT is lower than the coupling in polythiophene without any side chains calculated by Gierschner et al.. This leads to an overestimation of the conjugation length in rrP3HT which was corrected by a factor of 0.8. This

factor takes into account that the conjugation length of the 5 kD sample cannot exceed the degree of polymerization of the polymer chains known from MALDI-TOF MS. Figure 5(a) shows the resulting conjugation length as a function of poor solvent for defined and extracted P3HT samples. In addition, the corresponding position of the 0-0 absorption peak, taken from Figure 3, as well as the ratio of the first two absorption peaks is presented in Figure 5(b).

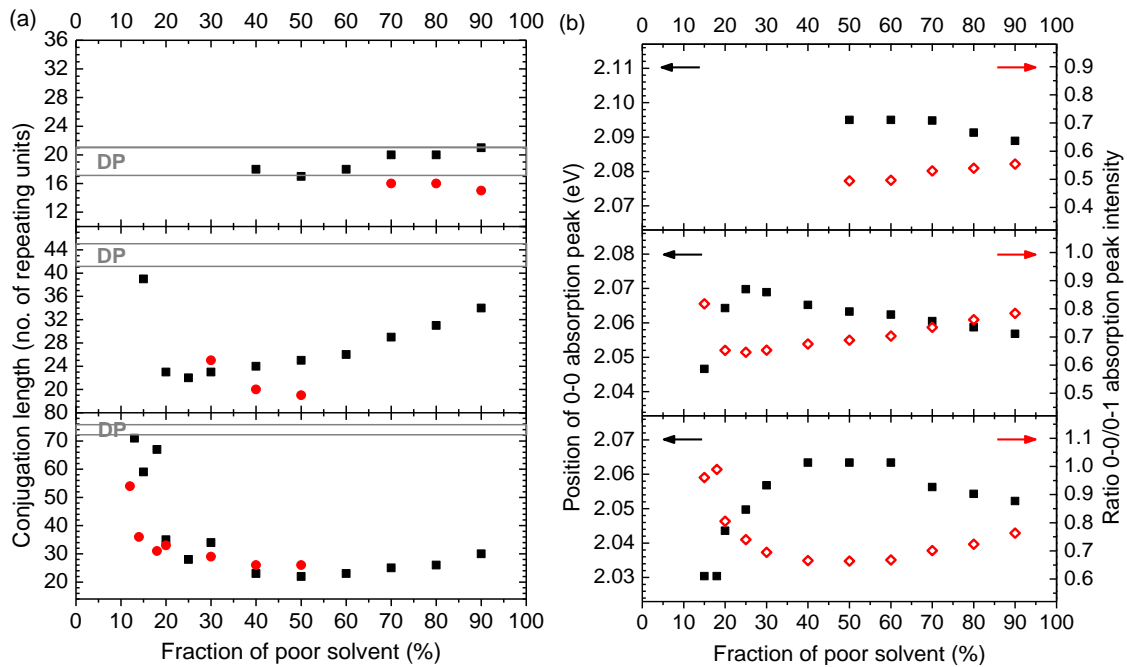


Figure 5: (a) The conjugation length derived from the excitonic coupling for chains of defined (black squares) and extracted (red circles) P3HT, given as the number of thiophene repeating units. The grey bar indicates the degree of polymerization, determined from MALDI-TOF with an error of ± 2 repeat units, for reference. The molecular weight increases from top to bottom showing the pairs of 5 kD/6 kD, 11 kD/14 kD and 19 kD/19 kD. (b) The position of the 0-0 absorption peak (black symbols) and the ratio of the first to absorption peaks (red symbols) as a function of poor solvent fraction for the extracted P3HT samples with $M_n = 5$ kD (top), 11 kD (center) and 19 kD (bottom).

We find that the 5 kD/6 kD samples have more or less constant conjugation lengths with increasing fraction of poor solvent, and that the extracted sample shows a shorter conjugation length than the defined P3HT sample. The defined samples with 11 kD and 19 kD show a minimum conjugation length at 25% and 50% of poor solvent, respectively, followed by a steady increase of conjugation length with decreasing solvent quality. Whereas the extracted sample with 19 kD shows a similar behavior to the 19 kD defined sample, the conjugation lengths of the 14 kD extracted sample has again a shorter conjugation length than the 11 kD defined sample. To assess the correlation to the degree of polymerization (DP), relative DP values were calculated from MALDI-TOF molecular weights. We like to point out that the 5 kD/6 kD samples show conjugation lengths in the region of their degree of polymerization, whereas the samples with higher molecular weight form aggregates whose conjugation length is much lower than their degree of polymerization in the saturation region of the fraction of aggregates. Moreover, the positions of the 0-0 absorption peaks correlate nicely with the

conjugation lengths calculated from the excitonic coupling, given by the ratio of the 0-0/0-1 absorption peak intensity, that is, the position of the first absorption peak shifts to maximum energy for solutions where the conjugation length calculated from the vibrational intensities is at a minimum. We note that these are two independently derived quantities.

From our investigations we know the fraction of aggregates (Figure 2), their conjugation length (Figure 5) and the degree of polymerization. Thus it is possible to infer information about the conformation of the aggregates. Our conclusions about the resulting conformations of the defined P3HT samples are summarized in Figure 6.

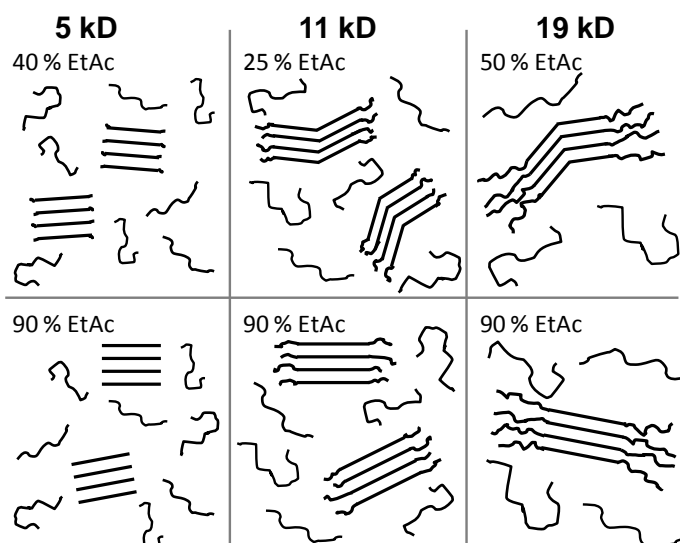


Figure 6: Possible scenarios for the packing behavior of defined P3HT chains for different molecular weights and different fractions of poor solvent.

For the 5 kD sample, we consider the polymer chains within the aggregates to be completely planarized and conjugated. The aggregates coexist with still dissolved chains in the solution even when 90% of poor solvent is used. This picture is based on the fact that the conjugation length derived from the spectral analysis corresponds to the degree of polymerization obtained by the MALDI-TOF MS. Additionally, it is supported by a moderate fraction of aggregates which does not saturate for high amount of poor solvent. The still dissolved chains are likely to be the shorter ones in the overall distribution.

For the 11 kD and 19 kD samples, there are some key features to be noticed. In all cases the length of the conjugated segments is shorter than the total degree of polymerization (see Figure 5a). Thus in principle, a polymer chain may comprise of one planarized segments and additional coiled segments or several planarized segments which are separated. This separation may be caused by coiled segments or simply by twists, kinks or folds.

Keeping this in mind we now consider the 11 kD sample for 25% of poor solvent and more. At 25% of poor solvent, the conjugation length for each conjugated segment is about 22 repeating units which correspond to 50% of the degree of polymerization. In principle, this still allows one or two conjugated segments in one polymer chain. When increasing the fraction of

poor solvent, the conjugation length enlarges up to 34 repeating units being 80% of the DP. This implies that for higher amounts of poor solvents there is only one conjugated segment for each chain within the aggregates. On the other hand, the fraction of aggregates does not enlarge equally with the conjugation length but remains constant at (55±5)%.

We now consider two scenarios.

(i) If we assume that, at 25% of poor solvent, there is only one planarized segment per chain then 50% of each chain within the aggregates is still dissolved. Overall, the solution consists of (55±5)% aggregated segments with the remainder being dissolved segments. In this scenario, the dissolved segments are then formed by half of each chain within the aggregates and some additional fully dissolved chains. Let us now consider a fraction of 90% of poor solvent in this scenario. At 90% of poor solvent, 80% of each chain within the aggregates is conjugated. Thus, only 20% of each chain within the aggregates can contribute to the fraction of dissolved segments in the solution. Compared to the situation with 25% of poor solvent, the overall fraction of aggregated segments in solution, and thus also of dissolved segments in solution, has not changed. Since only 20% of each chain within the aggregates are dissolved, there must be more fully dissolved chains in the solution to make up the same total fraction of dissolved segments in solution than at 20% of poor solvent. An increase in the number of fully dissolved chains with increasing fraction of poor solvent, however, seems unlikely. Let us now turn to the second possible case.

(ii) Consider there are two planarized segments at 25% of poor solvent. By the same reasoning we find that much more fully dissolved chains are present at 25% than at 90% of poor solvent. This seems more realistic.

Therefore, by comparing the degree of polymerization, the conjugation length and the fraction of aggregated segments present in solutions made with different fractions of poor solvent, we infer that the 11kD sample adopts a conformation comprising predominantly two planarized segments at low fraction of poor solvent and one planarized segment at high fraction of poor solvent.

Very similar considerations are valid for the 19 kD sample, for which a conjugation length of 22 repeat units (as found for 50% ethyl acetate) allows for two or three planarized segments. For 90% ethyl acetate, where the conjugation length is 30 repeating units, there can be only one or two planarized segments.

In addition to studying P3HT solutions, we want to know whether the results obtained for P3HT aggregates in solution can be transferred to P3HT films that were spun from solution already containing aggregates due to poor solvent fractions. Therefore, we measured the absorption of the P3HT thin films (see SI). The same quantitative analysis of the ratio of the first two absorption peaks as for the absorption spectra of the P3HT solutions leads to the excitonic coupling within the aggregates according to the work of Spano. These excitonic couplings for the film aggregates are listed in Table 3. We see that the aggregates of the

defined P3HT in the film show very similar excitonic couplings as the aggregates found in solution for maximum aggregation (see Figure 4). Therefore, we consider the aggregates in the defined P3HT films to be of the same nature as the aggregates in solution near maximum aggregation, or to be the same aggregates grown from aggregates in solution acting as nucleation points. Thus, we can control the formation of aggregates in the film via a control of solvent quality. This is true only for the defined P3HT samples.

Table 3: Excitonic coupling for films of defined and extracted P3HT spun from solutions with different ratios of good:poor solvent ($\text{CHCl}_3:\text{EtAc}$). The excitonic couplings were determined by means of the model by Spano for weakly interacting H-aggregates.

| | M_n [g/mol] | $\text{CHCl}_3:\text{EtAc}$ | Excitonic coupling [meV] |
|----------------|---------------|-----------------------------|--------------------------|
| Defined P3HT | 5100 | 100:0 | 70 |
| | | 80:20 | 70 |
| 11300 | 100:0 | 55 | |
| | | 85:15 | 45 |
| 18600 | 100:0 | 55 | |
| | | 85:15 | 35 |
| Extracted P3HT | 5600 | 100:0 | 60 |
| | | 80:20 | 70 |
| 13800 | 100:0 | 40 | |
| | | 80:20 | 45 |
| 19000 | 100:0 | 55 | |
| | | 80:20 | 35 |

Since this control only applies for defined P3HT samples, we studied whether this advantage can be transferred also to charge carrier mobilities within the films. For this reason we measured P3HT thin film transistors prepared from 100% chloroform solutions simply by spin coating without any post-treatment of the devices such as annealing. The resulting saturation mobilities are shown in Figure 7 as a function of molecular weight. Both, the extracted and the defined samples, show increasing charge carrier mobilities with increasing molecular weight. This effect is well-known and was expected. Furthermore, the defined samples with lower molecular weight (5 kD and 11 kD) reach significantly higher charge carrier mobilities than their comparable extracted samples. However, already for the samples with 19 kD, this difference in charge carrier mobility vanishes. Both samples, defined and extracted, reach charge carrier mobilities of 10^{-2} cm/Vs.

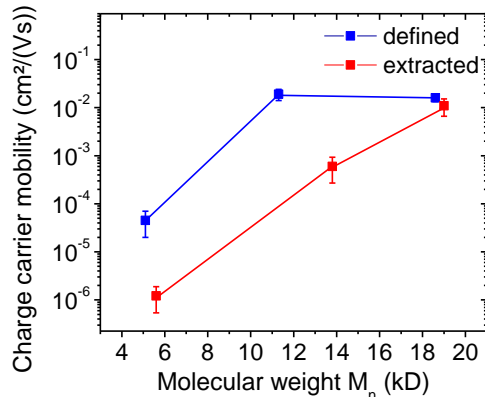


Figure 7: Charge carrier mobilities of defined and extracted P3HT samples as a function of molecular weight M_n . Films were spun from 100% chloroform solutions.

Discussion

The formation of P3HT aggregates in solution

P3HT is well-known to exist in two distinct conformations, that is a random coil conformation leading to an amorphous film, and a planarized conformation giving rise to aggregates and films with corresponding crystalline inclusions. There have been various approaches to force poly(3-hexylthiophene) chains to aggregate. Several preparation parameters affect the solubility of polymer chains and thus the formation of aggregates, such as temperature, concentration or quality of the solvent used.²³⁻²⁵ Clark et al. used solutions with high concentrations of P3HT whose temperature dependent solubility lead to polymer aggregates at sufficiently low temperatures.^{6,20} A similar approach to induce aggregates in P3HT solutions was chosen by Liu et al. who investigated the crystallization behavior of P3HT in respect to crystallization temperature, polymer concentration and molecular weight of the samples.²⁶ Likewise, Berson et al. as well as Oosterbaan et al. used highly concentrated and initially heated solutions of P3HT to induce P3HT nanofibers in the chilled solution and thus controlled the organization of the polymer chains.^{27,28} In contrast to that, Zhao et al. used ultrasonic oscillation to promote the formation of P3HT aggregates.²⁹ Treatments like thermal annealing, solvent vapor annealing or the usage of high boiling point solvents enhance the order of the polymer chains within the aggregates.²⁸ The approach by Park et al. refrained from any additional treatments. Park et al. made thin-film transistors from solutions containing small amounts of a non-solvent with poly(3-hexylthiophene)s of molecular weights in the range of $M_n = 35 \text{ kg/mol}$ to 45 kg/mol .³⁰

In our studies, we aimed at inducing aggregates in P3HT of molecular weights in the range of $M_n = 5 \text{ kg/mol}$ to 19 kg/mol in solution by varying the quality of the solvent. We studied the effect of different fractions of poor solvent, from 0% to 90%, within the P3HT solutions with respect to molecular weight dependence and the influence of the synthetic approach. The induced aggregates in solution were analyzed carefully to obtain the fraction of polymer chains which were aggregated due to low solvent quality. To relate the fraction of aggregate

absorption to the actual fraction of aggregates, the relative oscillator strength was introduced that describes the relative increase in oscillator strength comparing a coiled P3HT chain with a planarized chain in an aggregate. This method was presented by Clark et al. in³¹, where a relative oscillator strength of 1.39 ± 0.10 was obtained for solutions going from 70° C to room temperature. In our investigations, we found a dependence of the relative oscillator strength on the fraction of poor solvent. To be precise, our investigations showed a minimum value for the relative oscillator strength in solutions with 30% to 50% of poor solvent. For higher amounts of poor solvent the oscillator strength increases slightly. This is direct evidence for an increase of conjugation length within the aggregates since oscillator strength is proportional to the squared transition dipole moment which increases linear with the dipole length.³²

As for the fraction of aggregates, we showed that there is a limit to the maximum fraction of the polymer chains that can be forced to planarize and aggregate, even if 90% of poor solvent is used. This maximum fraction is about 50% to 60% for the 11 kD and 19 kD samples. This is in the order of the fraction of aggregated chains in solution induced by cooling published by Clark et al. being $39\% \pm 10\%$.²⁰ Obviously, there must be thermodynamic reasons that prevent the formation of entirely crystalline aggregates that would then precipitate from solution. One such factor may relate to the entropy of the system. For synthetic reasons, the connection between the first and the second 3-alkyl thiophenes unit is not head-to-tail, but instead it is head-to-head, inducing some disorder in each single chain.

As for the defined 5 kD sample, the onset of aggregation was lowered compared to the extracted 6 kD sample that did not show any aggregation below 70% of poor solvent. The defined 5 kD sample starts to aggregate already at 50% of poor solvent. Equally, the onset of aggregation is at higher fraction of poor solvent for the extracted 14 kD sample compared to the corresponding defined sample. Since the extracted sample was fractionized out of a very broad molecular mass distribution, the extracted sample consists of just those shorter chains that stopped growing during synthesis. It has been reported that this can result in lower regioregularity and thus in a relatively strong steric hindrance within the material.¹⁸ Moreover, the extracted samples usually have a broader polydispersity. The late onset of aggregation for extracted P3HT compounds with molecular weight below 19 kD is thus comparable to the effect of a lower order on the packing of polymer chains. The higher the disorder, the lower is the crystallinity and the less ordered is the packing of the P3HT chains.^{33,34} No effect of synthetic approach on aggregation onset as well as on aggregate fraction can be seen for the 19 kD sample since all chains with a smaller molecular weight are extracted out.

The conjugation-length dependence of excitonic coupling

Considering the nature of the aggregates induced in solution, we showed that the excitonic coupling within the aggregates is a function of solvent quality. We interpret this dependency as a conjugation length dependent dipole coupling as investigated theoretically by Gierschner et al.¹¹ Indeed, the excitonic coupling of the aggregates in solution as a function of

solvent quality show a maximum value for the defined 11 kD and 19 kD samples that correlates with a minimum in the conjugation length of the P3HT chains within the aggregates as evidenced through the minimum in the relative oscillator strength. In addition, the positions of the 0-0 absorption peaks in the isolated aggregate absorption spectra shift as a function of solvent quality, in agreement with the calculated conjugation lengths for these aggregates, giving direct experimental confirmation for the conjugation-length dependence of the excitonic coupling predicted theoretically (Figure 5). This is indeed remarkable. For Förster-type energy transfer, the dependence of the dipole-coupling mechanism on the extent of the conjugated system is well documented through measurements of energy transfer rates.^{35,36} In contrast, experimental evidence for the manifestation of this effect in the case of excitonic coupling in aggregates is found only rarely.

In addition, we demonstrate that the excitonic coupling and accordingly the conjugation length depends on molecular weight and synthetic approach. We show that the defined synthetic approach results in higher conjugation lengths for P3HT compounds of molecular weights below 19 kD compared to extracted compounds, whereas for higher molecular weights, the synthetic approach is not relevant if low molecular weight fractions are extracted out. While the effect of synthetic approach has not been studied yet, other effects e.g. the temperature dependence of the excitonic coupling in P3HT films were described in the literature. It is well known that temperature affects the conformation of P3HT chains. Pingel et al. showed that aggregates in P3dHT films have temperature dependent excitonic couplings.³⁷ Furthermore, Clark et al. published a study on the effect of the boiling point of the solvent, which affects the rate with which the film dries after spinning from solution.²⁰ Basically, the higher the solvent boiling point the lower is the resulting excitonic coupling and the higher is the obtained fraction of aggregates. This is in accordance with AFM results from Chang et al. who presented long P3HT ribbons in films spun from a high boiling point solvent.¹ In contrast to these studies, we did not post-treat our samples to enhance the change in excitonic coupling and conjugation length. The resulting change in excitonic coupling in our study is merely due to thermodynamic effects that force the polymer chains to minimize their interaction with the surrounding solvent molecules and thus start aggregation with decreasing solvent quality.³⁸

The packing behavior of P3HT aggregates in solutions and thin films.

Combining the calculated conjugation length with the corresponding fraction of aggregates, we obtain a model for the packing behavior of the polymer chains in solution. We have found that the organization of P3HT chains depends not only on molecular weight, but also on solvent quality. In particular, there is a solvent-dependent change in packing. Higher fractions of poor solvent lead to planarization of the aggregated middle sections of the polymer chains. For example, we conclude that the 5 kD sample packs as non-folded chains. In contrast, the 11 kD and the 19 kD sample form aggregates with kinks or even folded chains at lower

fractions of poor solvent, while they form non-folded chains at high fractions of poor solvent. This scenario is consistent with current understanding of the polymer crystallization process.²⁵ This result further agrees with observations made by Liu et al on the packing behavior of P3HT within nanofibers.²⁶ By means of high-resolution transition electron microscopy they obtained information on the width of nanoribbons. In combination with the contour length of the P3HT chains, this allows concluding on the packing behavior of the chains contained. Liu et al. showed for nanoribbons made of P3HT with $M_n = 9.3$ kD and 19.9 kD (M_n -values corrected for GPC overestimation) that the low molecular weight sample packs indeed as non-folded chains while chains in the high molecular weight sample have to be folded.²⁶ This is also consistent with studies of Wu et al. on a series of P3HT with molecular weights of $5\text{-}19$ kD.³⁹

We also note that according to our results, the aggregates of the 5 kD compounds consist of completely planar chains implying that their conjugation length is equivalent to the full contour length of 7.5 nm. A comparable low molecular weight sample with $M_n = 5.7$ kD was recently studied by Brinkmann and Rannou. They reported on the packing behavior and the semicrystalline structures in P3HT and showed that the low molecular weight sample packs in crystalline lamellar of 7-8 nm width.⁴⁰ This value confirms the conjugation length we obtained for the 5 kD sample. Thus, although our conclusions concerning the packing behavior of P3HT chains were based merely on spectroscopic studies, they are confirmed by the results on P3HT morphology from other groups.

For defined P3HT samples, we were able to transfer the aggregate interaction (excitonic coupling and conjugation length) obtained in solution into the thin film structure prepared by spin-coating. For example, in solution, the fraction of poor solvent controls the intermolecular coupling within the aggregates. For defined P3HT samples, we have found equal excitonic couplings in both, thin film aggregates and aggregates in solution. Thus, the aggregates induced in solution by changing the solvent quality are either the same aggregates found in the resulting film after spin-coating or they act at least as starting points for nucleation and growth. Therefore, a control over the excitonic coupling and conjugation length within aggregates in the resulting films is given by the control of the solvent quality.

Considering the charge carrier mobility in P3HT thin films, it is well known that the presence of aggregates or crystalline regions controls the mobility. Several aspects of this have been studied, among them the effect of crystallinity^{39,41}, the effect of the boiling point of the solvent^{42,43}, the effect of film thickness⁴⁴, the effect of the concentration of the solution³⁰ and the effect of the organization of the P3HT chains in the film²⁷. Our investigations concerning the charge carrier mobility in P3HT thin films focus on changes due to different molecular weights and different synthetic approaches. In addition to the well-known molecular weight dependence of charge carrier mobility, we observe a direct correlation between the fraction of aggregates in solution (Figure 2) and the resulting thin film mobility (Figure 7). For the defined and extracted 19 kD samples, the onset of aggregation in solution occurs early (at 10% poor

solvent), and in both cases similarly high fraction of aggregates up to 50% are obtained. The same is true for the defined 11 kD sample, where aggregates can take up even 60% in solution. For these three samples, the same charge carrier mobilities exceeding $10^{-2} \text{ cm}^2/\text{Vs}$ are obtained. For the extracted 14 kD sample, aggregation in solution takes place less easily, as evidenced by the higher fraction of poor solvent required and by the lower fractions of aggregates obtained. Concomitantly, the charge mobility is more than an order of magnitude lower than for the corresponding 11 kD defined sample. Aggregation is even more difficult for the 5 kD defined sample, translating equally in a reduced mobility until finally for the 6 kD extracted sample there is hardly any aggregation present in solution, and concomitantly the charge carrier mobility ranges at $10^{-6} \text{ cm}^2/\text{Vs}$. These changes in FET mobility cannot be attributed to differences in the excitonic coupling within the aggregates. Experimentally, comparison with Figure 4 shows that the changes in excitonic coupling with molecular weight and synthetic approach are less drastic. Furthermore, there is no a priori reason why a dipole-interaction based excitonic coupling should necessarily correlate with an exchange-interaction based charge transfer mechanism.

The observed correlation between the fraction of aggregates in solution and the thin film mobility may assist towards understanding the widely observed increase of charge carrier mobility with molecular weight.^{2,4} The reasons for the increase of mobility with molecular weight are still discussed. Zen et al. suggest that the increasing fraction of crystalline domains with increasing molecular weight controls the charge carrier mobility.⁴¹ In contrast, Brinkmann and Rannou suggest that an increasing fraction of bridging chains with increasing molecular weight increases the probability of charge transport through the less conductive amorphous domains of the film.⁴⁵ Both approaches are based on the idea that the charge transport through the film is limited by amorphous domains. Recently, Lan and Huang published a theoretical study that implies that charge carrier mobilities below $10^{-2} \text{ cm}^2/\text{Vs}$ are controlled by the number of crossing points between the crystalline domains, whereas mobilities above this value correspond to present bridging chains between the ordered domains.⁴⁶

The correlation we found between the fraction of aggregates in solution and the resulting thin film charge carrier mobility supports the arguments by Zen et al, at least for the range of molecular weights considered here. We observe the same high mobility for samples with very different molecular weight, that is 11 kD and with 19 kD, yet with the same propensity to aggregation.⁴¹ While the degree of aggregation in solution clearly does not need to translate into an equal aggregation in the film, it can serve as an indication of the propensity of the sample towards aggregation. The 11 kD and the 19 kD chains have about 44 and 74 repeat units, respectively. When forming aggregates in solution at a medium fraction of poor solvent (i.e. a moderate driving force towards aggregation), both have a conjugation length of about 22 repeat units, implying one or at most two kinks in the chain. Thus, or a chain as short as 11 kD, bridging chains between different crystallites are hard to imagine. Moreover, one would

expect more bridging chains for the 19 kD chain. As both samples show the same mobility this implies that either there are no bridging chains, or they do not contribute to the overall chain mobility. This argument is further strengthened by the fact that the mobility of $10^{-2} \text{ cm}^2/\text{Vs}$ we obtain for the defined 11 kD sample is the same mobility that is obtained by Kline and coworkers for 40 kD samples, where bridging chains would be conceivable.²

Acknowledgements

We thank Patrick Pingel and Rene Kalbitz for the FET measurements. Funding by the Graduiertenkolleg 1640 and SPP 1635 of the Deutsche Forschungsgemeinschaft is gratefully acknowledged. RHL thanks the Elite Netzwerk Bayern for a stipend according the Bayrisches Eliteförderungsgesetz.

References

- (1) Chang, J. F.; Sun, B. Q.; Breiby, D. W.; Nielsen, M. M.; Solling, T. I.; Giles, M.; McCulloch, I.; Sirringhaus, H. *Chem. Mater.* **2004**, 16, 4772-4776.
- (2) Kline, R. J.; McGehee, M. D.; Kadnikova, E. N.; Liu, J. S.; Frechet, J. M. J. *Adv. Mater.* **2003**, 15, 1519-1522.
- (3) McCullough, R. D.; Tristramnagle, S.; Williams, S. P.; Lowe, R. D.; Jayaraman, M. *J. Am. Chem. Soc.* **1993**, 115, 4910-4911.
- (4) Zen, A.; Pflaum, J.; Hirschmann, S.; Zhuang, W.; Jaiser, F.; Asawapirom, U.; Rabe, J. P.; Scherf, U.; Neher, D. *Adv. Funct. Mater.* **2004**, 14, 757-764.
- (5) Chang, J. F.; Clark, J.; Zhao, N.; Sirringhaus, H.; Breiby, D. W.; Andreasen, J. W.; Nielsen, M. M.; Giles, M.; Heeney, M.; McCulloch, I. *Phys. Rev. B* **2006**, 74, 115318.
- (6) Clark, J.; Silva, C.; Friend, R. H.; Spano, F. C. *Phys. Rev. Lett.* **2007**, 98, 206506.
- (7) Reid, O. G.; Malik, J. A. N.; Latini, G.; Dayal, S.; Kopidakis, N.; Silva, C.; Stingelin, N.; Rumbles, G. *J. Polym. Sci.; Part B: Polym. Phys.* **2012**, 50, 27-37.
- (8) Herrmann, D.; Niesar, S.; Scharsich, C.; Köhler, A.; Stutzmann, M.; Riedle, E. *J. Am. Chem. Soc.* **2011**, 133, 18220-18233.
- (9) Spano, F. C. *J. Chem. Phys.* **2005**, 122, 114701.
- (10) Beljonne, D.; Cornil, J.; Silbey, R.; Millie, P.; Bredas, J. L. *J. Chem. Phys.* **2000**, 112, 4749-4758.
- (11) Gierschner, J.; Huang, Y. S.; Van Averbeke, B.; Cornil, J.; Friend, R. H.; Beljonne, D. *J. Chem. Phys.* **2009**, 130, 6.
- (12) Pingel, P.; Zen, A.; Neher, D.; Lieberwirth, I.; Wegner, G.; Allard, S.; Scherf, U. *Appl. Phys. A: Mater. Sci. Process.* **2009**, 95, 67-72.
- (13) Khan, A. L. T.; Banach, M. J.; Kohler, A. *Synth. Met.* **2003**, 139, 905-907.
- (14) Sheina, E. E.; Liu, J. S.; Iovu, M. C.; Laird, D. W.; McCullough, R. D. *Macromolecules* **2004**, 37, 3526-3528.
- (15) Lohwasser, R. H.; Thelakkat, M. *Macromolecules* **2011**, 44, 3388-3397.
- (16) Skotheim, T. A.; Reynolds, J. R (eds.) In *Conjugated Polymers: Theory, Synthesis, Properties, and Characterization*; CRC Press, Taylor & Francis Group: Boca Raton, **2007**.

- (17) Loewe, R. S.; Khersonsky, S. M.; McCullough, R. D. *Adv. Mater.* **1999**, 11, 250-253.
- (18) Trznadel, M.; Pron, A.; Zagorska, M.; Chrzaszcz, R.; Pielichowski, J. *Macromolecules* **1998**, 31, 5051-5058.
- (19) Xu, W. T.; Li, L. G.; Tang, H. W.; Li, H.; Zhao, X. L.; Yang, X. N. *J. Phys. Chem. B*, **2011**, 115, 6412-6420.
- (20) Clark, J.; Chang, J. F.; Spano, F. C.; Friend, R. H.; Silva, C. *Appl. Phys. Lett.* **2009**, 94, 163306.
- (21) Becker, G. W.; Braun, D.; Carlowitz, B. (eds.) *In Die Kunststoffe Chemie, Physik, Technologie, Kunststoff Handbuch Band 1*; Carl Hanser Verlag: München, **1990**.
- (22) Brown, P. J.; Thomas, D. S.; Köhler, A.; Wilson, J. S.; Kim, J. S.; Ramsdale, C. M.; Sirringhaus, H.; Friend, R. H. *Phys. Rev. B: Condens. Matter Mater. Phys.* **2003**, 67, 064203.
- (23) Reiter G., Sommer J.-U., (Eds.) *In Polymer Crystallization: Observations, Concepts and Interpretations*; Springer-Verlag: Berlin, **2003**.
- (24) Reiter G., Stobl G. R. , (eds.) *In Progress in Understanding of Polymer Crystallization*; Springer-Verlag: Berlin, **2007**.
- (25) Hu, W. B.; Frenkel, D. *Polymer Crystallization Driven by Anisotropic Interactions In Interphases and Mesophases in Polymer Crystallization III* (ed. G. Allegra); Springer-Verlag: Berlin, **2005**, p. 1-35.
- (26) Liu, J. H.; Arif, M.; Zou, J. H.; Khondaker, S. I.; Zhai, L. *Macromolecules* **2009**, 42, 9390-9393.
- (27) Berson, S.; De Bettignies, R.; Bailly, S.; Guillerez, S. *Adv. Funct. Mater.* **2007**, 17, 1377-1384.
- (28) Oosterbaan, W. D.; Vrindts, V.; Berson, S.; Guillerez, S.; Douheret, O.; Ruttens, B.; D'Haen, J.; Adriaensens, P.; Manca, J.; Lutsen, L.; Vanderzande, D. *J. Mater. Chem.* **2009**, 19, 5424-5435.
- (29) Zhao, K.; Xue, L. J.; Liu, J. G.; Gao, X.; Wu, S. P.; Han, Y. C.; Geng, Y. H. *Langmuir* **2010**, 26, 471-477.
- (30) Park, Y. D.; Lee, H. S.; Choi, Y. J.; Kwak, D.; Cho, J. H.; Lee, S.; Cho, K. *Adv. Funct. Mater.* **2009**, 19, 1200-1206.
- (31) Clark, J. EPAPS Document, EAPPLAB94058913.
- (32) Turro, N. J. *In Modern Molecular Photochemistry*; University Science Books: Sausalito, California, **1991**.
- (33) Kim, Y.; Cook, S.; Tuladhar, S. M.; Choulis, S. A.; Nelson, J.; Durrant, J. R.; Bradley, D. D. C.; Giles, M.; McCulloch, I.; Ha, C. S.; Ree, M. *Nat. Mater.* **2006**, 5, 197-203.
- (34) Sirringhaus, H.; Brown, P. J.; Friend, R. H.; Nielsen, M. M.; Bechgaard, K.; Langeveld-Voss, B. M. W.; Spiering, A. J. H.; Janssen, R. A. J.; Meijer, E. W.; Herwig, P.; de Leeuw, D. M. *Nature* **1999**, 401, 685-688.
- (35) Beljonne, D.; Curutchet, C.; Scholes, G. D.; Silbey, R. J. *J. Phys. Chem. B* **2009**, 113, 6583-6599.
- (36) Beljonne, D.; Pourtois, G.; Silva, C.; Hennebicq, E.; Herz, L. M.; Friend, R. H.; Scholes, G. D.; Setayesh, S.; Mullen, K.; Bredas, J. L. *Proc. Natl. Acad. Sci. U. S. A.* **2002**, 99, 10982-10987.
- (37) Pingel, P.; Zen, A.; Abellon, R. D.; Grozema, F. C.; Siebbeles, L. D. A.; Neher, D. *Adv. Funct. Mater.* **2010**, 20, 2286-2295.

- (38) Hamley, I. W. In *Introduction to Soft Matter: Polymers, Colloids, Amphiphilic and Liquid Crystals*; John Wiley & Sons, Ltd. : Chichester, **2006**.
- (39) Wu, Z. Y.; Petzold, A.; Henze, T.; Thurn-Albrecht, T.; Lohwasser, R. H.; Sommer, M.; Thelakkat, M. *Macromolecules* **2010**, 43, 4646-4653.
- (40) Brinkmann, M.; Rannou, P. *Macromolecules* **2009**, 42, 1125-1130.
- (41) Zen, A.; Saphiannikova, M.; Neher, D.; Grenzer, J.; Grigorian, S.; Pietsch, U.; Asawapirom, U.; Janietz, S.; Scherf, U.; Lieberwirth, I.; Wegner, G. *Macromolecules* **2006**, 39, 2162-2171.
- (42) Cheng, H. L.; Lin, J. W.; Jang, M. F.; Wu, F. C.; Chou, W. Y.; Chang, M. H.; Chao, C. H. *Macromolecules* **2009**, 42, 8251-8259.
- (43) Surin, M.; Leclere, P.; Lazzaroni, R.; Yuen, J. D.; Wang, G.; Moses, D.; Heeger, A. J.; Cho, S.; Lee, K. *J. Appl. Phys.* **2006**, 100, 33712 .
- (44) Joshi, S.; Grigorian, S.; Pietsch, U.; Pingel, P.; Zen, A.; Neher, D.; Scherf, U. *Macromolecules* **2008**, 41, 6800-6808.
- (45) Brinkmann, M.; Rannou, P. *Adv. Funct. Mater.* **2007**, 17, 101-108.
- (46) Lan, Y. K.; Huang, C. I. *J. Phys. Chem. B* **2009**, 113, 14555-14564.

Supporting Information

Absorption spectra of aggregated chains

This section describes how we derived the absorption spectra of chains in the aggregated state. To induce poly(3-hexylthiophene) chains to aggregate, we prepared solutions with different ratios of good:poor solvent (chloroform:ethyl acetate). The measured absorption of these solutions is caused by coexisting coiled and aggregated chains. The resulting isosbestic point (see Figure 1 in the manuscript) indicates that there are only these two species of chains, namely dissolved, and thus coiled, polymer chains and planarized, aggregated chains. The latter show structured and red-shifted absorption compared to the coiled chains.

Figure SI 1 illustrates exemplarily for each molecular weight compound how the absorption spectra of the aggregated chains were extracted from the measured total spectra. The shape of the absorption spectrum of well dissolved, coiled P3HT was measured in 100% chloroform solution and scaled to fit the high energy shoulder of the examined solution spectrum without changing its position. This scaled spectrum of the coiled chains was then subtracted yielding the absorption spectrum due to pure aggregates present in the according solution.

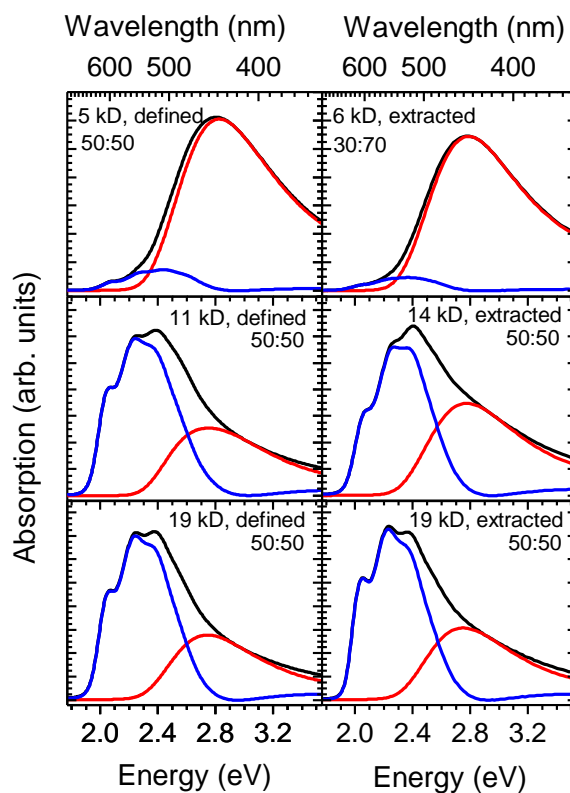


Figure SI 1: Measured absorption spectra for solutions with good:poor solvent ($\text{CHCl}_3:\text{EtAc}$) (black line) containing coexisting coiled and aggregated chains. The absorption of well dissolved, coiled P3HT in 100% chloroform (red line) was scaled to fit the high energy shoulder of the solution spectrum. The spectrum of the coiled chains was then subtracted yielding the absorption due to aggregates (blue line).

Determination of relative oscillator strength

For our interpretation, we need to know the fraction of chains that are aggregated. Above, we have derived which fraction of absorption is due to aggregates. However, the fraction of aggregate absorption is not equal to the fraction of aggregates, since the chain may have different oscillator strength in the coiled form and in the aggregated form. The relative oscillator strength describes the change in oscillator strength when going from coiled to aggregated P3HT chains. Knowledge of this relative oscillator strength is therefore necessary to determine the fraction of aggregates from the area of the aggregate absorption.

To determine the relative oscillator strength, we followed the procedure by Clark et al.¹ Figure SI 2 illustrates the procedure. As outlined above, the total absorption spectrum (blue solid line) can be deconvoluted into the absorption caused by dissolved, coiled chains (black dashed line) and the absorption caused by aggregated chains (blue dashed line). The change in absorption of the coiled chains, A_{coiled} , corresponds to the difference between the spectrum from 100% coiled chains (black solid line) and the fraction of absorption by the coiled chains in the measured spectrum (black dashed line). In the left part of Figure SI 2, A_{coiled} is indicated by the shaded area.

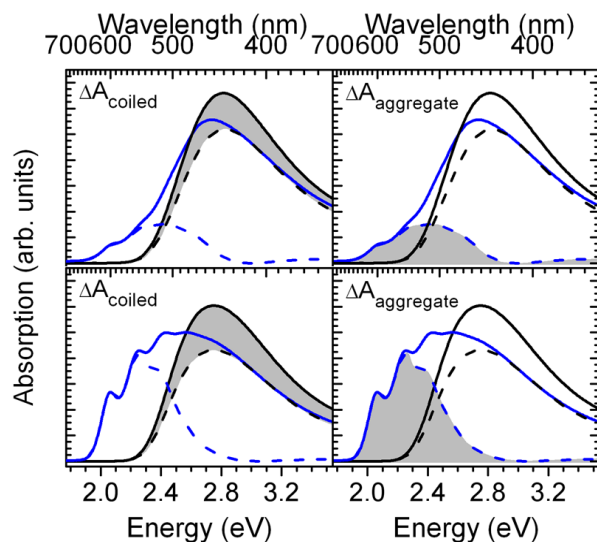


Figure SI 2: Exemplarily absorption spectra for P3HT solutions with solvent induced aggregate absorption (blue solid line) indicating the change in oscillator strength between coiled and aggregated chains (grey areas). The absorption of 100% well dissolved, coiled chains is presented as solid black line. The dashed lines show the absorption due to aggregated (dashed blue line) and coiled (dashed black line) chains, respectively. Top figures show absorption of 30:70 (CHCl₃:EtAc) solution of the defined 5 kD sample and bottom figures show 80:20 (CHCl₃:EtAc) solution of the 11 kD sample.

The corresponding increase in absorption of the aggregated chains, $A_{\text{aggregate}}$, is given by the absorption of the aggregated chains formed (blue dashed line). $A_{\text{aggregate}}$ is shown as shaded area in the right part of Figure SI 2. Any difference between the decrease of absorption by coiled chains and the increase in absorption by aggregated chains must arise from a change in relative oscillator strength F as follows.

$$F = -\frac{\Delta A_{aggregate}}{\Delta A_{coiled}}$$

The resulting change in relative oscillator strength F for solutions with different ratios of good:poor solvent (chloroform:ethyl acetate) for the defined and extracted poly(3-hexylthiophene) compounds is summarized in Figure SI 3. Clark et al. obtained a relative oscillator strength of (1.39 ± 0.10) for commercial P3HT in solution going from $70^{\circ} C$ to room temperature. This is in good agreement with the relative oscillator strength we obtained for the solutions of the 19 kD samples with 25% of poor solvent and higher.

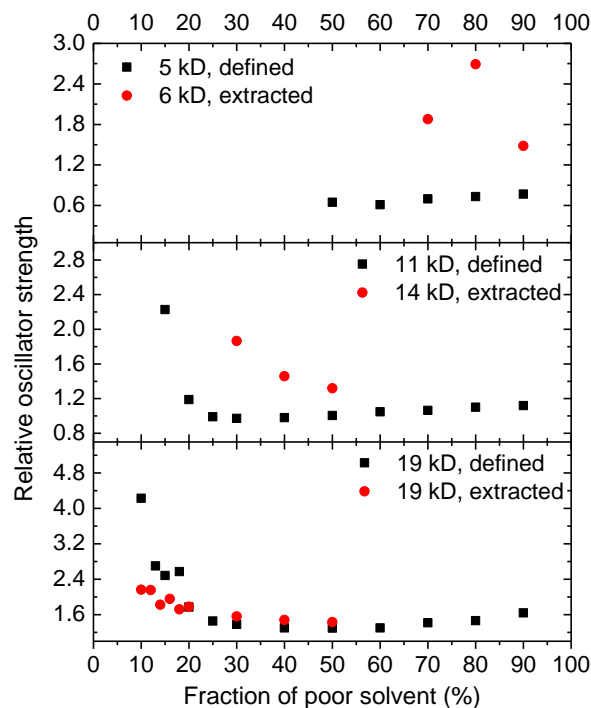


Figure SI 3: The relative oscillator strength between coiled and aggregated P3HT chains as function of poor solvent fraction for defined and extracted P3HT as indicated in the figure. The molecular weight increases from top to bottom.

Franck-Condon analysis

The quantitative analysis of the P3HT aggregate absorption yields the excitonic coupling J between the polymer chains within these aggregates. According to the work of Spano², the coupling is determined by the ratio of the first two absorption peaks, A_{0-0}/A_{0-1} , as follows

$$\frac{A_{0-0}}{A_{0-1}} = \frac{n_{0-0}}{n_{0-1}} \frac{\left(1 - \frac{J}{\omega_0} e^{-s} \sum_{\nu>0} \frac{S^\nu}{\nu! \nu}\right)^2}{S \left(1 - \frac{J}{\omega_0} e^{-s} \sum_{\nu \neq 1} \frac{S^\nu}{\nu! (\nu-1)}\right)^2}$$

where ω_0 is the effective vibrational energy of the single emitter and S its Huang Rhys parameter, n_{0-0} and n_{0-1} refer to the refractive index at the position of A_{0-0} and A_{0-1} . Thus, the correct determination of the excitonic coupling J requires the knowledge of Huang Rhys parameter S and the effective vibrational energy ω_0 of the single, i.e. non-aggregated, emitter. Both parameters can be extracted from a Franck-Condon analysis of the photoluminescence of the single emitter (a non-aggregated chain). Therefore, we measured photoluminescence spectra of dilute P3HT solutions in 100% chloroform. Figure SI4 shows the experimental photoluminescence data (blue symbols).

For the analysis of the excitonic coupling J , we need only a vibrational energy for an *effective* oscillation. Thus, a single mode Franck-Condon analysis is sufficient. In a Franck-Condon analysis, the photoluminescence spectrum is modeled as a sum of Gaussian shaped transitions, Γ , from the first excited state $S_1(m=0)$ to the ground state $S_0(m)$ with $m=1,2,3,\dots$ being the vibration quantum number.³ The fitting procedure demands a normalization of the photoluminescence signal $P(\hbar\omega)$ given by

$$\frac{P(\hbar\omega)}{n^3(\hbar\omega)^3 I_{0-0}} = \sum_m \frac{S^m}{m!} \Gamma \delta[\hbar\omega - (\hbar\omega_0 - m\hbar\omega_i)]$$

where I_{0-0} is the intensity of the emission from the 0-0 vibrational level of the first excited state to the 0-0 vibrational level of the ground state. The integer m denotes the excitation level of the vibration with energy $\hbar\omega_i$ and n is the refractive index of the surrounding material at photon energy $\hbar\omega$. Here, the material surrounding the single emitters was the solvent, chloroform. Its refractive index was calculated from the Cauchy parameters published by Samoc.⁴

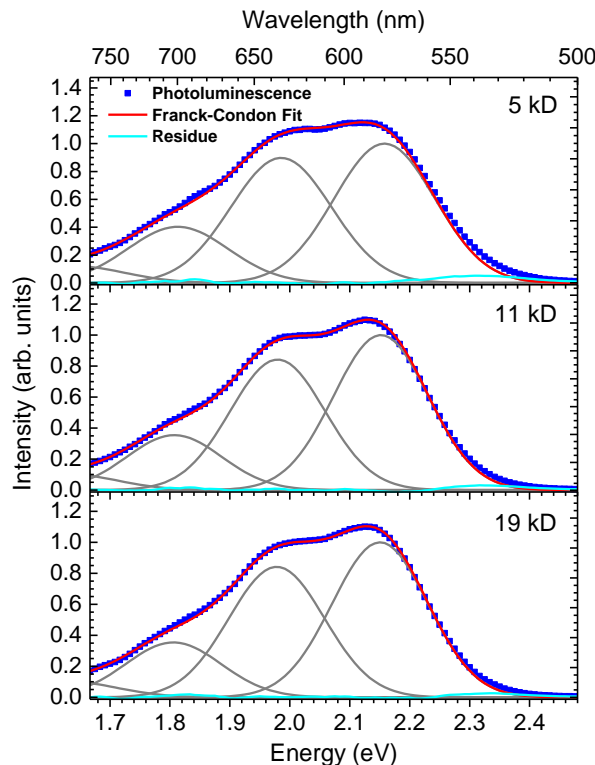


Figure SI 4: Single mode Franck-Condon fits (red line) for the single emitter emission spectra in dilute solution for defined P3HT. The molecular weight increases from top to bottom. The experimental data (blue symbols) were fitted with Gaussian functions (grey lines) at four vibration levels. The residue is presented as cyan line.

The Franck-Condon fits according to equation 2 were calculated using four vibrational levels ($m = 0, 1, 2, 3, 4$) of the effective oscillator $\hbar\omega_0$ and yield the fitting parameters summarized in Table 1. The Franck-Condon fits (red line in Figure 4) reproduce the experimental data with high accuracy. Thus, the resulting parameters S and ω_0 enable a precise calculation of the free excitonic coupling J .

Table SI 1: Fitting parameters of the Franck-Condon analyses for the poly(3-hexylthiophene) (P3HT) single emitter photoluminescence spectra: Huang Rhys parameter S , energy of effective oscillation ω_0 and Gaussian standard deviation σ .

| P3HT | S | ω_0 | σ |
|--------------|------|------------------------|----------|
| 5 kD | 0.90 | 1390 cm^{-1} | 0.084 eV |
| 11 kD | 0.84 | 1390 cm^{-1} | 0.079 eV |
| 19 kD | 0.84 | 1390 cm^{-1} | 0.080 eV |

Absorption spectra of thin films

We want to investigate whether the results obtained for P3HT aggregates in solution can be transferred to P3HT films that were spun from solution already containing aggregates due to poor solvent fractions. Therefore, we studied the absorption of the P3HT thin films, shown in Figure SI 5 normalized to the 0-1 absorption peak for the defined P3HT samples. The absorption spectra of the films show both, a structured absorption due to aggregated chains at low energies and absorption around 2.8 eV and higher due to non-aggregated coiled chains in amorphous regions. We find that films spun from solutions containing fractions of poor solvent have higher 0-0 absorption indicating aggregates with lower excitonic coupling and thus higher conjugation length. Similar absorption spectra can be obtained for the extracted P3HT samples as well.

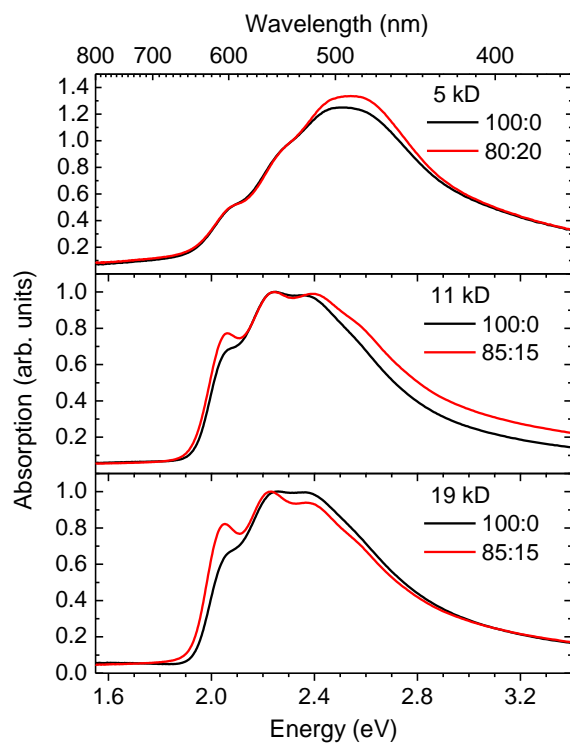


Figure SI 5: Absorption spectra of thin films made from defined P3HT, normalized to the second absorption peak. Films were spun from solutions with ratios of good:poor solvent ($\text{CHCl}_3:\text{EtAc}$) as indicated in the figure.

Assessment of thermal equilibrium state in solution

The absorption spectra of P3HT in a solvent mixture of chloroform and ethyl acetate do not show any changes on a 24 hour timescale. We therefore wanted to know whether the conformation obtained in such a solution corresponds to a thermal equilibrium state. To probe this, P3HT was dissolved in a chloroform:ethyl acetate 50:50 mixture at a concentration of 0.25 mg/ml prepared in two different ways. In the first approach, P3HT was fully dissolved in chloroform. Then, the necessary amount of ethyl acetate was added at once. In the second approach, P3HT was again fully dissolved in chloroform, but the necessary amount of ethyl

acetate was added very slowly (0.4 ml/h) in small amounts while stirring using an automated syringe. The absorption spectra resulting from the two modes of preparation are different, with larger aggregates falling out of solution in the second mode of preparation. From this difference we infer that the solutions prepared by the first mode are not in a thermal equilibrium state.

References

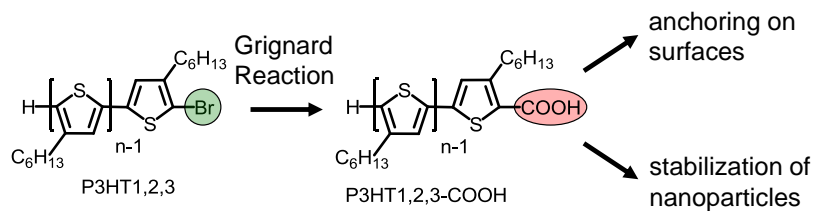
- (1) Clark, J.; Chang, J. F.; Spano, F. C.; Friend, R. H.; Silva, C. *Appl. Phys. Lett.* **2009**, 94, 3.
- (2) Spano, F. C. *J. Chem. Phys.* **2005**, 122, 114701.
- (3) Ho, P. K. H.; Kim, J. S.; Tessler, N.; Friend, R. H. *J. Chem. Phys.* **2001**, 115, 2709-2720.
- (4) Samoc, A. *J. Appl. Phys.* **2003**, 94, 6167-6174.

6. Synthesis and Characterization of Monocarboxylated Poly(3-hexylthiophene)s via Quantitative End-Group Functionalization

Ruth H. Lohwasser and Mukundan Thelakkat*

Applied Functional Polymers, Department of Macromolecular Chemistry I,
University of Bayreuth, Universitätsstraße 30, 95444 Bayreuth, Germany

* E-mail corresponding author: mukundan.thelakkat@uni-bayreuth.de



Published in *Macromolecules* **2010**, 43, 7611-7616

Abstract

We report the quantitative conversion of bromine end groups in regioregular poly(3-hexylthiophene)s (P3HTs) and the characterization of the resulting monocarboxylated P3HTs (P3HT-COOHs) carrying one carboxylic acid group at their chain ends. The monocarboxylation for three different chain lengths is carried out, and the resulting P3HT-COOHs are characterized with size exclusion chromatography, matrix-assisted laser desorption ionization spectroscopy with time-of-flight detection mass spectroscopy, and UV-vis spectroscopy. The thermal properties and crystallinity in bulk and thin films were studied in a comparison between P3HT and P3HT-COOHs. Differential scanning calorimetry and wide-angle X-ray scattering support the increasing crystallinity for the higher molecular weight samples. Preliminary OFET measurements show a good charge carrier mobility in the range of $10^{-3} \text{ cm}^2/(\text{Vs})$ for P3HT-COOHs with molecular weights of 5000 and 10800 g/mol.

Introduction

In recent years organic electronics is gaining increasing attention, especially in the fields of organic light-emitting diodes (OLEDs), organic field effect transistors (OFETs), and organic solar cells. A common hole conductor material used in these devices is regioregular poly(3-hexylthiophene) (P3HT).^{1,2} After its invention in the 1980s, one major step in the synthetic development was the use of an asymmetric monomer to gain P3HT with a regioregularity around 98%.³⁻⁵ Further, the invention of the Grignard metathesis polymerization (GRIM) by McCullough and Yokozawa allowed the control over molecular weight and narrow molecular weight distributions.^{6,7} Apart from the use of new side chains bearing oxyethylene, amino, or carboxylic acid functions,^{8,9} a lot of effort was put in the introduction of new polymer chain end groups via controlled ways. A good control of end groups and its functionalization is a prerequisite for e.g. the synthesis of block copolymers and for the anchoring onto surfaces.¹⁰⁻¹² Initial end-group functionalizations were often realized with multiple postpolymerization steps.^{13,14} Later, the *in situ* end-group functionalization by McCullough enabled a simpler introduction of functional groups like e. g. amino, hydroxy, vinyl, or alkynyl groups.¹⁵ Depending on the nature of the used end-capper, primarily mono- or difunctionalization was achieved. Despite the versatility of this method, one important end group for the coordination of nanoparticles or anchoring onto surfaces - the carboxylic acid group - was not yet reported. Recently, we showed a method for multifunctional carboxylation, where the functionalized P3HT showed good adsorption on TiO₂ and therefore could be used as a sensitizer in dye-sensitized solar cells. But a multicarboxylation resulted also in a complete loss of crystallinity.¹¹

Here we introduce a more controlled method for the selective and quantitative monocarboxylation of P3HT at only one chain end, where the polymer maintains its semicrystallinity after carboxylation. Further, we investigate the influence of the COOH end groups on thermal, optical, and electronic properties, depending on the chain length of the carboxylated polymer.

Experimental Section

Materials and Characterization

¹H NMR spectra were recorded in chloroform on a Bruker Avance 250 spectrometer at 300 MHz. Coupling constants are given in hertz. The spectra were calibrated according to solvent signal at 7.26 ppm. Size exclusion chromatography (SEC) measurements were carried out in THF using a UV detector from Waters and a mixed-C PL-Gel (PL) column. Polystyrene was used as external standard and 1,2-dichlorobenzene as an internal standard for calibration. FT-IR spectra were obtained from drop-cast films on the ATR unit with a Perkin-Elmer Spectrum 100 FT-IR spectrometer. UV-vis measurements were performed with a U-3000 spectrometer from Hitachi. Differential scanning calorimetry (DSC) measurements were done on a Perkin-Elmer Diamond DSC with a heating and cooling rate of 10 K/min. Matrix-assisted laser desorption ionization spectroscopy with time-of-flight detection mass spectroscopy (MALDI-ToF MS) measurements were performed on a Bruker Reflex I using dithranol as matrix and a mixture of 1000:1 (matrix:polymer). The laser intensity was set to around 70%. The reflection mode was calibrated with a fullerite mixture from Sigma-Aldrich (CAS 131159-39-2). WAXS measurements were performed at the beamline ID2 at the European Synchrotron Radiation Facility in Grenoble. The energy of the photons was 12.540 keV ($\lambda \sim 0.1$ nm). The samples were prepared on Kapton foils, and all diffractograms were corrected with the diffractogram of a pure foil.

The monomer 2,5-dibromo-3-hexylthiophene and the catalyst 1,3-bis(diphenylphosphino)propanenickel(II) chloride [Ni(dppp)Cl₂] were synthesized according to the literature.¹⁶ All glass apparatus for polymerization and polymer-analogous reactions were heated and cooled under argon. Dry THF was distilled over calcium hydride and potassium. *i*-PrMgCl (2 M in THF) and *t*-BuMgCl (1.7 M in THF) were purchased from Acros and titrated according to Krasovskiy and Knochel.¹⁷ CO₂ gas (99.995%, <5 ppm of H₂O, Riessner Gase) and hexamethyldisilazane (HMDS) (99%, Aldrich) for the OFETs were used as received. A commercial P3HT with a number-average molecular weight M_n of 19400 g/mol was purchased from Rieke metals for comparative studies.

General Procedure for the Synthesis of P3HT-COOH

The regioregular P3HTs (P3HT1-5) were synthesized according to published procedures.¹⁵ The polymers were used without any purification by fractionation. The procedure for the monocarboxylation is explained below with P3HT2 as a typical example. P3HT2 (348 mg) was dried under vacuum and dissolved in dry THF (68 mL) in a Schlenk flask. The solution was degassed via three freeze-pump-thaw cycles and 14.5 mL of *i*-PrMgCl (1.3 M, 150-200 molar excess compared to the bromine end groups) were added with a syringe. The solution was stirred overnight, and CO₂ was bubbled into the solution at room temperature for 5 min and then 1 h at 0 °C. After 1 h additional stirring at 0 °C the reaction was terminated with 2 N HCl. The solution was concentrated under reduced pressure; the polymer was dissolved in CHCl₃.

and precipitated in methanol. The functional polymer was filtered, washed with methanol in a Soxhlet overnight, and extracted with chloroform. Pure P3HT2-COOH (340 mg) was isolated from the chloroform extract by precipitation into methanol, filtering, and drying under vacuum. The following spectroscopic analysis is valid for all three P3HT-COOHs.

$\delta^1\text{H}$ (300 MHz; CDCl₃): 7.03 (0.045 H, s, H_{ar} of end group unit with COOH), 6.98 (1 H, br s, H_{ar}), 3.01 (0.09 H, t, α -CH₂ of end group unit with COOH), 2.80 (2 H, br, α -CH₂), 1.85–1.50 (2 H, br m, β -CH₂), 1.50–1.10 (6 H, br m), 1.0–0.75 (3 H, br m, CH₃).

FTIR ν_{max} (film)/cm⁻¹: 3055w, 2957s, 2928s, 2857s, 2644b, 2542b, 1665s, 1526w, 1457s, 1439s, 1378w, 829m, 724w.

OFET Preparation and Measurements

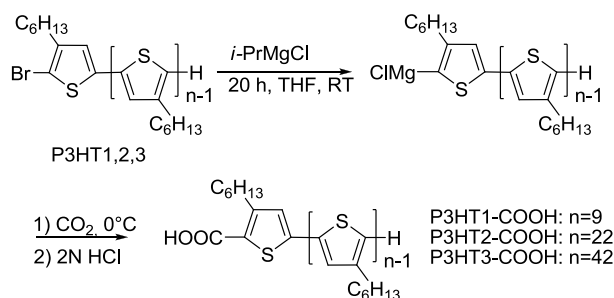
OFET substrates were purchased from Fraunhofer IMPS, Dresden. The geometry of the device was a bottom gate top electrode type, with n-doped (doping at wafer surface: $n \approx 3^{17} \text{ cm}^{-3}$) silicon as gate electrode and a 230 nm SiO₂ layer as gate dielectric. The source and drain electrodes were ITO (indium tin oxide) (10 nm) as adhesion layer with high work function and gold (30 nm). The analyzed channel length was 20 μm and the width 10 mm. The substrates were cleaned with acetone, H₂O₂/H₂SO₄ 15 min, VE-water, VE-water (ultrasonic bath 15 min), acetone (ultrasonic bath 15 min), and *i*-propanol (ultrasonic bath 15 min) and rinsed with hexane. The H₂O₂/H₂SO₄ solution should be handled with care because it is highly corrosive. After plasma etching for 15 min the substrates were hydrophobized with hexamethyldisilazane (HMDS) vapor for 3 h. Excess HMDS was washed off with hexane. All following steps were done under inert gas atmosphere in a glovebox. The active polymer layers were spin-coated at 2000 rpm from a 1 wt% solution in CHCl₃. Output and transfer characteristics were measured with a Hewlett-Packard 41555A semiconductor parameter analyzer. The hole transport mobilities were determined from the transfer characteristics according to eq 1.¹⁸ Since the mobility did not reach a saturation regime for all devices, all the given mobilities are for a fixed gate voltage of -40 V.

$$\mu_{\text{sat}} = \left(\frac{\partial \sqrt{I_{SD}}}{\partial V_G} \right)^2 \frac{2L}{WC_i} \quad (1)$$

Results and Discussion

Synthesis and End Group-Analysis

First three regioregular poly(3-hexylthiophene)s (P3HT1-3) with defined molecular weights between 1000 and 10000 g/mol were synthesized via the Grignard Metathesis polymerization developed by McCullough and co-workers.¹⁵ The number-average molecular weights (M_n) of these samples as determined according to size exclusion chromatography (SEC) are 1500 g/mol for P3HT1, 5000 g/mol for P3HT2, and 10200 g/mol for P3HT3 (Table 1). The absolute molecular weights were determined with matrix-assisted laser desorption ionization spectroscopy with time-of-flight detection mass spectroscopy (MALDI-ToF MS). The MALDI-ToF MS (M_n) values correspond to 1400, 3200, and 7000 g/mol. Thus, the degree of polymerization (as obtained by MALDI-ToF) corresponds to roughly 8 (P3HT1), 19 (P3HT2), and 42 repeating units (P3HT3). While the molecular weights determined with SEC and MALDI-ToF MS were nearly the same for P3HT1, the SEC molecular weights are usually overestimated for higher molecular weight P3HTs. This is expected if a rather stiff polymer like P3HT is measured with a column calibrated with a more flexible polystyrene standard.¹⁹ MALDI-ToF MS also indicates that the predominant end groups ($\geq 80\%$) after polymerization were a bromine arising from the starting unit and a hydrogen resulting from quenching the active chain end with hydrochloric acid (Figure 2). Scheme 1 shows the synthetic procedure for the monocarboxylation of P3HTs via a Grignard reaction. The bromine end groups were selectively and quantitatively transformed into an active Grignard species via a metathesis reaction with *i*-PrMgCl. The introduction of gaseous CO₂ and quenching the reaction with hydrochloric acid resulted in a quantitative conversion of the Br chain ends to COOH groups.



Scheme 1: Synthetic scheme for monocarboxylated poly(3-hexylthiophene)s (P3HT-COOHs) via a Grignard reaction at the bromine chain end with gaseous CO₂. Degrees of polymerization n , were calculated from MALDI-ToF MS.

The size exclusion chromatography traces of the monocarboxylated P3HT-COOHs are shown in Figure 1, and the respective data as compared with nonfunctionalized P3HTs are given in Table 1. After monocarboxylation the polydispersity index of all polymers remained low, and there were only minor shifts in the number-average molecular weights. Thus, only negligible chain coupling occurred, and the modification is well controlled. For the lowest molecular weight sample P3HT1-COOH, the M_n increased during functionalization by about 300 g/mol (SEC). This

is due to the fact that carboxylation improves the polarity of the polymer, and thus shorter functionalized chains were removed during Soxhlet extraction with methanol.

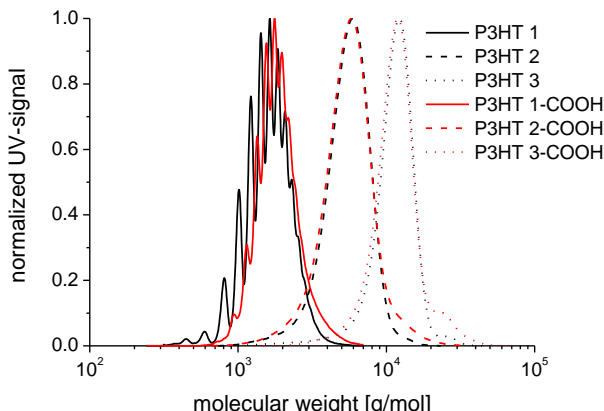


Figure 1: Size exclusion chromatography (SEC) traces of nonfunctionalized poly(3-hexylthiophene)s (P3HTs) and monocarboxylated poly(3-hexylthiophene)s (P3HT-COOHs) with different chain lengths. Number-average molecular weight M_n increases from 1800 to 10200 g/mol for P3HT1 to P3HT3. After functionalization no serious changes in the molecular weight distributions are observed.

Table 1: Molecular weights and molecular weight distributions (PDI) determined with size exclusion chromatography (SEC) and MALDI-ToF MS of nonfunctionalized poly(3-hexylthiophene)s (P3HTs) and monocarboxylated poly(3-hexylthiophene)s (P3HT-COOHs). DP = degree of polymerization; M_n = number-average molecular weight.

| Sample | M_n (SEC) [g/mol] | M_n (MALDI) [g/mol] | DP (MALDI) | PDI (SEC) |
|-------------|---------------------|-----------------------|------------|-----------|
| P3HT 1 | 1500 | 1400 | 8 | 1.11 |
| P3HT 2 | 5000 | 3200 | 20 | 1.15 |
| P3HT 3 | 10200 | 7000 | 42 | 1.15 |
| P3HT 1-COOH | 1800 | 1500 | 9 | 1.11 |
| P3HT 2-COOH | 5000 | 3200 | 20 | 1.17 |
| P3HT 3-COOH | 10800 | 7000 | 42 | 1.16 |

MALDI-TOF MS additionally allows an analysis of the end groups before and after carboxylation. Figure 2 shows the spectra of P3HT2 and P3HT2-COOH as a representative example (for others see Supporting Information). All the P3HTs exhibit >80% H/Br end groups. While the minor molecular weight peak series ($\leq 20\%$) with hydrogen/hydrogen end groups remained unchanged during functionalization, a quantitative conversion of the bromine end groups in the hydrogen/bromine series is observed. The peaks are shifted by 35 g/mol (2908 g/mol - 2873 g/mol = 35 g/mol), which is equivalent to the mass difference between a bromine atom (79.9 g/mol) and a carboxylic acid group (45 g/mol). The intensity ratio between H/H end groups and H/COOH end groups in P3HT2-COOH is nearly the same as the ratio between H/H and H/Br end groups in P3HT2, which also indicates the quantitative transformation. However, this assumption has to be taken with caution since it is only true if the desorption behaviors of P3HTs with bromine and carboxylic acid end groups are the same. But the quantitative transformation is further confirmed by ^1H NMR analysis. The $\alpha\text{-CH}_2$ signal of the end group unit with bromine at 2.57 ppm vanishes, and a new signal for the $\alpha\text{-CH}_2$ signal of the

COOH-terminated end group unit appears at 3.01 ppm. These signals have the same integral ratio in comparison to the α -CH₂ signal of the repeating units at 2.80 ppm

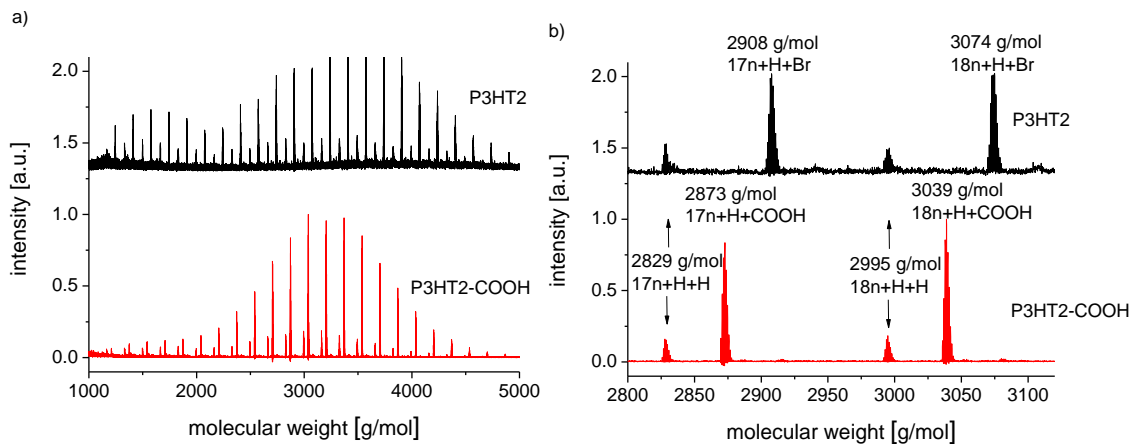


Figure 2: (a) MALDI-ToF MS spectra of nonfunctionalized poly(3-hexylthiophene) with a size exclusion molecular weight of 5000 g/mol (P3HT2) and the respective monocarboxylated poly(3-hexylthiophene) (P3HT2-COOH.) (b) Magnified section of the MALDI-ToF MS spectra for 17 and 18 repeating units with the molecular weights and end groups for all peak series. A high (>80%) content of H/Br chain ends for P3HT2 is obtained, which are quantitatively transformed into H/COOH end groups for P3HT2-COOH.

Optical Characterization

It is interesting to study the influence of one carboxylic end group on the thermal and optical properties in solution, bulk, and thin films, depending on the chain length of the monocarboxylated polymers. This is of utmost importance if these polymers are to be used as electronic materials in devices. While bromine end groups may have only sterical effects on the packing of P3HT, COOH groups have the ability to form hydrogen bonds and thus may behave different toward molecular packing. The existence of hydrogen bonds can be evidenced in the FT-IR spectra of the P3HT-COOHs (see Supporting Information). The C=O vibration of the carboxylic acid groups in P3HT-COOHs occur at 1665 cm⁻¹ and the O-H overtone vibrations at 2542 and 2644 cm⁻¹, corresponding to characteristic hydrogen-bonded acid groups.¹¹ The usual O-H stretching vibrations between 3000 and 3500 cm⁻¹ overlap with the C-H vibrations.

The three functionalized P3HT-COOHs were further characterized with UV-vis spectroscopy in THF solution (concentration 0.02 mg/mL) and thin films (thickness ca. 100 nm on quartz by spin coating from 1 wt% solution in CHCl₃). The respective data for thin films are shown in Figure 3 and that for solutions in the Supporting Information. Generally, the solution spectra for all P3HT-COOHs are comparable to the respective nonfunctionalized P3HTs. The λ_{max} values in solution vary from 415 to 443 nm for P3HT1-COOH to P3HT3-COOH. The spectrum of P3HT1-COOH is hypsochromically shifted, and a loss of optical density can be observed in comparison to P3HT2-COOH and P3HT3-COOH. This is not unexpected since the maximum conjugation length is not yet reached for a polymer with ca. 9 repeating units. For the two higher molecular weight samples P3HT2-COOH and P3HT3-COOH (for spectra see Supporting

Information) the optical density and the maximum absorption wavelength λ_{\max} are almost the same. A maximum conjugation seems reached.

In films, P3HTs exhibit more pronounced vibronic fine structure than the P3HT-COOHs. Generally, all maxima are shifted bathochromically in comparison to the solution spectra and vary between 447 and 510 nm with increasing chain length (Figure 3c). Similar to the solution spectra both P3HT1 and P3HT1-COOH show low λ_{\max} values and no vibronic fine structure in thin films as well. The bathochromic shift from solution to film is only 32 nm, and the optical density is lower than for the higher molecular weight samples. Low molecular weight P3HT1 or P3HT1-COOH do not crystallize in thin films, which is explained in detail in thermal characterization (see Table 2). Thus, for P3HT1 and P3HT1-COOH the bathochromic shift is only caused by a change of the polarity in film compared to the THF solution.²⁰ For the higher molecular weight samples (P3HT2-COOH, P3HT3-COOH), the λ_{\max} shift from solution to film spectra is around 70 nm (e.g., 439 to 511 nm; see Figure 3c). Additionally, a vibronic fine structure is observed as seen in the corresponding P3HTs. The fine structure is less pronounced than in the nonfunctionalized homologues shown in Figure 3a. This fine structure is typical for polymers with π - π -stacking and is more pronounced for the higher molecular weight sample P3HT3-COOH. It is obvious that unlike the earlier reported multicarboxylation method, where the functionalized P3HT completely loses its crystallinity, the controlled monocarboxylation leads to P3HT-COOHs with sufficient crystallization and π - π -stacking.¹¹

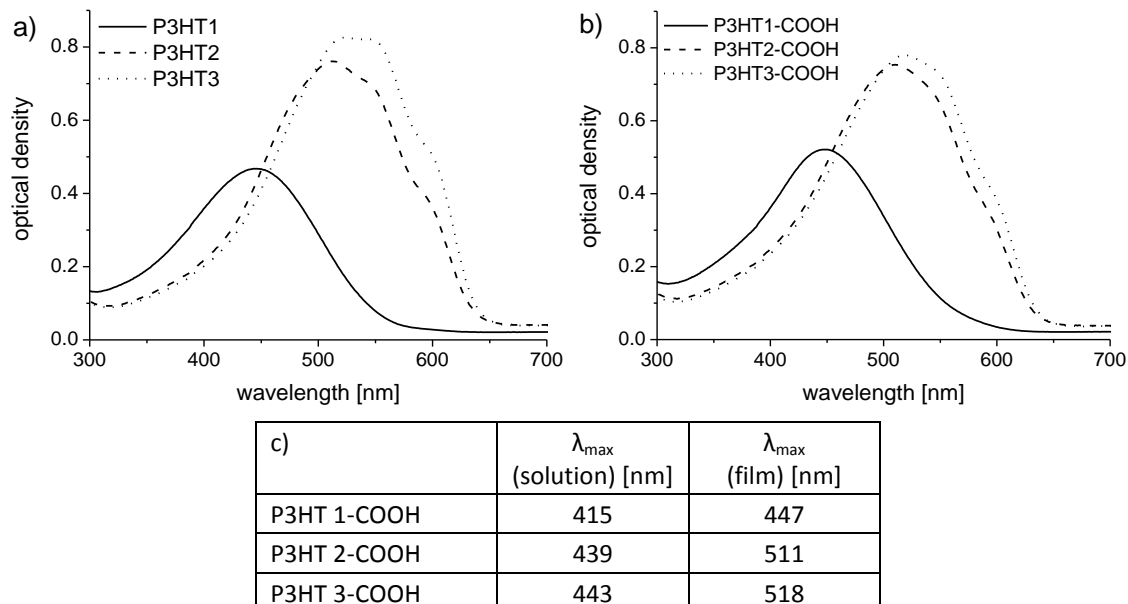


Figure 3: UV-vis spectra of (a) nonfunctionalized poly(3-hexylthiophene)s (P3HTs) and (b) monocarboxylated poly(3-hexylthiophene)s (P3HT-COOHs) measured on thin films on quartz (thickness ca. 100 nm spin-coated from 1 wt% solution in CHCl_3). (c) Maximum absorption wavelength λ_{\max} of the P3HT-COOHs in solution (0.02 mg/mL in THF) and in ca. 100 nm thick films on quartz. P3HT2-COOH and P3HT3-COOH show a vibronic fine structure in thin film, which is only little less pronounced than for P3HT2 and P3HT3. This indicates that both carboxylated P3HT-COOHs crystallize in thin films. For solution spectra, see the Supporting Information.

Thermal Characterization

More information about the crystallization behavior of the P3HT-COOHs can be gained from the thermal analysis. In general, all P3HT-COOHs showed a little lower degradation temperature (e.g., P3HT3-COOH onset 230 °C) than the nonfunctionalized P3HTs (P3HT3 onset 250 °C). This is expected due to the thermal instability of the carboxylic acid group. The differential scanning calorimetry (DSC) analysis showed that the COOH end groups also influence the melting behavior of the P3HT-COOHs as discussed below (Table 2).

Table 2: Melting temperature T_m in second heating cycle, recrystallization temperature T_c and melting enthalpy ΔH_m of monocarboxylated poly(3-hexylthiophene)s (P3HT-COOHs) and nonfunctionalized poly(3-hexylthiophene)s (P3HTs). T_{m2} is the melting point of the lamellar main chain stacking and T_{m1} is the melting point observed in low molecular weight P3HTs which cannot be assigned to a lamellar main chain packing.

| | T_{m1}/T_{c1} [°C] | T_{m2}/T_{c2} [°C] | ΔH_{m2} [J/g] |
|-------------|-------------------------|-------------------------|--------------------------|
| P3HT 1 | 23/-9 | - | - |
| P3HT 1-COOH | 53/- | - | - |
| P3HT 2 | 64/57 | 183/165 | 10 |
| P3HT 2-COOH | 59/- | 183/164 | 9 |
| P3HT 3 | - | 225/195 | 22 |
| P3HT 3-COOH | - | 219/191 | 11 |

The low-molecular-weight samples P3HT1 and P3HT1-COOH show a melting transition (T_{m1}) at 23 °C and 53 °C respectively (Table 2). While P3HT1 shows a recrystallization at -9 °C, the recrystallization is kinetically hindered for P3HT1-COOH. Only in the first heating cycle a melting transition is seen at 53 °C. No recrystallization is observed during cooling under DSC scan rates of 10 K/min. But after a few days storing at room temperature, the melting transition is recovered during the next heating cycle. These transitions are not at typical temperatures for main chain crystallization, which should have a transition at higher temperatures according to theoretical calculations. The main chain melting temperature T_{m2} can be calculated with eq 2, which shows the melting point depression of polymers and has been adapted to P3HT by Wegner et. al.^{21,22}

$$\frac{1}{T_{m2}} - \frac{1}{T_{m2}^0} = \frac{R}{\Delta H_{m2}^0} \frac{2}{n} \quad (2)$$

In this equation T_{m2}^0 is the melting temperature of a perfect crystal, ΔH_{m2}^0 the heat of fusion per mole of crystalline monomers, n the degree of polymerization (DP), and R the ideal gas constant. To calculate T_{m2}^0 and ΔH_{m2}^0 , DSC data from two additional polymer samples P3HT4 and P3HT5 (Table 3) were used, and $1/T_{m2}$ was plotted against $2/n$ (Figure 4). T_{m2}^0 and ΔH_{m2}^0 were calculated from the linear fit to be 273 °C and 13 J/g. Using these parameters, the theoretical main chain melting point (T_{m2}) of P3HT1 could be calculated to be 117 °C. We have recently shown that in low-molecular-weight P3HT with $M_n = 5000$ g/mol an additional melting point for the side chains is observed around 60 °C; the side-chain crystallization being

kinetically hindered for higher molecular weight samples.²³ Thus, the observed transitions T_{m1} in P3HT1 and P3HT1-COOH might be arising from side chain melting. An exact crystalline structure elucidation requires detailed SAXS/WAXS measurements.

Table 3: Main chain melting points T_{m2} of different poly(3-hexylthiophene)s along with the respective degree of polymerization (DP) as determined by MALDI-ToF MS. ^{a)}Calculated from eq 2 and linear fit of $1/T_{m2}$ against $2/n$ from Figure 4. P3HT 4 and P3HT 5 samples were additionally used to plot eq 2

| | T_{m2} [°C] | DP = n (MALDI) |
|--------|-------------------|----------------|
| P3HT 1 | 117 ^{a)} | 8 |
| P3HT 2 | 183 | 20 |
| P3HT 3 | 225 | 42 |
| P3HT 4 | 237 | 56 |
| P3HT 5 | 244 | 65 |

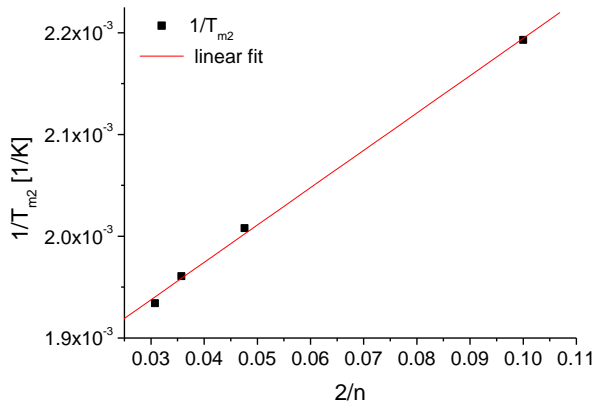


Figure 4: Plot of $1/T_{m2}$ against $2/n$ with a linear fit for the calculation of T^0_{m2} and ΔH^0_{m2} . T^0_{m2} is the melting temperature of a perfect crystal, and ΔH^0_{m2} is the heat of fusion per mole of crystalline monomers.

For P3HT2-COOH there is only a little influence of the COOH group on the thermal properties in comparison to P3HT2, bearing the bromine end group. Both polymers show a melting point of the main chain (T_{m2}) at 183 °C and a recrystallization at ca. 165 °C. Also, the melting enthalpies of the polymers are similar in the range of 9 J/g (P3HT2-COOH) and 10 J/g (P3HT2). The only difference is that P3HT2 exhibits a reversible side chain melting at 64 °C with a recrystallization at 54 °C. For P3HT2-COOH the side chains melt at 59 °C, but the recrystallization is again kinetically hindered, as in P3HT1-COOH. With a further increase in molecular weight from P3HT2-COOH to P3HT3-COOH, T_{m2} , T_{c2} , and ΔH_{m2} increase, but the shift in ΔH_{m2} is only small (2 J/g). A comparison with the nonfunctionalized P3HT3 ($\Delta H_{m2} = 22$ J/g) shows that the crystallinity of P3HT3-COOH ($\Delta H_{m2} = 11$ J/g) is lower. A maximum value of ΔH_{m2} seems to be reached for P3HT3-COOH with 11 J/g. As explained above, carboxylic acid groups can affect the crystallization by their capability to form hydrogen bonds. Hydrogen bonds are thermally stable interactions which may hinder the comparatively weaker π-π-interactions and thus lower the maximum ΔH_m . On comparison, the commercial P3HT sample with $M_n = 19400$ g/mol exhibits a ΔH_{m2} of 13 J/g. This indicates that the crystallinity of P3HT3-COOH is similar to

that of the commercial sample. As expected for high molecular weight P3HTs, no side chain melting was observed for these P3HT3, P3HT3-COOH, and the commercial sample. It is interesting to note that the multicarboxylated P3HT reported earlier was amorphous.¹¹

WAXS Analysis in Bulk

To gain more information about the crystal structure in bulk, wide-angle X-Ray measurements (WAXS) were performed.

Figure 5 shows the X-ray diffractograms of P3HT3-COOH and P3HT3 as a representative example (diffractogram of P3HT2-COOH and P3HT2 is given in the Supporting Information). DSC analysis shows that the crystallinity of the carboxylated P3HT3-COOH is lower than for P3HT3. Still both polymers show a well-defined X-ray pattern typical for highly regioregular P3HT: *h*00 reflections for the lamellar packing between main and side chains at *q* values of 7.9 (200) and 11.9 nm⁻¹ (300); a 0*k*0 reflection for the distance of the π-π-stacking and 00*l* reflections for the distance of the thiophene units along the chain at 16.3 nm⁻¹. Additionally mixed indices 120, 220, and 320 are observed at higher *q* values as shown in Figure 5, which indicate the order of the side chains as reported previously.²³ This confirms a highly ordered structure even for the carboxylated P3HT3-COOH.

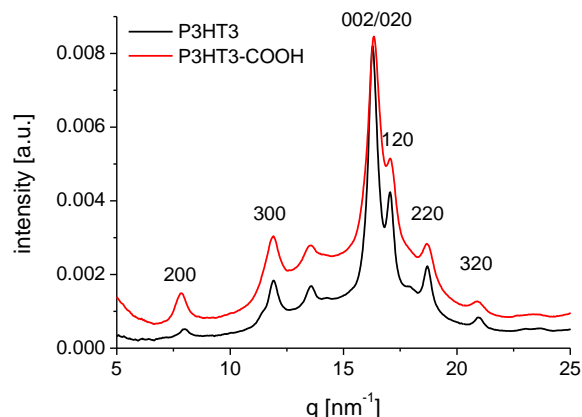


*Figure 5: Wide-angle X-ray diffractograms in bulk samples for nonfunctionalized poly(3-hexylthiophene) (P3HT3) and monocarboxylated poly(3-hexylthiophene) (P3HT3-COOH). Both polymers show *h*00 reflection for lamellar stacking of main and side chain, a 0*k*0 reflection for the π-π-stacking and 00*l* reflections for the order along the chain. The mixed *hk*0 indices at high *q* values indicate additional side chain order.*

Charge Carrier Mobility Measurements in OFET Devices

For the use in organic electronic devices, it is important to study the influence of the COOH group on the charge carrier mobility of the polymer. Usually the charge carrier mobility of P3HT, as measured in organic field effect transistors (OFETs), increases with molecular weight.²⁴ Only the two higher molecular weight samples P3HT2-COOH and P3HT3-COOH were studied in OFETs and compared with the respective P3HTs. Both polymers crystallize in thin films and thus are promising candidates for application in devices. Preliminary mobility measurements were performed in organic field effect transistors with the output

characteristics shown in the Supporting Information. For P3HT2 and P3HT2-COOH the mobilities were determined to be 2×10^{-3} and $1 \times 10^{-3} \text{ cm}^2/(\text{Vs})$. Since both polymers have similar melting enthalpies (9 and 10 J/g) and thus similar crystallinities, no influence of the COOH group on the mobility was observed. For P3HT3-COOH, the hole mobility was $2 \times 10^{-3} \text{ cm}^2/(\text{Vs})$. This is again conclusive with the thermal analysis which showed a melting enthalpy of P3HT3-COOH (11 J/g) in the same range as for P3HT2 and P3HT2-COOH. For the uncarboxylated P3HT3 with a high melting enthalpy of 22 J/g the mobility was 1 order of magnitude higher with a value of $1 \times 10^{-2} \text{ cm}^2/(\text{Vs})$. Thus, all measured mobilities could be correlated with crystallinity of the respective polymers. Despite the decrease in mobility of P3HT3-COOH compared to P3HT3, values in the range of $10^{-3} \text{ cm}^2/(\text{Vs})$ are still high and good enough for the application as a hole conductor dye in hybrid solar cells. This becomes clear by looking at the mobility of a regioregular commercial P3HT with a M_n of 19400 g/mol, which also showed a mobility in the range of $10^{-3} \text{ cm}^2/(\text{Vs})$ under the same conditions of device preparation and measurement. Thus, P3HT-COOHs are materials with a reasonable high mobility, depending on their molecular weight. Additionally, they carry anchoring groups for the coordination of nanoparticles or for the chemisorption on semiconductor metal oxides such as titanium dioxide. A qualitative proof of the anchoring of P3HT-COOH to TiO₂ is given in the Supporting Information.

Conclusion

In conclusion, three P3HT-COOHs bearing single carboxylic acid groups at the chain ends were synthesized. The successful and very selective functionalization was confirmed with MALDI-ToF MS. Optical analysis revealed that the higher molecular weight samples P3HT2-COOH and P3HT3-COOH are crystalline in thin films. Thermal analysis supports that the functional polymers still crystallize, but a maximum melting enthalpy seems reached for P3HT3-COOH with a molecular weight of 10800 g/mol and 42 repeating units. WAXS analysis shows that the crystals are highly ordered. The mobility of P3HT2-COOH and P3HT3-COOH is in the order of $10^{-3} \text{ cm}^2/(\text{Vs})$. This high mobility and the carboxylic acid anchoring group make them very promising candidates for the application in hybrid devices.

Acknowledgment

We acknowledge financial support for this research work from DFG SFB 840. R. H. Lohwasser thanks the elite network Bavaria for a research stipend. Thanks go also to M. Sommer for providing P3HT 1 as well as to A. Ringk, C. R. Singh, C. Probst, and S. Czich for help with the characterization. Further we acknowledge the European Synchrotron Radiation Facility (Dr. M. Sztucki and Dr. Narayanan) for measurement time and facilities at the beamline ID2.

Supporting Information Available: Figures showing FT-IR spectra, UV-vis spectra in solution, X-ray diffractograms, and output characteristics of OFET. This material is available free of charge via the Internet at <http://pubs.acs.org>.

References

- (1) Sirringhaus, H.; Tessler, N.; Friend, R. H. *Science* **1998**, *280*, 1741-1744.
- (2) Ma, W.; Yang, C.; Gong, X.; Lee, K.; Heeger, A. J. *Adv. Funct. Mater.* **2005**, *15*, 1617-1622.
- (3) Jen, K.-Y.; Miller, G. G.; Elsenbaumer, R. L. *Chem. Commun.* **1986**, 1346-1347.
- (4) Chen, T.; Rieke, R. D. *J. Am. Chem. Soc.* **1992**, *114*, 10087-10088.
- (5) McCullough, R. D.; Lowe, R. D. *Chem. Commun.* **1992**, 70-72.
- (6) Miyakoshi, R.; Yokoyama, A.; Yokozawa, T. *J. Am. Chem. Soc.* **2005**, *127*, 17542-17547.
- (7) Sheina, E. E.; Liu, J.; Iovu, M. C.; Laird, D. W.; McCullough, R. D. *Macromolecules* **2004**, *37*, 3526-3528.
- (8) Adachi, I.; Miyakoshi, R.; Yokoyama, A.; Yokozawa, T. *Macromolecules* **2006**, *39*, 7793-7795.
- (9) McCullough, R. D.; Zhai, L. *Adv. Mater.* **2002**, *14*, 901-905.
- (10) Iovu, M. C.; Craley, C. R.; Jeffries-El, M.; Krankowski, A. B.; Zhang, R.; Kowalewski, T.; McCullough, R. D. *Macromolecules* **2007**, *40*, 4733-4735.
- (11) Lohwasser, R.; Bandara, J.; Thelakkat, M. *J. Mater. Chem.* **2009**, *19*, 4126-4130.
- (12) Sommer, M.; Lang, A. S.; Thelakkat, M. *Angew. Chem. Int. Ed.* **2008**, *47*, 7901-7904.
- (13) Liu, J.; McCullough, R. D. *Macromolecules* **2002**, *35*, 9882-9889.
- (14) Liu, J.; Tanaka, T.; Sivula, K.; Alivisatos, A. P.; Fréchet, J. M. J. *J. Am. Chem. Soc.* **2004**, *126*, 6550-6551.
- (15) Jeffries-El, M.; Sauve, G.; McCullough, R. D. *Macromolecules* **2005**, *38*, 10346-10352.
- (16) Van Hecke, G. R.; Horrocks, W. *Inorg. Chem.* **1966**, *5*, 1968-1974.
- (17) Krasovskiy, A.; Knochel, P. *Synthesis* **2006**, *5*, 890-891.
- (18) Sze, S. M.; Ng, K. K. In *Physics of Semiconductor Devices*; Wiley-Interscience: Hoboken, NJ , **2007**.
- (19) Liu, J.; Loewe, R. S.; McCullough, R. D. *Macromolecules* **1999**, *32*, 5777-5785.
- (20) Trznadel, M.; Pron, A.; Zagorska, M.; Chrzaszcz, R.; Pielichowski, J. *Macromolecules* **1998**, *31*, 5051-5058.
- (21) Sperling, L. H. In *Introduction to Physical Polymer Science*, 4 th ed.; John Wiley & Sons, Inc.: Hoboken, NJ, **2006**; p. 301.
- (22) Zen, A.; Saphiannikova, M.; Neher, D.; Grenzer, J.; Grigorian, S.; Pietsch, U.; Asawapirom, U.; Janietz, S.; Scherf, U.; Lieberwirth, I.; Wegner, G. *Macromolecules* **2006**, *39*, 2162-2171.
- (23) Wu, Z.; Petzold, A.; Henze, T.; Thurn-Albrecht, T.; Lohwasser, R. H.; Sommer, M.; Thelakkat, M. *Macromolecules* **2010**, *43*, 4646-4653.
- (24) Kline, R. J.; McGehee, M. D.; Kadnikova, E. N.; Liu, J.; Frechet, J. M. J. *Adv. Mater.* **2003**, *15*, 1519-1522.

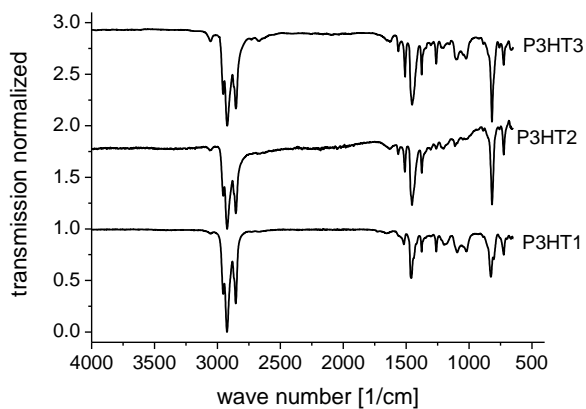
Supporting Info**FT-IR Spectra of P3HTs and Monocarboxylated P3HT-COOHs**

Figure SI-1: FT-IR spectra of nonfunctionalized poly(3-hexylthiophene)s P3HT1 (1500 g/mol), P3HT2 (5000 g/mol) and P3HT3 (10200 g/mol).

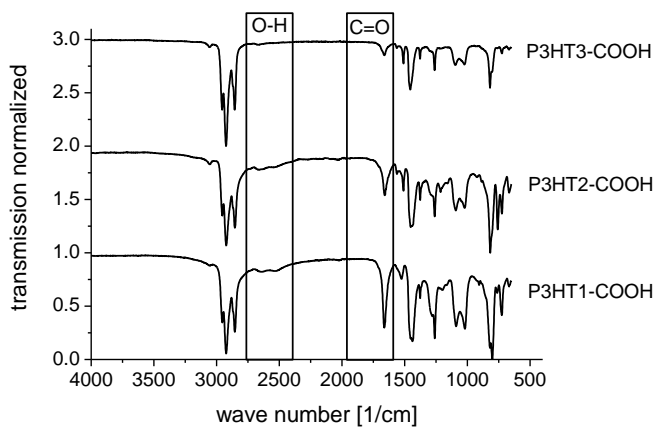


Figure SI-2: FT-IR spectra of monocarboxylated poly(3-hexylthiophene)s P3HT1-COOH (1800 g/mol), P3HT2-COOH (5000 g/mol) and P3HT3-COOH (10800 g/mol) with the respective signals for the carboxylic acid group. With increasing molecular weight from P3HT1-COOH to P3HT3-COOH the intensity of the carboxylic acid signals decrease, because of the lower % content of end groups with respect to polymer chains.

UV-vis Spectra of P3HTs and P3HT-COOHs in Solution

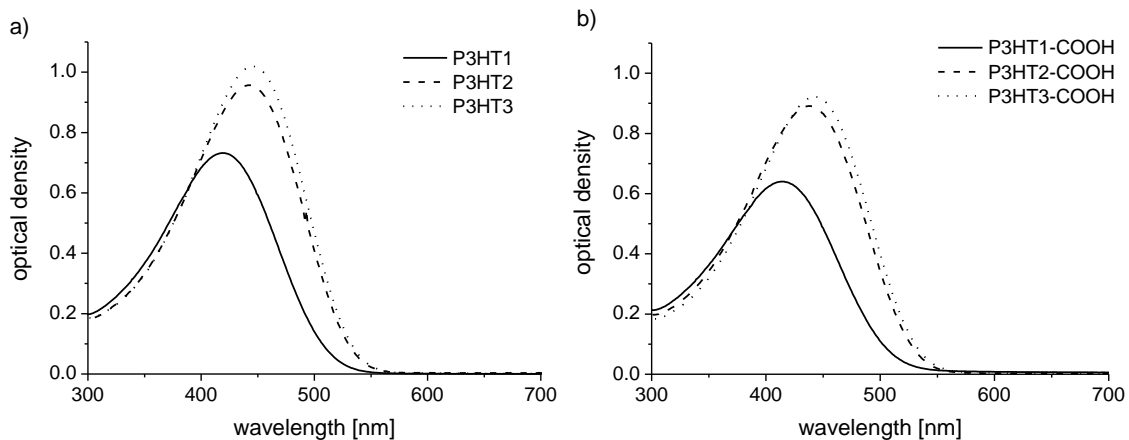


Figure SI-3: UV-vis spectra of (a) nonfunctionalized poly(3-hexylthiophene)s (P3HTs) (b) monocarboxylated poly(3-hexylthiophene)s (P3HT-COOHs) measured in THF solution (concentration 0.02 mg/ml). P3HT2-COOH and P3HT3-COOH show a similar absorption, while the maximum conjugation length is not yet reached for P3HT1-COOH. The absorption behavior of all P3HT-COOHs is similar to the respective noncarboxylated P3HTs.

MALDI-ToF MS Spectra of P3HT1-COOH and P3HT3-COOH

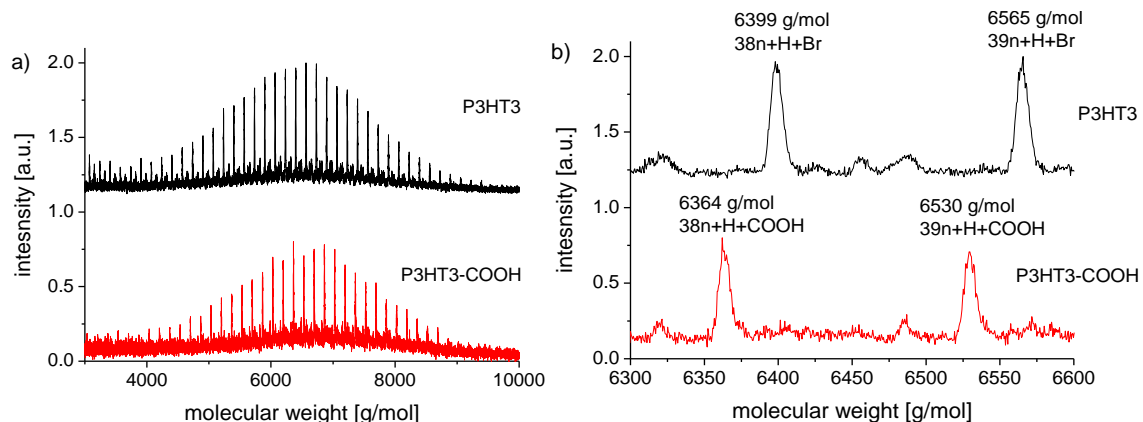


Figure SI-4: (a) MALDI-ToF MS spectra of nonfunctionalized poly(3-hexylthiophene) P3HT3 and monocarboxylated poly(3-hexylthiophene) P3HT3-COOH. (b) Magnified section of the MALDI-ToF MS spectra for 38 and 39 repeating units with the molecular weights and end groups for both peak series. Only one peak series with H/Br chain ends is obtained for P3HT3. The bromine ends are quantitatively transformed into COOH ends for P3HT3-COOH.

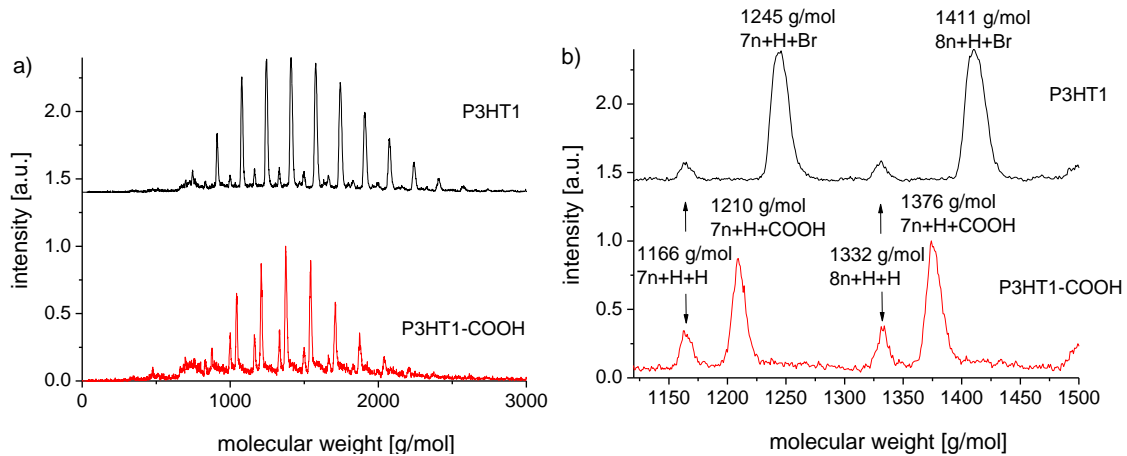


Figure SI-5: (a) MALDI-ToF MS spectra of nonfunctionalized poly(3-hexylthiophene) P3HT1 and monocarboxylated poly(3-hexylthiophene) P3HT1-COOH. (b) Magnified section of the MALDI-ToF MS spectra for 7 and 8 repeating units with the molecular weights and end groups for all peak series. A high content (>80%) of H/Br chain ends for P3HT1 is obtained, which are quantitatively transformed into H/COOH end groups for P3HT1-COOH.

WAXS Analysis in Bulk of P3HT2 and P3HT2-COOH

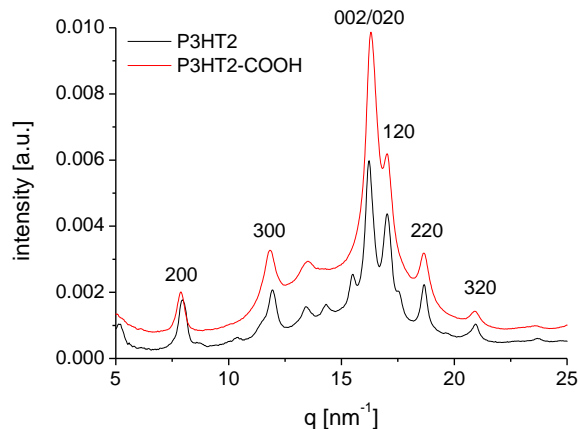


Figure SI-6: Wide angle X-ray diffractograms in bulk samples for non-functionalized poly(3-hexylthiophene) P3HT2 and monocarboxylated poly(3-hexylthiophene) P3HT2-COOH. Both polymers show $h00$ reflection for lamellar stacking of main and side chain, a $0k0$ reflection for the $\pi\text{-}\pi$ -stacking and $00l$ reflections for the order along the chain. The mixed $hk0$ indices at high q values indicate additional side chain order.

Output Characteristics of P3HT2-COOH and P3HT3-COOH

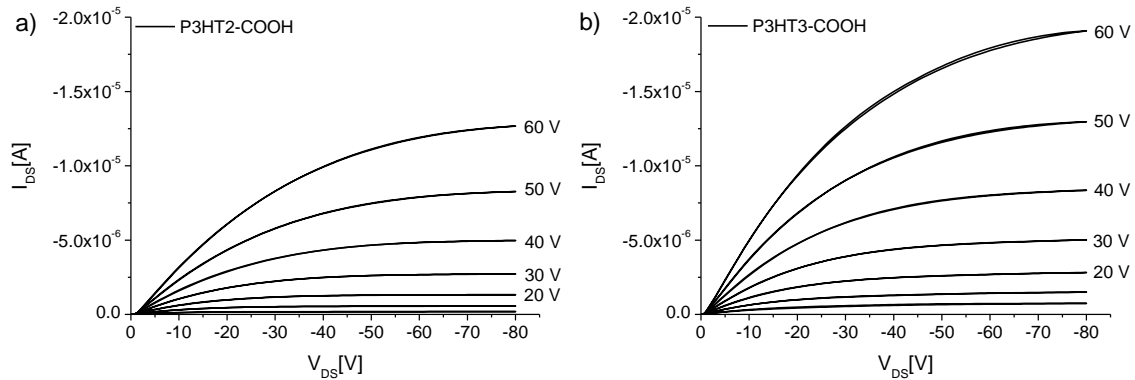


Figure SI-7: Output characteristics (I_{DS} - V_{DS}) of organic thin film transistors of (a) P3HT2-COOH and (b) P3HT3-COOH. The geometry was bottom gate device with SiO_2 as gate dielectric coated with a hexamethyldisilazane (HMDS) layer. The gate Voltage V_g was varied in -10 V steps from 0 V to -60 V.

Anchoring of P3HT2-COOH on TiO_2



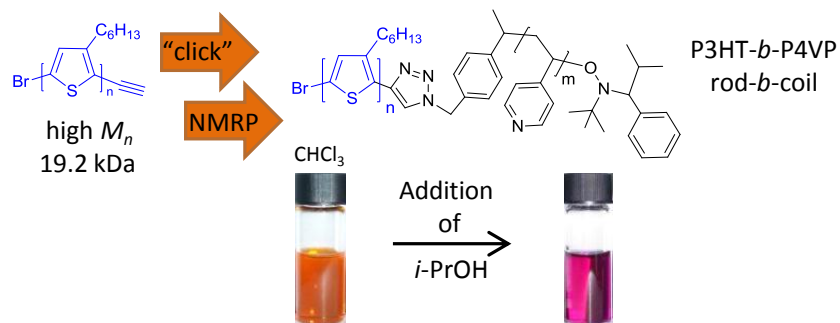
Figure SI-8: Picture of TiO_2 substrate anchored with P3HT2-COOH. The substrate was extensively washed with chloroform to guarantee that all physically attached polymer is washed away and only the chemisorbed P3HT2-COOH stays on the surface. The purple color clearly indicates P3HT2-COOH on the surface of TiO_2 .

7. Synthesis of Amphiphilic Rod-Coil P3HT-*b*-P4VP Carrying a Long Conjugated Block using NMRP and Click Chemistry

Ruth H. Lohwasser and Mukundan Thelakkat*

Applied Functional Polymers, Department of Macromolecular Chemistry I,
University of Bayreuth, Universitätsstraße 30, 95444 Bayreuth, Germany.

* E-Mail corresponding author: mukundan.thelakkat@uni-bayreuth.de



Submitted to *Macromolecules*

Abstract

We use a combination of click chemistry and nitroxide mediated radical polymerization (NMRP) for the incorporation of high molecular weight poly(3-hexylthiophenes) (P3HTs) segments into amphiphilic block copolymers. First a high molecular weight alkyne terminated P3HT was synthesized using catalyst transfer polymerization followed by in situ end capping with alkyne and by quenching with methanol. We found out that hydrochloric acid, the best quenching agent for non-functionalized P3HTs leads to addition reactions with the alkyne group and therefore is not suitable for alkyne terminated P3HT. With the use of copper catalyzed azide alkyne click reaction, P3HT-alkoxyamine is formed as a macroinitiator for NMRP. This was used to polymerize 4-vinylpyridine to get amphiphilic rod-coil P3HT-*b*-P4VP block copolymers with 55 and 77wt% of poly(4-vinylpyridine) (P4VP). We investigate how the optical and thermal properties as well as the phase separation behavior depend on the block ratios. These P3HT-*b*-P4VP copolymers are interesting for hybrid organic photovoltaics as well as for studying the colloidal structures of semiconductor amphiphilic systems. The high molecular weight rod influences the rod-rod interaction as described by the Maier-Saupe parameter ω and therefore has consequences in the microphase separation.

Introduction

Poly(3-hexylthiophene) (P3HT) is one of the widely studied conjugated polymers. It is intensively investigated for applications in organic electronic devices, such as photovoltaics, organic field effect transistors (OFETs) or organic light emitting diodes (OLEDs).^{1,2} It has also been incorporated into different types of block copolymers such as. P3HT-*b*-polystyrene, P3HT-*b*-poly(perylene bisimide acrylate), P3HT-*b*-fullerene, P3HT-*b*-polylactide, P3HT-*b*-poly(2-vinylpyridine) and others.³⁻⁹ A lot of different methods have been applied for the synthesis of the second block, ranging from anionic polymerization to ring opening metathesis polymerization (ROMP) and controlled radical polymerization methods.^{4,9-12} Also some work has been done which involved copper catalyzed azide alkyne cycloaddition reactions, better known as “click” chemistry.¹³⁻¹⁶ Most of these technics used relatively low molecular weight P3HTs (<10 kDa) corresponding to less than 40 repeating units.^{3,5,7,9,14,15,17,18} Only few reports are known for a high molecular weight P3HT block.^{4,12,13,19,20} However, for the application in organic electronic devices high charge carrier mobilities are necessary. From the literature it is known that the charge carrier mobility increases with molecular weight. A better interconnectivity between ordered domains and an increased crystallinity are discussed as the origin for the improved mobility of high molecular weight samples.²¹⁻²³ Therefore it is important to incorporate P3HTs with more than some 40 repeating units into a block copolymer to allow for good charge carrier mobility. Recently we also showed that the length of the P3HT block plays a major role for the efficiency of block copolymer solar cells. The block copolymers with a P3HT block of 17000 g/mol showed a much better external quantum efficiency than the blocks with a 8900 g/mol P3HT.²⁰ However, the direct in situ synthesis of

alkoxyamine macroinitiator resulted in appreciable amounts of difunctionalized derivative in addition to the desired monofunctionalized product when high molecular weight P3HT was used. Jeffries-El et al. have shown that P3HT can be functionalized with different end groups by reacting the active chain end with monofunctionalized Grignard reagents.²⁴ π -electron carrying Grignard reagents like ethynylmagnesium chloride lead to predominantly monofunctionalized P3HTs with only a low content of difunctionalized polymers. This alkyne function can be efficiently used in copper catalyzed azide alkyne reactions for polymer-polymer click or for the formation of P3HT macroinitiators.^{13-15,17} This was exploited earlier to obtain block copolymers containing low molecular weight P3HT segments.¹⁷ Here we adapted this method to prepare high molecular weight rod-coil block copolymers. Additionally, we demonstrate that the choice of the quenching reagent plays an important role in the successful functionalization with alkyne. Hydrochloric acid, which is the best quenching agent for non-functionalized P3HTs, leads to addition reactions with the alkyne group and therefore is not suitable. Further, we convert alkyne functionalized P3HT (P3HT-alkyne) into a high molecular weight macroinitiator for nitroxide mediated radical polymerization (NMRP) with the help of click chemistry. We use this macroinitiator for the polymerization of 4-vinylpyridine to get P3HT-*b*-P4VP block copolymers. P3HT is a hole conducting material and P4VP can coordinate electron conducting nanoparticles. Thus a fully functionalized system for hybrid solar cells could be achieved. It is known that the coordination of P4VP with nanoparticles is stronger than for P2VP because of the smaller steric hindrance of the nitrogen in position 4.²⁵ To the best of our knowledge, up to now only two reports of P3HT-*b*-P4VP are known in the literature.^{18,26} One using anionic polymerization and the other one using reversible addition fragmentation chain transfer (RAFT) for the synthesis of the second block. However, in both approaches, only small molecular weight P3HT blocks, could be incorporated. Apart from the potential application in organic photovoltaics, these P3HT-*b*-P4VP block copolymers are highly interesting as amphiphilic rod-coil systems for the formation of solution structures such as micelles, vesicles etc. and for understanding the phase separation and crystallization in such structures.²⁷⁻²⁹ Very recently Lee et al. reported about the change of stiffness of a short P3HT block of 6800 g/mol from a rigid rod to a semi-rigid chain to a flexible chain depending on the length of the second P2VP block.³⁰ These changes depend on the balance between the rod-rod interaction as described by the Maier-Saupe parameter ω and the length of the rod in contrast to the enthalpic interaction which depends on the Flory-Huggins interaction parameter χ (between the segments) and the total length of the block copolymer in the case of amorphous systems. Thus the phase behavior of block copolymers with a longer P3HT block and stronger rod-rod interactions are of high interest.

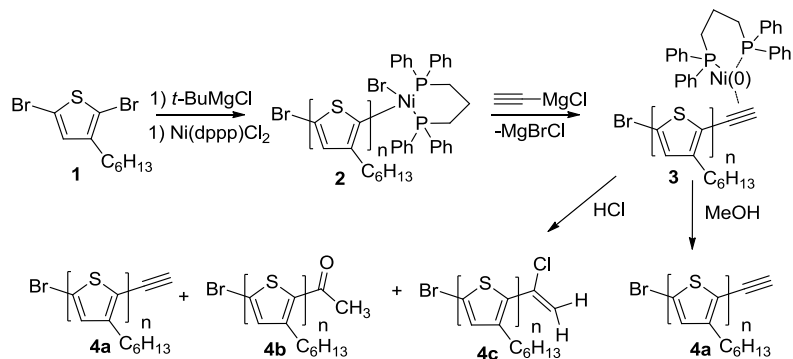
Two different block copolymers with P4VP contents of 55 and 77wt% were synthesized. Their thermal and optical properties are investigated and the preliminary bulk and solution structures depending on the different block ratios are shown.

Results and Discussion

Influence of Quenching Reagent on P3HT-alkyne

For the synthesis of a P3HT macroinitiator we used an alkyne functionalized P3HT. Jeffries-El et al. showed that P3HT-alkyne can easily be made by *in situ* end-capping of the active chain end with the monofunctionalized Grignard reagent ethynylmagnesium chloride.²⁴ Recently Li et al. found that this alkyne functionalized P3HT is sensitive to homocoupling during purification using a Soxhlet apparatus, which is catalyzed by residual metal traces.¹³ We observed similar behavior but the main reason for the formation of homocoupling seems not the residual metal traces but the increased temperature during hot extraction. We also found that when the reaction is quenched with methanol the catalyst remains as a solid, which is no longer soluble in chloroform. Dissolution of the P3HT-alkyne in chloroform, filtration and precipitation of the polymer in methanol several times at room temperature to remove the remaining catalyst traces yielded a monomodal distributed alkyne functionalized P3HT. Even though catalyst traces were removed by this cleaning process; we observed homocoupling if the solid polymer is stored at room temperature, indicating that it is a thermally initiated reaction. This could only be avoided by storing at temperatures below 0 °C.¹³

Here, we demonstrate that also the quenching reagent after functionalization plays a major role for the molecular weight distribution and the resulting end groups. Recently we showed that quenching the Kumada catalyst transfer polymerization (KCTP) of P3HT with methanol causes a small amount of chain-chain coupling by disproportionation.³¹ Therefore, hydrochloric acid was the preferred quenching reagent to gain monomodal distributed P3HT with 100% H/Br end groups.^{31,32} Generally in KCTP of P3HT, the catalyst is covalently bound to the chain end of the polymer before quenching. After end-capping with an alkyne Grignard reagent the situation is different. For example, the addition of ethynylmagnesium chloride to the active chain end leads to the formation of Ni(0)dppp which is found to form a stable π-complex (Scheme 1).³³ This is used to explain the predominately monofunctionalization by capping with unsaturated Grignard agents like allyl, ethynyl or vinyl.²⁴



Scheme 1. Mechanism for the formation of P3HT-alkyne via MeOH quenching and side reactions due to HCl as quenching reagent.

We found that for the alkyne functionalized P3HT, quenching the reaction with aqueous hydrochloric acid resulted in only very small amounts of the desired alkyne functionalized product. Instead it causes hydration and hydrohalogenation of the alkyne group as well as chain-chain coupling. To study this in details a small molecular weight sample was analyzed, because it allows MALDI-ToF MS measurements in the reflection mode and thus proper end group analysis. The addition products can be seen in MALDI-ToF MS by the presence of two new peak series (Figure 1a and 1b). The major peak series belongs to P3HT+C₂H+Br+HCl (e.g. for a 15-mer, 2635 g/mol = 15x166.3 g/mol + 25 g/mol + 79.9 g/mol + 36 g/mol) and the two minor ones to P3HT+C₂H+Br+H₂O (2617 g/mol = 15x166.3 g/mol + 25 g/mol + 79.9 g/mol + 18 g/mol) and the expected series for P3HT+C₂H+Br (2599 g/mol = 15*166.3 g/mol + 25 g/mol + 79.9 g/mol). Further evidence for these addition reactions can be gained from ¹H-NMR spectrum in Figure 1c.

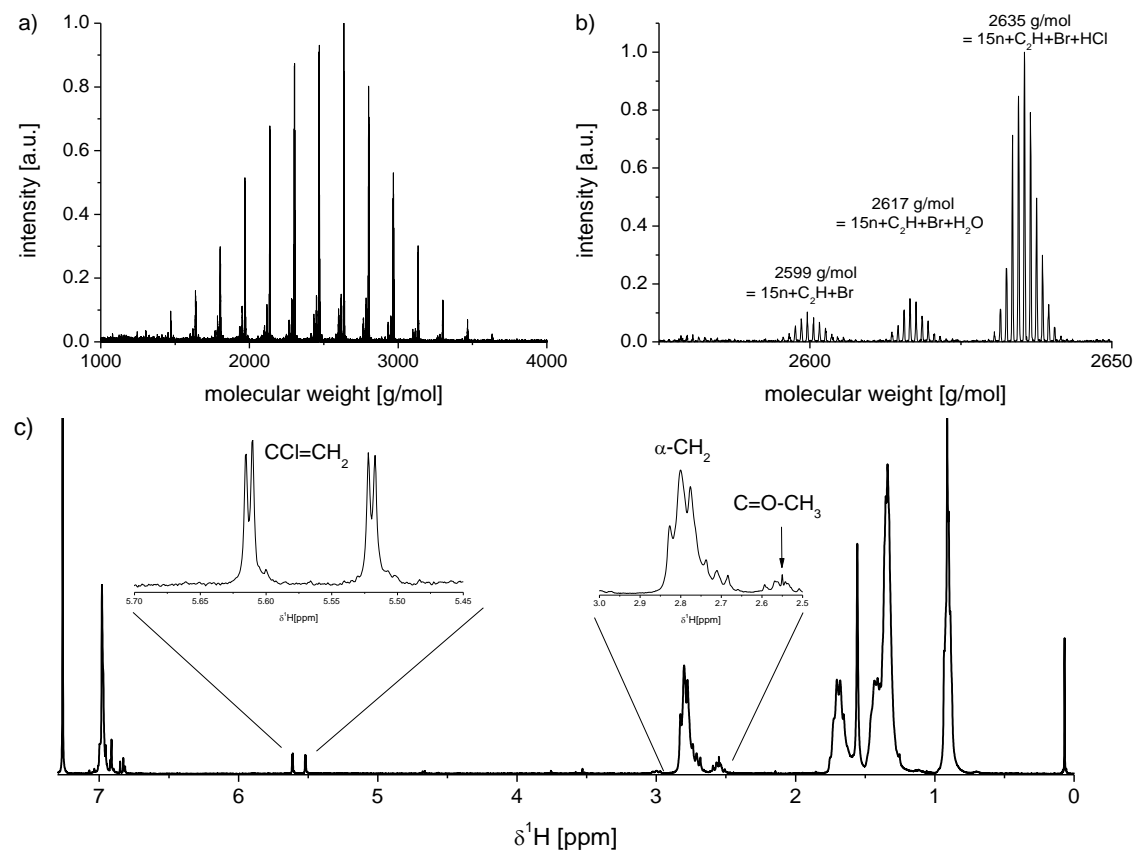


Figure 1. Spectra of P3HT obtained after quenching the end capping reaction of ethynylmagnesium chloride with hydrochloric acid at 0°C a) MALDI-ToF MS spectra measured in the reflection mode b) magnified part in the range of 15 repeating units c) ¹H-NMR spectrum. The respective end groups are indicated.

After quenching with HCl, almost no signal for the alkyne proton is visible at 3.53 ppm; instead three other end group signals appear; two doublets at 5.62 and 5.52 ppm as well as a very small singlet at 2.55 ppm (adjacent to the α-CH₂ signal of the alkyl chain at 2.80 ppm and overlapping with the α-CH₂ signal of the end group unit carrying a bromine at 2.57 ppm). The

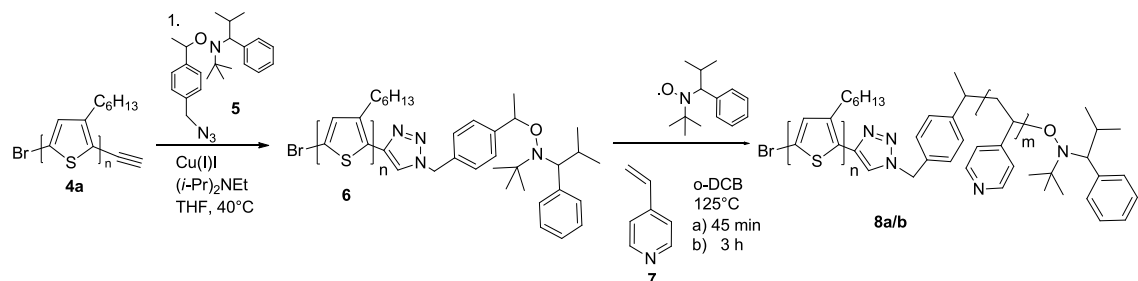
two doublets belong to the vicinal protons in **4c**, which is formed by the addition of HCl in a Markovnikov manner. The singlet at 2.55 ppm belongs to the CH₃ group of the methyl ketone which is formed by hydration resulting in **4b**. Because of keto enol tautomerie, the enol form transforms into the keto form as the final product. In the shown example, the intensity for the methyl ketone is very low because the main series is that of the hydrohalogenated product **4c** (supporting info shows ¹H-NMR and MALDI-ToF MS spectra of a sample with higher content of methylketone). The alkyne group of P3HT is electron rich because of the conjugation with the thiophene main chain and thus an electrophilic addition is promoted. Since aqueous HCl causes these addition reactions, it should not be used as a quenching reagent. Further a small shoulder at double the molecular weight is also observed (Figure SI 3 supporting information) due to chain-chain coupling.

After end capping with alkyne, Nickel is in a Ni(0) state. On quenching with MeOH, disproportionation which occurred for non-functionalized P3HTs is no longer possible for P3HT-alkyne. Thus methanol can be used as a suitable quenching reagent and the polymers show a monomodal distribution in size exclusion chromatography (SEC) (see Figure 3a and figure SI 3 supporting information). Additionally, the MALDI-ToF MS spectrum contains one main peak series belonging to P3HT with one bromine and one alkyne end group (see supporting information Figure SI 2). The smaller peak series arises due to difunctionalized P3HT. For example, in the sample from the quenching experiments, with a SEC number average molecular weight of 3200 g/mol, the major peak series corresponds to 90%. The influence of the chain length on the amount of dicapped P3HT was not investigated in detail. However, an even lower content of dicapped P3HT is expected with increasing molecular weight because the diffusion of Ni(0) to the bromine end groups slows with decreasing ratio of end groups to repeating units. For P3HT-alkynes with molecular weights of 20 kDa, it was difficult to verify this using MALDI-ToF MS because measuring in the reflection mode, which allows proper end group analysis, is no longer possible. The MALDI-ToF MS of a high molecular weight P3HT-alkyne, which was measured in the linear mode is shown in Figure 3b.

Synthesis of P3HT-*b*-P4VP

The synthesis route of the block copolymers P3HT-*b*-P4VP is shown in Scheme 2. P3HT-alkyne **4a** with a number average molecular weight of 19200 g/mol and a PDI of 1.14 was synthesized first, as explained in the section before. Here LiCl was used as an additive for obtaining a higher molecular weight because it speeds up polymerization.³¹ According to MALDI-ToF MS, this corresponds to a number average molecular weight of 12300 g/mol and about 74 repeating units. The NMRP-macronitiator was synthesized by reacting P3HT-alkyne with an alkoxyamine azide. For this, P3HT-alkyne **4a** was coupled with 2,2,5-trimethyl-3-(1'-p-azidomethylphenylethoxy)-4-phenyl-3-azahexane **5** using a copper catalyzed azide alkyne cycloaddition (Scheme 2). Cu(I)I and *N,N*-diisopropylethylamine were used as catalytic system in THF at 40°C.³⁴ The completion of this reaction was evidenced by ¹H-NMR spectroscopy (see

Figure 2). The signal of the alkyne proton of P3HT-alkyne (in **4a**) at 3.53 ppm vanishes and the two singlets belonging to the CH₂ units (two diastereomers) next to the azide shifts from 4.34 and 4.32 ppm (in **5**) to 5.60 and 5.56 ppm (in **6**) respectively. This shift in CH₂ signal and the complete disappearance of the alkyne proton signal clearly show a quantitative functionalization. Further, the other signals for the final alkoxyamine product are visible in the ¹H-NMR spectrum of P3HT macroinitiator **6**. The effect of the alkoxyamine on the hydrodynamic radius of P3HT is low and thus no significant shift was observed in SEC (Figure 3a).



*Scheme 2. Synthesis of P3HT-alkoxyamine macroinitiator **6** via copper catalyzed azide alkyne reaction and of P3HT-*b*-P4VP (**8a**, **8b**) using NMRP of 4-vinylpyridine.*

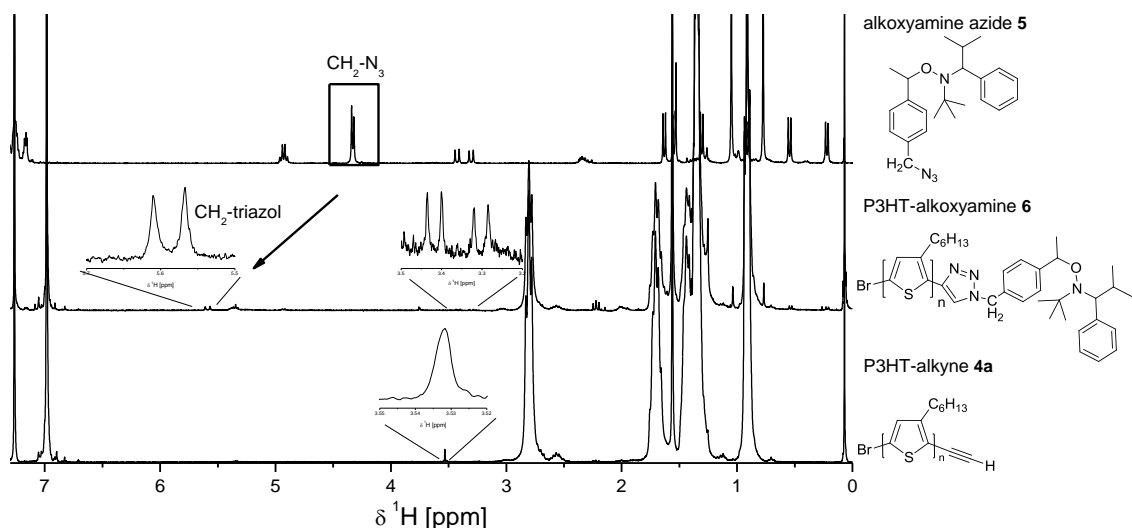


*Figure 2. ¹H-NMR spectra of P3HT-alkyne **4a**, P3HT-alkoxyamine **6** and 2,2,5-trimethyl-3-(1'-p-azidomethylphenylethoxy)-4-phenyl-3-azahexane **5** (alkoxyamine azide). In P3HT-alkyne **4a**, the signal for the alkyne proton at 3.53 ppm is enlarged. P3HT-alkoxyamine **6** shows no more signal for the alkyne proton in the region from 3.20 to 3.60 ppm, but additional signals belonging to the product alkoxyamine macroinitiator **6**. Further the two singlets; belonging to the CH₂ units of the two diastereomers next to the azide of **5**; shift from 4.34 and 4.32 ppm to 5.60 and 5.56 ppm because of the proximity to the triazole unit in P3HT-alkoxyamine **6**. This indicates a quantitative functionalization.*

Since the solubility of the individual segments, P3HT being a hydrophobic block and P4VP a hydrophilic block, are very different, it was important to choose the right solvent mixture for the synthesis of the block copolymers. Further, our earlier kinetic studies of NMRP of 4VP indicated the need to avoid a strong dilution of the monomer to allow for a good control of

polymerization.³⁵ Therefore, the 4-vinylpyridine (4VP) monomer itself was chosen as a solvent for P4VP and o-dichlorobenzene (o-DCB) as a solvent for P3HT. The volume ratio of 4VP:o-DCB was 1:1 and the ratio of monomer to macroinitiator to free nitroxide 3000:1:2. Unfortunately, because this huge excess of monomer was needed for a good solubility, it was not possible to perform kinetic studies. The intensity of the polymer signal in ¹H-NMR for the reaction mixture was too low in comparison to the monomer signal (due to the presence of 4VP as solvent) to enable the calculation of the percentage of conversion. Nevertheless, the polymerization proceeded quite fast at 125 °C and the amount of incorporated P4VP increased fast with polymerization time. P3HT-*b*-P4VP **8a** was obtained after 45 min and P3HT-*b*-P4VP **8b** after 3 h of polymerization resulting in two block copolymers with P3HT as the minor block (see Table 1). The initiation of the macroinitiator **6** was not complete as seen in the SEC curves of the raw products in the supporting information. But because of the amphiphilic nature of P3HT-*b*-P4VP, the remaining macroinitiator could be removed from the block copolymer by extraction with selective solvents for P3HT. First the block copolymers were washed with 1N HCl to protonate the P4VP block and to remove homopolymer which might have been formed during polymerization. In a second step the block copolymer was extracted with toluene in a Soxhlet apparatus until all P3HT macroinitiator **6** was removed. To recover the pure block copolymer it was deprotonated with diluted ammonia (NH₃:H₂O, v:v, 1:1) and extracted from the Soxhlet thimble with chloroform. Since P3HT-*b*-P4VP is an amphiphile performing SEC was difficult. The polymer was no longer soluble in THF, a common solvent for SEC of P3HT. Additionally the long P3HT block hindered solubility in any P4VP selective solvent. Therefore, THF containing 0.25wt% tetrabutylammoniumbromide was used as an eluent and the salt allowed for a sufficient solubility of the P4VP block. The SEC curves of the pure block copolymers are shown together with the P3HT-alkyne **4a** and P3HT macroinitiator **6** in Figure 3a. A clear shift of the molecular weight can be observed and no uninitiated macroinitiator is visible after purification. However, both block copolymers **8a** and **8b** show similar molecular weights in SEC and tailing is seen in the low molecular weight range. This tailing indicates interaction of the block copolymers with the column material. Determination of the molecular weights or polydispersities from SEC is not reasonable. The only reliable information, which can be gained, is that no significant amounts of macroinitiator are left after purification. Moreover, the final block copolymers show almost monomodal distributions. Thus, ¹H-NMR together with MALDI-ToF MS from the P3HT-alkyne was used for the reliable determination of the block length and molecular weight ratios as seen in Figure 3. The ¹H-NMR spectra were normalized to the aromatic proton of P3HT at 6.98 ppm. It can be clearly seen that the intensity of the aromatic protons of P4VP increases with polymerization time from **8a** to **8b**. Integration of the P3HT signal of the aromatic proton at 6.98 ppm and a comparison with the integral of the two aromatic protons of P4VP in the range of 6.70-6.00 ppm gives the mol percentage of P4VP as 66 mol% (**8a**) and 84 mol% (**8b**). Taking the molecular weights of the repeating units into

account ($m_{\text{3HT}} = 166.3 \text{ g/mol}$ and $m_{\text{4VP}} = 105.14 \text{ g/mol}$) the weight ratios of P4VP were 55 and 77wt% respectively. The block lengths were calculated by using the P3HT repeating units as calculated from MALDI-ToF MS of **4a** together with the molar block ratios from $^1\text{H-NMR}$ spectroscopy. Both block copolymers had the same macroinitiator with about 74 repeating units for P3HT block and **8a** has about 144 and **8b** 387 repeating units of 4VP (see Table 1).

Table 1. Overview of the synthesized polymers and block copolymers including data from GPC, $^1\text{H-NMR}$, MALDI-ToF MS and DSC.

| Polymer | $M_n(\text{GPC})/M_n(\text{MALDI-ToF}) [\text{kg/mol}]$ | $M_p (\text{GPC}) [\text{kg/mol}]$ | PDI (GPC) | wt% P4VP ($^1\text{H-NMR}$) | Repeating Units P3HT/P4VP | $T_g [\text{°C}]$ | $T_m [\text{°C}]$ | $T_c [\text{°C}]$ | $\Delta H_m [\text{J/g}]$ |
|--------------------------------|---|------------------------------------|-----------|-------------------------------|---------------------------|-------------------|-------------------|-------------------|---------------------------|
| P3HT-Alkyne 4a | 19.2 / 12.3 | 23.4 | 1.14 | 0 | 74 / - | - | - | - | - |
| P3HT-Alkoxyamine 6 | 19.9 / - | 24.2 | 1.14 | 0 | 74 / - | - | 228 / 238 | 196 | 19 |
| P3HT- <i>b</i> -P4VP 8a | 57.1 / - | 104.1 | 1.43 | 55% | 74 / 144 | 88 | 230 / 243 | 193 | 8 |
| P3HT- <i>b</i> -P4VP 8b | 55.3 / - | 101.8 | 1.49 | 77% | 74 / 387 | 145 | 224 | 172 | 2 |

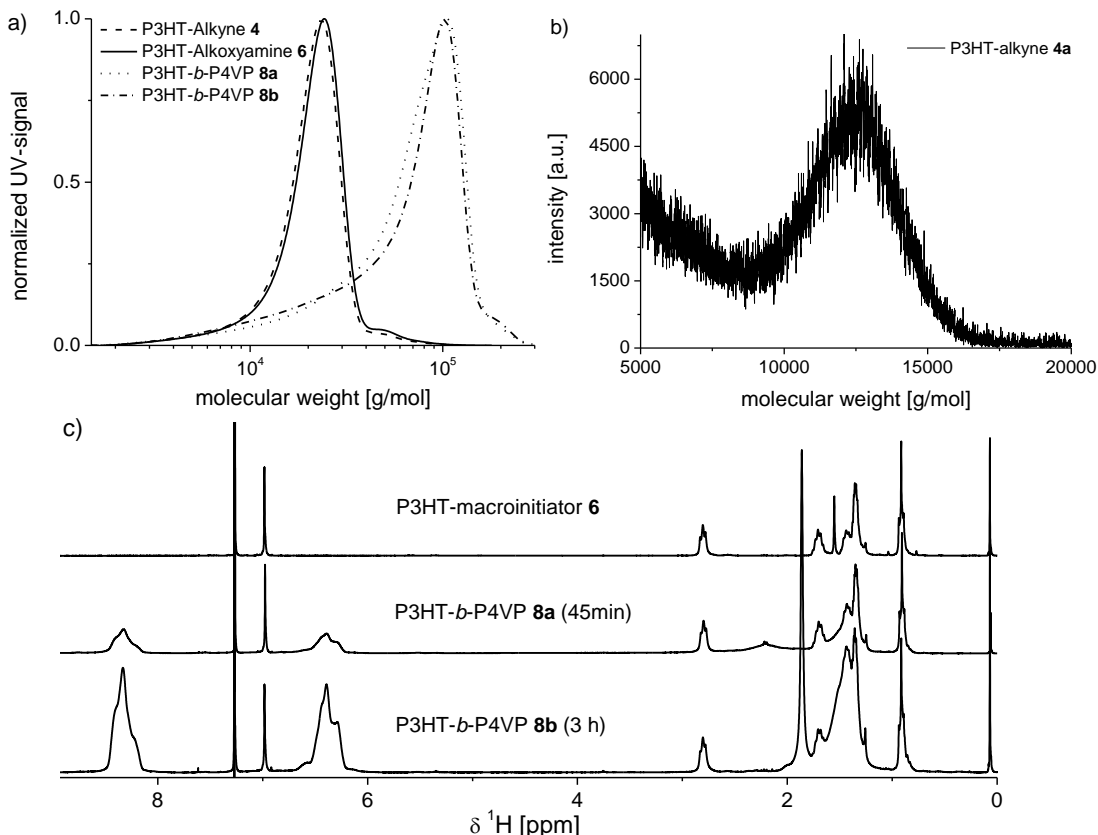


Figure 3. a) SEC curves of P3HT-alkyne **4a**, P3HT-macroinitiator **6** and P3HT-*b*-P4VP **8a** and **8b** measured with THF containing 0.25wt% tetrabutylammoniumbromide. b) MALDI-ToF MS spectra of P3HT-alkyne **4a** measured in the linear mode b) $^1\text{H-NMR}$ spectra of P3HT macroinitiator **6** and P3HT-*b*-P4VP **8a** and **8b**. For comparison, all spectra are normalized to the aromatic proton of P3HT at 6.98 ppm. The intensity of the aromatic protons of P4VP increases with increasing polymerization time from **8a** (45 min) to **8b** (3h).

Thermal and Optical Characterization of P3HT-*b*-P4VP

Both block copolymers and the P3HT-macroinitiator **6** were analyzed with differential scanning calorimetry (DSC) (see Figure 4 and Table 1). The P3HT-macroinitiator **6** has two melting points; a major one at 228 °C and the minor one at 238 °C. Recently, we showed that P3HT adopts a smectic liquid crystalline state between the crystalline and the isotropic phase.³⁶ This accounts for the observed two melting points. The melting enthalpy of P3HT is 19 J/g and on cooling from melt, it recrystallizes at about 196 °C. For the block copolymer **8a** with a P4VP content of 55wt%, no significant change in the melting (230 °C, 243 °C) and recrystallization (193 °C) temperatures is observed. However, the melting enthalpy is reduced to 8 J/g and an additional glass transition for the P4VP block is observed at 88 °C. By further increasing the P4VP block up to 77 wt% for P3HT-*b*-P4VP **8b**, the melting temperature decreases to 224°C and the recrystallization occurs at 172 °C. Thus the longer P4VP block (and lesser relative amount of P3HT) slightly decreases the size of the P3HT crystallites. Because of the low content of P3HT (23 wt%) the melting enthalpy is also reduced to 2 J/g. Since the chain length of P4VP is higher in **8b** in comparison to **8a** the glass transition temperature is increased to 145 °C, a typical value for high molecular weight P4VPs. The appearance of individual phase transitions due to each block indicates a possible phase separation in these block copolymers.

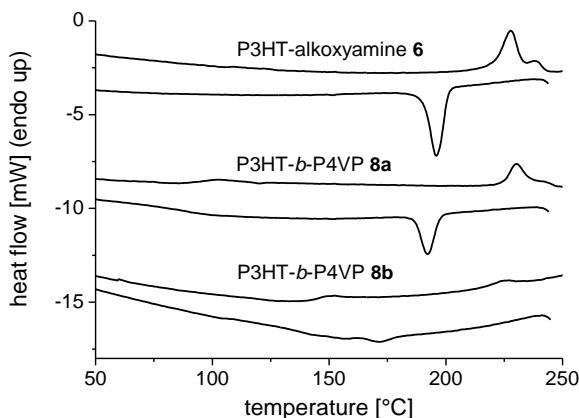


Figure 4. Second heating and first cooling curves from differential scanning calorimetry at a scan rate of 10K/min of P3HT-macroinitiator **6** and P3HT-*b*-P4VP **8a** and **8b**.

Further, these results show that the rod-rod interactions are considerably strong when a high molecular weight P3HT of 19200 g/mol is used. Thus for this high molecular weight system, the size of the P3HT crystallites is not influenced up to a coil content of about 55%. Even at a coil content of 77% the shift in the melting temperature and thus the change in crystallite size is small. In contrast, literature reports show that for P3HT-*b*-P2VP with a 6800 g/mol P3HT block, a coil content of 46% already causes a shift in the melting temperature of about 60 °C.³⁰

The polymers were further characterized with UV-vis spectroscopy in chloroform solution (0.04mg/mL) and thin films on quartz obtained by spin coating from 1wt% chloroform solutions. In solution, the P3HT-macroinitiator **6**, and both P3HT-*b*-P4VPs **8a** and **8b** show an absorption band around 449 nm belonging to S₀-S₁ transition due to π → π* excitations of

conjugated P3HT chromophore. The intensity of this band decreases with increasing P4VP content as expected (for solution spectra see supporting information). For all aromatic compounds an additional absorption band at 250-270 nm is observed for the non-conjugated aromatic rings due to any $\sigma \rightarrow \pi^*$ absorption common in aromatics. With increasing P4VP content the intensity of this UV-band (at 256 nm) increases. For **8b** with 77wt% P4VP the wavelength of maximum absorption intensity is no longer at 449 nm but at 256 nm.

In thin films the P3HT absorptions are shifted bathochromically in comparison to solution spectra. With decreasing P3HT content from P3HT-macroinitiator **6** to **8a** and **8b** the maximum is slightly shifted from 522 nm over 521 nm to 514 nm and the intensity of the P3HT absorption decreases. Further, the following changes in the band structure are seen (see Figure 5a). While the P3HT-macroinitiator (100wt% P3HT) shows typical vibronic bands of a crystalline P3HT at 550 and 600 nm, the intensity decreases with decreasing P3HT content in the block copolymers.³⁷ In P3HT-*b*-P4VP **8b** almost no fine structure is visible. Spin coating from chloroform causes a fast drying of the films and the polymers are in a non-equilibrium state of less aggregation. Therefore we annealed the films above the melting temperature and cooled them slowly to allow for crystallization of P3HT. After annealing above the melting point (see Figure 5b) the vibronic bands are visible for all polymers but their intensity still depends on the P3HT content. This is in accordance with the thermal measurements where the melting enthalpy and thus the crystallinity decreases with increasing P4VP content.

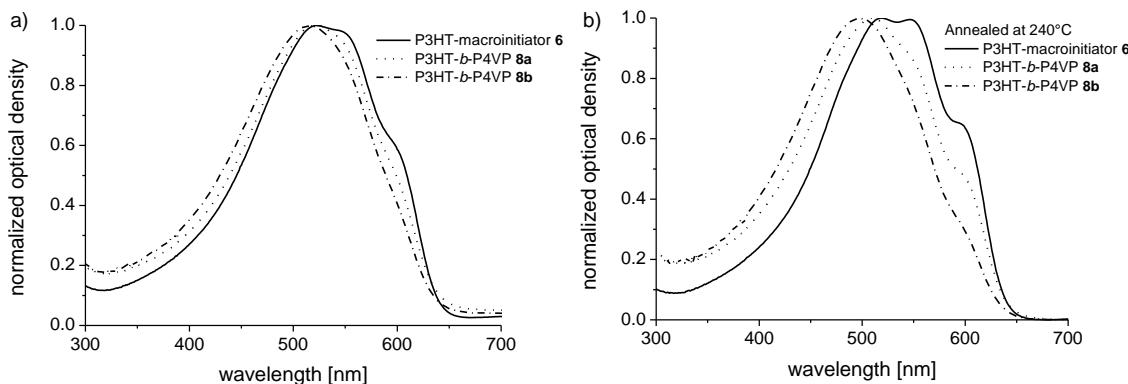


*Figure 5. UV-vis spectra of P3HT-macroinitiator **6**, P3HT-*b*-P4VP **8a** and **8b** films on quartz obtained by spin coating from 1wt% chloroform solution. The spectra are normalized to the P3HT absorption maxima at about 500 nm. a) as cast and b) annealed at 240°C for 5 min and cooled slow from melt.*

Characterization of the Bulk Structures

We further analyzed the phase separation of the P3HT-*b*-P4VP block copolymers in bulk using transmission electron microscopy (TEM). Figure 6 shows the TEM image of **8a** and **8b**. In both pictures a microphase separation is observed where P4VP appears as dark, because of staining with iodine. Because of the higher content of P4VP in **8b**, the extend of dark regions is larger in Figure 6b. The mixed structural features observed in TEM indicate a non-equilibrium state morphology. However, these pictures clearly show microphase separation. Further, optimization of annealing conditions as well as cooling rates may play a role for obtaining

equilibrium morphology in crystalline amorphous block copolymers such as P3HT-*b*-P4VPs. For better understanding of the build-up of phase separated structures, temperature dependent small angle X-ray measurements are underway for bulk and thin film samples.

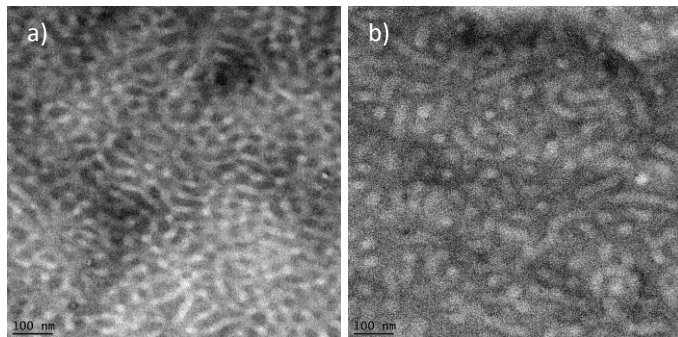


Figure 6. TEM images of P3HT-*b*-P4VP stained with iodine after 20 min annealing at 265 °C and quenching with liquid nitrogen a) 8a having 55%wt P4VP and b) 8b with 77wt% P4VP.

Characterization of the Solution Structures

Since P3HT-*b*-P4VP is an amphiphile, it should be possible to form colloidal structures in solvents which are selective for either block. Therefore, we dissolved the block copolymers in a nonselective solvent like chloroform and slowly added isopropanol, a selective solvent for the P4VP block. For both block copolymers **8a** and **8b** a color shift from orange to deep purple (indicating colloidal aggregation along with crystallization of P3HT chains) occurred and the colloidal solutions were stable over time. In contrast, addition of isopropanol to a chloroform solution of P3HT-alkyne **4a** led to a fast precipitation of the polymer. This indicates that in the block copolymer samples, the stabilization of the solutions of P3HT-*b*-P4VPs occurs by the formation of self-assembled structures with P4VP in the shell. Dynamic light scattering measurements of the colloidal solutions showed structures with a hydrodynamic radius of 51 nm for **8a** and 44 nm for **8b**, respectively and a slightly broader distribution for **8b** than for **8a** (Figure 7a).

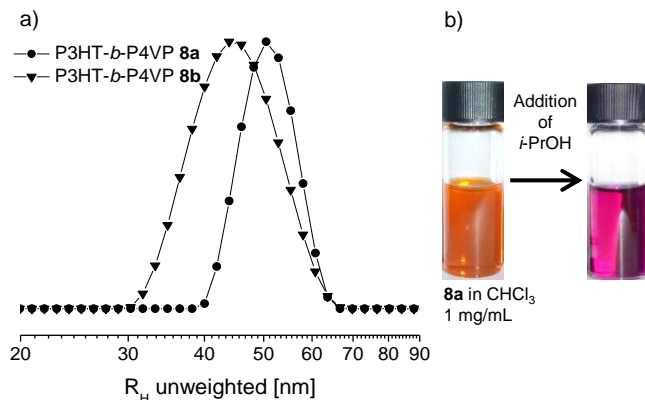


Figure 7. a) Dynamic light scattering curves of P3HT-*b*-P4VP polymers **8a** and **8b** after addition of isopropanol to a 1 mg/mL solution in CHCl_3 . b) Photograph of 1 mg/mL solution of **8a** in CHCl_3 and after addition of isopropanol ($i\text{-PrOH}$).

Further, UV-vis spectra of these colloidal solutions were measured to obtain preliminary information about the conformation of P3HT within the structures. The normalized UV-vis spectra are given in Figure 8. Both polymers show a broad absorption with distinct vibronic bands of P3HT. The absorption maximum is located at the vibronic band at about 558 nm and also a strong vibronic band is observed around 600 nm. However in **8a**, with a higher weight percent of P3HT, the intensity of the vibronic band at 600 nm is higher and thus the packing seems different than in **8b**. In comparison with the spectra of the annealed films in Figure 5b, the vibronic structures of both colloids are much more pronounced than in the film. The high intensity of the vibronic band in the colloidal solution indicates that P3HT is crystalline within the colloidal aggregates. An earlier report correlating the UV-vis absorption spectra and crystallinity in P3HT supports our conclusion.³⁷ Usually in coil selective solvents, rod-coil block copolymer with a crystalline core tend to form structures with a low curvature like cylindrical micelles, vesicle or lamella.³⁸ Further detailed investigations about the structure formation and the type of structures are currently underway.

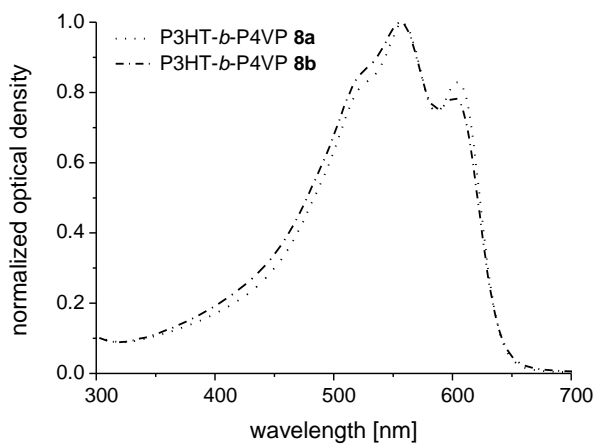


Figure 8. Normalized UV-vis spectra of colloidal solutions of P3HT-*b*-P4VP **8a** and **8b** obtained after addition of isopropanol to a 1 mg/mL solution in CHCl₃.

Conclusion

We synthesized high molecular weight P3HT-alkyne and optimized the quenching conditions. It is important to choose methanol as a quenching reagent. Hydrochloric acid leads to addition reactions, chain-chain coupling and a loss of alkyne end groups. From this P3HT-alkyne, by using the copper catalyzed azide-alkyne “click” reaction, P3HT-alkoxyamine with a high molecular weight of 19200 g/mol was synthesized as a macroinitiator for NMRP. Further, two block copolymers P3HT-*b*-P4VP with a P4VP content of 55 and 77wt% were obtained. The thermal and optical properties depend on the P4VP content. However, because of the long P3HT block, the influence of the P4VP segment on the size of the crystallites was small. Microphase separation was observed for both block copolymers. In solution, we observed the formation of colloidal structures which are confirmed to have crystalline cores of P3HT according to UV-vis studies. Because of the amphiphilic nature of P3HT-*b*-P4VP, its

semiconducting P3HT rod block and its nanoparticle coordinating P4VP coil block, it is an interesting system for detailed investigations of structure formation in solution and for organic hybrid devices.

Supporting Information. Experimental details, additional MALDI-ToF MS spectra, ¹H NMR spectra, SEC curves, and UV-vis spectra. This material is available free of charge via the Internet at <http://pubs.acs.org.at>.

Acknowledgment

We acknowledge financial support for this research work from DFG SFB 840. R. H. Lohwasser thanks the Elite Network Bavaria for a research stipend. Thanks to Melanie Förtsch and Annika Pfaffenberger for TEM measurements.

References

- (1) Sirringhaus, H.; Tessler, N.; Friend, R. H. *Science* **1998**, *280*, 1741-1744.
- (2) Ma, W.; Yang, C.; Gong, X.; Lee, K.; Heeger, A. J. *Adv. Funct. Mater.* **2005**, *15*, 1617-1622.
- (3) Boudouris, B. W.; Frisbie, C. D.; Hillmyer, M. A. *Macromolecules* **2008**, *41*, 67-75.
- (4) Liu, J.; Sheina, E. E.; Kowalewski, T.; McCullough, R. D. *Angew. Chem. Int. Ed.* **2002**, *41*, 329-332.
- (5) Richard, F.; Brochon, C.; Leclerc, N.; Eckhardt, D.; Heiser, T.; Hadzioannou, G. *Macromol. Rapid Commun.* **2008**, *29*, 885-891.
- (6) Sommer, M.; Lang, A. S.; Thelakkat, M. *Angew. Chem. Int. Ed.* **2008**, *47*, 7901-7904.
- (7) Zhang, Q.; Cirpan, A.; Russel, T. P.; Emrick, T. *Macromolecules* **2009**, *42*, 1079-1082.
- (8) Dai, C.; Yen, W.; Lee, Y.; Ho, C.; Su, W. *J. Am. Chem. Soc.* **2007**, *129*, 11036-11038.
- (9) Moon, H. C.; Anthonysamy, A.; Lee, Y.; Kim, J. K. *Macromolecules* **2010**, *43*, 1747-1752.
- (10) Higashihara, T.; Ohshimizu, K.; Hirao, A.; Ueda, M. *Macromolecules* **2008**, *41*, 9505-9507.
- (11) Iovu, M. C.; Craley, C. R.; Jeffries-El, M.; Krankowski, A. B.; Zhang, R.; Kowalewski, T.; McCullough, R. D. *Macromolecules* **2007**, *40*, 4733-4735.
- (12) Radano, C. P.; Schermen, O. A.; Stingelin-Stutzmann, N.; Müller, C.; Breiby, D. W.; Smith, P.; Janssen, R. A. J.; Mejier, E. W. *J. Am. Chem. Soc.* **2005**, *127*, 12502-12503.
- (13) Li, Z.; Ono, R. J.; Wu, Z.; Bielawski, C. W. *Chem. Commun.* **2011**, *47*, 197-199.
- (14) Tao, Y.; McCulloch, B.; Kim, S.; Segalman, R. A. *Soft Matter* **2009**, *5*, 4219-4230.
- (15) Urien, M.; Erothu, H.; Cloutet, E.; Hiorns, R. C.; Vignau, L.; Cramail, H. *Macromolecules* **2008**, *41*, 7033-7040.
- (16) Kolb, H. C.; Finn, M. G.; Sharpless K.B *Angew. Chem. Int. Ed.* **2001**, *40*, 2004-2021.
- (17) Britze, A.; Möllmann, V.; Grundmeier, G.; Luftmann, H.; Kuckling, D. *Macromol. Chem. Phys.* **2011**, *212*, 679-690.
- (18) Sary, N.; Richard, F.; Brochon, C.; Leclerc, M.; Leveque, P.; Audinot, J.; Berson, S.; Heiser, T.; Hadzioannou, G.; Mezzenga, R. *Adv. Mater.* **2009**, *21*, 1-6.

- (19) Rajaram, S.; Armstrong, P. B.; Kim, B. J.; Fréchet, J. M. J. *Chem. Mater.* **2009**, *21*, 1775-1777.
- (20) Sommer, M.; Hüttner, S.; Steiner, U.; Thelakkat, M. *Appl. Phys. Lett.* **2009**, *95*, 183308-.
- (21) Kline, R. J.; McGehee, M. D.; Kadnikova, E. N.; Liu, J.; Frechet, J. M. J. *Adv. Mater.* **2003**, *15*, 1519-1522.
- (22) Lan, Y.; Huang, C. *J. Phys. Chem. B* **2009**, *113*, 14555-14564.
- (23) Zen, A.; Saphiannikova, M.; Neher, D.; Grenzer, J.; Grigorian, S.; Pietsch, U.; Asawapirom, U.; Janietz, S.; Scherf, U.; Lieberwirth, I.; Wegner, G. *Macromolecules* **2006**, *39*, 2162-2171.
- (24) Jeffries-El, M.; Sauve, G.; McCullough, R. D. *Macromolecules* **2005**, *38*, 10346-10352.
- (25) Wang, M.; Kumar, S.; Lee, A.; Felorzabihi, N.; Shen, L.; Zhao, F.; Froimowicz, P.; Scholes, Gr. D.; Winnik, M. A. *J. Am. Chem. Soc.* **2008**, *130*, 9481-9491.
- (26) Palaniappan, K.; Hundt, N.; Sista, P.; Nguyen, H.; Heo, J.; Bhatt, M. P.; Han, Y.; Schmiedel, E. A.; Sheina, E. E.; Biewer, M. C.; Stefan, M. C. *J. Polym. Sci., Part A: Polym. Chem.* **2011**, *49*, 1802-1808.
- (27) Aissou, K.; Pfaff, A.; Giacomelli, C.; Travelet, C.; Müller, A. H. E.; Borsali, R. *Macromol. Rapid Commun.* **2011**, *32*, 912-916.
- (28) Huang, K.; Fang, Y.; Hsu, J.; Kuo, C.; Chang, W.; Chen, W. *J. Polym. Sci. A Polym. Chem.* **2011**, *49*, 147-155.
- (29) Patra, S. K.; Ahmed, R.; Whittell, G. R.; Lunn, D. J.; Dunphy, E. L.; Manners, I. *J. Am. Chem. Soc.* **2011**, *133*, 8842-8845.
- (30) Lee, Y. H.; Yen, W. C.; Su, W. F.; Dai, C. A. *Soft Matter* **2011**, *7*, 10429-10442.
- (31) Lohwasser, R. H.; Thelakkat, M. *Macromolecules* **2011**, *44*, 3388-3397.
- (32) Miyakoshi, R.; Yokoyama, A.; Yokozawa, T. *Macromol. Rapid Commun.* **2004**, *25*, 1663-1666.
- (33) Tolman, C. A.; Seidel, W. C.; Gosser, L. W. *Organometallics* **1983**, *2*, 1391-1396.
- (34) Benanti, T. L.; Kalaydjian, A.; Venkataraman, D. *Macromolecules* **2008**, *41*, 8312-8315.
- (35) Maria, S.; Susha, S.; Sommer, M.; Talapin, D. V.; Thelakkat, M. *Macromolecules* **2008**, *41*, 6081-6088.
- (36) Wu, Z.; Petzold, A.; Henze, T.; Thurn-Albrecht, T.; Lohwasser, R. H.; Sommer, M.; Thelakkat, M. *Macromolecules* **2010**, *43*, 4646-4653.
- (37) Zhokhavets, U.; Erb, T.; Gobsch, G.; Al-Ibrahim, M.; Ambacher, O. *Chem. Phys. Lett.* **2006**, *419*, 347-350.
- (38) Massey, J. A.; Temple, K.; Cao, L.; Rharbi, Y.; Raez, J.; Winnik, M. A.; Manners, I. *J. Am. Chem. Soc.* **2000**, *122*, 11577-11584.

Supporting Information

Materials and Characterization

¹H-NMR spectra were recorded in chloroform on a Bruker Avance 250 spectrometer at 300 MHz. Coupling constants are given in Hz. The spectra were calibrated according to the solvent signal at 7.26 ppm. Size exclusion chromatography measurements were performed utilizing a Waters 510 HPLC pump and stabilized THF with 0.25 wt% TBAB (tetrabutylammoniumbromide) as eluent at a flow rate of 0.5 mL/min. 100 µL of a solution was injected into a column setup comprising a guard column (PSS, 5 × 0.8 cm, SDV gel, particle size 5 µm, pore size 100 Å) and two separation columns (Varian, 30 × 0.8 cm, mixed C gel, particle size 5 µm). Polymer size distribution were monitored with a WATERS 486 tunable UV detector at 254 nm and a Waters 410 differential RI detector. Polystyrene was used as external standard and 1,2-dichlorobenzene as an internal standard for calibration. Matrix assisted laser desorption ionizations spectroscopy with time of flight detection mass spectroscopy (MALDI-ToF MS) measurements were performed on a Bruker Reflex III using dithranol as matrix and a mixture of 1000:1 (Matrix:Polymer). The Laser intensity was set to around 70%. Differential scanning calorimetry (DSC) measurements were done on a Perkin-Elmer Diamond DSC with a heating and cooling rate of 10 K/min. UV-vis measurements were performed with a U-3000 spectrometer from Hitachi. Sample for transmission electron spectroscopy were cut with a Ultramikrotom and measured on a Zeiss 9220mega. Dynamic light scattering measurements were done using an ALV DLS/SLS-SP 5022F compact goniometersystem with an ALV 5000/E cross correlator and a He–Ne laser (wavelength = 632.8 nm). The measurements were carried out in cylindrical scattering cells with a diameter of 10 mm at an angle of 90 ° and a temperature of 20 °C. The obtained correlation functions were analyzed with CONTIN algorithm and the apparent hydrodynamic radii were calculated according to the Stokes–Einstein equation. The samples were diluted before the measurement in a ratio of 1 to 3 with isopropanol to obtain good scattering intensity. It was controlled with UV-vis that no change in the packing occurs by dilution.

The monomer 2,5-dibromo-3-hexylthiophene, the catalyst 1,3-bis(diphenylphosphino)propanenickel(II) chloride [Ni(dppp)Cl₂] and 2,2,5-trimethyl-3-(1'-p-azidomethylphenylethoxy)-4-phenyl-3-azahexane were synthesized according to the literature.¹⁻³ All glass apparatus for polymerization were heated and cooled down under argon. Dry THF was distilled over calcium hydride and potassium. Dry 1,2-dichlorobenzene, ethynylmagnesium chloride (0.6 M in THF/toluene) and *t*-BuMgCl (1.7 M in THF) were purchased from Acros and the Grignard reagents were titrated according to Krasovskiy and Knochel.⁴ LiCl puriss p.a. water free was purchased from Fluka and dried prior to use. 4-Vinylpyridine (Aldrich, 95%) was dried over calciumhydride, distilled under reduced pressure, and degassed with nitrogen.

Experimental Part

Procedure for the Synthesis of P3HT-alkyne using LiCl

In a Schlenk flask LiCl was dried under vacuum at 140°C for 4h. After cooling to room temperature dry THF was added and stirred for 3 h to form a 0.5 M LiCl solution. In a dry schlenk flask 5.86 g (18 mmol) 2,5-dibromo-3-hexylthiophene was dissolved in 36 ml of 0.5 M LiCl solution and 13.1 ml (17.3 mmol) of *t*-BuMgCl were added with a syringe. After complete active Grignard monomer formation the solution was diluted with 129 ml dry THF. The polymerization was initiated with a suspension of 118 mg (0.22 mmol) Ni(dppp)Cl₂ in 1 mL THF. After 31 min the reaction was cooled with an ice bath and 9 ml (4.5 mmol) of ethynylmagnesium chloride were added with a syringe. After 11 min the reaction mixture was precipitated in MeOH. The polymer was dissolved two more times in CHCl₃, filtrated and precipitated in MeOH. After filtration and drying under vacuum 1.98 g of the pure polymer were obtained.

SEC $M_p = 23400 \text{ g mol}^{-1}$, $M_n = 19200 \text{ g mol}^{-1}$, $M_w = 21800 \text{ g mol}^{-1}$, $M_w/M_n = 1.14$;

$\delta^{1}\text{H}$ (300 MHz; CDCl₃) 6.98 (1 H, s, H_{ar}), 3.52 (0.013 H, s, CH of alkyne end group) 2.80 (2 H, t, J_{αβ} 7.6, α -CH₂), 1.82–1.60 (2 H, m, β -CH₂), 1.50–1.10 (6 H, m), 1.0–0.75 (3 H, m, CH₃);

Procedure for the Synthesis of P3HT-alkoxyamine

In a dry Schlenk flask 254 mg of 2,2,5-Trimethyl-3-(1'-p-azidomethylphenylethoxy)-4-phenyl-3-azahexane was dried under vacuum and 638 mg of P3HT-Alkyne were added. Both were dissolved in 123 ml dry THF and 3 mL of *N,N*-diisopropylethylamine was added with a syringe. After three freeze, pump, thaw cycles 130 mg of Cu(I)I were introduced and the reaction mixture was stirred at 40°C for 2 days. The reaction mixture was precipitated in MeOH with small amounts of NH₃. To remove excess Cu the polymer was dissolved in CHCl₃ and extracted with a 1:1 (v:v) mixture of NH₃ and water. After precipitation in MeOH 642 mg of pure macroinitiator were obtained.

SEC $M_p = 24200 \text{ g mol}^{-1}$, $M_n = 19900 \text{ g mol}^{-1}$, $M_w = 22700 \text{ g mol}^{-1}$, $M_w/M_n = 1.14$;

Procedure for the Synthesis of P3HT-*b*-P4VP

To a dry Schlenk tube 7.18 mg of 2,2,5-trimethyl-4-phenyl-3-azahexane-3-oxyl was added in chloroform and the solvent was evaporated under high vacuum. P3HT-alkoxyamine (202 mg, 0.016 mmol) was inserted and the tube was evacuated and flooded with argon for three times. The polymer was dissolved in 12 mL degassed o-dichlorobenzene (o-DCB) and 12 mL 4-vinlypyridine was added. The reaction mixture was degassed with three freeze, pump, thaw cycles and the polymerization was started by placing the mixture in a 125 °C hot oil bath. After 45 min the polymerization was stopped by cooling with liquid nitrogen. The raw polymer mixture was diluted with chloroform and precipitated in pentane. The polymer was filtered and washed with hydrochloric acid to protonate the P4VP block. In a soxhlet apparatus the remaining macroinitiator was removed by hot extraction with toluene. After drying under high

vacuum the polymer was deprotonated by washing with a one to one mixture of ammonia and water. The pure polymer (282 mg) was obtained by dissolution in chloroform, precipitation in pentane, filtration and drying under vacuum.

$\text{SEC } M_p = 104100 \text{ g mol}^{-1}$, $M_n = 57100 \text{ g mol}^{-1}$, $M_w = 81700 \text{ g mol}^{-1}$, $M_w/M_n = 1.43$;
 $\delta^1\text{H}$ (300 MHz; CDCl_3) 8.60–8.00 ($m^*2\text{H}$, m, H_{ar} P4VP), 6.98 ($n^*1\text{ H}$, s, H_{ar} , P3HT), 6.70–6.00 ($m^*2\text{H}$, m, H_{ar} P4VP), 2.80 ($n^*2\text{ H}$, t, $J_{\alpha\beta}$ 7.6, $\alpha\text{-CH}_2$, P3HT), 1.82–1.60 ($n^*2\text{ H}$, m, $\beta\text{-CH}_2$, P3HT), 1.50–1.10 ($n^*6\text{ H}$, m, P3HT and $m^*2\text{H}$, m, CH_2 P4VP), 1.0–0.75 ($n^*3\text{ H}$, m, CH_3); n = degree of polymerization of P3HT and m = degree of polymerization of P4VP.

Solution Structures

For the formation of the solution structures 1 mg P3HT-*b*-P4VP was dissolved in 1 mL of CHCl_3 . 4mL of isopropanol were slowly added under stirring with a flow rate of 1 mL/h using a syringe pump from neMESYS. The remaining CHCl_3 was removed and the samples were analyzed with UV-vis and dynamic light scattering.

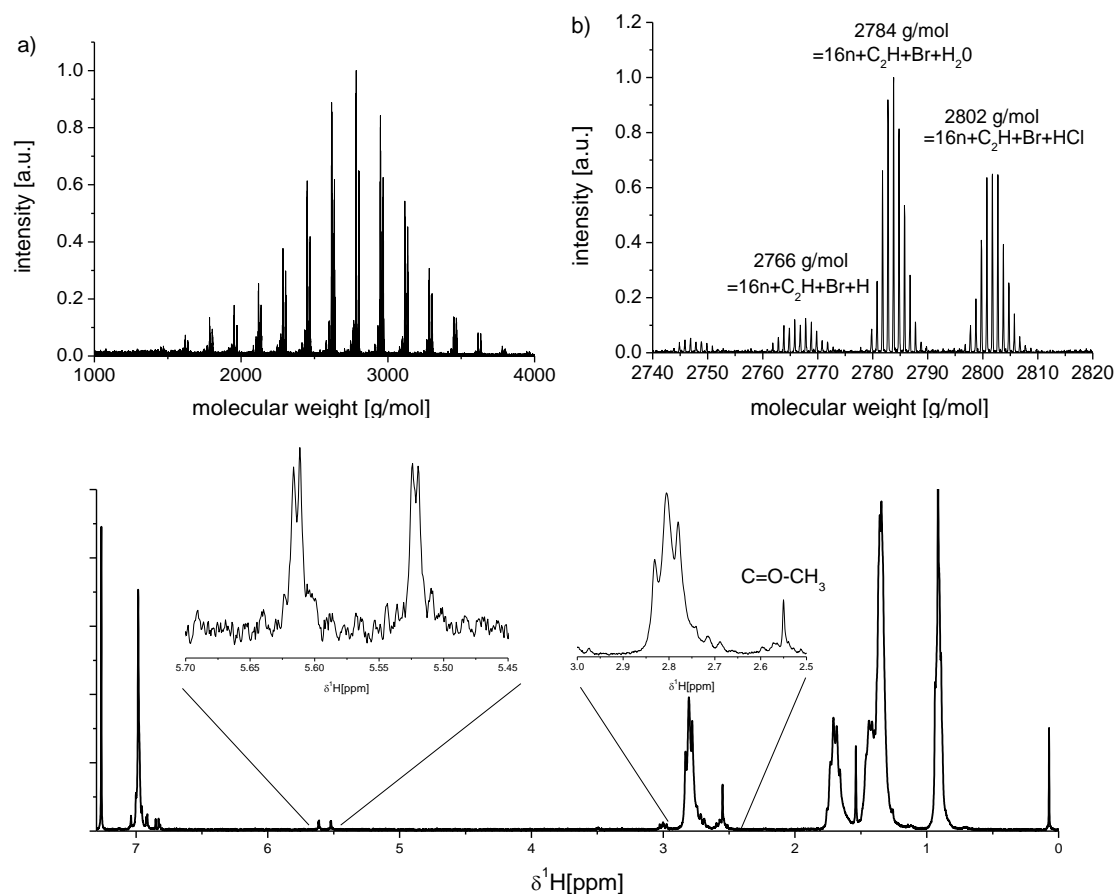


Figure SI 1: Spectra of P3HT obtained after quenching the end capping reaction of ethynylmagnesium chloride with hydrochloric acid at room temperature a) MALDI-ToF MS spectra b) magnified part in the range of 16 repeating units c) ${}^1\text{H-NMR}$ spectrum. The respective end groups are indicated.

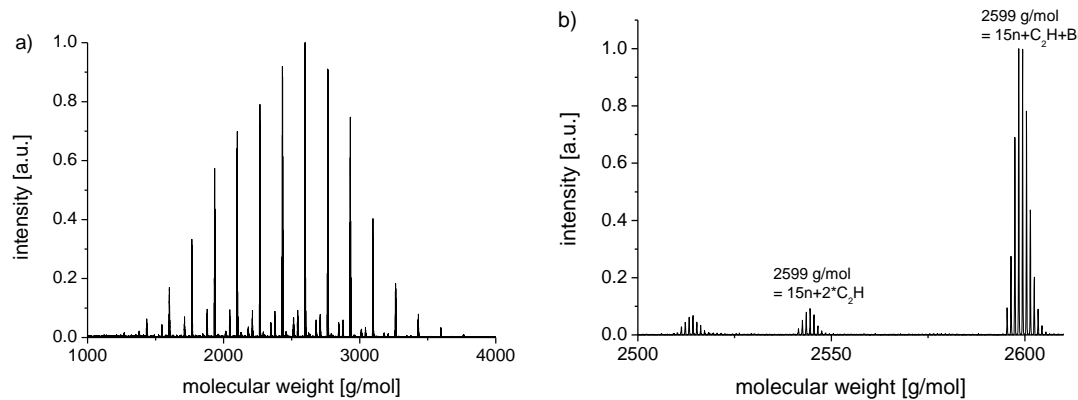


Figure SI 2: a) MALDI-ToF MS spectra of P3HT-alkyne quenched with methanol b) magnified part in the range of 15 repeating units. The main series belongs to alkyne and bromine terminated chain ends. Small amounts of alkyne alkyne terminated P3HT are visible.

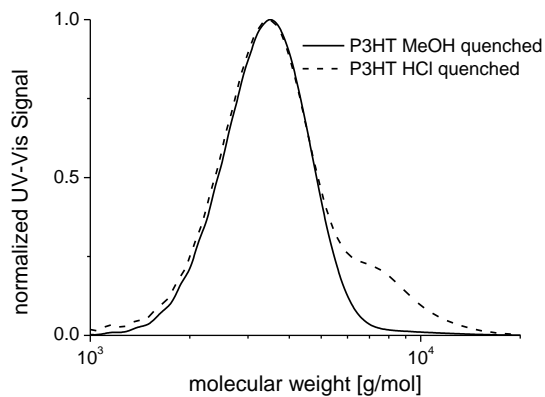


Figure SI 3: SEC curves of P3HT-alkyne quenched at 0°C with hydrochloric acid or methanol. Only for the sample quenched with hydrochloric acid small amounts of chain-chain coupling are visible.

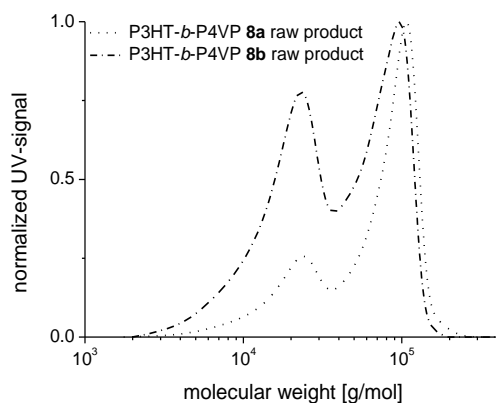


Figure SI 4: GPC curves of the raw products of P3HT-*b*-P4VP **8a** and **8b**.

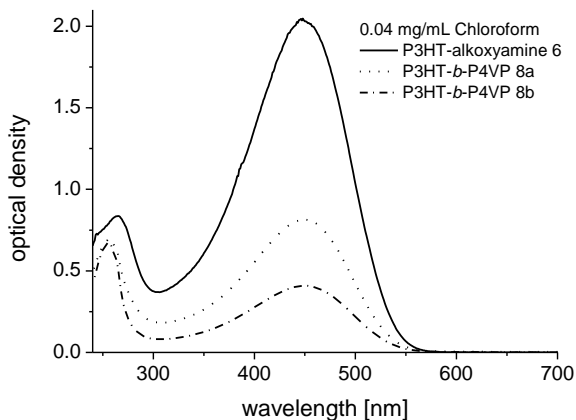


Figure SI 5: UV-vis spectra of P3HT-alkoxyamine 6 and P3HT-*b*-P4VP 8a and 8b in 0.04mg/mL solution in chloroform.

References

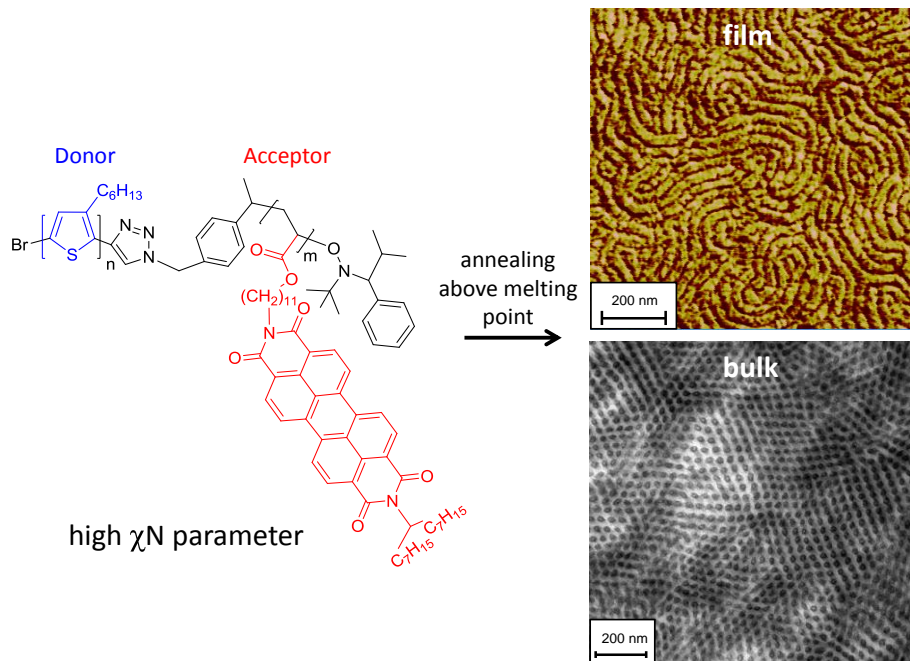
- (1) Benoit, D.; Chaplinski, V.; Braslau, R.; Hawker, C. J. *J. Am. Chem. Soc.* **1999**, *121*, 3904-3920.
- (2) Binder, W. H.; Gloger, D.; Weinstabl, H.; Allmaier, G.; Pittenauer E. *Macromolecules* **2007**, *40*, 3097-3107.
- (3) Van Hecke, G. R.; Horrocks, W. *Inorg. Chem.* **1966**, *5*, 1968-1974.
- (4) Krasovskiy, A.; Knochel, P. *Synthesis* **2006**, *5*, 890-891.

8. Donor-Acceptor, Crystalline-Crystalline P3HT-*b*-PPerAcr with Ordered Phase Separation in Bulk and Thin Film

Ruth H. Lohwasser, Andreas S. Lang, and Mukundan Thelakkat*

Applied Functional Polymers, Department of Macromolecular Chemistry I,
University of Bayreuth, Universitätsstraße 30, 95444 Bayreuth, Germany.

*E-mail corresponding author: mukundan.thelakkat@uni-bayreuth.de



intended for submission

Abstract

We show that a combination of copper catalyzed azide-alkyne click reaction and nitroxide mediated radical polymerization (NMRP) can be used for the synthesis of poly(3-hexylthiophene)-*block*-poly perylene bisimide acrylate (P3HT-*b*-PPerAcr) block copolymers. This synthetic strategy leads to clean diblock copolymers and high total molecular weights are possible. The here synthesized block copolymer has a high molecular weight P3HT block of 19.7 kDa and a PPerAcr content of 64wt%. Because of the increased chain length, the high χN parameter allows phase separation in the melt. Thus, for the first time typical hexagonally ordered cylindrical phase separation is observed for a crystalline-crystalline, donor-acceptor block copolymer after thermal annealing. Further, clear phase separated structures are seen in thin films, which is promising for application in organic photovoltaics.

Introduction

Conjugated polymers have become an intense field of research for chemists, physicists and engineers because of their high potential for application in organic electronics. The devices based on organic materials benefit from solution processability, possible fabrication on flexible substrates and light weight.¹ In organic photovoltaics excitation leads to the formation of a bound electron-hole pair, an exciton. Only if it reaches an interface within its lifetime free charge carriers are obtained. This requires interfaces between a donor and an acceptor material within the exciton diffusion length.¹ For organic photovoltaics the most efficient systems are based on a blend of a conjugated polymer as a hole conductor and a fullerene derivative as the electron conductor. Despite the steadily increasing efficiencies in the range of 5% for poly(3-hexylthiophene)² (P3HT) containing devices and 8.3% for low band gap systems³, improved morphological control and a higher long-term stability are desired. The morphological instability mainly originates from the non-equilibrium structures of blends and thus device performance strongly depends on preparation conditions and thermal history.^{2,4,5} This is crucial especially for low cost large area roll to roll processing where thermal annealing steps are involved in the processing conditions. Therefore, block copolymers containing both electron and hole conducting moieties have become of great interest.⁶⁻⁹ The idea of using block copolymers is to control the morphology by microphase separation and create interfaces in the range of the exciton diffusion length. In aligned block copolymer systems clear charge transport ways to the electrodes can be gained and the microphase separation guarantees morphological stability.¹⁰ Additionally, use of thick absorbing layers for efficient light harvesting are feasible without losing interfacial area. It was shown in the literature that the performance of microphase separated block copolymers was superior to their respective polymer polymer blends.^{11,12} Further, Hashimoto et al. showed that a donor-acceptor block copolymer with P3HT as a hole conducting block and a fullerene containing electron conducting block reaches efficiencies of 1.7% in a single active layer device.⁶ Even though the

performance cannot match that of an optimized polymer fullerene blend, the block copolymer showed better long term stability.

A large number of different block copolymers containing P3HT have been synthesized.¹³⁻¹⁶ Only few of them contained an active second block, which is an electron conductor on its own or can coordinate electron conducting nanoparticles.^{7,9,17-19} These block copolymers found application in solar cells as single active materials, in hybrid systems or as compatibilizers.^{6,18,20-23} In addition to P3HT block copolymers carrying fullerene segments as the electron conducting moiety, also block copolymers with poly perylene bisimide acrylates (PPerAcr) as electron conducting block were intensively studied.^{22,24} Thereby, the molecular parameters determining order and transport played an important role for their performance in devices. We recently showed that the length of the P3HT block plays a major role for the external quantum efficiency and that a balanced charge transport between the donor and the acceptor block is important for the efficiency.^{21,24} Even though phase separation has been observed for these materials, the microphase separation of these crystalline-crystalline block copolymers is very complex. It is not only dominated by the Flory-Huggins interaction parameter χN and the volume fraction, but also depends on interactions within one segment. For example, the self-assembly of rod-coil block copolymers containing a conjugated block is further influenced by the π - π interaction of the rod, its crystalline or liquid crystalline character and the asymmetry between the length of the rod and coil block.^{25,26} These additional interactions of the conjugated blocks are usually described by the Maier-Saupe interaction parameter.²⁷ Up to now the donor-acceptor, crystalline-crystalline P3HT-*b*-PPerAcr block polymers never showed the typical microphase separated structures known from coil-coil systems, but rather elongated fibrils which normally arise from crystallization of one of the blocks.^{7,22,23}

From these results some prerequisites for the synthesis of P3HT containing block copolymers arise. First requirement is a long P3HT block for good charge carrier mobility of holes. Secondly, a balanced charge transport of donor and acceptor blocks is necessary, which can be tuned by the block ratio. Here, we have recently demonstrated that a higher content of about 70wt% of PPerAcr is necessary for good performance in organic solar cells.²⁴ Finally, a high χN parameter should be realized for crystallization independent microphase separation in the melt. This requires a synthetic approach which allows the incorporation of a long P3HT block and a good control of the polymerization of the second block in order to increase the percentage of PPerAcr.

Recently we demonstrated that a combination of copper catalyzed azide-alkyne click reaction and nitroxide mediated radical polymerization (NMRP) is highly useful for the synthesis of P3HT block copolymers with a long P3HT block.²⁸ Here, we use this method to synthesize a donor-acceptor block copolymer with a high content of poly perylene bisimide acrylate as the electron conducting segment. No byproducts of triblock copolymer were formed as in the

earlier reported method of direct *in situ* synthesis of an alkoxyamine macroinitiator followed by polymerization.²¹ Further, we show that the high molecular weight and thus the increased χN parameter of the block copolymer allows order-disorder transition in melt. Hexagonally ordered cylindrical nanostructures could be achieved after thermal annealing in bulk. Also in thin films nanostructures of long range order were observed after annealing.

Experimental Part

Materials and Characterization

¹H-NMR spectra were recorded in chloroform on a Bruker Avance 250 spectrometer at 300 MHz. Coupling constants are given in Hz. The spectra were calibrated according to the solvent signal at 7.26 ppm. Size exclusion chromatography (Poly-SEC) measurements were performed utilizing a Waters 515-HPLC pump with stabilized THF as the eluent at a flow rate of 0.5 mL/min. A 20 μ L volume of a solution with a concentration of approximately 1 mg/mL was injected into a column setup, which consists of a guard column (Varian, 50 \times 0.75 cm, ResiPore, particle size 3 μ m) and two separation columns (Varian, 300 \times 0.75 cm, ResiPore, particle size 3 μ m). The compounds were monitored with a Waters UV detector at 254 nm. Polystyrene was used as external standard and *o*-dichlorobenzene as an internal standard for calibration. Matrix assisted laser desorption ionizations spectroscopy with time of flight detection mass spectroscopy (MALDI-TOF MS) measurements were performed on a Bruker Reflex III using Dithranol as matrix and a mixture of 1000:1 (Matrix : Polymer). The Laser intensity was set to around 70%. Differential scanning calorimetry (DSC) measurements were done on a Perkin-Elmer Diamond DSC with a heating and cooling rate of 10 K/min. UV-vis measurements were performed with a U-3000 spectrometer from Hitachi. Samples for transmission electron microscopy were cut with an Ultramikrotom, stained 5 min with RuO₄ and measured on a Zeiss 9220mega. AFM images were recorded on a Digital Instruments Dimension 3100 microscope operated in tapping mode. Raster electron microscopy images were recorded on a Zeiss 1530 FESEM. The monomer 2,5-dibromo-3-hexylthiophene, the catalyst 1,3-bis(diphenylphosphino)propanenickel(II) chloride [Ni(dppp)Cl₂], perylene bisimide acrylate PerAcr, 2,2,5-trimethyl-4-phenyl-3-azahexane-3-oxyl and 2,2,5-Trimethyl-3-(1'-*p*-azidomethylphenylethoxy)-4-phenyl-3-azahexane were synthesized according to the literature.²⁹⁻³² The P3HT-macronitiator was synthesized as recently published.²⁸ All glass apparatus for polymerization were heated and cooled down under argon. Dry THF was distilled over calcium hydride and potassium. Dry *o*-dichlorobenzene, ethynylmagnesium chloride (0.6 M in THF/toluene) and *t*-BuMgCl (1.7 M in THF) were purchased from Acros and the Grignard reagents were titrated according to Krasovskiy and Knochel.³³ LiCl puriss p.a. water free was purchased from Fluka and dried prior to use.

Synthesis of P3HT-*b*-PPerAcr

In a 5 mL Schlenk tube the P3HT-macroinitiator **3** (300 mg, 0.023 mmol), perylene bisimide acrylate PerAcr (1910 mg, 2.3 mmol) and free nitroxide 2,2,5-trimethyl-4-phenyl-3-azahexane-3-oxyl (1.03 mg, 0.0046 mmol) were mixed with 1300 μ l *o*-dichlorobenzene. After degassing with three freeze, pump, thaw cycles the mixture was stirred at 125°C. After 46 h the reaction was stopped through rapid cooling in liquid nitrogen. The highly viscous product was dissolved in chloroform and precipitated in acetone. The purple powder was extracted in a soxhlet apparatus with acetone, butanone and CHCl₂ to remove unreacted monomer and P3HT macroinitiator. The pure polymer was obtained after dissolution in chloroform and precipitation in methanol.

GPC M_p = 36400 g mol⁻¹, M_n = 35500 g mol⁻¹, M_w/M_n =1.19,

δ_H (300 MHz; CDCl₃) 8.65-7.32 (m*8H, br, H_{ar} PPerAcr), 6.98 (n*1H, s, H_{ar} P3HT), 5.21-4.45 (m*1H, br, CH swallow tail PPerAcr), 4.35-3.70 (m*4H, br, OCH₂ and NCH₂ PPerAcr), 2.80 (2 H, t, J_{αβ} 7.6, α -CH₂ P3HT), 2.30-1.05 (m*45H and n*8H, br, CH and CH₂ PPerAcr and P3HT), 1.00-0.70 (m*6H and n*3H, br, CH₃ PPerAcr and P3HT) n= degree of polymerization of P3HT and m = degree of polymerization of PPerAcr.

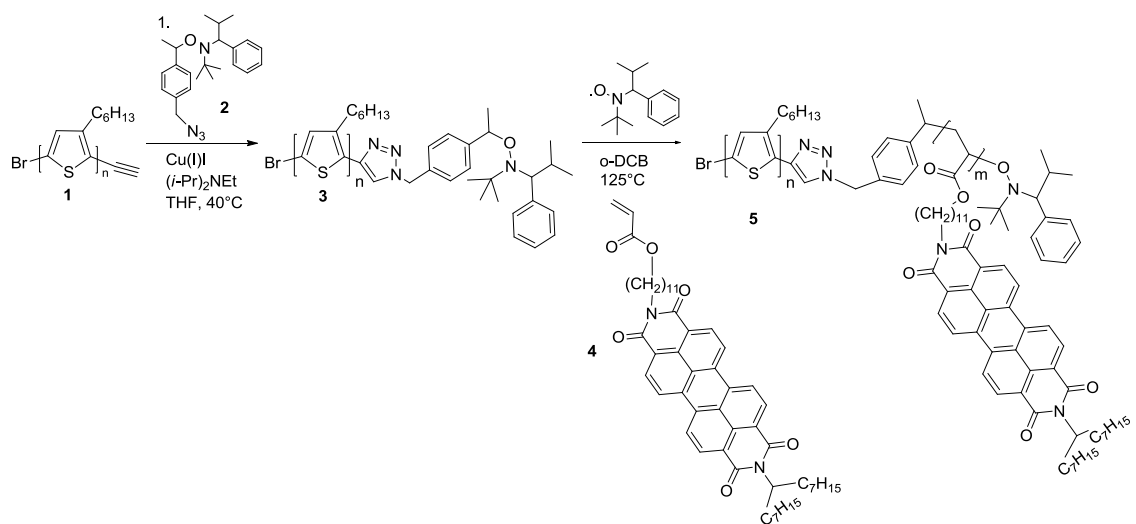
Results and Discussion

Synthesis

For the synthesis of the P3HT-macroinitiator, an alkyne functionalized P3HT (P3HT-alkyne **1**) was synthesized via Kumada catalyst transfer polymerization followed by end capping the active chain end with ethynylmagnesium chloride.³⁴ The alkyne group was further reacted in a copper catalyzed azide-alkyne reaction with 2,2,5-trimethyl-3-(1'-*p*-azidomethylphenylethoxy)-4-phenyl-3-azahexane **2** to form the alkoxyamine functionalized P3HT macroinitiator (P3HT-macroinitiator **3**) (Scheme 1). The number average molecular weight of the P3HT-macroinitiator as determined by size exclusion chromatography was 19700 g/mol and the polydispersity index (PDI) 1.15 (see Table 1 and Figure 1). According to matrix assisted laser desorption ionization mass spectrometry (MALDI-TOF MS) this corresponds to a M_n of 12400 g/mol and about 75 repeating units.

The ratio of perylene bisimide acrylate monomer **4** : P3HT-macroinitiator **3**: free nitroxide was chosen as 99:1:0.2 in order to get a high percentage of PPerAcr in the block copolymer. The polymerization was performed at 125°C and *o*-dichlorobenzene (*o*-DCB) was used as solvent. Because of the high viscosity of the polymerization mixture it is not possible to polymerize to very high conversions. After 46 h the polymerization mixture could no longer be stirred and the polymerization was stopped by cooling in liquid nitrogen. To remove the remaining monomer the polymerization mixture was dissolved in chloroform and precipitated in acetone, where only the monomer is soluble. Additionally, the traces of remaining monomer and macroinitiator were removed by soxhlet extraction using acetone, butanone and finally

dichloromethane. The resulting block copolymer had a number-average molecular weight of 35500 g/mol and a low polydispersity index (PDI) of 1.19. In contrast to the earlier method of in situ end-capping with a Grignard functionalized alkoxyamine, the present synthetic approach using P3HT-alkyne did not lead to a mixture of di- and triblocks, when a high molecular weight macroinitiator is used (Figure 1).²¹ The block ratios were determined with ¹H-NMR spectroscopy by comparing the integral of the α -CH₂ proton signals of P3HT with the integral of the methylene protons in proximity to the acrylate unit and the imide unit of the perylene bisimide acrylate. The weight ratio of PPerAcr was determined as 64wt%. Using the number of P3HT repeating units as determined from MALDI-TOF MS, this corresponds to 27 repeating units of PPerAcr.



*Scheme 1: Synthesis of P3HT-alkoxyamine macroinitiator **3** from P3HT-alkyne **1**, P3HT-alkoxyamine **3** and P3HT-*b*-PPerAcr **5** using a combination of copper catalyzed azide-alkyne click reaction and nitroxide mediated radical polymerization.*

*Table 1: Molecular weights, polydispersities and thermal properties of P3HT-alkyne **1**, P3HT-alkoxyamine **3** and P3HT-*b*-PPerAcr **5** as determined via SEC, MALDI-TOF MS, ¹H-NMR and differential scanning calorimetry. M_n = number-average molecular weight, M_p = peak molecular weight.*

| Polymer | M_n (SEC)/ M_n (MALDI) [kg/mol] | M_p (SEC) [kg/mol] | PDI (SEC) | Repeating Units P3HT/ PPerAcr | T_m [°C] | T_c [°C] | ΔH_m [J/g] |
|----------------------------------|---|-------------------------|--------------|--|--------------------|---------------|-----------------------|
| P3HT-alkyne 1 | 19.7 / 12.4 | 22.5 | 1.17 | 75 / - | - | - | - |
| P3HT-macroinitiator 3 | 19.7 / - | 23.0 | 1.15 | 75 / - | 226/236 | 197 | 17 |
| P3HT- <i>b</i> -PPerAcr 5 | 35.5 / - | 36.4 | 1.19 | 75 / 27 | 212 / 230 / 244 | 188 / 175 | 7.5 / 1.5 / 3.7 |

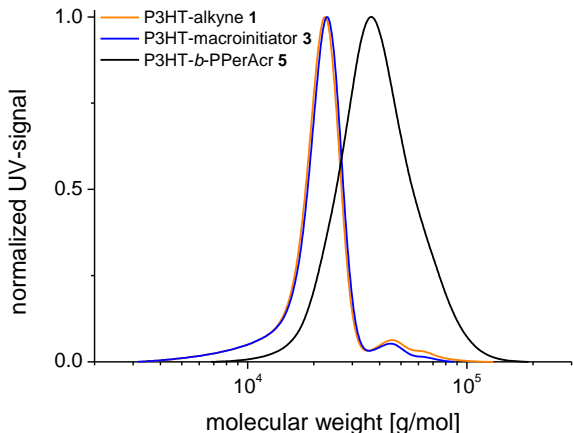


*Figure 1: Size exclusion chromatography traces of P3HT-alkyne **1**, P3HT-macroinitiator **3** and P3HT-*b*-PPerAcr **5**.*

Thermal and Optical Properties

Since both blocks of P3HT-*b*-PPerAcr are crystalline, the thermal behavior of the block copolymer strongly depends on the chain length of each block.³⁵ The P3HT-macroinitiator **3** has two melting points (T_m), a major one at 226°C and a minor one at 236°C (see Figure 2 and Table 1). This behavior can be explained by a layered phase with smectic symmetry which occurs before the isotropic melt.³⁶ The recrystallization temperature of the macroinitiator is around 197°C and the melting enthalpy is 17 J/g. For the P3HT-*b*-PPerAcr **5** three melting points are observed, one at 212°C with a melting enthalpy of 7.5 J/g, a small one at 230°C with a melting enthalpy of only 1.5 J/g and one at 244°C with an enthalpy of 3.7 J/g. Typically the melting point of PPerAcr homopolymer is around 190°C and only weakly depends on the chain length of the polymer, because it is a side chain and not a main chain crystalline polymer.^{21,37,38} For P3HT, the melting point strongly depends on the molecular weight and approaches a maximum value of ca. 245-250°C above a molecular weight of circa 15000 g/mol.³⁹ In the block copolymer, the melting points of both blocks shift to slightly higher values compared to the respective homopolymers, melting at 211°C (PPerAcr) and at 244°C (P3HT). For understanding the origin of the small melting peak at 230°C detailed XRD analysis is underway. In the block copolymer recrystallization occurs at 188°C and a small peak at 175°C can be seen in the enlarged part in Figure 2b. These values are smaller than the recrystallization temperature of P3HT homopolymer but higher than that of PPerAcr homopolymer which normally occurs around 170°C.³⁵

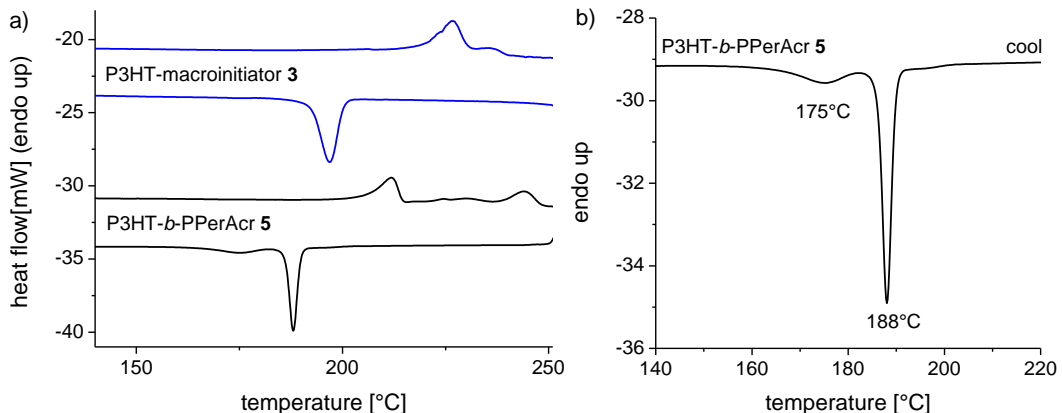


Figure 2: a) Differential scanning calorimetry curves of P3HT-alkoxyamine **3** and P3HT-*b*-PPerAcr **5** for the second heating and cooling cycles measured at a scan rate of 10K/min. b) Enlarged part of the cooling curve of P3HT-*b*-PPerAcr **5** which shows a small peak at around 175°C.

We obtained additional information about the block copolymer from UV-vis spectroscopy in solution and thin films. Figure 3a shows the normalized solution spectra of the P3HT-macroinitiator **3**, PPerAcr homopolymer (for detail information about the polymer see reference 35) and the P3HT-*b*-PPerAcr **5** in THF (0.02 mg/mL). The P3HT-macroinitiator **3** has a single nonstructured absorption band at 446 nm belonging to S₀-S₁ transition due to π → π* excitations. In contrast, the PPerAcr homopolymer shows the three characteristic vibronic structures of S₀-S₁ at 470, 490 and 525 nm. The ratio of A₀₋₀ to A₀₋₁ indicates that PPerAcr is highly aggregated in solution, which is common for side chain homopolymers of perylene bisimides.⁴⁰ As expected, the block copolymer spectrum in solution is a superposition of the spectra of both homopolymers. The vibronic bands of PPerAcr are still visible but the absorption is broadened towards smaller wavelength because of the contribution of P3HT. In thin films spin coated from 1wt% solution in CHCl₃ the situation changes. The spectrum of P3HT **3** is bathochromically shifted by 79 nm with a new maximum at 525 nm. Further, vibronic bands appear at 550 and 600 nm, which are typical for a crystalline P3HT film.⁴¹ For the PPerAcr homopolymer, the situation is different, no significant shift of the maximum appears, merely a small increase in the intensity of the low energetic vibronic shoulder (A₀₋₀) occurs. This causes a slight broadening of the spectrum towards higher wavelength. The film spectrum of P3HT-*b*-PPerAcr **5** looks similar to that of the PPerAcr homopolymer. The contribution of P3HT is only visible by a small broadening of the spectrum to lower energies and a further increase in the vibronic band at 530 nm. This is caused by a superposition with the film absorption maximum of P3HT **3** at 525 nm. The vibronic bands of P3HT at 550 nm and 600 nm are not visible in the block copolymer spectrum which indicates a low crystallinity of the P3HT block directly after spin coating. We further annealed the film of P3HT-*b*-PPerAcr above the melting points of both blocks at 252°C and cooled down slowly in order to see if we can observe a crystallization of P3HT inside the block copolymer.

Figure 3c shows the UV-vis spectra of an as spun film of P3HT-*b*-PPerAcr **5** together with its annealed film and the annealed one of the P3HT-macroinitiator **3**. For the P3HT-macroinitiator **3** annealing only slightly pronounces the vibronic bands at 550 nm and 600 nm. In contrast, for P3HT-*b*-PPerAcr **5** the effect is very considerable. The spectrum is broadened towards higher wavelength and the vibronic bands for crystalline P3HT are seen for the first time. This indicates that thermal annealing above the melting point is very effective in increasing the crystallinity of the P3HT block after spin coating from a fast evaporating solvent like CHCl₃.

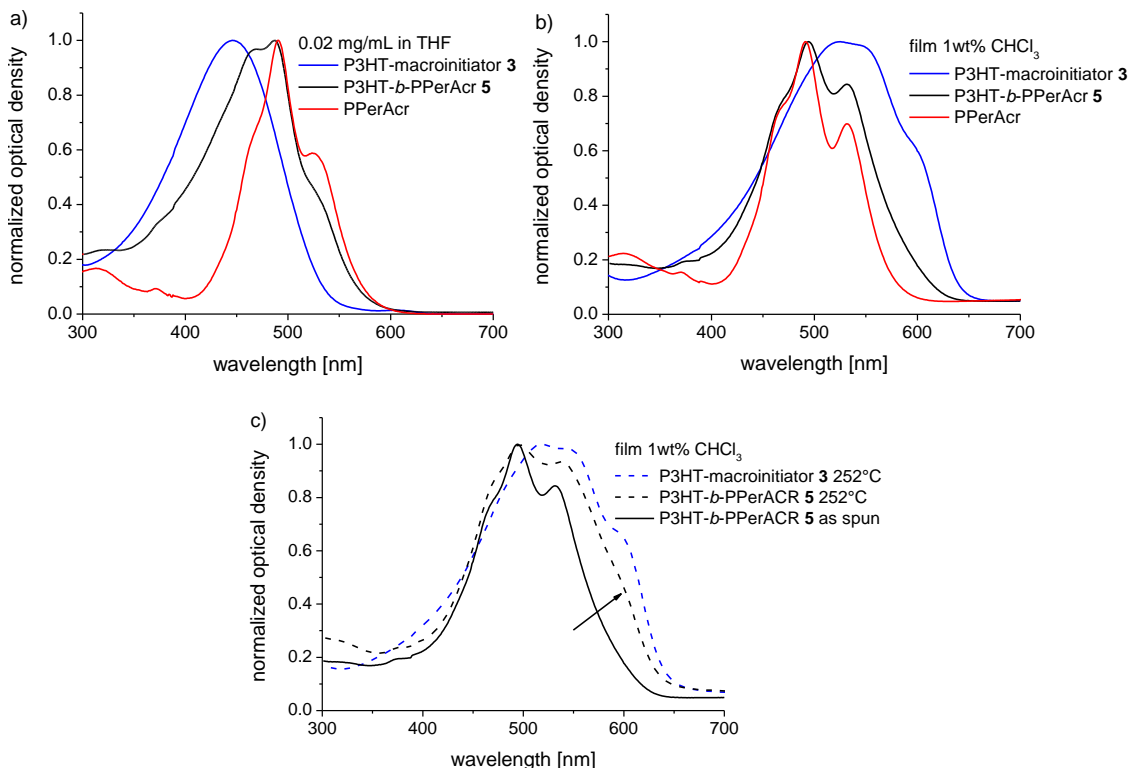
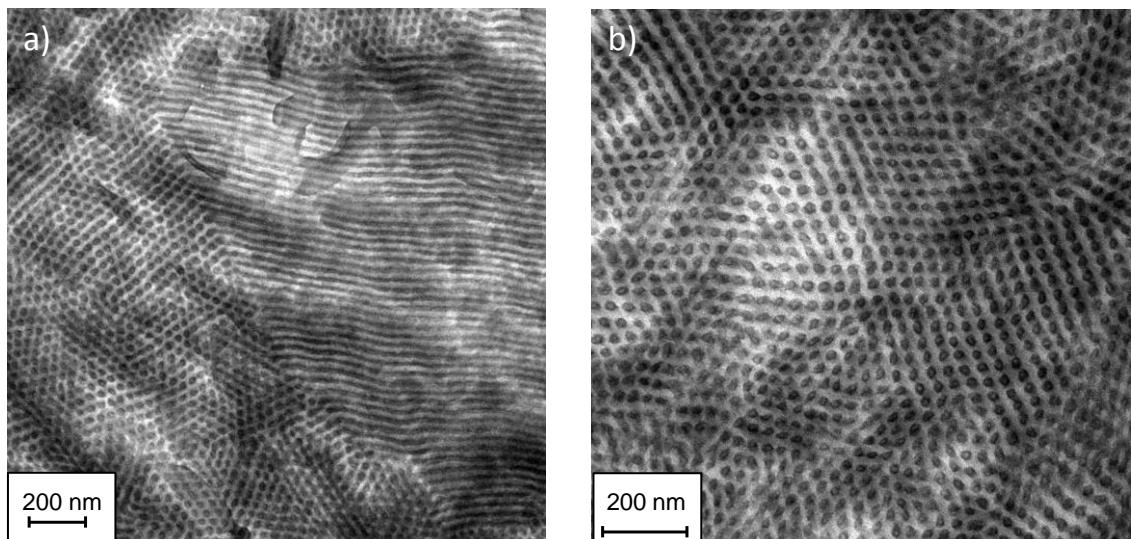


Figure 3: UV-vis spectra of P3HT-macroinitiator **3**, P3HT-*b*-PPerAcr **5** and PPerAcr homopolymer a) in a 0.02 mg/mL solution in THF and b) in thin films spin coated from 1wt% chloroform solutions. c) Films of P3HT-*b*-PPerAcr **5** and of P3HT-macroinitiator **3** after spin coating and annealing above the melting temperature.

Morphological Investigations

With the new synthetic approach, we prepared an exclusively diblock copolymer of P3HT-*b*-PPerAcr **5** and we were able to increase the molecular weight and thus the χN parameter in comparison to our previous studies.²¹ Therefore, it was interesting to investigate what effect these changes have on the microphase separation behavior in bulk and thin film. For this, we annealed a bulk sample of P3HT-*b*-PPerAcr **5** above its melting point for 2 h to erase any thermal history and then cooled it down slowly at a cooling rate of 1°C/min to allow for slow recrystallization. Transmission electron microscopy (TEM) images of the bulk sample stained with RuO₄ are presented in Figure 4. A clear microphase separation with hexagonally ordered cylinder morphology is observed. According to the literature, staining with RuO₄ selectively

stains the P3HT phase.²³ Thus, the dark cylinders comprise of P3HT and the bright matrix arises from the PPerAcr block. Such curved structures are rather unexpected for a crystalline-crystalline system but fit to the respective volume ratios of 37% for P3HT and 63% for PPerAcr. The volume ratios were calculated from the densities determined by X-ray diffraction and the respective weight ratios determined from ¹H-NMR. This is the first time that such a typical ordered phase structure of coil-coil block copolymers is observed for a crystalline-crystalline donor-acceptor system. Up to now only disordered cylinders or fibrillar structures have been observed due to the low value of the χN parameter.^{7,22,23} Further, these disordered fibrillar structures only appeared after solvent annealing and no defined structures could be observed after thermal annealing above the melting point.^{22,23,35} Preliminary small angle X-ray scattering (SAXS) measurements of our block copolymer show that for the first time microphase separation in the melt occurs, which can be explained by the high χN parameter. The phase separation in melt was lamellar with a long period of about 46 nm. Further detailed XRD investigations are underway to understand the formation of the cylindrical structures after recrystallization of both blocks.



*Figure 4: Transmission electron microscopy images of a bulk sample of P3HT-*b*-PPerACR 5 annealed for 2 h in the melt and slow cooling to room temperature with a cooling rate of 1°C/min. The P3HT phase was stained with RuO₄. a) Standing and lying cylinders. b) high magnification with hexagonally ordered cylinders.*

To see if this clear phase separation from bulk can be translated to thin film, we spin coated films from a 0.5wt% solution of chloroform on silicon. Using atomic force microscopy imaging no phase separation was visible on top of the thin films directly after spin coating. This fits to the results from UV-vis, which showed a disordered P3HT absorption with low crystallinity for the as spun film. However, clear microphase separation was observed after annealing the thin film above T_m for 20 min and slowly cooling to room temperature (Figure 5a). Nanostructures of long range order occur due to order-disorder transition. As known from UV-vis spectra in

thin films, annealing above T_m increases the crystallinity of the P3HT and as seen in Figure 5a it results in an ordered nanostructured bulk heterojunction. This demonstrates that the microphase separated melt allows fast ordering, which is important for device fabrication. The domain sizes may deviate slightly from the real values because of the influence of the shape of the AFM-tip. Therefore, we made additional raster electron microscopy images. Unfortunately, the contrast of the unstained film was very low (Figure 5b left). After staining with RuO₄ for 5 min the contrast was improved but the sample slightly degraded which can be seen by the dots formed on top of the self-assembled structures (Figure 5b right). The observed domain sizes are in the range of the exciton diffusion length with about 10 nm for the minor domain and about 30 nm for the major phase. These features were observed for even thinner films spin coated from 0.25wt% CHCl₃ solution and independent on the underlying substrate e.g. silicon, poly(3,4-ethylenedioxythiophene) poly(styrenesulfonate) PEDOT-PSS, a typical bottom layer in organic solar cells, or Kapton. The top images do not allow the exact determination of the type of structure; either lying cylinders or standing lamella are possible. This was hard to distinguish in films with a thickness in the range of the microphase separated structures.

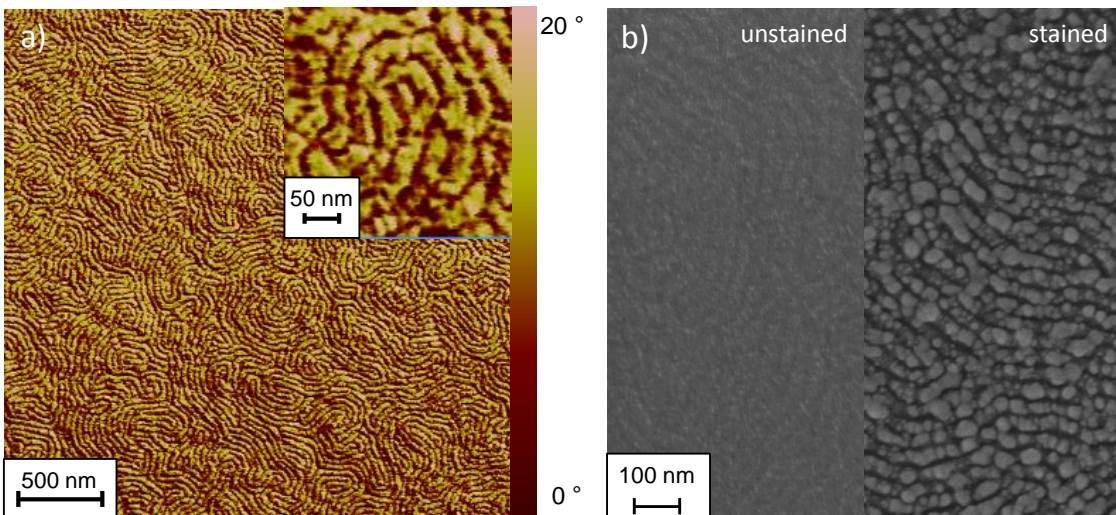


*Figure 5: Images of circa 50 nm thick films spin coated from a 0.5 wt% chloroform solution of P3HT-*b*-PPerAcr 5, annealing 20 min above the melting temperature and slowly cooling to room temperature. a) Atomic force microscopy phase image of a film on silicon containing an inset with higher resolution b) Raster electron microscopy image of a film on Kapton left) unstained and right) stained with RuO₄ for 5 min.*

Conclusion

In conclusion, we showed that using a combination of copper catalyzed azide-alkyne click reaction and NMRP it is possible to synthesize exclusively diblock copolymers of P3HT-*b*-PPerAcr with a high molecular weight. The P3HT block had a molecular weight of 19700 g/mol and the content of PPerAcr was 64wt%. The long conjugated block is valuable for high charge transport mobility in P3HT and the high content of PPerAcr is very promising for a balanced charge transport. The high molecular weight of 35500 g/mol of the block copolymer

leads to a high χN parameter, which allowed microphase separation in the melt. Thus, after annealing a bulk sample above the melting temperature for the first time hexagonally ordered cylindrical phases were observed for a crystalline-crystalline donor-acceptor block copolymer. Further, these structures could be transferred to thin film, in which a long range order over the whole film was obtained. The domain sizes are in the range of the exciton diffusion length which makes this block copolymer very promising for organic photovoltaics. Further X-ray diffraction measurements are underway to understand the formation of a cylindrical phase from a molten lamellar structure and the orientation of the nanostructure in thin films.

Acknowledgment

We acknowledge financial support for this research work from DFG SPP 1355. R. H. Lohwasser thanks the Elite network Bavaria for a research stipend. Thanks also to Melanie Förttsch, Annika Pfaffenberger and Carmen Kunert for TEM, Martina Heider for REM as well as to Kerstin Schindler for AFM measurements. Thanks also to Gaurav Gupta for the SAXS measurements.

References

- (1) Coakley, K. M.; McGehee, M. D. *Chem. Mater.* **2004**, *16*, 4533-4542.
- (2) Ma, W.; Yang, C.; Gong, X.; Lee, K.; Heeger, A. J. *Adv. Funct. Mater.* **2005**, *15*, 1617-1622.
- (3) Green, M. A.; Emery, K.; Hishikawa, Y.; Warta, W. *Prog. Photovolt: Res. Appl.* **2011**, *19*, 84-92.
- (4) Erb, T.; Zhokhavets, U.; Gobsch, G.; Raleva, S.; Stühn, B.; Schilinsky, P.; Waldauf, C.; Brabec, C. J. *Adv. Funct. Mater.* **2005**, *15*, 1193-1196.
- (5) Van Duren, J. K. J.; Yang, X.; Loos, J.; Bulle-Lieuwma, C. W. T.; Sieval, A. B.; Hummelen, J. C.; Janssen, R. A. J. *Adv. Funct. Mater.* **2004**, *14*, 425-434.
- (6) Miyanishi, S.; Zhang, Y.; Tajima, K.; Hashimoto, K. *Chem. Commun.* **2010**, *46*, 6723-6725.
- (7) Sommer, M.; Lang, A. S.; Thelakkat, M. *Angew. Chem. , Int. Ed.* **2008**, *47*, 7901-7904.
- (8) Stalmach, U.; De Boer, B.; Videlot, C.; Van Hutten, P. F.; Hadzioannou, G. *J. Am. Chem. Soc.* **2000**, *122*, 5464-5472.
- (9) Tu, G.; Li, H.; Forster, M.; Heiderhoff, R.; Balk, L. J.; Scherf, U. *Macromolecules* **2006**, *39*, 4327-4331.
- (10) Shah, M.; Ganesan, V. *Macromolecules* **2009**, *43*, 543-552.
- (11) de Boer, B.; Stalmach, U.; van Hutten, P. F.; Melzer, C.; Krasnikov, V. V.; Hadzioannou, G. *Polymer* **2001**, *42*, 9097-9109.
- (12) Lindner, S. M.; Hüttner, S.; Chiche, A.; Thelakkat, M.; Krausch, G. *Angew. Chem., Int. Ed.* **2006**, *45*, 3364-3368.
- (13) Boudouris, B. W.; Frisbie, C. D.; Hillmyer, M. A. *Macromolecules* **2008**, *41*, 67-75.
- (14) Higashihara, T.; Ueda, M. *Macromolecules* **2009**, *42*, 8794-8800.
- (15) Liu, J.; Sheina, E. E.; Kowalewski, T.; McCullough, R. D. *Angew. Chem., Int. Ed.* **2002**, *41*, 329-332.

- (16) Radano, C. P.; Schermen, O. A.; Stingelin-Stutzmann, N.; Müller, C.; Breiby, D. W.; Smith, P.; Janssen, R. A. J.; Mejier, E. W. *J. Am. Chem. Soc.* **2005**, *127*, 12502-12503.
- (17) Dai, C.; Yen, W.; Lee, Y.; Ho, C.; Su, W. *J. Am. Chem. Soc.* **2007**, *129*, 11036-11038.
- (18) Sary, N.; Richard, F.; Brochon, C.; Leclerc, M.; Leveque, P.; Audinot, J.; Berson, S.; Heiser, T.; Hadzioannou, G.; Mezzenga, R. *Adv. Mater.* **2009**, *21*, 1-6.
- (19) Sivula, K.; Ball, Z. T.; Watanabe, N.; Fréchet, J. M. *J. Adv. Mater.* **2006**, *18*, 206-210.
- (20) Rajaram, S.; Armstrong, P. B.; Kim, B. J.; Fréchet, J. M. *J. Chem. Mater.* **2009**, *21*, 1775-1777.
- (21) Sommer, M.; Hüttner, S.; Steiner, U.; Thelakkat, M. *Appl. Phys. Lett.* **2009**, *95*, 183308.
- (22) Zhang, Q.; Cirpan, A.; Russel, T. P.; Emrick, T. *Macromolecules* **2009**, *42*, 1079-1082.
- (23) Tao, Y.; McCulloch, B.; Kim, S.; Segalman, R. A. *Soft Matter* **2009**, *5*, 4219-4230.
- (24) Singh, C. R.; Sommer, M.; Himmerlich, M.; Wicklein, A.; Krischock, S.; Thelakkat, M.; Hoppe, H. *Phys. Status Solidi RRL* **2011**, *5*, 247-249.
- (25) Liu, C.; Lin, C.; Kuo, C.; Lin, S.; Chen, W. *Prog. Polym. Sci.* **2011**, *36*, 603-637.
- (26) Olsen, B. D.; Segalman, R. A. *Mater. Sci. Eng., R* **2008**, *62*, 37-66.
- (27) Pryamitsyn, V.; Ganesan, V. *J. Chem. Phys.* **2004**, *120*, 5824-5838.
- (28) Lohwasser, R. H.; Thelakkat, M. *Macromolecules* **2011**, submitted.
- (29) Van Hecke, G. R.; Horrocks, W. *Inorg. Chem.* **1966**, *5*, 1968-1974.
- (30) Benoit, D.; Chaplinski, V.; Braslau, R.; Hawker, C. J. *J. Am. Chem. Soc.* **1999**, *121*, 3904-3920.
- (31) Binder, W. H.; Gloger, D.; Weinstabl, H.; Allmaier, G.; Pittenauer E. *Macromolecules* **2007**, *40*, 3097-3107.
- (32) Langhals, H.; Saulich, S. *Chem. Eur. J.* **2002**, *8*, 5630-5643.
- (33) Krasovskiy, A.; Knochel, P. *Synthesis* **2006**, *5*, 890-891.
- (34) Jeffries-El, M.; Sauve, G.; McCullough, R. D. *Macromolecules* **2005**, *38*, 10346-10352.
- (35) Sommer, M.; Hüttner, S.; Thelakkat, M.; *Semiconductor Block Copolymers for Photovoltaic Applications In Ideas in Chemistry and Molecular Sciences: Advances in Nanotechnology, Materials and Device* (Ed: Pignataro, B.), WILEY-VCH Verlag GmbH & Co. KGaA, Weinheim, **2010**, Ch. 12.
- (36) Wu, Z.; Petzold, A.; Henze, T.; Thurn-Albrecht, T.; Lohwasser, R. H.; Sommer, M.; Thelakkat, M. *Macromolecules* **2010**, *43*, 4646-4653.
- (37) Lang, A. S.; Neubig, A.; Sommer, M.; Thelakkat, M. *Macromolecules* **2010**, *43*, 7001-7010.
- (38) Lindner, S. M.; Thelakkat, M. *Macromolecules* **2004**, *37*, 8832-8835.
- (39) Zen, A.; Saphiannikova, M.; Neher, D.; Grenzer, J.; Grigorian, S.; Pietsch, U.; Asawapirom, U.; Janietz, S.; Scherf, U.; Lieberwirth, I.; Wegner, G. *Macromolecules* **2006**, *39*, 2162-2171.
- (40) Lindner, S.; Kaufmann, N.; Thelakkat, M. *Org. Electron.* **2007**, *8*, 69-75.
- (41) Zhokhavets, U.; Erb, T.; Gobsch, G.; Al-Ibrahim, M.; Ambacher, O. *Chem. Phys. Lett.* **2006**, *419*, 347-350.

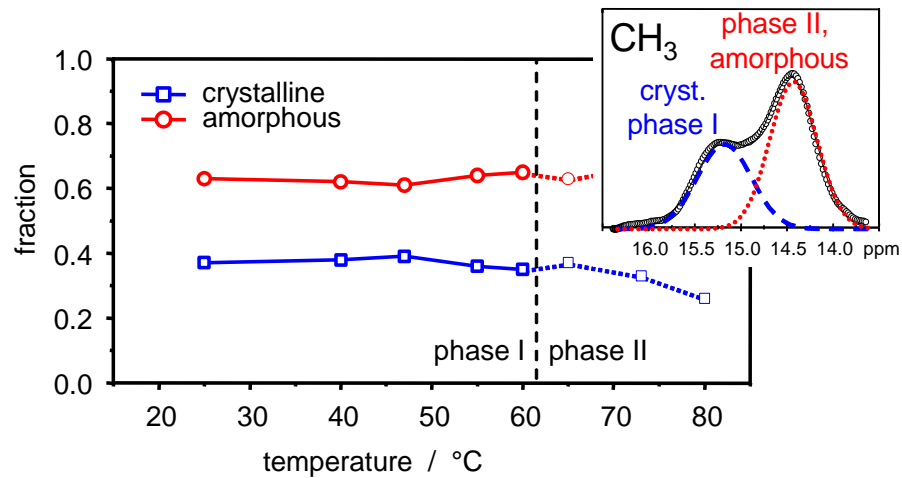
9. High Crystallinity and Nature of Crystal-Crystal Phase Transformations in Regioregular Poly(3-hexylthiophene)

Ovidiu F. Pascui,^{a)} Ruth Lohwasser,^{b)} Michael Sommer,^{b)} Mukundan Thelakkat,^{b)} Thomas Thurn-Albrecht,^{a)} Kay Saalwächter,^{*,a)}

^{a)} Institut für Physik, Martin-Luther-Universität Halle-Wittenberg, 06099 Halle, Germany

^{b)} Angewandte Funktionspolymere, Makromolekulare Chemie I, Universität Bayreuth, 95440 Bayreuth, Germany

* E-mail corresponding author: kay.saalwaechter@physik.uni-halle.de



Abstract

Molecular weight and stereoregularity affect the morphology and the crystallinity of conjugated polymers, and are thus of pivotal relevance for the mobility of charge carriers in electro-optical device applications. Currently, poly(3-alkylthiophenes) are discussed as one of the most promising classes of materials for photovoltaic applications. Here, we use ^{13}C solid-state NMR to determine the crystallinity and details on crystal-crystal phase transformations in regioregular head-to-tail poly(3-hexylthiophene) of well-defined molecular weight, and demonstrate that the crystallinity was previously severely underestimated. Typical crystallinities are at least around 37% for the lowest molecular weights and as high as about 64% upon increasing MW, corresponding to a corrected maximum value for the reference melting enthalpy of $\Delta H_m^\infty \approx 37 \text{ J/g}$ for use in DSC experiments. Using 1D ^{13}C spectra and 2D experiments that measure the strength of $^{13}\text{C}-^1\text{H}$ dipolar couplings, we observe that the crystal-crystal phase transition between a 3D- and a 2D-ordered crystalline phase at around 60°C entails a structural disordering process of the alkyl side chains, while not affecting rigidity and conformation of the backbones. This phase transition is suppressed at higher molecular weights due to a kinetic suppression of the formation of the alkyl-ordered low-temperature phase.

Introduction

Conjugated polymers such as poly(3-alkylthiophenes), P3ATs, have attracted considerable interest due to their semiconducting properties, resulting in potential application in organo-electronic devices like light emitting diodes (LED), organic field-effect transistors (OFET), and photovoltaic cells.¹⁻³ The solubility, fusibility, and stability of these semiconducting conjugated polymers render them easily processable,⁴ enabling the production of printed electronics on flexible substrates. The electronic and optical properties of polymeric alkylthiophenes depend strongly on the stereoregularity,⁵⁻⁷ solvent⁷ and molecular weight (MW) of the sample.⁸⁻¹³ Varying the MW by one order of magnitude results in a 4 orders of magnitude change in the mobility of the charge carriers in the sample.¹⁰ This effect is at least to a large extent related to the corresponding changes in crystallinity.^{9,14-16} Accordingly, the charge carrier mobility at room temperature is almost 3 orders of magnitude higher for highly regular (98%) head-tail, P3HT as compared with that of samples with lower HT content (81%),⁵ while for even more irregular samples, the electronic conductivity drops by another factor of 20 to 50.¹⁷⁻¹⁹ The regioregularity, i.e., the percentage of stereoregular head-to-tail (HT) attachments of the alkyl side chains to the 3-position of the thiophene ring,¹⁷ is controlled by the nature of the catalyst used for polymerization. In recent years, more and more refined synthetic methods were developed to produce highly regioregular P3ATs with high reproducibility,^{17,20,21} and correspondingly the quality of the investigated materials constantly improved.

P3HT is a semicrystalline polymer, and its crystalline structure is highly anisotropic. It exhibits π - π stacking of the planar backbones in the *b* direction and a larger scale nanophase-separated structure in the *a* direction caused by segregation between main and side chains as shown in Figure 1.^{22,23} The unit cell is commonly described as orthorhombic, and more detailed investigations show deviations pointing at a monoclinic⁹ structure. Winokur et al.²⁴ initially suggested a structure with disordered side chains²⁵ in the otherwise crystalline material. Later, the presence of tilting of the side chains²⁶ and, recently,²⁷ evidence for the existence of interdigitated and tilted but disordered side chains were reported for P3ATs with long alkyl chains. While the melting of the side chains at high temperature in P3ATs with longer alkyl chains was observed by DSC previously,^{28,29} clear evidence for a separate side-chain melting taking place in P3HT was obtained only recently based on combined DSC and X-ray scattering results.³⁰ These experiments gave evidence for a corresponding phase transition around 60°C and were obtained on a P3HT sample with defined molecular weight and high regioregularity. Side-chain melting gives rise to a loss of correlation between neighboring layers of main chains (in *a* direction). Figure 2 shows a schematic presentation of the structure in the corresponding phases. These results suggest that P3HT is a highly heterogeneous material in terms of molecular packing and mobility.

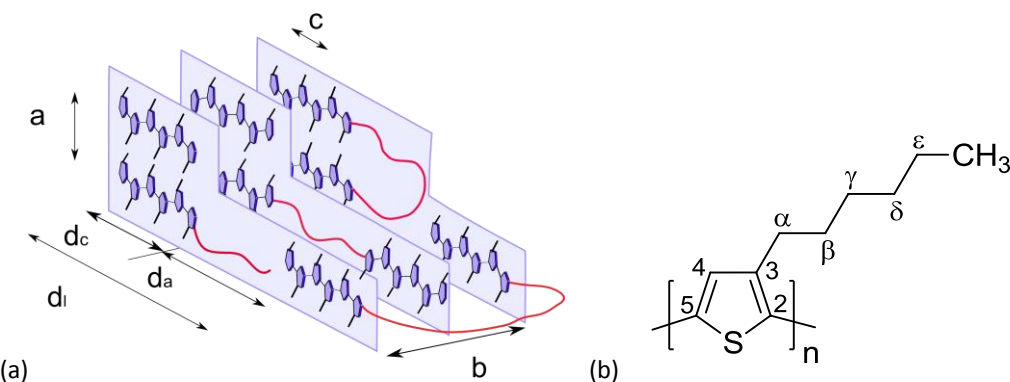


Figure 1: (a) Typical microstructure of regioregular P3HT, with curvy lines representing segments in the amorphous domain. Crystal lattice parameters *a*, *b*, *c*; thickness of the lamellar crystals *d_c*; thickness of the amorphous layers *d_a*; long period *d_l* = *d_a* + *d_c*. (b) Numbering scheme of the carbons in the repeat unit of P3HT.

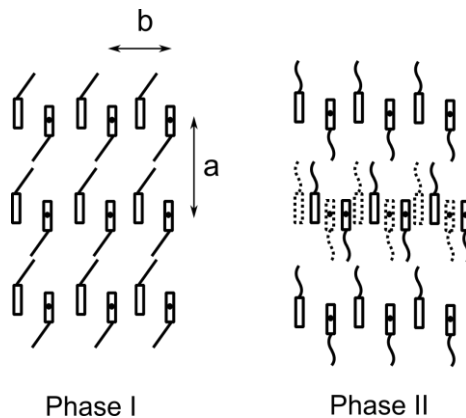


Figure 2: Schematic of phases I and II: low temperature - regular 3D-crystal with ordered main and side chains. High temperature - regular packing of the main chains only. The side chains are molten and disordered. Correspondingly different main chain layers lose correlation with each other as illustrated for the central layer.

Given the strong correlation between mobility of the charge carriers and molecular weight, mostly caused by structural features, our knowledge about the exact structure of P3HT is rather limited. Presently, there is no reliable method to determine the crystallinity of a given sample of P3HT. There is evidence that the extrapolated value for ΔH of 100% crystalline P3HT given in reference 23 is significantly too large.³⁰ A calibration for crystallinity based on scattering experiments is not available. Additionally, the situation in a material like P3HT is rather complex, as in addition to the fact that there are crystalline and amorphous parts in the sample, the possibility has to be taken into account that main chains and side chains display different degrees of order. Information about the latter question can only indirectly be obtained from scattering experiments, while solid-state NMR, as a local technique, promises to supply additional information.

NMR methods have been applied to investigate several aspects of P3AT's. Liquid-state NMR, on the one hand, is an indispensable tool in determining the stereo/regioregularity of P3HT, including ^1H and ^{13}C signal assignments.^{20,28,29,31} Solid-State NMR, on the other hand, was used to analyze the molecular dynamics in regioregular poly(3-butylthiophene), P3BT, and poly(3-dodecylthiophene), P3DDT, close to the glass transition temperature.³² Bolognesi et al. used nonquantitative ^{13}C MAS NMR spectra to analyze the thermal behavior of the poly(3-octylthiophene), P3OT. The existence of two different crystalline phases at room temperature besides the amorphous phase was concluded.³³ A low-temperature crystalline phase, characterized by all-*trans* conformations^{34,35} of the side chains, disappears after heating above 60°C, while the other phase, with a small amount of *trans* conformations, is stable at higher temperatures; the crystallinity appeared unaffected, as concluded from X-ray diffraction.³³ Further, a narrowing of the signals of the backbone carbons at 100°C was attributed to an increased mobility associated with a transition to a smectic phase in a narrow temperature interval³³ before melting.

Here, we present quantitative ^{13}C MAS NMR experiments on two highly regioregular P3HT samples with well-defined chemical structure and molecular weight which were recently investigated by a combination of DSC and wide-angle X-ray scattering.³⁰ The experiments allow the quantitative distinction of alkyl side chains belonging to crystalline and amorphous parts of the chain and confirm that at higher temperatures above the phase transition mentioned before the order of the side chains even in the crystalline part of the sample is lost, while the main chains remain unaffected. These results are consistent with the scenario suggested before based on evidence of scattering experiments³⁰ and is in line with the qualitative results obtained by Bolognesi et al. for P3OT.³³ The NMR crystallinity determined herein quantitatively reflects the fraction of P3HT units with well-ordered side-chain arrangement, associated with the low-temperature phase I. The NMR crystallinity thus constitutes an overall minimum value that, given the usual small deviations between crystallinities derived from different methods, can be compared with DSC results of the same sample in order to derive a more reliable upper estimate of ΔH_m of P3HT to be used as a proper reference for DSC experiments. The previous estimate by Malik and Nandi²³ in fact led to underestimations of crystallinity of P3HT by about a factor of 3.

In a second set of advanced 2D DIPSHIFT NMR experiments the mobility of the main and side chains is assessed. Our results indicate clear correlations between the molecular mobility, the local conformation, and the structure of the different crystalline phases of P3HT. Finally, a first experiment on higher molecular weight material is presented for comparison. In line with DSC results, we show that higher MW samples are characterized by a lower content of ordered alkyl side chains which we attribute to a kinetic suppression of the ordering process taking place at the phase transition around 60°C.

Experimental part

Samples. Regioregular poly(3-hexylthiophene) was synthesized using the Grignard methathesis polymerization developed by McCullough et al.³⁶ Using this method, highly HT regioregular samples were obtained (97% as measured by ^1H NMR). The samples are of well-controlled molecular weight and low polydispersity, as demonstrated by the M_n and M_w determined by size-exclusion chromatography (SEC). The corresponding data are shown in Table 1. From now on, we shall address the different samples as P3HT 3 and P3HT 6, by reference to their M_n from mass spectroscopy (MALDI), since the absolute values determined by SEC are too large due to the expanded-coil conformation of the stiff P3HT chains, rendering the calibration via the hydrodynamic volume of poly(styrene) standards imprecise. The same samples were previously investigated by small- and wide-angle X-ray scattering.³⁰

Table 1. Molecular characteristics of samples used in this study.

| | M_n / kDa | M_w / kDa | PDI (SEC) | M_n by MALDI / kDa |
|--------|-------------|-------------|-----------|----------------------|
| P3HT 3 | 5.2 | 6.0 | 1.15 | 3.2 |
| P3HT 6 | 7.9 | 10.1 | 1.28 | 6.6 |

Figure 3 shows calorimetric data of the two samples obtained from a DSC measurement using a Diamond DSC from Perkin-Elmer. Background contributions were subtracted resulting in measuring the apparent heat capacity $c_p(T)$. While the signal around 0°C was attributed to the glass transition, two structural transitions show up, as confirmed by temperature-dependent X-ray scattering experiments.³⁰ The peak around 50-60°C is related to the transition from phase I to phase II, and the peak at higher temperatures corresponds to crystal melting. While the first peak is weaker in P3HT 6, the second becomes larger in sample P3HT 6. The fact that the melting peak changes not only the position but also the shape (i.e., higher ΔH_m) indicates that not only the thickness of the crystals but also the crystallinity increases with increasing the molecular weight. A quantitative interpretation of the DSC data in terms of crystallinity is difficult, given the fact that the enthalpy of melting given in the literature seems inconsistent with results from x-ray scattering and might be uncertain.^{23,30} It should be noted that the melting enthalpy of both samples increases somewhat over time upon annealing at room temperature, with final values of 13.8 J/g (P3HT 3) and 23.6 J/g (P3HT 6) being reached after about 20 min.

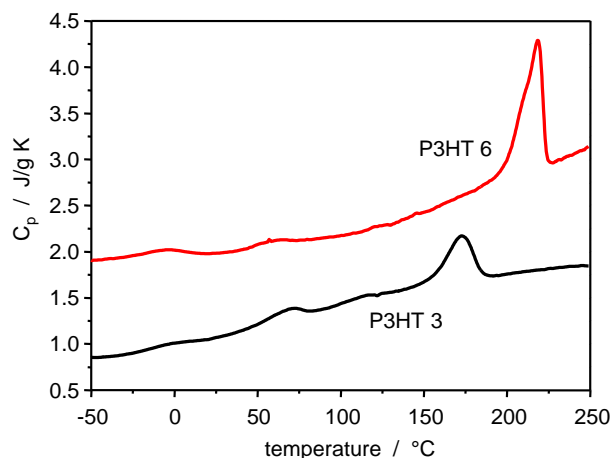


Figure 3: DSC curves for P3HT 3 (bottom) and P3HT 6 (top) as obtained during heating (20K/min) directly after cooling to -50°C. The enthalpies of melting as obtained by integration over the melting peak are 9.8 J/g for P3HT 3 and 20.9 J/g for P3HT 6. The data for P3HT 6 are shifted upwards by 1 J/g K. Note that the melting enthalpies increase to 13.8 and 23.6 J/g, respectively, after annealing at room temperature.

Solid-State NMR. Three types of experiments using solid-state ^{13}C magic-angle spinning (MAS) NMR techniques were performed in order to assess the conformational state of the main and side chains, the quantitative phase composition, and the dynamics of different CH_n groups in the sample as a function of temperature. First, it is important to note that ^{13}C chemical shifts taken from simple 1D spectra are indicative of the conformation of the respective chemical moieties.^{34,35} The conformational state measured in this experiment corresponds to an average on the millisecond time scale, given basically by the inverse chemical-shift span covered by the possible static conformations (about 5 ppm corresponding to 500 Hz at 100 MHz Larmor frequency). Two different schemes of excitation were used: Cross-polarization (CP) MAS NMR

is well-suited for a time-efficient, yet nonquantitative acquisition of ^{13}C spectra. It is based on transferring the high polarization of protons to the initially less polarized ^{13}C . A second advantage is that the shorter T_1 relaxation time (time to reach the equilibrium spin population after excitation) of protons determines the time scale on which individual transients can be repeated. The CP process is, however, nonquantitative in that the different phases (crystalline and amorphous) are not polarized according to their mass ratio. The true phase composition, on the other hand, can be taken from integrals in fully relaxed single-pulse excitation (SPE) spectra. This takes a much longer time due to the lower ^{13}C polarization and because spectra need to be acquired with a transient repetition time (recycle delay) exceeding the rather long ^{13}C T_1 . The actual T_1 values of the different CH_n moieties were determined in a second set of experiments using the method of Torchia.³⁷ The temperature dependence of T_1 allows a distinction between groups with molecular motion taking place either below or above the time scale given by the inverse Larmor frequency, i.e., about 100 MHz. Finally, we use an advanced 2D Dipolar Chemical Shift Correlation³⁸⁻⁴⁰ (DIPSHIFT) experiment that is based on the chemically resolved ^{13}C MAS spectra. The DIPSHIFT pulse sequence affords a selective precession of nuclear spin states due to heteronuclear dipolar couplings only, while suppressing all other interactions. The final signal thus reflects the CH dipolar coupling in terms of a modulation pattern, which depends on a DIPSHIFT evolution time t_1 , extending from 0 to the rotor period T_R , and going through a minimum at $t_1 = T_R/2$. Roughly, the depth of the minimum and the steepness of the modulation curve at $t_1 = 0$ and $t_1 = T_R$ reflect the exact magnitude of the coupling, which can be obtained by comparing with simulations. The full CH dipolar coupling (around 20 kHz for a rigid CH bond) is obtained if molecular motion of the CH internuclear vector is slow on the interaction time scale ($\tau_c^{-1} \ll 20$ kHz), while a fast-limit averaged CH dipolar is measured if the inverse correlation time (rate of the process) is much faster ($\tau_c^{-1} \gg 20$ kHz), typically above 100 kHz. For the latter case, the measured ratio of the experimental residual to the static-limit dipolar coupling is equal to a dynamic order S parameter that reflects the amplitude of molecular rotations and tumbling motions of the internuclear $^{13}\text{C}-^1\text{H}$ vector with respect to the B_0 field. The dynamic order parameter S corresponds to a time average of the second Legendre polynomial P_2 over a typical period of at least $1/(20$ kHz)

$$S = \left\langle \frac{1}{2}(3\cos^2 \alpha(t) - 1) \right\rangle_t \quad (1)$$

where α is the angle of a given CH vector with respect to the local symmetry axis of motion. Fast isotropic motion thus averages the dipolar coupling to zero.

NMR experiments were performed on a Bruker Avance III spectrometer, operating at the resonance frequency of 100.5 MHz, with a static field of 9.4 T. The temperature-dependent MAS experiments were performed at a spinning frequency $\omega_R/2\pi = 7000$ Hz. The rotation frequency stability was within ± 1 Hz, while the sample temperature for each spinning rate was

calibrated⁴¹ and is expected to be stable within $\pm 0.3^\circ$. Typical lengths for the 90° pulses were 3.7 and $3.35\ \mu s$ for the ^{13}C and ^1H , respectively, where the latter specifies the power level for TPPM (two-pulse phase modulation) dipolar decoupling. The CP contact time used in some of the experiments was 2 ms, if not specified otherwise. For all pulse sequences using CP, a recycle delay of 3 s was used, while for SPE experiments, a recycle delay of 10 s was used to ensure the equilibrium of the magnetization, as proven by the T_1 relaxation time measurements discussed below. NMR spectra were calibrated using α -glycine (176.2 ppm) as an external shift reference. For the 2D DIPSHIFT experiments,^{38-40,42-43} the offset frequency during the frequency-switched Lee-Goldburg (FSLG) homodecoupling was $\Omega/2\pi = 52838\ \text{Hz}$. Alanine and glycine were used to calibrate the DIPSHIFT modulation curves and thus to obtain references to the static-limit dipolar coupling constants of CH_n groups. Deconvolutions of spectral lines were performed with Gaussian, Lorentzian, or mixed line shape functions using the curve fit tool of the Origin software.

Results and Discussion

^{13}C SPE and CP MAS NMR Spectra

Temperature dependent ^{13}C SPE MAS spectra of P3HT 3 recorded at 7 kHz MAS are presented in Figure 4. The resonances belonging to the main-chain carbons in the thiophene rings appear in the 140-120 ppm region. The assignment of the lines for the backbone carbons is according to references 32 and 44. The region containing the backbone signals was scaled to equal height for all temperatures, hence the apparent difference in signal-to-noise (S/N) as compared to the alkyl regions. The repetition delay of 10 s is in fact sufficient for a quantitative observation of the alkyl carbons, while the main-chain carbons have impractically long T_1 (see below). For all temperatures, we observe a significant contribution of the amorphous phase of the polymer, which is represented by the broad background signal in the aromatic main-chain part of the spectrum, indicating conformational disorder. The exact line positions for main- and side-chain resonances obtained by spectrum deconvolution are given in Table 2.

The SPE spectrum at 25°C exhibits two peaks for the methyl group in the aliphatic region, corresponding to the different conformations of the side chains (Table 2). The downfield peak (15.47 ppm) is associated with an average *trans* conformation at the chain end, while the upfield peak (14.51 ppm) is associated with the side chains with a higher *gauche* content.^{33-35,45} Usually, one associates the chains in *trans* conformation with the more ordered crystalline phase (c), while the chains in a noncrystalline/amorphous phase (a) adopt more *gauche* conformations on average.

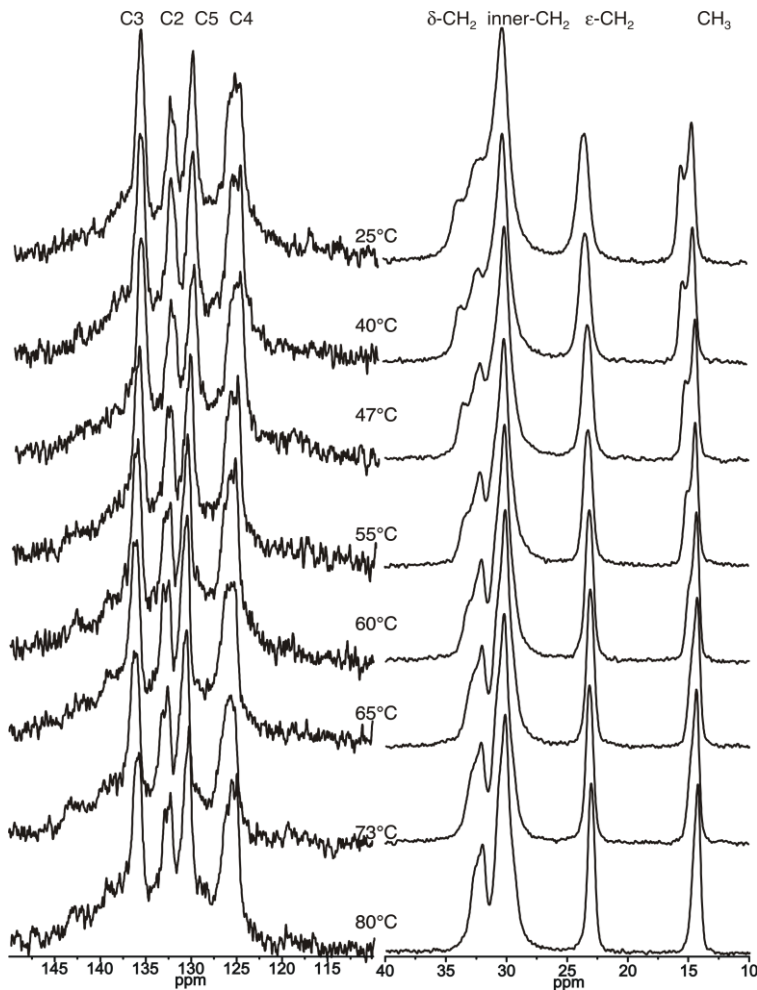


Figure 4: ^{13}C SPE MAS spectra of the P3HT 3 sample, with a recycle delay of 10s and the temperatures indicated (spinning frequency 7 kHz).

Table 2: ^{13}C chemical shifts (ppm) of the alkyl chains in P3HT 3 from SPE MAS spectra.

| P3HT 3 | | | | | | | |
|--------|--------|--------|--------|--------|-----------------------|-------------------|-----------------|
| T/°C | C3 | C2 | C5 | C4 | inner CH ₂ | ε-CH ₂ | CH ₃ |
| 25 | 136.09 | 132.90 | 130.35 | 125.24 | 33.60/32.06/30.15 | 23.45 | 15.47/14.51 |
| 40 | 136.25 | 132.74 | 130.67 | 125.08 | 33.50/32.06/30.15 | 23.45 | 15.31/14.35 |
| 47 | 136.25 | 132.90 | 130.35 | 125.24 | 33.50/32.06/30.15 | 23.29 | 15.15/14.20 |
| 55 | 135.93 | 132.90 | 130.51 | 125.24 | 33.34/32.22/30.15 | 23.13 | 15.14/14.35 |
| 60 | 135.91 | 132.82 | 130.47 | 125.21 | 32.07/30.17 | 23.18 | 14.35 |
| 65 | 135.95 | 132.43 | 130.42 | 125.25 | 32.07/30.15 | 23.13 | 14.33 |
| 73 | 136.02 | 132.53 | 130.44 | 125.56 | 32.06/30.15 | 23.11 | 14.31 |
| 80 | 136.29 | 132.60 | 130.57 | 125.71 | 32.17/30.31 | 23.16 | 14.30 |

With increasing temperature, the *trans* peak of the methyl, c-CH₃, unit shifts to lower ppm values, which means that the side chains in the crystalline phase reorganize themselves from an ordered crystalline structure to a less ordered one, with increasing time-averaged *gauche* content. At and above 60°C, the crystalline peak (now phase II) is merely a shoulder on the

gauche peak and cannot be reliably separated any more. Below we will prove that this composite signal is indeed a superposition of carbons in different phases, i.e., the crystalline phase II and the amorphous phase.

The inner CH₂ groups resonate in the 30-33 ppm region. As detailed in Table 2, we detect three resonances in this spectral region at room temperature. According to ref 45, the α -, β - and γ -CH₂ resonate around 29-30 ppm, while the δ -CH₂ resonance is usually shifted downfield (i.e., to high ppm). Considering that the downfield signal at 33.6 ppm behaves similarly as the trans peak of the methyl group with increasing temperature, disappearing above 60°C, we take that this resonance rises from the inner methylenes adopting mainly *trans* conformations. The remaining signal at 32.06 ppm is assigned to δ -CH₂. It is difficult to assign the peak at 33.6 ppm to an individual methylene group; therefore, we restrict ourselves to state that this resonance represents methylenes in mostly the *trans* configuration. The highest and broader signal at 30.15 ppm possibly represents a mix of *trans* and *gauche* conformers and is just addressed as the “inner CH₂” peak. Its overall temperature dependence is weak. The last methylenes in the side chains, ϵ -CH₂, resonate at 23.45 ppm; increasing the temperature leads to line narrowing and a small upfield shift.

¹³C CP MAS spectra recorded with a short contact time (200 μ s) are presented in Figure 5. Because of the short CP time used, polarization is mostly transferred over the strongest ¹H-¹³C couplings, which means that the rigid components of the material are overemphasized. This results for instance in a significantly larger (and also temperature-dependent) *trans* signal of the CH₃ groups, and these spectra thus confirm the assignments discussed above. The fact that the aliphatic peak at 33.6 ppm is now higher and better resolved than the one at 32.06 ppm consolidates the assumption that the downfield peak belongs to methylenes with higher *trans* content.

The relative intensity of the broad background signal of the aromatic backbone, attributed to the amorphous phase, is lower than in the SPE MAS spectra, and this observation also holds for short and long CP times. This indicates that the backbone in the amorphous phase also undergoes motion at least in the range of tens of kHz and in an appreciable angular range, leading to some averaging of the associated CH dipolar couplings, explaining the lower intensity for short CP times. The fact that the signal is not much higher at longer CP suggests rather short rotating-frame spin-lattice relaxation times (T_{1p}) indicative of appreciable spectral density in the 50 kHz range (i.e., the rf frequency used for CP). Furthermore, the comparably larger broad amorphous background in the SPE spectra also indicates shorter amorphous T_1 relaxation times, which may also imply significant mobility also on the ~100 MHz scale. All interpretations corroborate the assignment of the broad background to the amorphous phase. Finally, we note that the chemical shifts of the crystalline main-chain resonances are not changing significantly with temperature, indicating that, apart from small effects induced by

the changes in the average side-chain conformation, the average backbone conformation remains essentially unaffected by the crystal-crystal phase transformation.

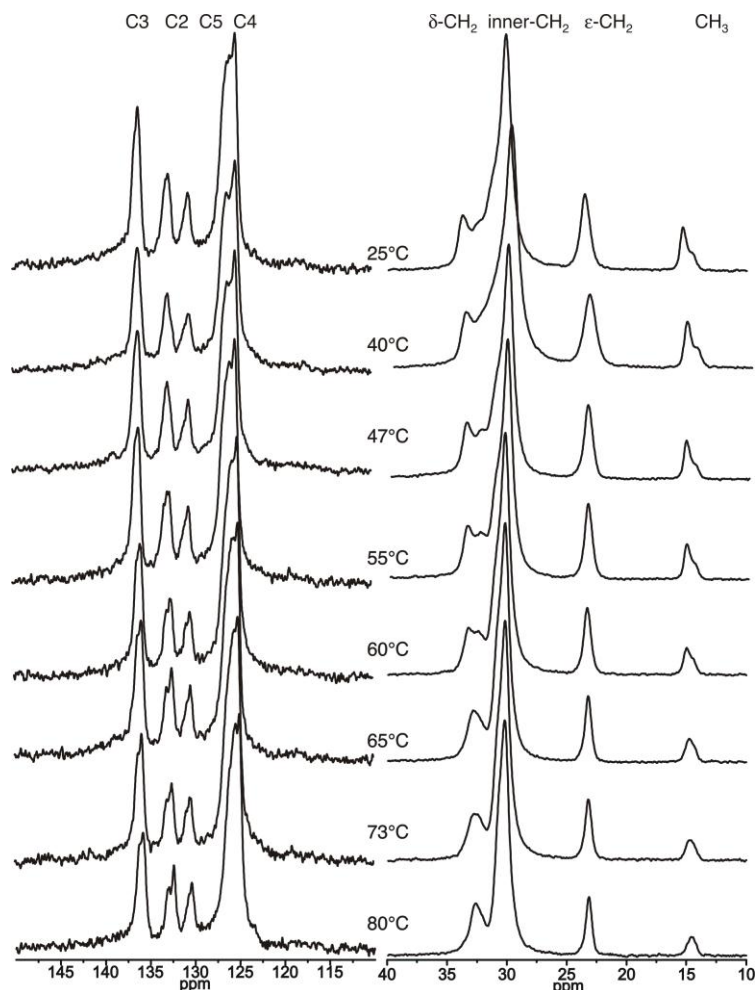


Figure 5: Temperature-dependent ^{13}C CP-MAS spectra for P3HT 3, recorded at a spinning frequency of 7 kHz and with a contact time of 200 μs ; the temperature is indicated.

Determination of Crystallinity and Crystal-Crystal Phase Transitions.

The alkyl chain signals reflecting higher *trans* or *gauche* content in the ^{13}C MAS NMR spectra constitutes a direct way to determining the minimum crystallinity of P3HT 3. We simply integrate the quantitative respective resonances in the fully relaxed SPE spectra shown in Figure 4. The two well-resolved CH_3 resonances are best suited for this purpose and were subjected to a deconvolution analysis based on two line shape functions; the best fits of the experimental spectra were obtained with Gaussian line shapes (see Figure 6). The ratio of the integrals of the lines corresponding to the crystalline phase I and the gauche-rich (amorphous and possibly crystalline phase II) regions, respectively, directly reflects the minimum degree of crystallinity that can be attributed also to the backbone.

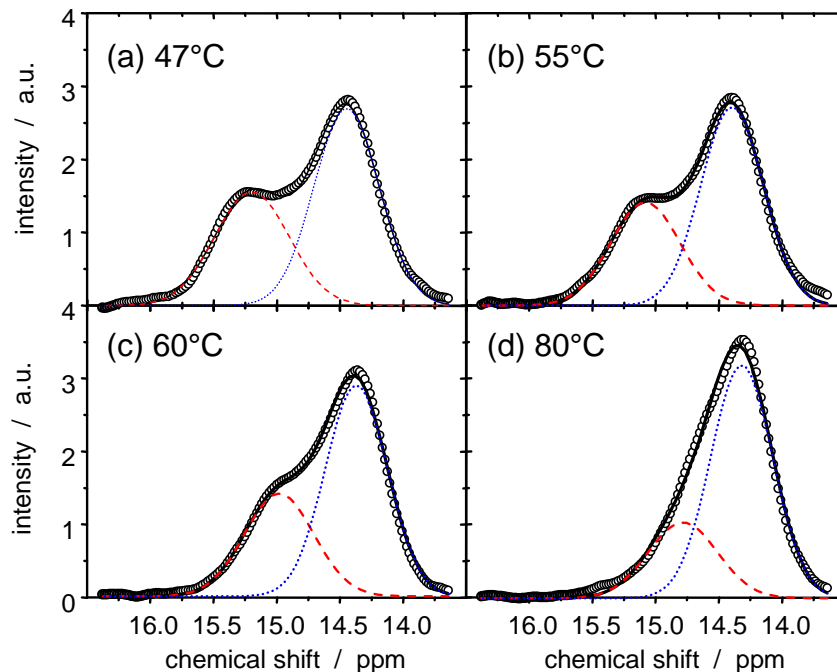


Figure 6: Component analysis of the fully relaxed ^{13}C SPE MAS NMR spectra of CH_3 in P3HT 3. ● are the experimental data, dashed (red) and dotted (blue) lines correspond to the crystalline and mostly amorphous components, respectively, while the continuous lines are the composite line shape.

The crystallinity and the amorphous-phase content in P3HT 3 as determined by the component analysis are plotted as a function of temperature in the upper part of Figure 7. The averaged crystallinity detected in the low-MW sample that we investigated is 37%, with small overall variations. Note that the values are subject to potentially large systematic errors above 60°C, where the reliability of the deconvolution procedure is limited due to the merely approximated line shape (see Figure 6d). The chemical shift data on the lower part of Figure 7 demonstrate that the average *gauche* content increases with temperature in both the crystalline and the amorphous phase, which is an expected behavior. The temperature dependence of the *gauche* content in the crystalline phase I is, however, rather strong and reflects a pretransitional phenomenon upon reaching the phase I-II transition (one may argue that the *gauche* content may serve as an order parameter in a thermodynamic sense). This transition is thus directly shown to be of dynamic nature, with the increasingly mobile side chains ultimately being responsible for a structural decoupling of adjacent 2D layers made up of well- π -packed main chains.

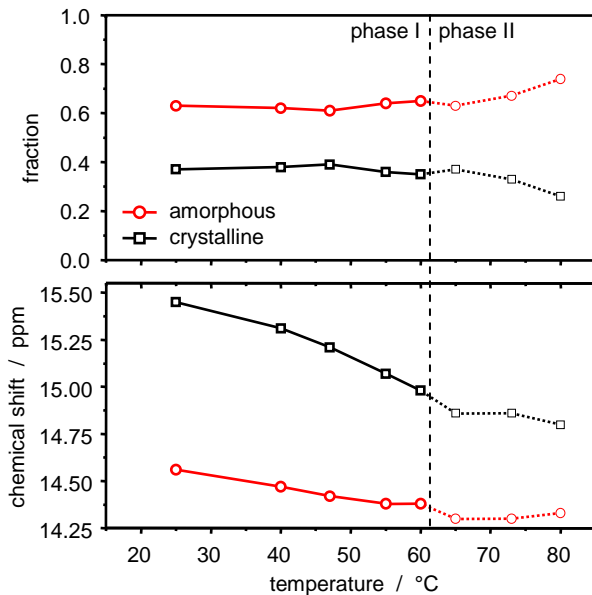


Figure 7: Crystallinity and amorphous-phase content in P3HT 3 as determined from the component analysis of the two CH_3 resonances (top), and evolution of the chemical shifts for the respective peaks as also obtained from the component analysis (bottom). The dashed line indicates the crystalline-crystalline phase transition, above which the two resonances overlap and the deconvolution becomes unstable.

A crystallinity of 37% is about 2.5 times larger than the one estimated for this sample based on our DSC investigations (Figure 3). After prolonged annealing of the sample at room temperature, DSC measurements gave a heat of fusion $\Delta H_m^\infty = 13.8 \text{ J/g}$ (measurement not shown). A comparison with the extrapolated value for 100% crystalline material $\Delta H_m^\infty = 99 \text{ J/g}$ determined by Malik and Nandi would give a crystallinity of only 14%.²³ As a support, the degree of crystallinity that we determine from the NMR spectra can better explain the WAXS data for this specific sample;³⁰ therefore, we conclude that the literature value of reference 23 must be corrected to at most $\Delta H_m^\infty \approx 37 \text{ J/g}$.

Main-Chain and Side-Chain Mobility.

In this section, we will now present more quantitative results on the molecular mobility in the different phases, supporting the above conclusions and providing a detailed picture of the properties of the different phases in the material and the temperature-dependent changes. This pertains in particular to the fact that we categorized the different phases by a different time-averaged *trans* content of the alkyl resonances. Now we prove that the side chains are indeed highly (yet anisotropically) mobile in all phases, while fast backbone mobility is constrained to small angles and can be viewed as essentially rigid and unaffected by the crystal-crystal phase transformation. The mobility of the backbone has a potential effect on the efficiency of the π - π packing and could thus play a role in determining the electronic properties in P3ATs. The investigation of the importance of this effect, to be evaluated against the general effect of higher crystallinity providing more effective long-range charge transport, will be the subject of future work.

In a second series of experiments, Torchia's CP-based T_1 spin-lattice relaxation experiment³⁷ was performed on the same sample for the relevant temperature range. As T_1 relaxation is mainly caused by molecular motion on the time scale of the inverse Larmor frequency, the temperature dependence of T_1 gives a qualitative account of the frequency of molecular mobility. If T_1 increases with temperature, this is attributed to faster preaveraging, i.e., the frequency of molecular motion is above the Larmor frequency. Inversely, if T_1 decreases with temperature, the frequency of molecular mobility moves into the sensitive window; i.e., the typical frequency at low temperature is below the Larmor frequency. The resulting relaxation times are presented in Table 3.

Table 3: T_1 relaxation times (in s) measured for P3HT 3 with Torchia's experiment.³⁷

| T/°C | C3 | C2 | C5 | C4 | inner CH ₂ | ε -CH ₂ | c-CH ₃ | a-CH ₃ |
|------|-------|-------|-------|------|--------------------------|--------------------------------|-------------------|-------------------|
| 25 | 14.05 | 26.68 | 23.54 | 8.06 | 0.47 | 0.71 | 1.67 | 1.41 |
| 40 | 13.14 | 23.27 | 19.05 | 8.36 | 0.50 | 0.79 | 1.89 | 1.72 |
| 47 | 13.24 | 23.68 | 17.53 | 7.93 | 0.52 | 0.86 | 2.06 | 1.98 |
| 60 | 14.12 | 28.56 | 22.26 | 6.81 | 0.54 | 0.95 | 2.34 | 2.33 |
| 73 | 10.45 | 13.17 | 7.79 | 5.14 | 0.56 | 1.05 | | 2.54 |

All relaxation curves could be well fitted with a single-exponential decay. The relaxation times of the alkyl signals are all below 2.5 s, proving that a recycle delay of 10 s was sufficient for quantitative SPE spectra. The T_{1s} of the *trans* c-CH₃ and *gauche* peaks a-CH₃ of the methyl group are similar, becoming identical above 60°C, where the separation of the *trans* and *gauche* configurations is not possible anymore. Both the methyl and the methylene T_{1s} increase with temperature, demonstrating that the conformational jump dynamics is always faster than ~100 MHz. Note the longer T_{1s} of the methyl groups, which arise from an effectively weak CH dipolar coupling as a result of even faster preaveraging by methyl rotation.

As expected, the T_{1s} of the unprotonated backbone carbons are rather long due to the lack of substantial CH dipolar couplings as the major relaxation channel. The T_1 of the protonated C4 is much longer than those of the alkyl resonances, indicating slower and/or more restricted dynamics over the whole temperature range. This value is now decreasing with temperature, placing the time scale for the small-angle librations into the branch below ~100 MHz (see the discussion of the DIPSHIFT data below for the exclusion of large-angle excursions). Note that the backbone T_{1s} are dominated by the crystalline phase, as a 2 ms CP was used in the experiment, for which the broad amorphous contribution is not large, in particular because the sharp signals are integrated over a narrow ppm range.

Rigidity (or a restriction to small-angle librations) is directly indicated by the magnitude of CH dipolar couplings, as obtained from the 2D DIPSHIFT experiment. In previous work,⁴⁶ we used this experiment to investigate the mobility of *trans*- and *gauche*-rich chain conformers in polymers such as poly(ethylene-co-acrylic acid). The principle of the method is the measurement of potentially reduced ¹³C-¹H heteronuclear dipolar couplings D and comparing

it to the static-limit value. The ratio $S = D_{\text{exp}}/D_{\text{stat}}$ (see eq. 1) is a dynamic order parameter that reflects temperature-dependent changes in the degree of anisotropy of fast rotational or tumbling motions exceeding the 100 kHz range. An intensity modulation of each ^{13}C signal in the CP MAS spectrum is recorded as a function of an indirect timing variable t_1 that varies from 0 to the rotor period, T_R . For $t_1 < T_R/2$ the intensity constantly decreases, with the steepness of the decrease directly reflecting the magnitude of the $^{13}\text{C}-^1\text{H}$ heteronuclear dipolar coupling. For $t_1 > T_R/2$, the spectrum intensity rises again to reach its initial intensity (I_0 for $t_1 = 0$) again at $t_1 = T_R$, reflecting the time dependence of the sample rotation ("rotor echo"). Note that for higher spinning speeds the intensity modulation becomes less pronounced; therefore, weak couplings should be investigated at slower MAS. In cases where the dynamics is not in the fast limit (rate constant $k < 100$ kHz), the initial spectrum intensity is not fully recovered at $t_1 = T_R$,⁴⁷ and in such cases, the rate constant k of the motion (inverse correlation time) can be estimated.

DIPSHIFT experiments were performed at temperatures below and above the crystal-crystal phase transition of P3HT 3. The results obtained for the alkyl chains and the backbone (C4) are presented in Figure 8. The results show that in the case of the backbone (Figure 8a) the strength of the detected dipolar coupling is not changing with the temperature, which leads us to conclude that the mobility of the backbones does not change at all over this temperature range. The estimated dipolar coupling is somewhat below the expected rigid-limit value (corresponding to $S_{\text{C4-H}} = 0.79$), which is expected as this signal contains a small and apparently rather constant contribution from the more mobile amorphous regions.

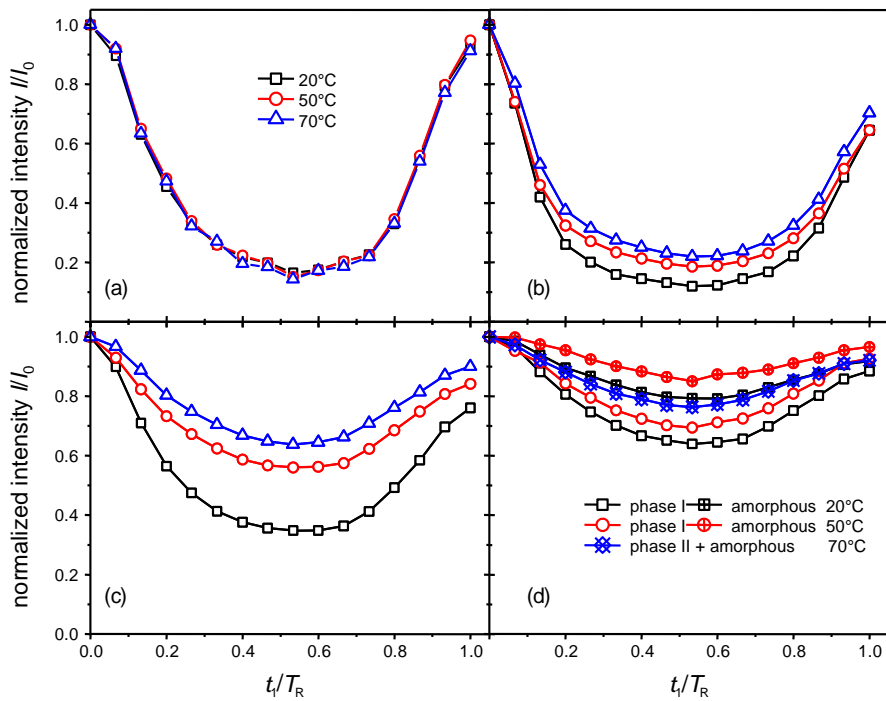


Figure 8: DIPSHIFT curves recorded in P3HT 3 sample; (a) C4 backbone, (b) inner- CH_2 , (c) $\varepsilon\text{-CH}_2$ and (d) trans-rich (phase I, c) and gauche-rich (amorphous, a) CH_3 . (a) was recorded at 4700 kHz MAS, and (b) – (d) at 2500 Hz.

For the alkyl chains, where higher mobility is expected, we used a slower spinning rate (2500 Hz) which roughly doubles the effect of the ^{13}C - ^1H coupling as compared to the curves recorded with a rotation frequency of 4700 Hz. In the case of the inner- CH_2 methylenes (Figure 8b), we detect a decisive change in the amplitude of the motion with increasing the temperature from 20 to 70°C. Comparing the size of their intensity “dip” at $T_R/2$ with those of the outer part of the chain (Figure 8c), alkyl groups in the vicinity of the thiophene ring are seen to be more restricted than the ends. Such a mobility gradient is certainly expected. Increasing the temperature and approaching the crystal-crystal phase transition at 60°C, the whole side chain becomes more mobile, with more pronounced changes toward the chain ends.

Note that the loss of intensity for the final points ($t_1/T_R \approx 1$) in Figure 8b-d is in this case not the result of intermediate motions in the kilohertz range. The reference experiments on rigid- CH_n model substances show the same behavior under the given experimental conditions, proving that the (weak) apparent decay is a result of radio frequency and timing imperfections at the slower MAS frequency, where more errors accumulate during the longer rotor period. Therefore, the alkyl mobility is always in the fast limit (> 100 kHz), and the changes in the data indicate that merely the amplitude of angular excursions is increasing.

For the CH_3 resonances (Figure 8d), the data indicate a difference in the mobility of the *trans*- and *gauche*-rich side chains. At room temperature, the signal from the *trans* segments in the crystalline phase I (c- CH_3) reflects a more anisotropic dynamics than the signal from the amorphous fraction (a- CH_3). Upon increasing the temperature, both populations are becoming more mobile, yet at 70°C, where only one signal is observed, we observe a modulation that is roughly in-between the response of the separated signals at 50°C. This is important and directly proves that the side chains in phase II are still more ordered than the amorphous side chains. The resulting overlapped signal is thus proven to be an inhomogeneous superposition of signals from two dynamically distinct phases, i.e., phase II and the amorphous phase. It should still be possible to determine the relative contributions of the two phases by studying the (potentially bicomponent) behavior of the composite signal in simple relaxation experiments or more elaborate magnetization filters. This will also be the subject of future work.

Using a custom written FORTRAN program to numerically solve the powder-averaging integral that is part of the theoretical formula describing the dipolar time modulation of the signal, we simulated the time evolution of the NMR signal under the influence of the reduced dipolar coupling in the DIPSHIFT experiment for different coupling strengths and compared them with experimental results, thus obtaining estimated values for the dipolar coupling constants. So-obtained (apparent) values always deviate from real values due to differences between simulated and real coupling topologies and due to a pulse sequence scaling factor which can differ from the theoretical value as a result of setup imperfections (radio-frequency

inhomogeneities, etc.). Therefore, our fitted results were compared with analogous results obtained from fits to our experiments on rigid-limit model substances (glycine for CH_2 groups and alanine for CH_3). The ratio of these apparent couplings gives the dynamic order parameter $S = D_{\text{exp}}/D_{\text{stat}}$ with good confidence. Its expected values range from 1 (full rigidity) to 0 (isotropic motion), and the results are plotted in Figure 9.

The evolution of the order parameters with temperature fully confirms the above qualitative interpretation. It is important to emphasize the meaning of the apparent increase of S detected on the gauche-rich CH_3 signal at the highest temperature (70°C), which can only be explained by the fact this signal is now a superposition of the amorphous phase (for which $S \approx 0.25$ could be estimated; see dotted line in Figure 9) and the newly formed phase II. The high value of ~ 0.48 at 70°C is consistent with the mobility in phase II being not much higher (if at all) than in phase I, yet with higher *gauche* content on average, as inferred from the signal position. This indicates a structural rearrangement accommodating more side-chain conformers, which is consistent with the observations from X-ray scattering.³⁰ Certainly, the disordering observed in NMR explains perfectly the X-ray results, namely a loss of position correlation between different layers of main chains. As for absolute values, $S > 0.5$ for the last $\varepsilon\text{-CH}_2$ group in fact excludes a full rotational motion of the chain, as is for instance found in hexagonal rotator phases of long alkanes. Since the CH dipolar vectors are on average perpendicular to the expected symmetry axis of motion (= extended side-chain axis), a reduction by at least 50% would be expected for that case. Note that a simple 180° jump motion around the extended-chain axis conserves the dipolar tensor orientation and would not lead to any apparent dynamic averaging. We can thus conclude that the chain end performs conformational jumps over a limited set of positions, with possibly some additional librations.

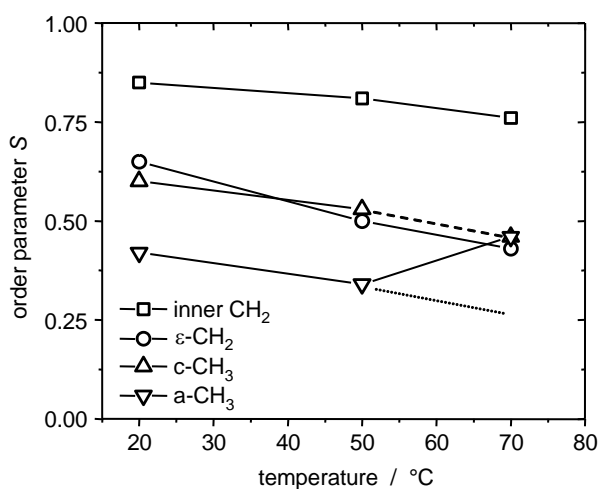


Figure 9: Order parameter S for the P3HT 3 side chains versus the temperature. The dashed line indicates that the $c\text{-CH}_3$ peak moves under the $a\text{-CH}_3$ peak, and the dotted line indicates a possible trend for the pure amorphous phase.

While all together the results are in line with the conclusions drawn from X-ray scattering, there is detailed information obtained by NMR that goes much beyond. Side-chain mobility depends on the position on the side chain with the most mobile parts being at the chain ends. Also, the temperature dependence seems rather smooth in the small temperature interval of the experiment. Additionally, there is some information available about the absolute time scale of molecular motion of the different molecular groups; most importantly, there is a strong mobility difference between main and side chain.

Effect of M_n on Chain Mobility and Crystallinity.

Several studies showed that the mobility of charge carriers in P3HT increases with increasing molecular weight of the sample.⁸⁻¹³ We have thus investigated the P3HT 6 sample with a higher molecular weight (see Table 1), which exhibits a substantially increased crystallinity as judged from DSC, in order to investigate the effect of molecular weight on the main/side chain mobility and the NMR-detected phase distribution. Both the CP and SPE MAS spectra at different temperatures show no relevant differences as compared to those recorded for the P3HT 3. P3HT 6 features slightly sharper lines for the main and side chains, and this difference could arise from either an increased mobility and/or a more ordered structure.

The only very relevant difference is found for the side-chain CH₃ signals at lower temperature, as shown in Figure 10. Obviously, the amount of alkyl-ordered phase I is lower in the higher MW sample, which is at a first glance in contradiction to the higher DSC estimate of crystallinity. Using our deconvolution procedure for SPE spectra, we find a phase I fraction of 28%, which should be compared to 37% for P3HT 3. This apparent contradiction can be resolved by taking into account that in the DSC scan for the higher MW (Figure 3) the endotherm at around 60° is less visible (it in fact almost vanishes for even higher MW, data not shown). This phenomenon has been interpreted as a result of a kinetic suppression of the phase I formation on cooling for high molecular weights in the context of our X-ray scattering results.³⁰ This assumption is here confirmed on a molecular basis and demonstrates that our “NMR crystallinity”, more precisely the phase I content, is only a lower limit. Also in P3HT 3, we cannot fully exclude some regions that do not transform into phase I. These issues will be addressed in future annealing studies. Note that our crystallinity estimates for the two samples correspond to extended annealing at room temperature, yet changes may be possible by annealing at elevated temperature, e.g., around the phase I – phase II transition or just below melting.

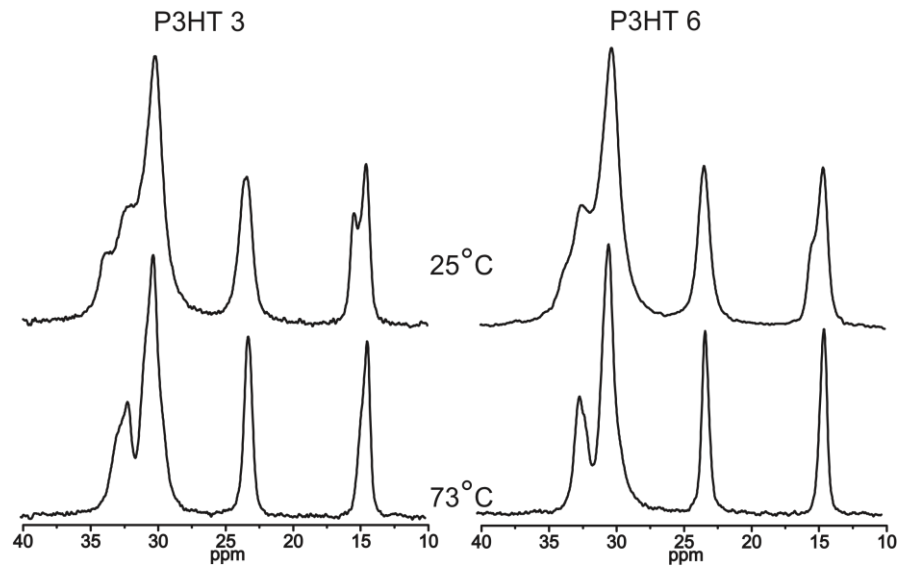


Figure 10: SPE MAS spectra (aliphatic region) of P3HT 3 and P3HT 6 at two relevant temperatures.

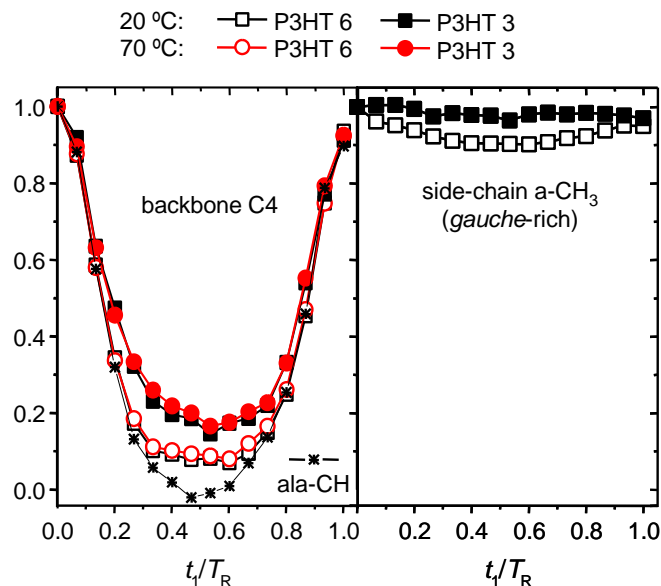


Figure 11: DIPSHIFT curves of C4 and α -CH₃ for P3HT with different MW and at different temperatures. The stars in the C4 plot on the left are for the alanine CH group, corresponding to a complete rigidity.

Independent proof of our interpretation that the higher MW material is rich in phase II already at room temperature is again inferred from the mobility information obtained from the DIPSHIFT experiment. Figure 11 shows the modulation curves for the backbone C4 as well as the *gauche*-rich methyl resonance (α -CH₃), all recorded at a spinning rate of 4700 Hz. The full symbols are data recorded for the sample with the lowest molecular weight (P3HT 3) while the empty symbols are for P3HT 6 sample. The faster MAS leads to less pronounced modulations of the CH₃ signal as compared to Figure 8d; however, together with the higher DSC crystallinity, the conclusion is clear: the higher MW sample shows a significantly more pronounced modulation, indicating that the α -CH₃ signal is in fact a superposition of most

mobile amorphous regions and phase II with lower local mobility. This is consistent with a kinetically suppressed phase transition; i.e., molecular motion is too slow to develop order without prolonged annealing.

Further, the temperature independence of the backbone C4 response again demonstrates that the temperature-dependent side-chain mobility as well as a partial crystal-crystal phase transition at around 50-60°C does not affect the dynamics of the main chain at all. The even stronger modulation observed for P3HT 6, corresponding to $S_{C4-H} = 0.92$, can straightforwardly be explained by an even lower contribution of underlying (more mobile) amorphous signal components, in agreement with the higher crystallinity. The modulation is even closer to rigid-limit behavior, suggesting that the fast C4-H bond fluctuations (that do exist and are the reason for its T_1 relaxation behavior) are constrained to rather small angles. The finding also shows that the side-chain mobility (which is higher in P3HT 6 with its higher phase II content) does not significantly affect the backbone rigidity.

Assuming for a moment a negligible contribution of the broad amorphous background, the difference between the two samples could then be explained by a difference in the angular range of the fluctuations on the given time scale, which would mean that the higher crystallinity, along with the larger lamellar thickness, leads to a better packing in a more ordered structure as in the lower molecular weight. An investigation into whether this effect is relevant for electronic transport will be a central subject of our future work.

Conclusions

Structure, dynamics, and crystallinity at moderate temperatures in two highly HT-regioregular P3HT samples were investigated using ^{13}C MAS NMR spectroscopy and DSC. DSC measurements show a crystal-crystal phase transition around 60°C. Based on X-ray scattering results the transition was suggested to correspond to a transition from a well-organized 3D crystalline structure (phase I) in which the side chains are well ordered to a 2D crystalline structure (phase II), where the side chains are more mobile and have a high *gauche* content but are still less mobile than in the amorphous phase. For the higher molecular weight this transition is weaker while a higher melting enthalpy indicates a higher overall crystallinity. This picture could be fully confirmed by NMR measurements showing the expected differences in molecular mobility in the different molecular regions. Regarding the absolute crystallinity, using literature data²³ for the reference melting enthalpy, the expected crystallinity in the P3HT 3 sample would be around 14%. Quantitative ^{13}C NMR yields a phase I content of 37% which represents a minimum value for the crystallinity, leading to a corrected maximum reference value for the melting enthalpy of $\Delta H_m^\infty \approx 37 \text{ J/g}$. and proving the literature value incorrect. Taking this value for calibration of the other material, P3HT 6 has a crystallinity of about 64%. Such substantial crystallinities in P3HT were as yet not reported, and this knowledge is essential for discussions about the effect of crystallinity on the charge carrier mobility in poly (3-alkylthiophenes) in general.

NMR experiments focusing on the angular range of fast reorientations of CH bonds were used to monitor the mobility of the main and side chains with chemical resolution below and above the crystal-crystal phase transition at 60°C. These results reveal that the mobility and the average conformation of the main chains is neither affected by temperature nor by the crystal-crystal phase transition; however, in the side chains, an increasing degree of mobility and a reorganization of the chain ends toward on average conformations with higher gauche content in phase II are indicated. Experiments on a sample with higher molecular weight show that the crystal-crystal phase transition from phase II to phase I on cooling is kinetically suppressed, meaning that at room temperature higher MW material is predominantly in phase II, while the backbones are on average even less mobile. The known better device performance, i.e., the higher charge carrier mobility in samples with larger molecular weight, is thus shown to correlate with absolute crystallinity, highlighting a way to possibly further improve these materials.

On the methodological side, we point out again that the used NMR methods, sensitive to local structure and mobility, proved indispensable in confirming the structural model that was previously suggested, but could not be proven on the sole basis of diffraction data. Such a combined approach is especially useful for materials such as the present one, which, despite being made up of homopolymers, form complex nanoscopic structures and exhibit pronounced dynamic heterogeneity even within the crystalline phase(s). The present investigation concentrated on fast dynamics of the main and side chains, yet other authors proved that the backbones exhibit a slower dynamics (slow conformational jumps), as accessible by exchange NMR spectroscopy methods.³² Such processes could also be relevant for the device performance, as they directly affect the π–π packing. Investigations regarding the slow dynamics in the backbones, as well as aging studies focusing on changes in the phase I/II composition of our well-defined P3HT samples, and on practically relevant thin-film samples are ongoing.

Acknowledgement

This work was supported by the Deutsche Forschungsgemeinschaft (SPP 1355) and the state of Saxony-Anhalt. We acknowledge infrastructural support from the European Union (ERDF programme) and further thank Frau Herfurt for technical help with the DSC experiments.

References

- (1) Forrest S., *Nature*, **2004**, *428*, 911-918.
- (2) Li G., Shrotriya V., Huang J., Yao Y., Moriarty T., Emery K., Yang Y., *Nat. Mater.*, **2005**, *4*, 864-868.
- (3) Kim Y., Cook S., Tuladhar S., Choulis S., Nelson J., Durrant J., Bradley D., Giles M., McCulloch I., Ha C., Ree M., *Nat. Mater.*, **2006**, *5*, 197-203.
- (4) Roncali J., *Chem. Rev.* **1997**, *97*, 173-205.
- (5) Sirringhaus H., Brown P. J., Friend R. H., Nielsen M. M., Bechgaard K., Langeveld-Voss B. M. W., Spiering A. J. H., Janssen R. A. J., Meijer E. W., Herwig P., de Leeuw D. M., *Nature*, **1999**, *401*, 685-688.
- (6) Xu B., Holdcroft S., *Macromolecules*, **1993**, *23*, 4457-4460.
- (7) Bao Z., Lovinger A. J., Dodabalpur A., *Appl. Phys. Lett.*, **1996**, *69*, 3066.
- (8) Kline R. J., McGehee M. D., Kadnikova E. N., Liu J., Fréchet J. M. J., Toney M. F., *Macromolecules*, **2005**, *38*, 3312-3319.
- (9) Brinkmann M., Rannou P., *Macromolecules*, **2009**, *42*, 1115-1130.
- (10) Kline R. J., McGehee M. D., *Adv. Mater.*, **2003**, *15*, 1519-1522.
- (11) Goh C., Kline J., McGehee M. D., Kadnikova E. N., Fréchet J. M. J., *Appl. Phys. Lett.*, **2005**, *86*, 122110.
- (12) Neher D., *Adv. Funct. Mater.*, **2004**, *14*, 757-764.
- (13) Esenturk O., Melinger J. S., Heilweil E. J., *J. Appl. Phys.*, **2008**, *103*, 023102.
- (14) Zen A., Saphiannikova M., Neher D., Grenzer J., Grigorian S., Pietsch U., Asawapirom U., Scherf U., Lieberwirth I., Wegner G., *Macromolecules*, **2006**, *39*, 2162-2171.
- (15) Joshi S., Grigorian S., Pietsch U., Pingel P., Zen A., Neher D., Scherf U., *Macromolecules*, **2008**, *41*, 6800-6808.
- (16) Joshi S., Grigorian S., Pietsch U., *Phys. Stat. Sol. A*, **2008**, *205*, 488-496.
- (17) McCullough R. D., *Adv. Mater.*, **1998**, *10*, 93-116.
- (18) Mao H., Xu B., Holdcroft S., *Macromolecules*, **1993**, *23*, 1163-1169.
- (19) McCullough R. D., Tristram-Nagle S., Williams S. P., Lowe R. D., Jayaraman M., *J. Am. Chem. Soc.*, **1993**, *115*, 4910-4911.
- (20) Chen T.-A., Wu X., Rieke R. D., *J. Am. Chem. Soc.*, **1995**, *117*, 233-244.
- (21) Sheina E. E., Liu J.S., Iovu M. C., Laird D. W., McCullough R. D., *Macromolecules* **2004**, *37*, 3526-3528.
- (22) Pankaj S., Hempel E., Beiner M., *Macromolecules* **2009**, *42*, 716-724.
- (23) Malik S., Nandi A. K., *J. Polym. Sci. Part B: Polym. Phys.* **2002**, *40*, 2073-2085.
- (24) Prosa T. J., Winokur M. J., Moulton J., Smith P., Heeger A. J., *Macromolecules*, **1992**, *25*, 4364-4372.
- (25) Brinkmann M., Wittmann J.-C., *Adv. Mater.*, **2006**, *18*, 660-863.
- (26) Prosa T. J., Winokur M. J., McCullough R. D., *Macromolecules*, **1996**, *29*, 3654-3656.
- (27) Kline R. J., DeLongchamp D. M., Fischer D. A., Lin E. K., Richter L. J., Chabinyc M. L., Toney M. F., Heeney M., McCulloch I., *Macromolecules*, **2007**, *40*, 7960-7965.

- (28) Chen T.-A., Rieke R. D., *J. Am. Chem. Soc.*, **1992**, *114*, 10087-10088.
- (29) Barbarella G., Bongini A., Zambianchi M., *Macromolecules*, **1994**, *27*, 3039-3045.
- (30) Wu Z., Petzold A., Henze T., Thurn-Albrecht T., Lohwasser R., Sommer M., Thekkalat M., *Macromolecules*, **2010**, *43*, 4646-4653.
- (31) Ferrari M., Mucci A., Schenetti L., *Magn. Reson. Chem.*, **1995**, *33*, 657-663.
- (32) Yazawa K., Inoue Y., Yamamoto T., Asakawa N., *Phys. Rev. B*, **2006**, *74*, 094204.
- (33) Bolognesi A., Porzio W., Provasoli A., Botta C., Comotti A., Sozzani P., Simonutti R., *Macromol. Chem. Phys.*, **2001**, *202*, 2586-2591.
- (34) Tonelli A. E., *Macromolecules*, **1978**, *11*, 565-567.
- (35) Earl W. L., VanDerHart D. L., *Macromolecules*, **1979**, *12*, 762-767.
- (36) Sheina E. E., Liu J., Iovu M. C., Laird D. W., McCullough R. D., *Macromolecules*, **2004**, *37*, 3526-3528.
- (37) Torchia D. A., *J. Magn. Reson.*, **1978**, *30*, 613-616.
- (38) Hong M., Gross J. D., Griffin R. G., *J. Phys. Chem. B*, **1997**, *101*, 5869-5874.
- (39) Munowitz M. G., Griffin R. G., *J. Chem. Phys.*, **1981**, *76*, 2848.
- (40) Harris R. K., Jackson P., Merwin L. H., Say B. J., Hägele G., *J. Chem. Soc. Faraday Trans. 1*, **1988**, *84*, 3649-3672.
- (41) Bielecki A., Burum D. P., *J. Magn. Reson.*, **1995**, *A116*, 215-220.
- (42) Hester R. K., Ackerman J. L., Neff B. L., Waugh J. S., *Phys. Rev. Lett.*, **1976**, *36*, 1081-1083.
- (43) Schaeffer J., McKay R. A., Stejskal E. O., *J. Magn. Reson.*, **1983**, *52*, 123-129
- (44) Barbarella G., Casarini D., Zambianchi M., Favaretto L., Rossini S., *Adv. Mater.*, **1996**, *8*, 69-73.
- (45) VanDerHart D. L., *J. Magn. Reson.*, **1981**, *44*, 117-125.
- (46) Meyer C., Pascui O. F., Reichert D., Sander L. C., Wise S. A., Albert K., *J. Sep. Sci.*, **2006**, *29*, 820-828.
- (47) deAzevedo E. R., Saalwachter K., Pascui O. F., de Souza A. A., Bonagamba T. J., Reichert D., *J. Chem. Phys.*, **2008**, *128*, 104505.

10. Subsurface Mapping of Amorphous Surface Layers on Poly(3-hexylthiophene)

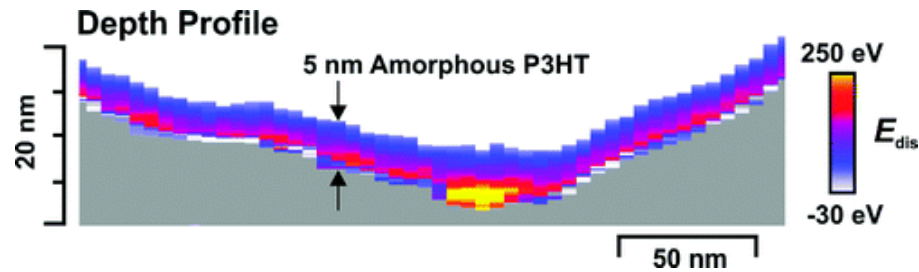
M. Zerson^{1,*}, E.-C. Spitzner¹, C. Riesch¹, R. Lohwasser², M. Thelakkat², and R. Magerle^{1,*}

¹Fakultät für Naturwissenschaften, Technische Universität Chemnitz, Chemnitz, Germany

²Angewandte Funktionspolymere, Makromolekulare Chemie I, Universität Bayreuth, Bayreuth, Germany

*E-mail corresponding authors: mario.zerson@physik.tu-chemnitz.de;

robert.magerle@physik.tu-chemnitz.de



published in *Macromolecules* **2011**, *44*, 5874-5877

Conjugated polymers like poly(3-hexylthiophene) (P3HT) and other thiophene-based polymers are promising materials for polymeric electronic devices and are considered as prototype semiconducting polymers for fundamental studies.¹ P3HT exhibits excellent electronic properties, in particular, high charge-carrier mobility. This is attributed to the intermolecular π - π stacking of the conjugated backbones, causing delocalization of the electronic states within the crystalline regions of semicrystalline P3HT.^{2,3} The correlation between the electronic properties and the complex hierarchical microstructure of semicrystalline polymers for organic electronic devices, including P3HT, is currently of great interest. P3HT forms lamellar crystals that are embedded in an amorphous matrix. The detailed microstructure and crystallinity depend on the stereoregularity of the polymer backbone, the molecular weight, the structure of the side chains, and the details of the film processing conditions.⁴⁻⁶ In general, a large degree of order within the crystalline regions is considered to be essential for a high charge-carrier mobility.^{2,3} Processing and annealing conditions can either improve or deteriorate the electrical properties of P3HT. Additionally, when cast from solution, crystalline P3HT fibers can be formed and deposited on the surface.^{7,8} The nanoscale morphology of P3HT is frequently inferred from atomic force microscopy (AFM) images of the surface of thin films and is related to changes in the material's electronic properties, which may affect an organic electronic device's performance. The detailed surface structure is also of particular importance for the charge-transfer process between the polymeric material and the electrodes. Up to now, studies have addressed the morphology of crystalline regions at the surface of polythiophene films.^{2,4} However, little attention has been paid to the distribution of the amorphous components at the surface of polythiophene films. Sakai *et al.* have reported a 3 nm thick amorphous layer on crystalline regions of polypropylene, a common semicrystalline polymer.⁹ With depth-resolved AFM imaging, we have recently shown that the edges of crystalline lamella in polypropylenes with a low degree of crystallinity are covered by an \sim 10 nm thick amorphous layer.¹⁰⁻¹²

In this communication, we use this method for extending our study on the surface structure of a well-defined, regioregular type of P3HT with depth-resolved AFM. In particular, we determine the local thickness of compliant surface layers by measuring the small but finite indentation of the AFM tip into the surface. We discovered that the entire surface of highly crystalline thin films of a well-defined, regioregular type of P3HT is covered by an amorphous layer of P3HT. On the as-cast film, the amorphous layer is 7 nm thick. After annealing at 230°C, it decreases to 5 nm. The presence of the amorphous surface layer can have important consequences on the electronic properties of P3HT surfaces and the performance of thin-film electronic devices using P3HT.

We study a highly regioregular type of P3HT with a well-defined molecular weight $M_n = 10.2 \text{ kg/mol}$ (measured with size-exclusion chromatography) and a low polydispersity index 1.19 synthesized by Grignard metathesis polymerization as described previously.^{4,13} The hierarchical-structure-formation process of polymer crystallization and side-chain ordering has been studied for P3HT of this molecular weight with X-ray diffraction and differential scanning calorimetry.⁴ Here, about 100 nm thick films were prepared by spin-casting a 1wt% solution of P3HT in chloroform onto polished Si wafers covered with a native oxide layer. One film was annealed above the melting temperature $T_m = 227^\circ\text{C}$ of this particular P3HT. Annealing took place at 230°C for 20 min in an Ar atmosphere followed by slow cooling (within ~ 30 min) to room temperature. The detailed AFM data acquisition and analysis protocols are described in ref 12. Briefly, for constructing a depth profile, the amplitude A and the phase φ of the oscillating cantilever are recorded as a function of the tip-sample distance. From this amplitude-phase-distance (APD) data, the position of the true surface, h_0 , and the tip indentation \tilde{z} into the compliant film are determined.¹⁴ The tip indentation \tilde{z} is used as a depth coordinate relative to the true surface h_0 for the construction of the depth profiles of k_{TS} , the conservative contribution to the tip-sample interaction,¹⁵ and E_{dis} . The latter is the energy dissipated between the tip and the sample during one tip oscillation cycle, which is a measure of the dissipative part of the tip-sample interaction.¹⁶

Figure 1 shows conventional AFM height and phase images of an as-cast P3HT film. The displayed area was chosen to show the characteristic features frequently found in AFM images of P3HT.^{2,4,5} The two 30 nm wide, crystalline P3HT fibers oriented diagonally across the imaged area are ~ 10 nm high. Such fibers are known to form in solution^{7,8} and are deposited on the film surface during spin-casting. Furthermore, a fine texture of ~ 10 nm wide bright stripes is visible in the phase image (Figure 1b). These stripes correspond to the lamellar crystalline regions within the semicrystalline P3HT. The isolated 70 nm large round dark area visible in the phase image corresponds to a 10 nm deep depression in the conventional AFM height image. APD data were measured at 75×22 points within the area marked by the white rectangle. The shape of the true surface reconstructed from the APD data (Figure 1c) shows fewer corrugations than the conventional AFM height image (Figure 1a). Also, the two fibers have a broader shape. The difference between the shape of the true surface and the conventional AFM height image is due to the indentation of the AFM tip into the compliant surface layer. For both methods, the tip indentation depends on the amplitude ratio A/A_0 . From maps of APD data, maps of the tip indentation can be determined (not shown here) which reflect local differences in the compliance of the material. Furthermore, these maps of local material properties can elucidate quantities such as the conservative contribution to the tip-sample

interaction, k_{TS} (Figure 1e), and the maximal energy E_{dis}^{max} dissipated between the tip and the sample at each pixel (Figure 1d). In the E_{dis}^{max} map, the fibers appear dark, corresponding to less dissipated energy and a lower loss modulus than the surrounding material. In the k_{TS} map, the P3HT fibers appear as bright stripes, indicating that they are stiffer than the surrounding material. The maps of k_{TS} and E_{dis}^{max} validate the interpretation of the conventional AFM phase image (Figure 1b). The 70 nm large round dark area in the upper half of the AFM phase image has significantly lower k_{TS} and higher E_{dis}^{max} values than its surroundings. Furthermore, no depression is observed at this spot in the true surface map. We therefore consider this area to represent a domain of a soft (compliant) material that is segregated at the surface.

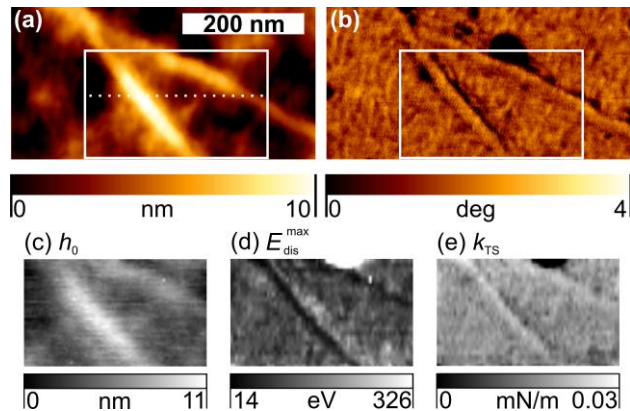


Figure 1: (a, b) AM-AFM height and phase images of an as-cast P3HT film. Bright (dark) areas in (b) correspond to the crystalline (amorphous) regions. The white rectangle indicates the area where the APD data were measured. Corresponding maps reconstructed from the APD data: (c) true surface h_0 , (d) maximum dissipated energy E_{dis}^{max} , and (e) k_{TS} computed for an amplitude ratio of $A/A_0 = 0.9$. The dotted line marks the position of the depth profiles shown in Figure 3.

While annealing the sample above its melting temperature, all crystals melt, and during the cooling process, the material crystallizes again. The resulting surface structure (Figure 2) resembles the lamellar structure previously observed for P3HT with this molecular weight.⁴ Conventional AFM height images of a larger area (not shown here) show an increase in the roughness as well as a nanoscale texture similar to that of the corresponding phase images (Figure 2b). The latter shows well-differentiated regions of bright stripes that are aligned parallel locally. These bright stripes correspond to the characteristic crystalline lamellae. Another feature frequently observed in conventional AFM phase images of P3HT is 20-50 nm wide dark domains, marked by D in Figure 2b, which are similar to those on the as-cast film. After annealing, these domains are smaller and less frequent than before annealing.

APD data were measured at 50×50 points within the area indicated (as white square) in Figure 2a,b. The true surface reconstructed from the APD data has the same shape as the AFM height image, however, without the fine nanoscale texture. The map of the maximal energy E_{dis}^{max} dissipated between the tip and the sample (Figure 2d) shows the same pattern as the

conventional AFM phase image, however, with an inverted contrast. The dark stripes in the AFM phase image correspond to bright stripes in the E_{dis}^{max} map. These regions correspond to the soft, amorphous regions between the crystalline lamella. In the k_{TS} map, they appear as bright stripes (Figure 2e). The round, dark spots in the AFM phase image (marked by D) correspond to bright dots in the E_{dis}^{max} map and dark dots in the k_{TS} map. We therefore attribute these dots to the domains of a soft (compliant) material that is segregated at the surface. The interpretation of the AFM phase image, the E_{dis}^{max} map, and the k_{TS} map is in accordance with previous results on semicrystalline polypropylene as well as block copolymers forming hard domains within a soft matrix.^{12,14}

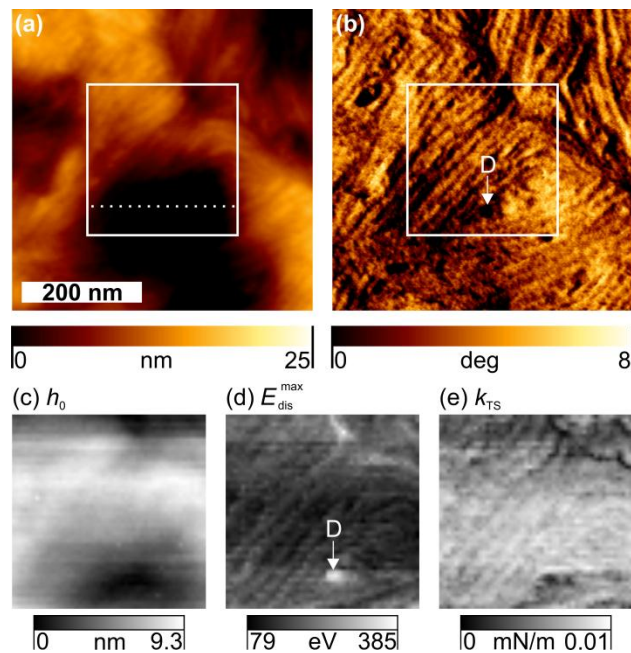


Figure 2: Same as Figure 1 for a P3HT film annealed at 230 °C for 20 min. In (d), an approximately 30-nm-large domain with high values of E_{dis}^{max} is marked by the letter D.

From the maps of the APD data, we determined the dissipated energy E_{dis} and the conservative contribution to the tip-sample interaction k_{TS} as a function of the indentation depth \tilde{z} . The depth profiles of k_{TS} and E_{dis} are shown in Figure 3 for the as-cast and the annealed P3HT film. The depth profiles have been reconstructed at the positions marked with dashed lines in the height images in Figures 1a and 2a. The enlarged details of the AFM phase images at the position of the cross sections are shown in Figures 3c and 3f, respectively. The conservative contribution to the tip-sample interaction k_{TS} increases with indentation depth \tilde{z} and reaches its highest value at the greatest value of the indentation depth (Figure 3a). Larger depths cannot be probed with this technique. The maximum indentation depth can be directly inferred from the depth profiles. It is a measure of the local thickness of a compliant layer that is covering the surface.

On the as-cast film, the mean thickness of this compliant layer is 7 nm with a standard deviation of 1 nm. After annealing at 230°C, the laterally averaged thickness of this compliant layer is reduced to 5 ± 1 nm. We identify this soft surface layer as the amorphous fraction of the semicrystalline P3HT. Because of the high purity of the P3HT used for this study, the possibility that this soft layer originates from any impurities segregating at the surface can be excluded. Our data show that the entire surface and, in particular, the crystalline lamellae and the crystalline fibers are covered by this amorphous layer of P3HT. The shape of the true surface shows no regular structure (texture) that is reminiscent of the average distance of the crystalline lamellae. On this length scale (< 100 nm), the true surface is flat. The glass transition temperature of the type of P3HT is -10°C ;⁴ therefore, at room temperature, the amorphous P3HT is a highly viscous fluid and the surface tension causes the formation of a smooth surface. Two factors could contribute to an accumulation of amorphous P3HT at the film surface. First, less crystallizable material is rejected from the growth front as the lamellae grow toward the surface. Second, if the surface tension of amorphous P3HT is lower than that of crystalline P3HT, this could inhibit the crystal growth front from reaching the surface. The reduction in the thickness of the amorphous layer after annealing is most likely caused by the further growth of crystalline lamellae toward the film surface, which accompanies the growth of lamellae within the film plane. The presence of an amorphous surface layer is in accordance with earlier findings on the surface properties of semicrystalline polypropylene.^{9,11,12}

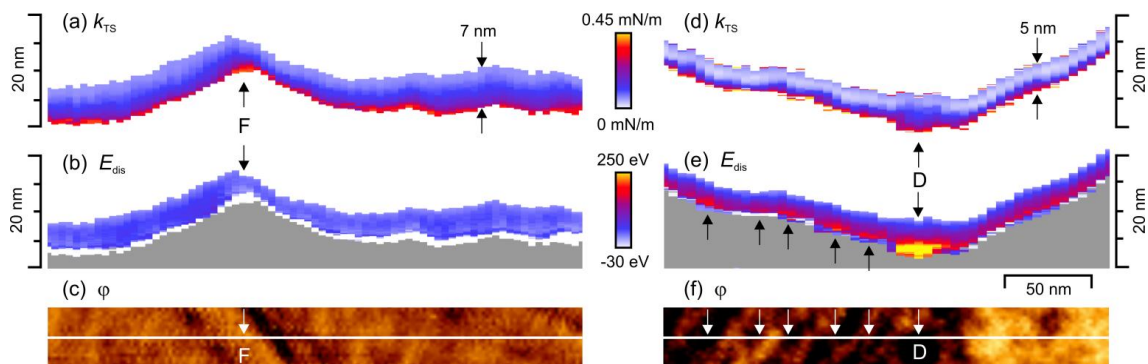


Figure 3: (a, b) Depth profiles of k_{TS} and E_{dis} for an as-cast P3HT film at the position indicated in the AFM phase image shown in (c) and in the height image in Figure 1a. The gray area corresponds to depths larger than the largest tip indentation. (d, e) Depth profiles of k_{TS} and E_{dis} for the P3HT film annealed at 230°C for 20 min measured at the position indicated in the phase image shown in (f) and in the height image in Figure 2a. The arrows mark the local maxima of E_{dis} , which correspond to the amorphous regions between the crystalline lamellae. On the as-cast film, the laterally averaged thickness of the amorphous top layer is 7 nm. After annealing at 230°C, the amorphous layer is on average 5 nm thick.

In summary, we have demonstrated depth-resolved mapping of the subsurface structure of a semiconducting semicrystalline polymer. Our data show that the entire surface of a highly regioregular P3HT, including crystalline regions and crystalline fibers, is covered by an amorphous layer. On the as-cast film, it is on average 7 nm thick. After annealing at 230°C, its

thickness decreases to 5 nm. The presence of the amorphous surface layer can have important consequences. For instance, it can influence the charge-transfer process between P3HT and electron acceptor materials as well as the charge extraction at the electrodes. It might also influence the alignment of electronic levels at these interfaces. Since annealing causes changes within the amorphous surface layer, possible contributions of amorphous surface layers toward electronic properties and/or device performance should be considered.

Acknowledgement

This work has been supported by the Deutsche Forschungsgesellschaft (SPP 1355) and the Volkswagen Foundation.

References

- (1) Perepichka, I. F.; Perepichka, D. F., *Handbook of Thiophene-Based Materials: Applications in Organic Electronics and Photonics*. John Wiley & Sons, Ltd: 2009.
- (2) Kline, R. J.; McGehee, M. D.; Kadnikova, E. N.; Liu, J.; Fréchet, J. M. J.; Toney, M. F. *Macromolecules* **2005**, 38, 3312-3319.
- (3) Sirringhaus, H.; Brown, P. J.; Friend, R. H.; Nielsen, M. M.; Bechgaard, K.; Langeveld-Voss, B. M. W.; Spiering, A. J. H.; Janssen, R. A. J.; Meijer, E. W.; Herwig, P.; de Leeuw, D. M. *Nature* **1999**, 401, 685-688.
- (4) Wu, Z.; Petzold, A.; Henze, T.; Thurn-Albrecht, T.; Lohwasser, R. H.; Sommer, M.; Thelakkat, M. *Macromolecules* **2010**, 43, 4646-4653.
- (5) Hugger, S.; Thomann, R.; Heinzel, T.; Thurn-Albrecht, T. *Colloid Polym. Sci.* **2004**, 282, 932-938.
- (6) Gang, L.; Vishal, S.; Yan, Y.; Yang, Y. *J. Appl. Phys.* **2005**, 98, 043704.
- (7) Oosterbaan, W. D.; Vrindts, V.; Berson, S.; Guillerez, S.; Douheret, O.; Ruttens, B.; D'Haen, J.; Adriaensens, P.; Manca, J.; Lutsen, L.; Vanderzande, D. *J. Mater. Chem.* **2009**, 19, 5424-5435.
- (8) Ihn, K. J.; Moulton, J.; Smith, P. *J. Polym. Sci. Part B: Polym. Phys.* **1993**, 31, 735-742.
- (9) Sakai, A.; Tanaka, K.; Fujii, Y.; Nagamura, T.; Kajiyama, T. *Polymer* **2005**, 46, 429-437.
- (10) Dietz, C.; Zerson, M.; Riesch, C.; Gigler, A. M.; Stark, R. W.; Rehse, N.; Magerle, R. *Appl. Phys. Lett.* **2008**, 92, 143107.
- (11) Dietz, C.; Zerson, M.; Riesch, C.; Franke, M.; Magerle, R. *Macromolecules* **2008**, 41, 9259-9266.
- (12) Spitzner, E.-C.; Riesch, C.; Magerle, R. *ACS Nano* **2011**, 5, 315-320.
- (13) Sheina, E. E.; Liu, J.; Iovu, M. C.; Laird, D. W.; McCullough, R. D. *Macromolecules* **2004**, 37, 3526-3528.
- (14) Knoll, A.; Magerle, R.; Krausch, G. *Macromolecules* **2001**, 34, 4159-4165.
- (15) Schröter, K.; Petzold, A.; Henze, T.; Thurn-Albrecht, T. *Macromolecules* **2009**, 42, 1114-1124.
- (16) García, R.; Gómez, C. J.; Martínez, N. F.; Patil, S.; Dietz, C.; Magerle, R. *Phys. Rev. Lett.* **2006**, 97, 016103.

11. Tailor-Made Synthesis of Poly(3-hexylthiophene) with Carboxylic End Groups and its Application as a Polymer Sensitizer in Solid-State Dye-Sensitized Solar Cells

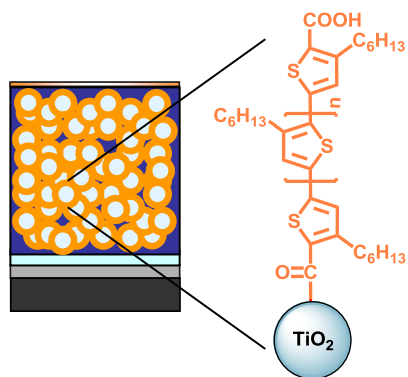
Ruth H. Lohwasser,^a Jayasundera Bandara^{ab} and Mukundan Thelakkat^{*a}

^aAdvanced Functional Polymers, Department of Macromolecular Chemistry I,

University of Bayreuth, 95444 Bayreuth, Germany

^bInstitute of Fundamental Studies, Kandy, Sri Lanka

*E-Mail corresponding author: mukundan.thelakkat@uni-bayreuth.de



Abstract

We report the first synthesis of regioregular poly(3-hexylthiophene) with carboxylic end groups (P3HT-COOH), show its potential to anchor onto mesoporous TiO₂ and show its application as a polymer sensitizer in a solid-state dye-sensitized solar cell. The incorporation of COOH groups was done by a polymer analogous reaction on P3HT. The product is characterized in comparison with P3HT and low molecular weight model molecules of substituted thiophene. These model compounds are efficient tools to identify end groups in P3HT and P3HT-COOH. The solar cell with 2,2',7,7'-tetrakis-(*N,N*-di-4-methoxyphenylamino)-9,9'-spiro-bifluorene (spiro-OMeTAD) as a hole conductor and P3HT-COOH as a polymer sensitizer on mesoporous TiO₂ shows a short-circuit current of 3.7 mA cm², an open circuit voltage of 0.54 V and a power conversion efficiency of 0.9%.

Introduction

Dye-sensitized solar cells are one of the most promising alternatives to conventional photovoltaics. The highest reported efficiencies for cells with liquid I/I₃⁻ electrolytes and polypyridyl Ru(II)-sensitizers are around 11%.¹ Despite these good performances they still haven't found commercial application due to sealing and long term stability issues.² From the point of view of cost reduction and commercialization, alternatives to expensive Ru-dyes and inconvenient liquid electrolytes are necessary. Initial success in solving these problems has already been shown by replacing the liquid electrolyte with a solid hole conductor and by using organic dyes.³⁻⁷ Recently conjugated polymers were reported as polymer sensitizers that are inexpensive alternatives to the standard Ru-dyes.⁸⁻¹¹ Poly(3-hexylthiophene) (P3HT) is a good candidate due to its high charge carrier mobility of up to 0.1 cm²V⁻¹s⁻¹.¹² Poly(3-alkylthiophenes) with carboxylic groups in the alkyl side chain have already been reported. Many attempts have also been made to introduce new end groups to poly(3-alkylthiophenes) to widen their application and allow end group-driven self-assembly onto surfaces.¹³⁻¹⁵

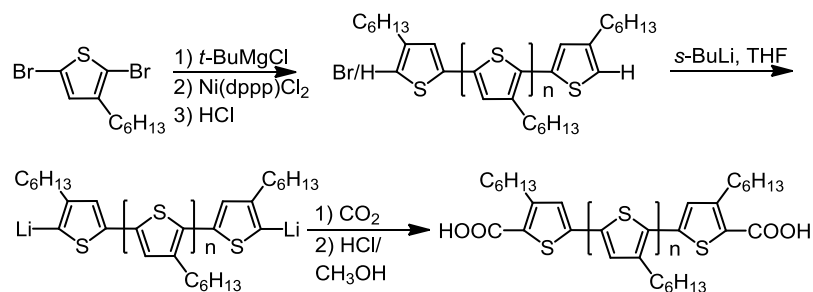
Here we report the first synthesis of highly regioregular P3HT with carboxylic acid end groups, show its potential to anchor onto mesoporous TiO₂ and show its use as a polymer sensitizer in a solid-state dye-sensitized solar cell.

Results and discussion

Synthesis and characterization

The COOH end groups were introduced by a polymer analogous functionalization on defined P3HT and both polymers were compared. P3HT was synthesized by the Grignard metathesis polymerization (GRIM) developed by McCullough and coworkers.¹⁶ According to the proposed mechanism of GRIM, each polymer chain should bear homogeneously H/Br end groups after polymerization; bromine originating from the starting unit and hydrogen which is formed when quenching the growing chain with hydrochloric acid.^{17,18} In fact one usually gets a mixture of the expected H/Br and unexpected H/H end groups. The origin of these H/H end

groups is not yet clear and complicates further controlled polymer analogous functionalization of P3HT. To functionalize both chain ends one must find a method that is independent of the nature of the end groups. Therefore, we choose a lithiation reaction which reacts with the bromine as well as with the hydrogen end groups. The regioregular P3HT was treated with secondary butyl lithium, gaseous carbon dioxide and a mixture of hydrochloric acid in methanol to obtain the carboxylated polymer P3HT-COOH (Scheme 1).



Scheme 1: Synthesis and end group functionalization of regioregular P3HT.

Fig. 1a shows the size exclusion chromatography (SEC) traces of P3HT and P3HT-COOH. P3HT has a narrow molecular weight distribution with a polydispersity index (PDI) of 1.15 and a peak molecular weight (M_p) of 5900 g mol⁻¹ with respect to polystyrene standards. According to MALDI-TOF MS this corresponds to a number average molecular weight of 3200 g mol⁻¹ meaning it has 19 repeating units. Thus the molecular weight of P3HT is usually overestimated in SEC if calibrated with polystyrene. The introduction of COOH end groups leads to a broadening of the molecular weight distribution (PDI = 1.68) and a shift of M_p to a lower value of 4700 g mol⁻¹ in SEC. Since protic groups tend to interact with the SEC column material, they cause slower elution of P3HT-COOH and broadening of the molecular weight distribution. The monomodal distribution shows that during the ionic functionalization method no chain–chain coupling occurred, a common problem with post-polymerization functionalization of polymers. Additional proof of COOH end groups is given by the FTIR spectrum in Fig. 1b. Compared to the spectrum of P3HT, the P3HT-COOH spectrum has three additional signals; a C=O vibration at 1665 cm⁻¹ and O–H vibrations at 2542 cm⁻¹ and 2644 cm⁻¹. Moreover, the FTIR bands of the COOH groups are at wave numbers corresponding to hydrogen bonded acid groups. This is further confirmed by comparison with a low molecular weight model molecule, 3-hexylthiophene-2-carboxylic acid (3HT-COOH) (Fig. 1b). While 3-hexylthiophene is a liquid, the introduction of an acid group solidifies 3HT-COOH by building intermolecular hydrogen bonds. Actually, the FTIR signals of the carboxyl group of 3HT-COOH are at the same wave numbers as for the analogous polymer P3HT-COOH. These hydrogen bonds in P3HT-COOH also strongly influence the thermal properties of the polymer. P3HT has a melting point at 174 °C, which is typical for its molecular weight. In contrast P3HT-COOH does not melt before degradation.

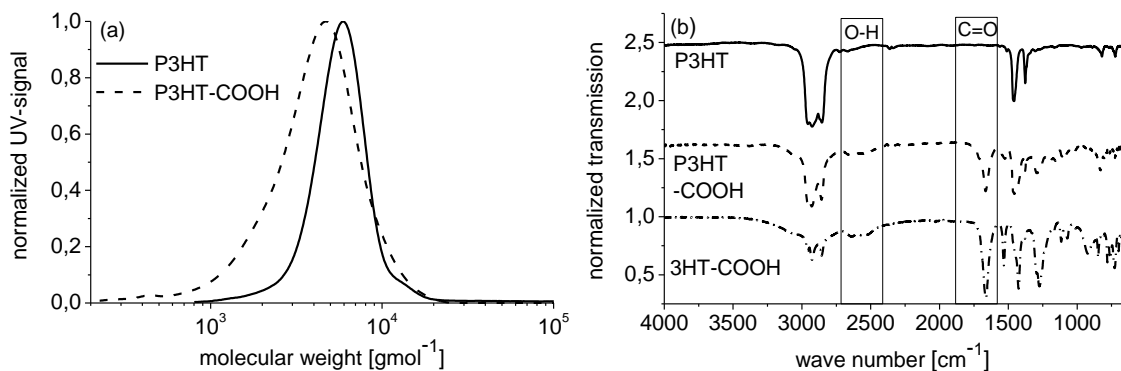


Fig. 1 (a) SEC curves of P3HT (solid) and P3HT-COOH (dashed); (b) FTIR spectra of P3HT (solid) and P3HT-COOH (dashed) in films on a silicon wafer and 3-hexylthiophene-2-carboxylic acid (3HT-COOH) (dash-dotted) as a solid.

Fig. 2 shows ¹H-NMR spectra of P3HT and its analogue P3HT-COOH. It is known that different P3HT end groups are visible in the ¹H-NMR spectra. The introduction of the COOH groups leads in general to a broadening of the signals for P3HT-COOH which is typical for molecules with hydrogen bonds. In the region of the aromatic protons (Fig. 2b left) both polymers have one main signal at 6.98 ppm. The small signal at 6.90 ppm for P3HT belongs to the end group unit with a hydrogen. In P3HT-COOH this signal vanished but a new signal for the end group unit with a COOH appeared at 7.03 ppm. Changes also occur in the region of the α -CH₂ protons. As well as the main signal at 2.80 ppm there are signals at 2.62 ppm (in P3HT) or 3.01 ppm (in P3HT-COOH) belonging to the α -CH₂ protons of the respective end group units. These signals are at the same positions as the main α -CH₂ signals for the respective low molecular model molecules, 3-hexylthiophene (2.62 ppm) and 3HT-COOH (3.01 ppm). This is possible because the α -CH₂ protons are not directly connected to the conjugated system. The analogy shows that low molecular weight model molecules are efficient in identifying diverse end groups in P3HT. An integration of the signals at 2.8 ppm and 3.01 ppm in P3HT-COOH gives quantitative information about the amount of COOH end groups. The integral ratio of these two signals is 17 : 2, which is consistent with a difunctionalized polymer with 19 repeating units as determined by MALDI-TOF MS.

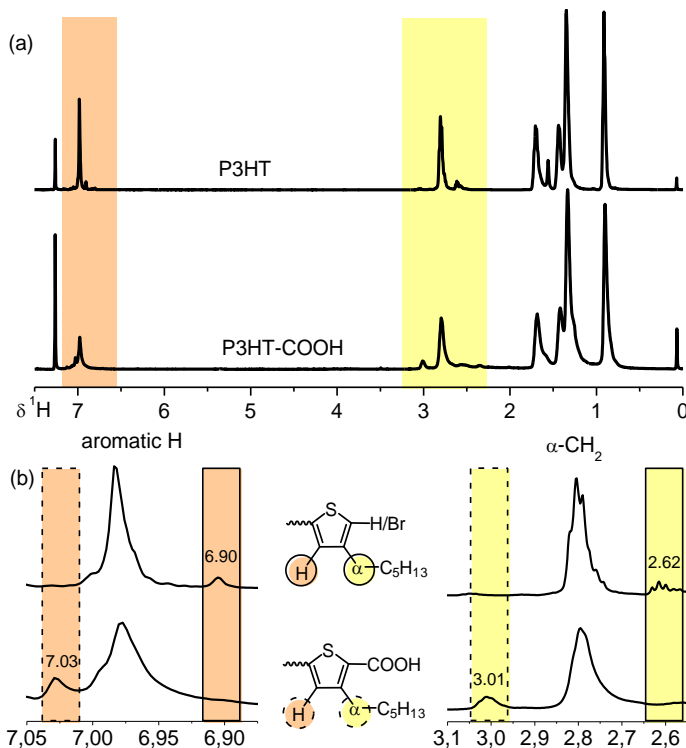


Fig. 2 (a) ^1H -NMR spectra of P3HT and P3HT-COOH for comparison measured at 500 MHz. (b) Close up of the aromatic region (left) and the α -CH₂ region (right) of the spectra. The rectangles mark the signals belonging to the end group units with the respective COOH or H/Br end groups.

Fig. 3a shows the normalized UV-vis spectra of both polymers measured on thin films (~200 nm) on quartz. While P3HT has vibronic bands typical of $\pi-\pi$ stacking, this fine structure is missing in the spectrum of P3HT-COOH. Additionally the maximum absorption (λ_{\max}) is significantly hypsochromically shifted from 506 nm in P3HT to 446 nm in P3HT-COOH. The hydrogen bonds in P3HT-COOH can fix the polymer chain in a disordered conformation and thus hinder the $\pi-\pi$ stacking. This assumption is also supported by the fact that P3HT-COOH shows no vibronic bands even after annealing. Hydrogen bonds are thermally stable interactions and hinder the comparatively weaker electrostatic $\pi-\pi$ interactions. Thus the missing $\pi-\pi$ stacking causes the hypsochromic shift of the λ_{\max} and the loss of the fine structure in the UV-vis spectrum. Another contribution to this blueshift of 60 nm is the electron-withdrawing nature of the carboxyl groups.

The missing order is further confirmed by wide angle X-ray diffraction measurements of bulk samples in Fig. 3b. Unfunctionalized P3HT shows typical reflections for regioregular poly(3-hexylthiophene) (h00)-reflections due to lamellar packing of main and side chains in the measured range, (00l)-reflections for the repeating distance of the aromatic rings along the main chain and (020)-reflections for the $\pi-\pi$ stacking distance.¹⁹ In contrast, the diffraction pattern of P3HT-COOH shows an almost completely amorphous structure. Thus the COOH end groups can form a hydrogen bonded network which hinders the typical crystallisation of regioregular P3HT.

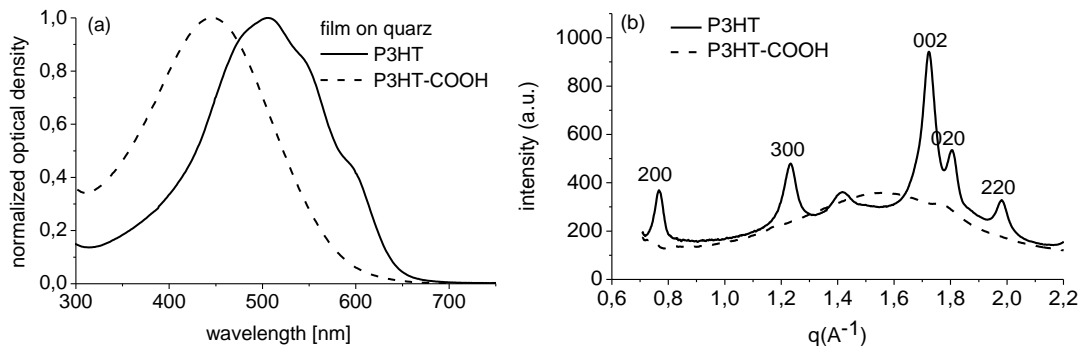


Fig. 3 (a) Normalized UV-vis spectra of P3HT (solid) and P3HT-COOH (dashed) measured on thin films (~200 nm) on quartz. (b) Wide angle X-ray scattering (WAXS) measurements of P3HT (solid) and P3HT-COOH (dashed) in bulk. (h00)-Reflections due to lamellar packing of main and side chains, (00l)-reflections for the repeating distance of the aromatic rings along the main chain and (020)-reflections for the π - π stacking distance. In comparison to the highly ordered P3HT, P3HT-COOH shows a rather amorphous structure in UV-vis and WAXS measurements.

Dye-uptake test on mesoporous TiO₂

To study the chemisorption of P3HT-COOH on mesoporous TiO₂, dye-uptake tests were performed on TiO₂ electrodes used for dye-sensitized solar cells. These electrodes consist of mesoporous TiO₂ prepared on top of a compact TiO₂ layer on FTO (fluorine-doped tin oxide) glass. Solutions (1 wt%) of P3HT and P3HT-COOH in CHCl₃ were applied to the substrates. Fig. 4 displays the substrates coated with (a) P3HT and (b) P3HT-COOH before and (c) P3HT and (d) P3HT-COOH after rinsing with chlorobenzene and the respective UV-vis absorption spectra after washing.

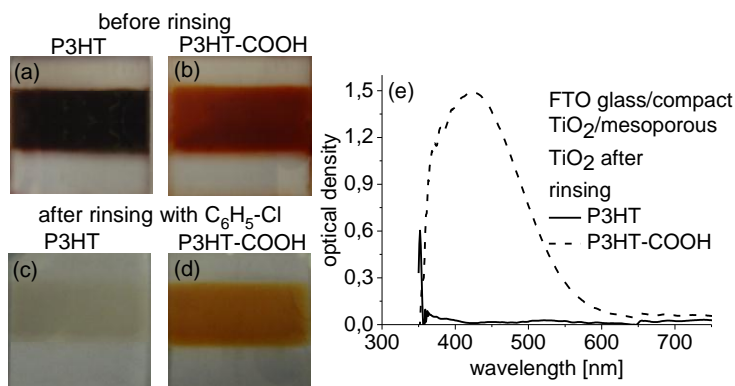


Fig. 4 Pictures of FTO glass/compact TiO₂/mesoporous TiO₂ coated with (a) P3HT, (b) P3HT-COOH before and (c) P3HT, (d) P3HT-COOH after rinsing with chlorobenzene. (e) UV-vis spectra of P3HT (solid) and P3HT-COOH (dashed) on FTO glass/compact TiO₂/mesoporous TiO₂ after rinsing with chlorobenzene. Unfunctionalized P3HT is rinsed away completely, while P3HT-COOH still shows an optical density of 1,5 at λ_{\max} after rinsing.

The difference in color between P3HT (purple) and P3HT-COOH (orange) coated TiO₂ substrates can be explained by the difference in the absorption spectra of the two polymers shown in Fig. 3a. It demonstrates that the missing π - π stacking and the hypsochromic shift of the λ_{\max} are visible with the naked eye. The UV-vis spectra of the substrates after rinsing (Fig.

4e) demonstrate that only P3HT-COOH chemisorbs on the mesoporous TiO₂. The optical density of P3HT-COOH after rinsing is still around 1.5 for I_{max} while P3HT is removed completely. The reason for the poor spectral quality at low wavelengths is the high UV absorption of the TiO₂-FTO substrate.

Application as a polymer sensitizer

The chemisorption test obviously demonstrates that the COOH groups in end group carboxylated P3HT-COOH are strong enough to anchor onto mesoporous TiO₂ and allow its use as a polymer sensitizer in dye-sensitized solar cells. To complete the device preparation, the P3HT-COOH coated mesoporous TiO₂ electrode was filled with a solid hole conductor 2,2',7,7'-tetrakis-(*N,N*-di-4-methoxyphenylamino)-9,9'-spiro-bifluorene (spiro-OMeTAD) and finally coated with a Au electrode. To prove that P3HT-COOH does not block the pores and allows filling of the whole mesoporous layer, scanning electron microscopy (SEM) images of the solar cell before and after filling with hole conductor are compared (Fig. 5). From the complete crosssection of such a solid-state cell (Fig. 5a), it is obvious that the hole conductor fills the sensitized film very efficiently even down to the bottom. The comparison of the coated titania and non-coated titania in Fig. 5b and c reveals the same. While in Fig. 5c, bare TiO₂ nanocrystals can be observed, the filling with spiro-OMeTAD smooths the edges of the crystals as seen in Fig. 5b. Since the image of the filled mesoporous TiO₂ layer in Fig. 5b is from the bottom of the solar cell, it proves that there is a deep infiltration. It can also be seen in the SEM image (Fig. 5a) that there is a very thin over standing layer of the solid hole conductor (spiro-OMeTAD) on top, which helps to avoid any shorting between the titania and top electrode.

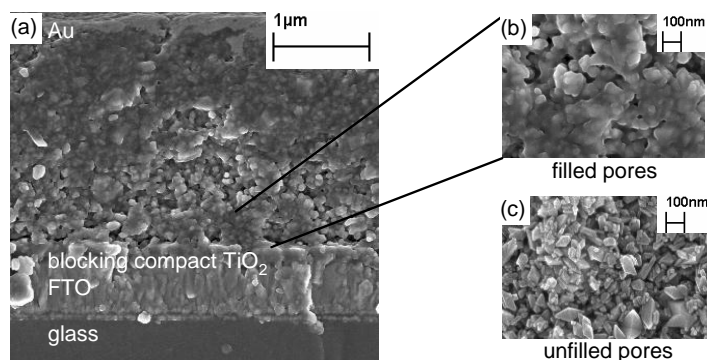


Fig. 5 (a) SEM image of the solar cell consisting of FTO/glass/compact TiO₂/mesoporous TiO₂/P3HT-COOH/spiro-OMeTAD/Au. (b) Magnification of the bottom part of the mesoporous TiO₂ layer filled with P3HT-COOH and spiro-OMeTAD. (c) SEM image of bare TiO₂ nanocrystals. Comparison of (b) and (c) proves that there is a deep infiltration of the hole conductor even down to the bottom most part of the active layer.

Fig. 6a shows a schematic representation of the device architecture and the current–voltage characteristics of the solar cell measured under AM 1.5 spectral conditions and under sunlight intensity. P3HT–COOH as a polymer sensitizer allows a better surface coverage of TiO₂, thus helping to avoid any recombination between the titania and hole conductor. Additionally, P3HT chains can also act as a hole conductor and thus contribute to charge transport. However these complementary functions could not be differentiated here in the first test results. The device with a P3HT–COOH as a polymer sensitizer shows good current–voltage characteristics in the dark and under illumination (Fig. 6b). A typical behavior of a photodiode without a current up to an open circuit voltage of 0.54 V is indicated by the dark current (dashed line). The short-circuit current is 3.7 mA cm⁻², the fill factor is 46% and the efficiency is 0.9%. These are very promising values for a polymer sensitized solid-state device.

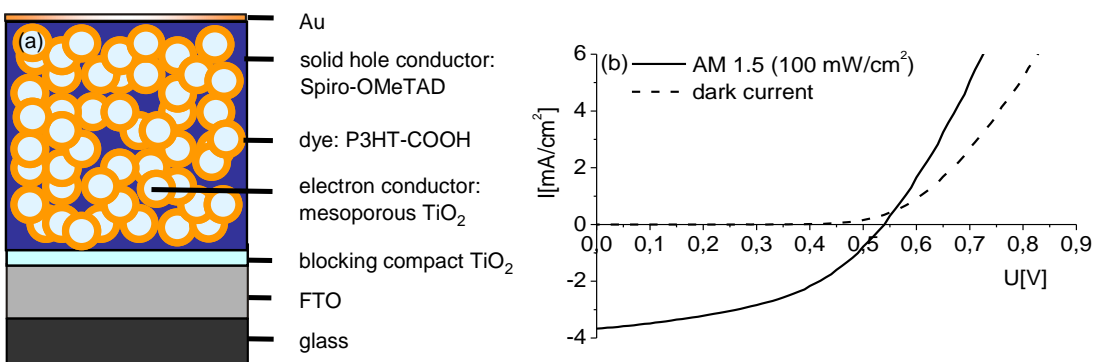


Fig. 6 (a) Device structure of the solar cell as a schematic. (b) Current–voltage characteristic of the solar cell in dark (dashed) and under illumination (solid) at AM 1.5 at 100 mW cm⁻². Typical values are: open circuit voltage = 0.54 V, short-circuit current = 3.7 mA cm⁻², fill factor = 46% and power conversion efficiency = 0.9%.

Conclusion

In conclusion, P3HT with COOH end groups was synthesized and its chemisorption on mesoporous TiO₂ was studied. The solar cells prepared with P3HT–COOH as a sensitizer and spiro-OMeTAD as a solid hole conductor showed a good efficiency of 0.9%. This is promising because the absorption of P3HT can be tuned by introducing different side chain substituents. Adjusting the chain length is also a method to improve the absorption, charge transport mobility and the performance of the solar cell.^{20,21} Since P3HT–COOH can also act as a hole conductor, this may enable the construction of solar cells with one component fulfilling both functions of sensitization and hole transport. Previously we have shown that dyes, carrying polymeric donor groups, can also retard recombination in a highly efficient way.²² It is not yet clear if this is also the case for P3HT–COOH. Therefore, detailed studies of transfer and recombination dynamics with time-resolved absorption spectroscopy are under investigation.

Experimental

General information

¹H-NMR spectra were recorded in chloroform on a Bruker DRX 500 spectrometer at 500 MHz. Coupling constants are given in Hz. SEC measurements were carried out in THF using a UV detector from Waters and a mixed-C PL-Gel (PL) column. Polystyrene was used as external standard and 1,2-dichlorobenzene as an internal standard for calibration. FTIR spectra were obtained from drop-cast films on silicon wafers with a BIORAD Digilab FTS-40. UV-vis measurements were performed with a U-3000 spectrometer from Hitachi. X-Ray measurements were made at the DUBBLE beamline ID 26 at ESRF in Grenoble. The used wavelength was 1.0415 Å and wide angle X-ray data were collected with a microstrip gas chamber detector. The monomer 2,5-dibromo-3-hexylthiophene and the catalyst 1,3-bis(diphenylphosphino)propanenickel(II) chloride [Ni(dppp)Cl₂] were synthesized according to the literature.^{23,24} All glass apparatus for polymerization and polymer-analogous reactions were baked out and cooled down under argon. Dry THF was distilled over calcium hydride and potassium. Tertiary butyl magnesium chloride 2.0 M in THF was purchased from Fluka and titrated according to Krasovskiy and Knochel.²⁵ Secondary butyl lithium [1.3 M solution in cyclohexane–hexane (Acros)] and CO₂ gas (99.995% <5 ppm H₂O, Rießner Gase) were used as received.

Solar cell preparation and characterization

The solar cells were prepared according to Karthikeyan and Thelakkat with nanocrystalline-titanium dioxide pastes from Energy Research Center (ECN), Netherlands.⁵ The hole conductor used was a mixture of spiro-OMeTAD, Li(CF₃SO₂)₂N and *tert*-butylpyridine (tbp) in an optimized composition.⁵ The I–V characterization was carried out using a calibrated xenon lamp with suitable filters to obtain AM 1.5 spectral irradiation and an intensity of 100 mW cm⁻². The lamp was regularly calibrated with ISE Call lab, Freiburg silicon solar cell (WPVS cell). The I–V values were recorded using a Keithley 6517 source measure unit.

Synthesis of P3HT

P3HT was synthesized according to published procedures.¹³ The polymer was used without purification by fractionation and yielded 2.25 g (70%) of a purple powder. GPC $M_p = 5900 \text{ gmol}^{-1}$, $M_n = 5200 \text{ gmol}^{-1}$, $M_w = 6000 \text{ gmol}^{-1}$, $M_w/M_n = 1.15$; MALDI-TOF MS $M_n = 3200 \text{ gmol}^{-1}$, $M_w = 3400 \text{ gmol}^{-1}$, $M_w/M_n = 1.15$;

δ_H (500 MHz; CDCl₃) 6.98 (1 H, s, Har), 6.90 (1 H, s, H_{ar} of end group unit with H end group), 2.80 (2 H, t, J_{αβ} 7.6, α-CH₂), 2.62 (2 H, t, α-CH₂ of end group unit with hydrogen), 1.85–1.50 (2 H, m, β-CH₂), 1.50–1.10 (6 H, m), 1.0–0.75 (3 H, m, CH₃); FTIR ν_{max} (film)/cm⁻¹ 3056w, 2955s, 2927s, 2857s, 1512w, 1456m, 1378m, 821m, 726w. UV-vis λ_{max} film)/nm 506.

Synthesis of P3HT-COOH

P3HT (566 mg, $M_n = 5200 \text{ g mol}^{-1}$) was dried under vacuum and dissolved in dry THF (243 mL). The solution was cooled down to -78 °C and secondary butyl lithium in hexane (2.3 mL, 2.99 mmol) was added in one portion. After 1 h of stirring the solution was heated to 40 °C for 20 min to inactivate excess s-BuLi. The solution was cooled down to -78 °C again and gaseous CO₂ was introduced for 1 h. After 30 min of additional stirring, the reaction was terminated with a mixture of HCl and methanol (v : v, 1 : 9). The functional polymer was filtered, washed with methanol and extracted with chloroform. Pure P3HT-COOH (576 mg) was isolated from the chloroform extract by precipitation into methanol, filtering and drying under vacuum.

GPC $M_p = 4700 \text{ gmol}^{-1}$, $M_n = 2800 \text{ gmol}^{-1}$, $M_w = 4700 \text{ gmol}^{-1}$, $M_w/M_n = 1.68$. δ_{H} (500 MHz; CDCl₃) 7.03 (1 H, s, H_{ar} of end group unit with COOH), 6.98 (1 H, br s, H_{ar}), 3.01 (2 H, t, α -CH₂ of end group unit with COOH), 2.80 (2 H, br, α -CH₂), 1.85–1.50 (2 H, br m, β -CH₂), 1.50–1.10 (6 H, br m), 1.0–0.75 (3 H, br m, CH₃); FTIR ν_{max} (film)/cm⁻¹ 3055w, 2957s, 2928s, 2857s, 2644b, 2542b, 1665s, 1526w, 1457s, 1439s, 1378w, 829m, 724w. UV-vis λ_{max} (film)/nm 446.

Acknowledgements

We acknowledge financial support for this research work from DFG SPP 1355 and Eurocores-Sons-II (SOHYDs). J. Bandara thanks the AvH foundation for stipend. R. H. Lohwasser thanks the elite network Bavaria for financial support. Further we acknowledge the European Synchrotron Radiation Facility for the ID26–DUBBLE–Dutch-Belgian beamline. Special thanks go to Christian Müller from Linköpings University for his support at the beamline and for evaluation of the X-ray data.

References

- (1) M. Grätzel, *Prog. Photovoltaics*, **2006**, 14, 442.
- (2) M. Grätzel, *Nature*, **2001**, 414, 338.
- (3) U. Bach, D. Lupo, P. Comte, J. E. Moser, F. Weissortel, J. Salbeck, H. Spreitzer, M. Grätzel, *Nature*, **1998**, 395, 583.
- (4) J. Hagen, W. Schaffrath, P. Otschik, R. Fink, A. Bacher, H. W. Schmidt, D. Haarer, *Synth. Met.*, **1997**, 89, 215.
- (5) C. S. Karthikeyan, M. Thelakkat, *Inorg. Chim. Acta*, **2008**, 361, 635.
- (6) K. Tennakone, V. P. S. Perera, I. R. M. Kottekoda, G. R. R. A. Kumara, *J. Phys. D: Appl. Phys.*, **1999**, 32, 374.
- (7) J. Yum, D. P. Hagberg, S. Moon, K. M. Karlsson, T. Marinado, L. Sun, A. Hagfeldt, M. K. Nazeeruddin, M. Grätzel, *Angew. Chem., Int. Ed.*, **2009**, 48, 1576.
- (8) G. K. R. Senadeera, K. Nakamura, T. Kitamura, Y. Wada, S. Yanagida, *Appl. Phys. Lett.*, **2003**, 83, 5470.
- (9) G. K. R. Senadeera, T. Kitamura, Y. Wada, S. Yanagida, *Sol. Energy Mater. Sol. Cells*, **2005**, 88, 315.
- (10) K. Shankar, G. K. Mor, H. E. Prakasam, O. K. Varghese, C. A. Grimes, *Langmuir*, **2007**, 23, 12445.
- (11) S. Yanagida, G. K. R. Senadeera, K. Nakamura, T. Kitamura, Y. Wada, *J. Photochem. Photobiol., A: Chem.*, **2004**, 166, 75.
- (12) H. Sirringhaus, N. Tessler, R. H. Friend, *Science*, **1998**, 280, 1744.
- (13) M. Jeffries-El, G. Sauve, R. D. McCullough, *Macromolecules*, **2005**, 38, 10346.
- (14) B. M. W. Langeveld-Voss, R. A. J. Janssen, A. J. H. Spiering, J. L. J. Van Dongen, E. C. Vonk, H. A. Claessens, *Chem. Commun.*, **2000**, 81.
- (15) J. Liu and R. D. McCullough, *Macromolecules*, **2002**, 35, 9882.
- (16) R. S. Loewe, P. C. Ewbank, J. Liu, L. Zhai and R. D. McCullough, *Macromolecules*, **2001**, 34, 4324.
- (17) R. Miyakoshi, A. Yokoyama, T. Yokozawa, *J. Am. Chem. Soc.*, **2005**, 127, 17542.
- (18) E. E. Sheina, J. Liu, M. C. Iovu, D. W. Laird, R. D. McCullough, *Macromolecules*, **2004**, 37, 3526.
- (19) S. Hugger, R. Thomann, T. Heinzel, T. Thurn-Albrecht, *Colloid Polym. Sci.*, **2004**, 282, 932.
- (20) R. J. Kline, M. D. McGehee, E. N. Kadnikova, J. Liu, J. M. J. Fréchet, *Adv. Mater.*, **2003**, 15, 1519.
- (21) W. Ma, J. Y. Kim, K. Lee, A. J. Heeger, *Macromol. Rapid Commun.*, **2007**, 28, 1776.
- (22) S. A. Haque, S. Hana, K. Peter, E. Palomares, M. Thelakkat, J. R. Durrant, *Angew. Chem., Int. Ed.*, **2005**, 44, 5744.
- (23) R. S. Loewe, M. S. Khersonsky and R. D. McCullough, *Adv. Mater.*, **1999**, 11, 250.
- (24) G. R. Van Hecke and W. Horrocks, *Inorg. Chem.*, **1966**, 5, 1968.
- (25) A. Krasovskiy and P. Knochel, *Synthesis*, **2006**, 5, 890.

12. List of Publications

1. R. H. Lohwasser, M. Thelakkat, "Synthesis of Amphiphilic Rod-Coil P3HT-*b*-P4VP Carrying a Long Conjugated Block using NMRP and Click Chemistry", submitted to *Macromolecules*.
2. C. Scharsich, R. Lohwasser, M. Sommer, U. Asawapirom, U. Scherf, M. Thelakkat, D. Neher, A. Köhler, "On the Control of Aggregate Formation in Poly(3-hexylthiophene) by Solvent, Molecular Weight and Synthetic Method", *J. Polym. Sci., Part B: Polym. Phys.*, accepted.
3. M. Zerson, E.-C. Spitzner, C. Riesch, R. Lohwasser, M. Thelakkat, R. Magerle, "Subsurface Mapping of Amorphous Surface Layers on Poly(3-hexylthiophene)", *Macromolecules*, **2011**, 44, 5874-5877.
4. R. H. Lohwasser, M. Thelakkat, "Toward Perfect Control of End Groups and Polydispersity in Poly(3-hexylthiophene) via Catalyst Transfer Polymerization", *Macromolecules*, **2011**, 44, 3388-3397.
5. B. Wrackmeyer, E. V. Klimkina, T. Kupcik, R. Lohwasser, "1,1-Ethylboration of Trimethyl(methoxypropargyl)- and Chloro(dimethyl)methoxypropargylsilane. A Novel 1,2,5-Oxasilaborolane", *Z. Naturforsch.*, **2011**, 66b, 98-102.
6. O. F. Pascui, R. H. Lohwasser , M. Sommer, M. Thelakkat, T. Thurn-Albrecht, K. Saalwächter, "High Crystallinity and Nature of Crystal-Crystal Phase Transformations in Regioregular Poly(3-hexylthiophene)", *Macromolecules* **2010**, 43, 9401–9410.
7. R. H. Lohwasser, M. Thelakkat, "Synthesis and Characterization of Monocarboxylated Poly(3-hexylthiophene)s via Quantitative End-Group Functionalization" *Macromolecules*, **2010**, 43, 7611–7616.
8. Z. Wu, A. Petzold, T. Henze, T. Thurn-Albrecht, R. H. Lohwasser, M. Sommer, M. Thelakkat, "Temperature and Molecular Weight Dependent Hierarchical Equilibrium Structures in Semiconducting Poly(3-hexylthiophene)", *Macromolecules*, **2010**, 43, 4646–4653.
9. R. H. Lohwasser, J. Bandara, M. Thelakkat, "Tailor-Made Synthesis of Poly(3-hexylthiophene) with Carboxylic End Groups and its Application as a Polymer Sensitizer in Solid-State Dye-Sensitized Solar Cells", *J. Mater. Chem.*, **2009**, 19, 4126-4130.

Danksagung

Vielen herzlichen Dank an alle, die direkt oder indirekt zum Gelingen dieser Arbeit beigetragen haben.

Zuerst möchte ich mich bei meinem Betreuer Prof. Dr. Mukundan Thelakkat für das spannende Thema, seine unermüdliche Bereitschaft zur Diskussion, seine konstruktive Kritik und die interessanten Einblicke in alle Facetten der Forschung bedanken. Auch die vielseitigen Kooperationen und die Möglichkeit meine Arbeit auf internationalen Tagungen vorzustellen, waren für mich eine große Bereicherung. Besonders deine menschliche Art, dein persönlicher und offener Umgang sind keine Selbstverständlichkeit. Vielen Dank!

Herrn Prof. Dr. H. W. Schmidt möchte ich für die Bereitstellung eines gut ausgestatteten Labors danken.

Die Universität Bayern e. V. hat mich mit einem Graduiertenstipendium finanziell drei Jahre lang unterstützt und auch die Kosten für Tagungen und Forschungsaufenthalte im Ausland übernommen. Danke!

Viele verschiedene Kooperationspartner haben mir gezeigt, wie viel mehr man durch unterschiedliche Blickwinkel über ein Thema lernen kann. Vielen Dank an Zhiyong Wu, Gaurav Gupta, Jens Balko, Prof. Saalwächter und Prof. Thurn-Albrecht von der Universität Halle, Christina Scharsich und Anna Köhler von der Universität Bayreuth, Mario Zerson und Prof. Magerle von der Universität Chemnitz sowie Chetan Raj-Singh und Harald Hoppe von der TU Ilmenau.

Mein herzlicher Dank gilt auch meinen Arbeitskollegen in der Makromolekularen Chemie 1 für die angenehme Arbeitsatmosphäre, die Hilfsbereitschaft, den lockeren Umgang und die fachlichen Diskussionen. Vor allem möchte ich mich beim GPC Team - Klaus Kreger, Robin Pettau, Christina Löffler, Michael Sommer, Andreas Lang und Katharina Neumann – bedanken, die geduldig und zügig meine große Anzahl an Proben gemessen habe. Vielen Dank, Klaus, für die Versuche mit verschiedensten Lösungsmittelkombinationen und die hilfreichen Diskussionen. Bei den „Afupo’s“ möchte ich mich für die Unterstützung und die netten Kochabende bedanken. Dankeschön vor allem an Bandara Jayasundera für die Einweisung in die Präparation der Solarzellen und die viele Arbeit die du investiert hast.

Großer Dank gilt auch unseren akademischen Räten, Techniker/innen und unserer Sekretärin: Dr. Christian Neuber, Dr. Reiner Giesa, Christina Löffler, Jutta Failner, Sandra Ganzleben, Doris Hanft, Andreas Küst, Helga Wietasch und Petra Weiß, die durch viele organisatorische Arbeiten im Hintergrund uns den Rücken frei halten.

Bei Helga möchte ich mich für ihre Unterstützungen bei der Synthese, aber vor allem für ihre gute Laune und den Spaß bedanken, den wir zusammen hatten. Auch wenn ich mal weg bin, wünsche ich dir jeden Donnerstag ein „Schönes Wochenende“.

Vielen Dank auch an meine Laborkollegen für viele fachliche Diskussionen, die lustige Atmosphäre, die persönliche Unterstützung und ein offenes Ohr.

Ein großes Dankeschön speziell an Marina Behr, Anne Neubig und Katharina Neumann fürs genaue Korrekturlesen der Arbeit, aber auch der einzelnen Manuskripte.

Ein besonderer Dank gilt dem Team am REM und TEM, die mich vor allem in den letzten Monaten dieser Arbeit tatkräftig unterstützt haben. Vielen Dank Carmen Kunert, Melanie Förtsch, Martina Heider, Annika Pfaffenberger, Dr. Beate Förster, Dr. Markus Drechsler und Werner Reichstein für euer Interesse und eure Ausdauer, bei den oft nicht ganz einfachen Proben.

Für die AFM Messungen möchte ich mich bei Kerstin Schindler und Zhicheng Zheng bedanken. Vielen Dank an Eva Betthausen und Joachim Schmelz für die DLS Einweisung und die Diskussionen, Christopher Synatschke und Dr. Anja Goldman für die Unterstützung am MALDI und Marietta Böhm für die GPC Messungen in der MCII.

Ein herzliches Dankeschön an meine Familie, für ihre uneingeschränkte Unterstützung in jeder Lebenslage, ihr offenes Ohr, ihre Motivation aber auch den Hinweis mal eine Pause zu machen.

Nicht zuletzt möchte ich dir, Markus, danken, für deine Geduld, deine Ruhe, die schöne gemeinsame Zeit und den Rückhalt, den du mir gibst.

Vielen Herzlichen Dank!

Erklärung

Hiermit erkläre ich, dass ich die Arbeit selbständig verfasst und keine anderen als die von mir angegebenen Quellen und Hilfsmittel benutzt habe.

Ferner erkläre ich, dass ich anderweitig mit oder ohne Erfolg nicht versucht habe, diese Dissertation einzureichen. Ich habe keine gleichartige Doktorprüfung an einer anderen Hochschule endgültig nicht bestanden.

Bayreuth, Dezember 2011

Ruth Lohwasser